Electromechanical couplings and growth instabilities in semiconductors

Laurent Guin

université PARIS-SACLAY

NNT : 2018SACLX105

Thèse de doctorat

Electromechanical Couplings and Growth Instabilities in Semiconductors

Thèse de doctorat de l'Université Paris-Saclay
préparée à l'École polytechnique

Ecole doctorale n°579 Sciences Mécaniques et Energétiques, Matériaux et Géosciences (SMEMAG)
Spécialité de doctorat : Mécanique des solides

Thèse présentée et soutenue à Palaiseau, le 14 décembre 2018, par

M. LAURENT GUIN

Composition du Jury :

M. Mathis PLAPP Directeur de recherche CNRS et Professeur, École polytechnique (Laboratoire de Physique de la Matière Condensée)	Président
M. Timothy HEALEY Professeur, Cornell University (Department of Mathematics)	Rapporteur
M. Roberto PARONI Professeur, Università di Pisa (Dipartimento di Ingegneria Civile e Industriale)	Rapporteur
M. Kaushik BHATTACHARYA Professeur, California Institute of Technology (Department of Mechanical and Civil Engineering)	Examinateur
M. Lionel BUCHAILLOT Directeur de recherche CNRS, Institut d'Électronique, de Microélectronique et de Nanotechnologie (IEMN)	Examinateur
M. Petros DAFNIOTIS Docteur Ingénieur, DuPont de Nemours (Transportation & Advanced Polymers)	Examinateur
M. Michel JABBOUR Professeur, École polytechnique (Laboratoire de Mécanique des Solides)	Directeur de thèse
M. Pere ROCA I CABARROCAS Directeur de recherche CNRS et Professeur, École polytechnique (Laboratoire de Physique des Interfaces et des Couches Minces)	Co-directeur de thèse
M. Nicolas TRIANTAFYLLIDIS Professeur, École polytechnique (Laboratoire de Mécanique des Solides)	Invité (Co-encadrant)
M. Jean RAPHANEL Directeur de recherche CNRS, École polytechnique (Laboratoire de Mécanique des Solides)	Invité

ELECTROMECHANICAL COUPLINGS AND GROWTH INSTABILITIES IN SEMICONDUCTORS

Laurent GUIN: *Electromechanical couplings and growth instabilities in semiconductors*, December 2018.

CONTENTS

ABSTRACT

In the last decades, solid mechanics has gone beyond its original issues of mechanical properties of materials and structures to embrace problems coming from other scientific fields and in particular physics. Semiconductors, the base materials of all electronic devices, are a prime example where crystalline solids show multiphysics couplings. Indeed, mechanics plays there an important role both in the fabrication process and in the operation of electronic devices.

In this work, we examine these two aspects by studying first the couplings between electronic transport phenomena and mechanical deformations and second the morphological instabilities that develop in semiconductor epitaxial growth.

First, developing a fully-coupled theory of deformable semiconductors that includes mechanical, electrical and electronic fields, we show for the first time the existence of an electronic contribution to mechanical stress. While for crystalline semiconductors this contribution is weak, the effect of strains on electronic transport remains significant through their modification on band energy levels, density of states and mobility of electrons and holes.

Considering the advent of new technologies of flexible electronics, we apply the general theory to compute through asymptotic expansions, the effect of bending—causing non-uniform strains—on the current-voltage characteristic of a p-n junction, the basic device of solar cells.

To complete this picture, we measure the changes induced by uniaxial stresses on the electronic characteristic of a silicon heterojunction solar cell.

In the second part of this work, going down to the atomic scale, we consider the problem of epitaxial growth on vicinal surfaces. On these surfaces, the crystal grows through the propagation of the atomic steps, which may develop step bunching, an instability whereby the regular step spacing breaks down, resulting in an alternating pattern of wide atomic terraces and step bunches.

Through a comprehensive linear stability analysis of the step dynamics governing equations, we discuss the influence of each physical mechanism on the step bunching instability. In particular, we clarify the impact on stability of the dynamics, of the recently pointed out adatom jump effect, and of elasticity, beyond the assumption of nearest-neighbor interactions.

In addition, we show that our general stability results, i.e., obtained without neglecting the dynamics terms, are significantly different from those derived with the quasistatic approximation, even in regimes of slow deposition or evaporation where the latter was considered sufficient. Not only valuable from a theoretical prospective, these new results provide possible explanations for some cases of step bunching observed in silicon and gallium arsenide.

In view of these new aspects, we reexamine the problem of step bunching under electromigration and show that the adatom jump and dynamics effects

do not affect the stability dependence on the direction of the electromigration current.

Finally, we investigate the mechanical properties at the atomic scale of another crystalline material with semiconducting properties, polycrystalline graphene. Using molecular dynamics simulations, we develop a cohesive zone model for fracture along grain boundaries.

RÉSUMÉ

Ces dernières décennies, la mécanique des solides est allée au-delà de ses problématiques originelles ayant trait aux propriétés mécaniques des matériaux et des structures pour embrasser des questions issues d'autres champs scientifiques et en particulier de la physique. Les semi-conducteurs, matériaux de base de tous les dispositifs électroniques, sont un bon exemple où des solides cristallins présentent des couplages mutiphysiques. En effet, la mécanique y joue un rôle important, à la fois dans le processus de fabrication et dans l'utilisation des dispositifs électroniques.

Dans ce travail, nous examinons ces deux aspects en étudiant dans une première partie les couplages entre les phénomènes de transport électronique et les déformations mécaniques et dans une seconde partie les instabilités morphologiques qui apparaissent lors de la croissance épitaxiale des semi-conducteurs.

Premièrement, en développant une théorie entièrement couplée des semi-conducteurs déformables qui inclut les champs mécaniques, électrique et électroniques, nous montrons, pour la première fois, l'existence d'une contribution électronique à la contrainte mécanique. Alors que pour les semi-conducteurs cristallins cette contribution est faible, l'effet des déformations sur le transport électronique demeure important par les modifications qu'elles induisent sur les niveaux d'énergie de bandes, les densités d'états et les mobilités des électrons et des trous.

Compte tenu de l'avènement de nouvelles technologies d'électronique flexible, nous mettons en application la théorie générale pour calculer, au moyen de développements asymptotiques, l'effet de la flexion – qui entraîne des déformations non uniformes – sur la caractéristique courant-tension d'une jonction p-n, la brique élémentaire des cellules solaires.

Pour compléter ce tableau, nous mesurons les changements induits par des contraintes uniaxiales sur la caractéristique électronique de cellules solaires silicium à hétérojonction.

Dans la deuxième partie de ce travail, en descendant à l'échelle atomique, nous étudions le phénomène de la croissance épitaxiale sur des surfaces vicinales. Sur ces surfaces, le cristal croît par propagation de marches atomiques, qui peuvent développer de la mise en paquets, une instabilité par laquelle l'espacement régulier entre marches est brisé, donnant lieu à un motif alternant entre de larges terrasses atomiques et des paquets de marches.

Au travers d'une analyse de stabilité linéaire exhaustive des équations de la dynamique des marches, nous discutons de l'influence de chaque mécanisme physique sur l'instabilité de la mise en paquets. En particulier, nous clarifions l'incidence sur la stabilité de la dynamique, de l'effet de saut d'adatomes ainsi que de l'élasticité, au-delà de l'hypothèse d'interactions de plus proches voisins.

De plus, nous montrons que nos résultats généraux de stabilité, c'est-à-dire obtenus sans négliger les termes dynamiques, sont significativement différents de ceux obtenus avec l'approximation quasi-statique, et ce, même dans les régimes de déposition ou d'évaporation lentes où cette dernière était considérée comme suffisante. Non seulement intéressants d'un point de vue théorique, ces nouveaux résultats fournissent des explications possibles pour certains cas de mise en paquets observés sur le silicium et l'arséniure de gallium.

Compte tenu de ces nouveaux aspects, nous réexaminons le phénomène de la mise en paquets sous électromigration et montrons que les effets de saut d'adatomes et de la dynamique n'affectent pas la dépendance de la stabilité à la direction du courant d'électromigration.

Enfin, nous étudions les propriétés mécaniques, à l'échelle atomique, d'un autre matériau cristallin aux propriétés semi-conductrices, le graphène polycristallin. En utilisant des simulations de dynamique moléculaire, nous développons un modèle de zone cohésive pour la rupture le long des joints de grains.

FOREWORD

The thesis work presented here was undertaken at École polytechnique between the *Laboratoire de Mécanique des Solides (LMS)* and the *Laboratoire de Physique des Interfaces et des Couches Minces (LPICM)* under the supervision of Professor Michel Jabbour and Professor Nicolas Triantafyllidis from the mechanics laboratory and Professor Pere Roca i Cabarrocas from the physics laboratory.

It is supported by the "IDI 2015" project funded by the IDEX Paris-Saclay, ANR-11-IDEX-0003-02.

Some of the results presented here have already been published as:

Guin, L., M. Jabbour, and N. Triantafyllidis (2018). "The p-n junction under nonuniform strains: general theory and application to photovoltaics." In: *Journal of the Mechanics and Physics of Solids* 110, pp. 54–79. DOI: 10.1016/j.jmps.2017.09.004.

Before addressing the questions developed in this manuscript, I first worked on the mechanical properties of a particular material that has some semi-conducting properties: graphene. Started at Columbia University under the supervision of Professor Jeffrey Kysar and Professor Jean Raphanel, this work was finalized at École polytechnique in my first year of PhD. I reproduce in Appendix F the corresponding article published as:

Guin, L., J. L. Raphanel, and J. W. Kysar (2016). "Atomistically derived cohesive zone model of intergranular fracture in polycrystalline graphene." In: *Journal of Applied Physics* 119.24, p. 245107. DOI: 10.1063/1.4954682.

REMERCIEMENTS

La connaissance scientifique ne se laisse pas aborder facilement. Les concepts scientifiques, les outils mathématiques, les dispositifs expérimentaux sont autant de sources de difficultés et d'obstacles à dépasser. Au contraire, les personnes qui m'ont entouré ces trois dernières années n'ont eu de cesse de prodiguer aide, soutien et encouragements. Aussi j'ai grand plaisir, au terme de cette étape, à réserver quelques mots pour les remercier.

En premier lieu, je souhaite remercier chaleureusement mes trois encadrants de thèse, Michel Jabbour, Pere Roca i Cabarrocas et Nicolas Triantafyllidis. Au delà de ce qu'ils m'ont transmis de leurs connaissances, de leur approche et de leur vision de la recherche scientifique, ils m'ont réservé une posture bienveillante et encourageante, à l'origine de relations de qualité. Combinant finement conduite, insistance, écoute et confiance ils m'ont offert la possibilité d'un réel épanouissement intellectuel tout en déployant des efforts notables pour m'initier dans toutes les dimensions de la recherche académique. Pour toutes ces raisons, je leur suis très reconnaissant.

Mes remerciements s'adressent également aux membres du jury pour l'attention et les commentaires qu'ils ont porté sur ce travail. En particulier, les rapporteurs, Roberto Paroni et Timothy Healey, ainsi que le président du jury Mathis Plapp et les examinateurs Kaushik Bhattacharya, Lionel Buchaillot et Petros Dafniotis. Je remercie également Jean Raphanel, membre invité du jury, qui m'a guidé, avec Jeffrey Kysar dans mes premiers pas dans la recherche scientifique. La qualité de cette première expérience a significativement contribué à mon choix de poursuivre en thèse.

L'environnement de travail des laboratoires LMS et LPICM ne peut être que célébré. A ce titre, je remercie vivement les ingénieurs des deux laboratoires et en particulier Vincent De Greef, Jean-Christophe Eytard, Hakim Gharbi, Jean-Charles Vanel et Wanghua Chen pour l'aide expérimentale qu'ils m'ont fournie et les utiles conseils qu'ils m'ont apportés.

Par ailleurs, je tiens à remercier l'ensemble des collègues doctorants, post-doctorants et permanents dont l'ouverture et la sympathie font la bonne ambiance des deux laboratoires. En particulier, j'adresse mes remerciements à ceux qui, par le hasard du calendrier, par le plaisir de leur compagnie et, pour certains, par leur amitié ont agréablement enrichi ces trois dernières années : Alexandre E.S., Alexandre J., Anchal, Anthony, Arthur, Blandine, Erato, Erwan, Florent, Jean-Pierre et Siva. A ces personnes, je joins mon ami fluidicien Léopold, inlassable scientifique venu apporté sa pierre à l'édifice et Jérémie qui m'a généreusement ouvert une porte sur la pratique musicale.

Enfin, ce petit bout de chemin jusqu'au doctorat doit évidemment beaucoup à l'exceptionnel noyau familial dont l'amour m'accompagne depuis les contrées ensoleillées.

Part I

A THEORY OF DEFORMABLE SEMICONDUCTORS WITH APPLICATION TO PHOTOVOLTAICS

1 INTRODUCTION

The discovery of semiconductors is one of the most significant scientific and technological breakthroughs of the second half of the twentieth century. Mechanical effects play an important role in the behavior of semiconductors, as first discovered by Bardeen and Shockley (1950). Strains were subsequently put to use in applications such as piezoresistors (Barlian et al., 2009), metal–oxide–semiconductor field-effect transistors (MOSFETs) which incorporate strained silicon technology to exploit the mobility enhancement induced by specific types of uniaxial stresses (Thompson et al., 2004, 2006; Chu et al., 2009), and quantum-well lasers, for which the changes induced in the band structure result in significant improvements of their performance (Adams, 2011; Coleman, 2000).

Different aspects of the coupling between the mechanical and electronic responses of semiconductors have been investigated by solid-state physicists and mechanicians. The emphasis in the first community is on scale bridging, i.e., predicting the influence of strain on the macroscopic properties, based on the electronic band structure. The second group, using methods of continuum mechanics and thermodynamics, has developed theoretical models of the coupled electro-mechanical problem. The goal of the present work is to derive, while using ideas from solid-state physics, a thermodynamically consistent and fully coupled continuum model of finitely deformable semiconductors, and, motivated by photovoltaics, to use this model to compute the current-voltage characteristic of a *p*-*n* junction under strain gradients. In addition, aware that in real life devices such as solar cells many parasitic phenomena —such as space charge recombination, surface recombination, internal resistance— lead to experimental current-voltage characteristic that deviate from the ideal one we measure experimentally the changes in current-voltage characteristics of solar cells induced by a uniaxial stress.

LITERATURE REVIEW In the solid-state physics literature, starting with the work of Bardeen and Shockley (1950), theoretical studies have addressed the effect of strain on the band structure of a semiconductor. The band structure, associated with the atomic lattice, determines the characteristics of the distribution and motion of electrons and holes in the semiconductor (Kittel, 2004). Modifications of the atomic lattice geometry due to mechanical strains induce changes in the band energy levels, described by *deformation potentials*, and in the densities of states of the bands (Bardeen and Shockley, 1950; Herring and Vogt, 1956; Bir et al., 1974; Fischetti and Laux, 1996). These changes in the band structure affect, in turn, the mobility of charge carriers, which are responsible for the semiconductor's *piezoresistive effect* (Smith, 1954; Kanda, 1991; Kleimann et al., 1998).

Aside from the dependence of electronic parameters on strain, it was found that the presence of a *nonuniform* strain field in a semiconductor changes the nature of the electronic transport. Indeed, standard models of electronic transport rely on the assumption of spatial homogeneity of the semiconductor, whereas the presence of nonuniform strains result in a *inhomogeneous* semiconductor. While Bardeen and Shockley (1950) noticed early on the possibility of "*gradual shifts in energy bands resulting from deformations of the crystal lattice*," it is Kroemer (1957) who introduced the notion of *quasi-electric field* to account for the effects of spatial gradients in material properties (band's energy level, density of states) on the electronic transport, giving as an example of an inhomogeneous semiconductor "*a semiconductor under nonuniform elastic strain*." Later, the drift-diffusion equations modeling the electron and hole transport were generalized to inhomogeneous semiconductors (Marshak and Vliet, 1978; Marshak and Vliet, 1984; Manku and Nathan, 1993) by adding two new drift terms involving the gradient of the conduction and valence band edge energies and the gradient of densities of states. These generalizations were derived from fundamental computations based on the Boltzmann transport equation for free carriers in inhomogeneous semiconductors.

In addition to strain-induced changes in the electronic properties of the semiconductor itself, studies were carried out on the effect of uniform strains on the electronic response of a semiconductor device: *the piezojunction effect*. Both experimentally and with microscopic models, the piezojunction effect was studied for devices such as the *p-n* junction (see e.g., Wortman et al., 1964; Wortman and Hauser, 1966; Kanda, 1967) and, more recently, the transistor in the thorough work of Creemer and French (2000) (see also Creemer et al., 2001; Creemer, 2002). It was found that strains of the order of 10^{-3} can change the current in the device by about ten percent. These works are concerned with devices at the scale of the micrometer for which classical models are valid. Recently, Freund and Johnson (2001) (see also Johnson et al., 1998; Johnson and Freund, 2001) addressed the influence of strain on electronic devices at the nanometer scale for which a quantum mechanical description becomes necessary. Their approach solves in two steps the mechanics and electronics problems. First the boundary-value problem (BVP) associated with the purely mechanical response is solved, the result of which is then used to write the Schrödinger equation for the wave-function of electrons with perturbations induced by the strain field. In our analysis of the *p-n* junction in Chapter 3, we develop such a two-step approach in the framework of classical models of electronic transport, which has not been carried out before.

In all the above studies, mostly in the solid-state physics literature, the question considered concerns the influence a strain field has on the electronic transport properties of a semiconductor. However, the mechanical, electrostatic and electronic responses of semiconductors interact through mutual couplings. In the mechanics literature, semiconductors are modeled as continua, leading to boundary-value problems where the mechanical, electrostatic and electronic fields are coupled. This was done by Lorenzi and Tiersten (1975), who developed a theory of the fully coupled problem where the unknown fields consist

of the strain field, the electromagnetic field, and the free carriers distributions. The governing equations of the coupled problem are established by writing the general principles of mechanics, electromagnetism and electronics, and restrictions on the form of the constitutive relations are derived from thermodynamics. However, in this work, no explicit form is given for the constitutive relations, which makes it difficult to establish a connection with the governing equations used in semiconductor physics. This point is addressed in Section 2.3 of the present work.

More recently, Xiao and Bhattacharya (2008) derived a theory of the deformable semiconductor in the context of semiconducting ferroelectrics, their main focus being on the polarization dependence of strain and the associated phase changes. Whereas one can find common features between the general theory developed by these authors and ours, the couplings addressed are not the same. In particular, as a result of their neglect of strain effects on electronic properties, the chemical potential that appears in their model is, unlike ours, independent of strain.

Finally, in relation to the mathematical analysis of continuum models for electronic transport in rigid semiconductors, we refer the reader to the book of Markowich (1986) and the papers of Markowich and Ringhofer (1984) and Please (1982). Given that boundary-value problems of semiconductor devices are singularly perturbed at the interfaces (e.g., at *p*-*n* interfaces), these authors developed asymptotic methods to address the existence and analytical computation of solutions to these problems.

SUMMARY OF THE WORK In the present work, we first derive a fully coupled electrostatic-electronic-mechanical theory of deformable semiconductors wherein the thermodynamically consistent formulation of the interaction between electric field and polarizable matter is combined with the modeling of the transport of charge carriers. Specializing to crystalline semiconductors and using results of mechanics, electromagnetism and statistical physics, a functional form of the free energy—from which the constitutive relations derive—is proposed. This establishes a link with applications and provides a different insight into the transport equations of the semiconductor physics literature. In the derivation of constitutive relations, a new mechanism is uncovered: the electronic state (electron and hole densities) contributes to the mechanical equilibrium through a new term in the total stress. The interest of writing the equations of the fully coupled problem, along with explicit constitutive relations, is that the orders of magnitude of the mechanical, electrostatic and electronic effects can be compared. We find that, for crystalline silicon, the effect of the electronics and electrostatics on the mechanical equilibrium can be neglected. This explains why, in applications of interest, the mechanical problem can be solved independently, while there remains, as the coupling of importance, the effect of strain on the electronic transport. We hence justify the implicit assumption of the solid-state physics literature that the effect of strain on electronics can be studied on its own, noting that, in other settings to be determined, the electronic contribution to the stress could become significant.

Following the development of the general theory, we consider an application in which strain non-uniformity plays an essential role. Motivated by the strain effects on the performance of photovoltaic cells—for which it has been shown that uniform strains play a role (Lange et al., 2016)—we compute the current-voltage response of a *p-n* junction subjected to nonuniform strains which result from bending. Using asymptotic expansions of the generalized drift-diffusion equations, we compute, to first order in strain, the changes in current-voltage characteristic. We show that the effect of nonuniform strain is equivalent to that of a uniform strain evaluated at a particular mid-point of the *p-n* junction. With this result, we compute the change in dark current of a typical monocrystalline silicon solar cell and find variations up to twenty percent for strains of the order of 0.2%.

Given that actual solar cells do not simply behave as ideal *p-n* junctions, we carry out an experimental study of the changes that strains induce on their dark current-voltage characteristics. To this end, we use silicon heterojunction solar cells loaded under uniaxial stress along the $\langle 110 \rangle$ crystallographic direction. From the current-voltage characteristics measured at various strains (maximum strain 7×10^{-4}) we obtain the strain-dependence of the diffusion saturation current. Changes up to -3% are obtained, and the reversibility of the these changes with strain is verified. Noting a large uncertainty of the theoretical predictions —essentially due to a limited knowledge of the strain-induced change in the density of states of the valence band—- the magnitude of the strain effect is found in agreement with theoretical predictions for that particular crystal direction.

OUTLINE This part is organized as follows: In Chapter 2, we derive a continuum theory of deformable semiconductors, that accounts for coupling between mechanics, electrostatics and charge-carrier transport. The balance laws are formulated in Section 2.1 and restrictions on the constitutive relations are obtained in Section 2.2. Section 2.3 specializes to crystalline semiconductors by providing explicit forms of the constitutive relations.

We then compute in Chapter 3 the strain-induced change in the current-voltage characteristic of a *p-n* junction under bending. The electronic transport problem is set in a one-dimensional framework in Section 3.1 and then solved using asymptotic methods in Section 3.2. The results are applied in Section 3.3 to determine the change in the dark current of a typical monocrystalline silicon solar cell deformed on a curved surface. Details of the 3D-to-1D reduction of the electronic parameters and the choice of the resulting 1D coefficients for silicon are given in Appendix A, while the asymptotic expansions are detailed in Appendix B.

Finally, in Chapter 4 we report the experimental results of the effect of strain on the dark current-voltage characteristic of the silicon heterojunction solar cell. The characteristics and fabrication process of the solar cell are given in Section 4.1 while the measurements and predictions of the strain effect are discussed in Section 4.2 and Section 4.3, respectively.

2

CONTINUUM FORMULATION FOR DEFORMABLE SEMICONDUCTORS

In this chapter, we derive the field equations that govern the mechanical, electromagnetic and electronic responses of a finitely deformable semiconductor.

Denote by $\mathcal{B}_0$ and $\mathcal{B}_t$ the regions of space occupied by the semiconductor in the reference and current configurations, respectively. A material point with position $\mathbf{X}$ in the reference configuration is mapped at time t to the spatial point $\mathbf{x} = \chi(\mathbf{X}, t)$.

The semiconductor consists of a continuum with electron-donor and electron-acceptor impurities, rigidly bound to it, with concentrations[1] $N_d(\mathbf{x}, t)$ and $N_a(\mathbf{x}, t)$, respectively. Since the impurities are bound to the continuum, the dependence on time of the functions $N_d(\mathbf{x}, t)$ and $N_a(\mathbf{x}, t)$ is solely due to the motion of the continuum. We assume that the donors and acceptors are ionized (an assumption that is valid in practice at room temperature for silicon, see Sze and Ng, 2006), so that the nuclei induce a volume charge density $q\rho C$ where q is the elementary charge, $\rho(\mathbf{x}, t)$ the mass density and $C(\mathbf{x}, t)$ is defined by

$$C := N_d - N_a. \tag{2.1}$$

Charge transport in the semiconductor occurs through free carriers, which consist of electrons (of charge $-q$) and holes (of charge q) moving freely in the conduction and valence bands, respectively. Note that the holes, located as they are in the valence band, represent an absence of electrons in that band. The two bands spread over the entire semiconductor and the concentrations of electrons in the conduction band and of holes in the valence band are denoted by $n(\mathbf{x}, t)$ and $p(\mathbf{x}, t)$, respectively. As a result, the charge density reads

$$q\rho(C + p - n). \tag{2.2}$$

In addition to the spatial motion of electrons and holes within their bands, it is possible for an electron to jump locally between the valence and conduction bands, an event represented by the recombination or generation of an electron-hole pair. Aside from the charges of impurities, the bound charges due to the polarizability of the material are accounted for by the specific polarization $\mathbf{P}(\mathbf{x}, t)$ which represents dipole moment per unit mass.

Given that material velocities in deformable semiconductors are negligible with respect to the speed of light and restricting attention to electrical loading at sufficiently low frequency, the magnetic effects are expected to be negligible compared to the electric ones. We hence ignore all the magnetic fields (magnetic field, magnetic induction, magnetization).

1 Throughout the paper, *concentration* denotes number of particles (atoms, ions, electrons or holes) per unit mass.

In establishing the field governing equations, we write the balance laws in the current configuration on *material control volumes* $\mathcal{P}_t \subseteq \mathcal{B}_t$. To model the coupling between the mechanics and the electric field, we follow the approach of Kovetz (2000),[2] while the energetics associated with the transport of free carriers is written in the vein of the works of Gurtin and Vargas (1971) and Fried and Gurtin (1999, 2004) on the transport of chemical species. These works, and consequently the present one, follow the philosophy of the Coleman-Noll procedure (Coleman and Noll, 1963) to obtain information on the constitutive relations.

Note that for tensor calculus we follow the coordinate-free dyadic notation: for any vector fields $\mathbf{v}(\mathbf{x},t)$ and $\mathbf{w}(\mathbf{x},t)$ and rank-2 tensor fields $\mathbf{T}(\mathbf{x},t)$ and $\mathbf{R}(\mathbf{x},t)$, we have in a Cartesian basis:

$$\begin{cases} (\nabla\mathbf{v})_{ij} = v_{j,i}, \quad (\mathbf{v}\nabla)_{ij} = v_{i,j}, \quad (\nabla\cdot\mathbf{v}) = v_{i,i}, \qquad (\nabla\cdot\mathbf{T})_i = T_{ji,j}, \\ (\mathbf{v}\mathbf{w})_{ij} = v_i w_j, \ (\mathbf{T}\cdot\mathbf{v})_i = T_{ij}v_j, \quad \mathbf{T}\cdot\cdot\mathbf{R} = T_{ik}R_{ki}, \qquad \mathbf{T}:\mathbf{R} = T_{ik}R_{ik}. \end{cases} \tag{2.3}$$

2.1 GENERAL PRINCIPLES

First, we write the general principles: the laws of electromagnetism and the usual balance laws of continuum mechanics and thermodynamics.

2.1.1 *Maxwell equations*

Let $\mathbf{d}(\mathbf{x},t)$ be the electric displacement related by definition to the electric field $\mathbf{e}(\mathbf{x},t)$ and specific polarization $\mathbf{P}(\mathbf{x},t)$ by

$$\mathbf{d} = \epsilon_0\mathbf{e} + \rho\mathbf{P}, \tag{2.4}$$

where ϵ_0 is the vacuum permittivity. Where the fields are sufficiently smooth, local form of the Gauss's law reads

$$\nabla\cdot\mathbf{d} = q\rho(C + p - n). \tag{2.5}$$

Further, under the hypothesis of negligible magnetic fields, Maxwell-Faraday's law has the form

$$\nabla\times\mathbf{e} = \mathbf{0}, \tag{2.6}$$

from which we infer the existence of an electric potential $\varphi(\mathbf{x},t)$ defined up to a constant by

$$\mathbf{e} = -\nabla\varphi. \tag{2.7}$$

Finally, denoting by $\boldsymbol{\jmath}(\mathbf{x},t)$ the total current density—of conduction and convection—of free charges, Ampère's law, in view of the negligible magnetic fields, reduces to

$$\frac{\partial\mathbf{d}}{\partial t} = -\boldsymbol{\jmath}. \tag{2.8}$$

2 For the equivalence between alternative formulations of the balance laws for electromagnetic continua see Steigmann (2009)

Note that Maxwell equations are valid not only in the semiconductor but in surrounding space as well.

2.1.2 *Mass conservation*

Assuming that electrons and holes have no mass, the integral form of mass conservation reads

$$\frac{\mathrm{d}}{\mathrm{d}t}\int_{\mathcal{P}_t}\rho\,\mathrm{d}v = 0, \tag{2.9}$$

which, by the Reynolds transport theorem, yields the local form

$$\dot{\rho} + \rho(\nabla\cdot\dot{\mathbf{x}}) = 0, \tag{2.10}$$

where the superposed dot denotes the material time derivative.

2.1.3 *Balance of free carriers*

Let $\jmath_n(\mathbf{x},t)$ be the current density of free electrons (number of electrons per unit time and surface area) and denote by $R(\mathbf{x},t)$ the source/sink term[3] that accounts for the creation and destruction of electrons in the conduction band due to the recombination-generation of electron-hole pairs (see e.g., Pierret, 1987, Chapter 5). The balance of electrons in the conduction band reads in integral form

$$\frac{\mathrm{d}}{\mathrm{d}t}\int_{\mathcal{P}_t}\rho n\,\mathrm{d}v = -\int_{\mathcal{P}_t}R\,\mathrm{d}v - \int_{\partial\mathcal{P}_t}\jmath_n\cdot\mathbf{n}\,\mathrm{d}a, \tag{2.11}$$

where $\mathbf{n}$ denotes the outward unit normal to $\partial\mathcal{P}_t$. Localization of (2.11) furnishes

$$\rho\dot{n} = -R - \nabla\cdot\jmath_n. \tag{2.12}$$

Similarly, denoting by $\jmath_p(\mathbf{x},t)$ the hole current density, the local form of the balance of holes in the valence band is given by

$$\rho\dot{p} = -R - \nabla\cdot\jmath_p. \tag{2.13}$$

Note that it is the same R that appears in (2.12) and (2.13). As illustrated in Figure 2.1, the case $R>0$ ($R<0$) accounts for the transition of an electron from the conduction to the valence band (from the valence to the conduction band), i.e., a recombination (generation) of an electron-hole pair. While in practice these transitions may involve states where electrons are located in intermediate trap levels, by using a unique term R, we consider that in the final balance of the recombination-generation processes, intermediate states are not occupied.

Finally note that the total current density of free charges appearing in Ampère's law (2.8) can be written in terms of $\jmath_n$ and $\jmath_p$ as

$$\jmath = q\rho(C+p-n)\dot{\mathbf{x}} + q(\jmath_p - \jmath_n). \tag{2.14}$$

3 R is defined as the number of electron that *leave* the conduction band per unit time and per unit volume, which justifies the minus sign in (2.11).

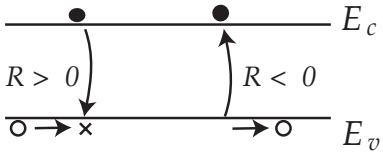

Figure 2.1: Schematic of interband recombination-generation of electron-hole pairs. When $R > 0$, an electron transitions from the conduction to the valence band, where it fills a hole, thereby reducing the total number of holes in the valence band by one. Conversely, for $R < 0$, the transition of an electron to the conduction band creates a hole in the valence band.

2.1.4 *Balance of linear momentum*

For the balance of linear momentum, we follow the approach in Kovetz (2000) by introducing a total Cauchy stress tensor $\boldsymbol{\sigma}(\mathbf{x}, t)$ whose related total traction $\mathbf{t} = \mathbf{n} \cdot \boldsymbol{\sigma}$ accounts for the force per unit area exerted across an elementary oriented surface $\mathbf{n}\mathrm{d}a$ by both the nearby material and the electric field. In that way, we assume the action of the electric field on matter to be completely described by surface forces distributed in the entire body, whose values are provided by a constitutive relation along with the mechanical surface tractions.

With that prospective, denoting by $\mathbf{f}(\mathbf{x}, t)$ the (purely mechanical) specific body force, the balance of linear momentum reads

$$\frac{\mathrm{d}}{\mathrm{d}t} \int_{\mathcal{P}_t} \rho \dot{\mathbf{x}} \, \mathrm{d}v = \int_{\mathcal{P}_t} \rho \mathbf{f} \, \mathrm{d}v + \int_{\partial \mathcal{P}_t} \mathbf{t} \, \mathrm{d}a. \tag{2.15}$$

Localization then yields

$$\rho \ddot{\mathbf{x}} = \nabla \cdot \boldsymbol{\sigma} + \rho \mathbf{f}. \tag{2.16}$$

2.1.5 *Balance of angular momentum*

Denoting by $\times$ the cross product, the balance of angular momentum of a material volume $\mathcal{P}_t$ written with respect to the origin O reads

$$\frac{\mathrm{d}}{\mathrm{d}t} \int_{\mathcal{P}_t} \mathbf{x} \times (\rho \dot{\mathbf{x}}) \, \mathrm{d}v = \int_{\mathcal{P}_t} \mathbf{x} \times (\rho \mathbf{f}) \, \mathrm{d}v + \int_{\partial \mathcal{P}_t} \mathbf{x} \times \mathbf{t} \, \mathrm{d}a, \tag{2.17}$$

Consistent with (2.15), all electrical contributions to the external moment are included in the surface density of moment $\mathbf{x} \times \mathbf{t}$.

By a classic derivation, applied here to the total stress tensor, one can show (see e.g., Chadwick, 1976) that (2.17) combined with (2.16) leads to the symmetry of the total Cauchy stress tensor:

$$\boldsymbol{\sigma} = \boldsymbol{\sigma}^T. \tag{2.18}$$

2.1.6 *Energy balance*

Let $\varepsilon(\mathbf{x}, t)$ be the total specific energy[4] (i.e., the sum of the kinetic, internal, and electrostatic energies per unit mass). Denote by

$$\mathcal{M} := \int_{\mathcal{P}_t} \rho \mathbf{f} \cdot \dot{\mathbf{x}} \, \mathrm{d}v + \int_{\partial \mathcal{P}_t} \mathbf{t} \cdot \dot{\mathbf{x}} \, \mathrm{d}a \tag{2.19}$$

the power expended by body and surface forces,

$$\mathcal{Q} := \int_{\mathcal{P}_t} \rho r \, \mathrm{d}v - \int_{\partial \mathcal{P}_t} \mathbf{q} \cdot \mathbf{n} \, \mathrm{d}a \tag{2.20}$$

the heating due to heat source $r(\mathbf{x}, t)$ and heat flux density $\mathbf{q}(\mathbf{x}, t)$,

$$\mathcal{R} := - \int_{\partial \mathcal{P}_t} [(\dot{\mathbf{x}} \times \mathbf{d}) \times \mathbf{e}] \cdot \mathbf{n} \, \mathrm{d}a \tag{2.21}$$

the electric energy flux density,[5] and let

$$\mathcal{S} := - \int_{\partial \mathcal{P}_t} (\mu_n \jmath_n + \mu_p \jmath_p) \cdot \mathbf{n} \, \mathrm{d}a \tag{2.22}$$

be the energy flow associated to free carriers, where $\mu_n(\mathbf{x}, t)$ and $\mu_p(\mathbf{x}, t)$ are the chemical potentials of electrons and holes defined as the energy carried by these two particles, respectively.[6] The energy balance applied to $\mathcal{P}_t$ reads

$$\frac{\mathrm{d}}{\mathrm{d}t} \int_{\mathcal{P}_t} \rho \varepsilon \, \mathrm{d}v = \mathcal{M} + \mathcal{Q} + \mathcal{R} + \mathcal{S}, \tag{2.23}$$

Localization delivers

$$\rho \dot{\varepsilon} = \rho \mathbf{f} \cdot \dot{\mathbf{x}} + \nabla \cdot (\boldsymbol{\sigma} \cdot \dot{\mathbf{x}}) + \rho r - \nabla \cdot \mathbf{q} - \nabla \cdot [(\dot{\mathbf{x}} \times \mathbf{d}) \times \mathbf{e}] - \nabla \cdot (\mu_n \jmath_n) - \nabla \cdot (\mu_p \jmath_p). \tag{2.24}$$

Further, we note that the material time derivative formula applied to $\mathbf{d}$, when combined with the Ampère's law (2.8), the Gauss's law (2.5) and (2.14) yields

$$\dot{\mathbf{x}} \cdot \nabla \mathbf{d} = \dot{\mathbf{d}} - \frac{\partial \mathbf{d}}{\partial t} = \dot{\mathbf{d}} + (\nabla \cdot \mathbf{d}) \dot{\mathbf{x}} + q(\jmath_p - \jmath_n), \tag{2.25}$$

which, on appeal to standard tensor identities,[7] allows us to rewrite the local flux of electric energy density as

$$-\nabla \cdot [(\dot{\mathbf{x}} \times \mathbf{d}) \times \mathbf{e}] = [\dot{\mathbf{d}} + q(\jmath_p - \jmath_n)] \cdot \mathbf{e} + [-\mathbf{d}\mathbf{e} + (\mathbf{e} \cdot \mathbf{d})\mathbf{I}] \cdot \cdot (\dot{\mathbf{x}} \nabla), \tag{2.26}$$

4 Note that in the present formulation, the potential energy of the charge densities in the electric potential φ is not included in ε. Accordingly, the power of the usual Lorentz force (that derives from φ in the absence of magnetic field) on free charges is part of the external supply: it comes as a part of the power contribution $\mathcal{R}$.

5 The expression $(\dot{\mathbf{x}} \times \mathbf{d}) \times \mathbf{e}$ for the electric energy flux density results from the specialization of the cross product $\mathcal{E} \times \mathcal{H}$ of the Galilean invariants of the magnetic and electric fields (Kovetz, 2000, Chapter 15) to situations in which the magnetic field is absent.

6 In this way, we follow the approach of Gurtin and Vargas (1971), noting that alternative formulations are possible (Müller, 1968; Goddard, 2011). In their Remark 2.3, Gurtin and Vargas show that the different formulations are equivalent.

7 These tensor identities are
$\nabla \cdot ((\dot{\mathbf{x}} \times \mathbf{d}) \times \mathbf{e}) = (\nabla \times (\dot{\mathbf{x}} \times \mathbf{d})) \cdot \mathbf{e} - (\dot{\mathbf{x}} \times \mathbf{d}) \cdot (\nabla \times \mathbf{e})$, $\nabla \times (\dot{\mathbf{x}} \times \mathbf{d}) = \dot{\mathbf{x}}(\nabla \cdot \mathbf{d}) - \mathbf{d}(\nabla \cdot \dot{\mathbf{x}}) + \mathbf{d} \cdot (\nabla \dot{\mathbf{x}}) - \dot{\mathbf{x}} \cdot (\nabla \mathbf{d})$.

where $\mathbf{I}$ is the identity rank-2 tensor. Finally, on introducing the total specific internal energy

$$u := \varepsilon - \frac{1}{2}\dot{\mathbf{x}} \cdot \dot{\mathbf{x}} \tag{2.27}$$

and using the linear momentum balance (2.16) to eliminate the power of the external body force as well as the balances (2.12) and (2.13) of free carriers, the energy balance (7.18) has the form

$$\begin{aligned}\rho \dot{u} = {} & [\boldsymbol{\sigma} - \mathbf{d}\mathbf{e} + (\mathbf{e} \cdot \mathbf{d})\mathbf{I}] \cdot\cdot (\dot{\mathbf{x}} \nabla) + \mathbf{e} \cdot \dot{\mathbf{d}} + \rho r - \nabla \cdot q \\ & - \nabla(\mu_n - q\varphi) \cdot \jmath_n - \nabla(\mu_p + q\varphi) \cdot \jmath_p + \rho(\mu_n \dot{n} + \mu_p \dot{p}) + (\mu_n + \mu_p) R.\end{aligned} \tag{2.28}$$

2.1.7 *Entropy imbalance*

Let η be the specific entropy, and denote by T the absolute temperature. The second law of thermodynamics takes the form of the classical Clausius-Duhem inequality:

$$\frac{\mathrm{d}}{\mathrm{d}t} \int_{\mathcal{P}_t} \rho \eta \, \mathrm{d}v \geq \int_{\mathcal{P}_t} \frac{\rho r}{T} \, \mathrm{d}v + \int_{\partial \mathcal{P}_t} \frac{\mathbf{q} \cdot \mathbf{n}}{T} \, \mathrm{d}a. \tag{2.29}$$

When combined with (2.28), the local form of (2.29) takes the form

$$\begin{aligned}& \rho(T\dot{\eta} - \dot{u}) + [\boldsymbol{\sigma} - \mathbf{d}\mathbf{e} + (\mathbf{e} \cdot \mathbf{d})\mathbf{I}] \cdot\cdot (\dot{\mathbf{x}} \nabla) + \mathbf{e} \cdot \dot{\mathbf{d}} + \rho(\mu_n \dot{n} + \mu_p \dot{p}) \\ & \quad - \nabla(\mu_n - q\varphi) \cdot \jmath_n - \nabla(\mu_p + q\varphi) \cdot \jmath_p + (\mu_n + \mu_p) R - \frac{1}{T} \mathbf{q} \cdot (\nabla T) \geq 0.\end{aligned} \tag{2.30}$$

Introducing the specific free-energy

$$\psi := u - T\eta - \frac{\epsilon_0}{2\rho} \mathbf{e} \cdot \mathbf{e}, \tag{2.31}$$

we can recast (2.30) as a free-energy imbalance:

$$\begin{aligned}& \rho(\dot{\psi} + \eta \dot{T}) - \left[\boldsymbol{\sigma} - \mathbf{d}\mathbf{e} + \frac{\epsilon_0}{2}(\mathbf{e} \cdot \mathbf{e})\mathbf{I}\right] \cdot\cdot (\dot{\mathbf{x}} \nabla) - \rho \mathbf{e} \cdot \dot{\mathbf{P}} - \rho(\mu_n \dot{n} + \mu_p \dot{p}) \\ & \quad + \nabla(\mu_n - q\varphi) \cdot \jmath_n + \nabla(\mu_p + q\varphi) \cdot \jmath_p - (\mu_n + \mu_p) R + \frac{1}{T} \mathbf{q} \cdot (\nabla T) \leq 0.\end{aligned} \tag{2.32}$$

2.2 CONSTITUTIVE RELATIONS

To complete the set of general principles, constitutive laws are needed for

$$\psi,\ \eta,\ \mathbf{e},\ \boldsymbol{\sigma},\ \mu_n,\ \mu_p,\ \jmath_n,\ \jmath_p,\ \mathbf{q},\ \text{and } R.$$

We assume these fields to depend on $\mathbf{F}, \mathbf{P}, n, p$, and T, where $\mathbf{F}(\mathbf{x}, t)$ is the deformation gradient. Further, guided by (2.32), we assume that $\jmath_n$ and $\jmath_p$ depend also on $\nabla(\mu_n - q\varphi)$ and $\nabla(\mu_p + q\varphi)$, respectively, and $\mathbf{q}$ on ∇T.

2.2.1 *Thermodynamic restrictions*

We apply the Coleman-Noll procedure (Coleman and Noll, 1963), as extended by Kovetz and Gurtin and Vargas to include electrostatic and species transport, respectively, in order to place restrictions on the constitutive relations. Consequently, for a specific free energy $\psi(\mathbf{F}, \mathbf{P}, n, p, T)$, the free-energy imbalance (2.32) can be rewritten as

$$\begin{aligned}\Big[\rho\Big(\frac{\partial\psi}{\partial\mathbf{F}}\cdot\mathbf{F}^T\Big)^T - \boldsymbol{\sigma} + \mathbf{d}\mathbf{e} - \frac{\epsilon_0}{2}(\mathbf{e}\cdot\mathbf{e})\mathbf{I}\Big]\cdot\cdot(\dot{\mathbf{x}}\nabla) + \rho\Big[\frac{\partial\psi}{\partial\mathbf{P}} - \mathbf{e}\Big]\cdot\dot{\mathbf{P}}\\ + \Big[\frac{\partial\psi}{\partial n} - \mu_n\Big]\rho\dot{n} + \Big[\frac{\partial\psi}{\partial p} - \mu_p\Big]\rho\dot{p} + \Big[\eta + \frac{\partial\psi}{\partial T}\Big]\rho\dot{T} + \nabla(\mu_n - q\varphi)\cdot\jmath_n\\ + \nabla(\mu_p + q\varphi)\cdot\jmath_p + \frac{1}{T}\mathbf{q}\cdot(\nabla T) - (\mu_n + \mu_p)R \le 0.\end{aligned} \tag{2.33}$$

The necessary conditions for (2.33) to hold are

$$\begin{cases}\boldsymbol{\sigma} = \rho\Big(\dfrac{\partial\psi}{\partial\mathbf{F}}\cdot\mathbf{F}^T\Big)^T + \mathbf{d}\mathbf{e} - \dfrac{\epsilon_0}{2}(\mathbf{e}\cdot\mathbf{e})\mathbf{I},\\ \mathbf{e} = \dfrac{\partial\psi}{\partial\mathbf{P}}, \quad \eta = -\dfrac{\partial\psi}{\partial T},\\ \mu_n = \dfrac{\partial\psi}{\partial n}, \quad \mu_p = \dfrac{\partial\psi}{\partial p}.\end{cases} \tag{2.34}$$

It follows that (2.33) simplifies to the reduced dissipation inequality

$$\nabla(\mu_n - q\varphi)\cdot\jmath_n + \nabla(\mu_p + q\varphi)\cdot\jmath_p + \frac{1}{T}\mathbf{q}\cdot(\nabla T) - (\mu_n + \mu_p)R \le 0. \tag{2.35}$$

Ignoring possible cross couplings between the dissipative fluxes and the associated thermodynamic forces we postulate the following linear relations:

$$\begin{cases}\jmath_n = -n\Big(\dfrac{\rho}{q}\mathbf{M}_n\Big)\cdot\Big(\nabla(\mu_n - q\varphi)\Big),\\ \jmath_p = -p\Big(\dfrac{\rho}{q}\mathbf{M}_p\Big)\cdot\Big(\nabla(\mu_p + q\varphi)\Big),\\ \mathbf{q} = -\mathbf{K}\cdot(\nabla T),\end{cases} \tag{2.36}$$

where $\mathbf{M}_n(\mathbf{F}, \mathbf{P}, T)$ and $\mathbf{M}_p(\mathbf{F}, \mathbf{P}, T)$ are the positive semi-definite mobility tensors for electrons and holes, and $\mathbf{K}(\mathbf{F}, \mathbf{P}, T)$ is the positive semi-definite conductivity tensor. Here, the mobilities $\mathbf{M}_n$ and $\mathbf{M}_p$ are assumed independent

of n and p. Further, it is physically reasonable to assume the heat flux to be independent of n and p.

These constitutive relations satisfy (2.35). The factor ρ/q in $(2.36)_{1,2}$ is such that the dimension of the mobility tensors is length square per unit potential and time, in agreement with the conventions of semiconductor physics. The terms $\mu_n - q\varphi$ and $\mu_p + q\varphi$ are the electrochemical potentials for electrons and holes, respectively.[8]

Finally, the constitutive law for the recombination-generation term R shall satisfy:

$$(\mu_n + \mu_p)R \geq 0. \tag{2.37}$$

2.2.2 *Material frame indifference*

In this section, we apply the principle of material frame indifference to the different constitutive laws. In particular, it explicitly shows the symmetry of $\boldsymbol{\sigma}$. To respect the principle of material frame indifference, the specific free energy $\psi(\mathbf{F}, \mathbf{P}, n, p, T)$ has to satisfy (Kovetz, 2000, Chapter 15; Tadmor et al., 2012, Chapter 6) the relation

$$\psi(\mathbf{F}, \mathbf{P}, n, p, T) = \psi(\mathbf{Q} \cdot \mathbf{F}, \mathbf{Q} \cdot \mathbf{P}, n, p, T), \tag{2.38}$$

for any proper orthogonal tensor $\mathbf{Q}$. Using the polar decomposition $\mathbf{F} = \mathbf{R} \cdot \mathbf{U}$ and choosing $\mathbf{Q} = \mathbf{R}^T = \mathbf{U}^{-1} \cdot \mathbf{F}^T$ we obtain:

$$\psi(\mathbf{F}, \mathbf{P}, n, p, T) = \psi(\mathbf{U}, \mathbf{U}^{-1} \cdot \mathbf{F}^T \cdot \mathbf{P}, n, p, T). \tag{2.39}$$

It follows that ψ can be expressed as a function of $\mathbf{U}$, $\mathbf{F}^T \cdot \mathbf{P}$, n, p, T or equivalently as a function of the same set of variable with $\mathbf{C} = \mathbf{F}^T \cdot \mathbf{F} = \mathbf{U}^2$ instead of $\mathbf{U}$. Using the form

$$\psi = \widehat{\psi}(\mathbf{C}, \mathbf{F}^T \cdot \mathbf{P}, n, p, T), \tag{2.40}$$

the free-energy automatically satisfies (2.38) for any proper orthogonal tensor $\mathbf{Q}$. The original function $\psi(\mathbf{F}, \mathbf{P}, n, p, T)$ can be written in terms of the new function $\widehat{\psi}(\mathbf{C}, \mathbf{F}^T \cdot \mathbf{P}, n, p, T)$:

$$\psi(\mathbf{F}, \mathbf{P}, n, p, T) = \widehat{\psi}(\mathbf{C}, \mathbf{F}^T \cdot \mathbf{P}, n, p, T). \tag{2.41}$$

With the purpose of establishing the symmetry of the total Cauchy stress defined by (2.34) we derive from (2.41) the identities

$$\begin{cases} \dfrac{\partial \psi}{\partial \mathbf{F}} = 2\mathbf{F} \cdot \dfrac{\partial \widehat{\psi}}{\partial \mathbf{C}} + \mathbf{P} \dfrac{\partial \widehat{\psi}}{\partial (\mathbf{F}^T \cdot \mathbf{P})}, \\ \dfrac{\partial \psi}{\partial \mathbf{P}} = \dfrac{\partial \widehat{\psi}}{\partial (\mathbf{F}^T \cdot \mathbf{P})} \cdot \mathbf{F}^T = \mathbf{F} \cdot \dfrac{\partial \widehat{\psi}}{\partial (\mathbf{F}^T \cdot \mathbf{P})}. \end{cases} \tag{2.42}$$

8 In parts of the physics literature, $\mu_n - q\varphi$ and $\mu_p + q\varphi$ are called the *total chemical potentials*, whereas μ_n and μ_p are referred to as the *internal chemical potentials*. In the semiconductor literature, $\mu_n - q\varphi$ is the quasi-Fermi level of electrons, while $\mu_p + q\varphi$ corresponds to the opposite of the quasi-Fermi level of holes (see Kittel and Kroemer, 1980, Chapter 13).

In view of these identities, we rewrite (2.34) in terms of the function $\widehat{\psi}$:

$$\boldsymbol{\sigma} = \rho\left(2\mathbf{F}\cdot\frac{\partial\widehat{\psi}}{\partial\mathbf{C}}\cdot\mathbf{F}^T + \mathbf{P}\mathbf{e} + \mathbf{e}\mathbf{P}\right) + \epsilon_0\left(\mathbf{e}\mathbf{e} - \frac{1}{2}(\mathbf{e}\cdot\mathbf{e})\mathbf{I}\right) = \boldsymbol{\sigma}^T, \tag{2.43}$$

which shows the symmetry of $\boldsymbol{\sigma}$.

As a result of the frame indifference of the specific free energy $\widehat{\psi}$, the fields $\boldsymbol{\sigma}$, $\mathbf{e}$, η, μ_n and μ_p given by (2.43),

$$\mathbf{e} = \mathbf{F}\cdot\frac{\partial\widehat{\psi}}{\partial(\mathbf{F}^T\cdot\mathbf{P})}, \quad \eta = -\frac{\partial\widehat{\psi}}{\partial T}, \quad \mu_n = \frac{\partial\widehat{\psi}}{\partial n}, \quad \text{and} \quad \mu_p = \frac{\partial\widehat{\psi}}{\partial p}, \tag{2.44}$$

are also frame indifferent, i.e., they automatically satisfy for every proper orthogonal tensor $\mathbf{Q}$ the following relations:

$$\begin{cases} \boldsymbol{\sigma}(\mathbf{Q}\cdot\mathbf{F}, \mathbf{Q}\cdot\mathbf{P}, n, T) = \mathbf{Q}\cdot\boldsymbol{\sigma}(\mathbf{F}, \mathbf{P}, n, T)\cdot\mathbf{Q}^T, \\ \mathbf{e}(\mathbf{Q}\cdot\mathbf{F}, \mathbf{Q}\cdot\mathbf{P}, n, T) = \mathbf{Q}\cdot\mathbf{e}(\mathbf{F}, \mathbf{P}, n, T), \\ \eta(\mathbf{Q}\cdot\mathbf{F}, \mathbf{Q}\cdot\mathbf{P}, n, T) = \eta(\mathbf{F}, \mathbf{P}, n, T), \\ \mu_n(\mathbf{Q}\cdot\mathbf{F}, \mathbf{Q}\cdot\mathbf{P}, n, T) = \mu_n(\mathbf{F}, \mathbf{P}, n, T), \\ \mu_p(\mathbf{Q}\cdot\mathbf{F}, \mathbf{Q}\cdot\mathbf{P}, n, T) = \mu_p(\mathbf{F}, \mathbf{P}, n, T). \end{cases} \tag{2.45}$$

In addition, we require the electron, hole and heat current densities to be frame indifferent, i.e.,

$$\begin{cases} \jmath_n(\mathbf{Q}\cdot\mathbf{F}, \mathbf{Q}\cdot\mathbf{P}, n, T, \mathbf{Q}\cdot\nabla(\mu_n - q\varphi)) = \mathbf{Q}\cdot\jmath_n(\mathbf{F}, \mathbf{P}, n, T, \nabla(\mu_n - q\varphi)), \\ \jmath_p(\mathbf{Q}\cdot\mathbf{F}, \mathbf{Q}\cdot\mathbf{P}, p, T, \mathbf{Q}\cdot\nabla(\mu_p + q\varphi)) = \mathbf{Q}\cdot\jmath_p(\mathbf{F}, \mathbf{P}, p, T, \nabla(\mu_p + q\varphi)), \\ \mathbf{q}(\mathbf{Q}\cdot\mathbf{F}, \mathbf{Q}\cdot\mathbf{P}, T, \mathbf{Q}\cdot\nabla T) = \mathbf{Q}\cdot\mathbf{q}(\mathbf{F}, \mathbf{P}, n, T, \nabla T). \end{cases} \tag{2.46}$$

Given (2.36), necessary and sufficient conditions for (2.46) to hold are

$$\begin{cases} \mathbf{M}_n(\mathbf{Q}\cdot\mathbf{F}, \mathbf{Q}\cdot\mathbf{P}, T) = \mathbf{Q}\cdot\mathbf{M}_n(\mathbf{F}, \mathbf{P}, T)\cdot\mathbf{Q}^T, \\ \mathbf{M}_p(\mathbf{Q}\cdot\mathbf{F}, \mathbf{Q}\cdot\mathbf{P}, T) = \mathbf{Q}\cdot\mathbf{M}_p(\mathbf{F}, \mathbf{P}, T)\cdot\mathbf{Q}^T, \\ \mathbf{K}(\mathbf{Q}\cdot\mathbf{F}, \mathbf{Q}\cdot\mathbf{P}, T) = \mathbf{Q}\cdot\mathbf{K}(\mathbf{F}, \mathbf{P}, T)\cdot\mathbf{Q}^T. \end{cases} \tag{2.47}$$

2.3 CRYSTALLINE SEMICONDUCTORS

Since crystalline semiconductors are brittle materials, we specialize the above finite-deformation theory to small strains. In doing so, we restrict our attention to isothermal processes.

2.3.1 *Small-strain assumption*

Under the above assumptions, the deformation is described by the small-strain tensor

$$\varepsilon = \frac{1}{2}\big(\mathbf{u}\nabla + \nabla\mathbf{u}\big), \tag{2.48}$$

where $\mathbf{u} = \mathbf{x} - \mathbf{X}$ is the displacement field. The condition

$$\|\varepsilon\| = (\varepsilon : \varepsilon)^{1/2} \ll 1 \tag{2.49}$$

is satisfied since strains remain less than 10^{-2} in crystalline materials. At first-order in ε, (2.43) is approximated by

$$\boldsymbol{\sigma}(\varepsilon, \mathbf{P}, n, p) = \rho\left(\frac{\partial\widehat{\psi}}{\partial\varepsilon} + \mathbf{P}\mathbf{e} + \mathbf{e}\mathbf{P}\right) + \epsilon_0\left(\mathbf{e}\mathbf{e} - \frac{1}{2}(\mathbf{e}\cdot\mathbf{e})\mathbf{I}\right). \tag{2.50}$$

In accordance with the small-strain assumption, changes of volume are neglected and ρ is taken to be constant.

2.3.2 *Choice of a free energy*

We postulate an additive decomposition of the specific free energy into mechanical, electrostatic and electronic components:

$$\widehat{\psi}(\varepsilon, \mathbf{P}, n, p) := \widehat{\psi}_{mech}(\varepsilon) + \widehat{\psi}_{elecs}(\mathbf{P}) + \widehat{\psi}_{elecn}(\varepsilon, n, p). \tag{2.51}$$

This additive decomposition of the free energy is natural given that the semiconductor under investigation is assumed to be a centrosymmetric crystal, i.e., a material that does not exhibit piezoelectricity. For a non-centrosymmetric semiconductor with piezoelectric behavior, an additional coupling term between strain and polarization of the form $\widehat{\psi}_{piezo}(\varepsilon, \mathbf{P}) = \varepsilon : \mathbf{N}\cdot\mathbf{P}$, with $\mathbf{N}$ a constitutive rank-3 tensor, should be added to the right hand side of (2.51).

One feature that distinguishes (2.51) from exisiting constitutive models (e.g., Xiao and Bhattacharya, 2008) is the dependence of the electronic component $\widehat{\psi}_{elecn}$ on strain. Specifically, this dependence accounts for the strain-induced changes of the electronic band structure. Further, a more general constitutive relation for the free energy of a deformable semiconductor would allow for a dependence of $\widehat{\psi}_{elecn}$ on polarization. However in the absence of a strong electric field, we expect this dependence to be negligible.[9] Finally, in the small-strain

9 The transport of electrons and holes is nonetheless related to polarization through the gradient of the electric potential as can be seen in the derivation of the current-density relations $(2.55)_2$ and (2.56).

regime, the permittivity ϵ_r of the material can be assumed constant. Hence, $\widehat{\psi}_{elecs}$ does not depend on strain.

For a linearly elastic material, the mechanical part is given by

$$\widehat{\psi}_{mech}(\varepsilon) := \frac{1}{2\rho}\varepsilon : \mathbf{c} : \varepsilon, \tag{2.52}$$

with $\mathbf{c}$ the elasticity tensor of the material.

The electrostatic part of the free energy $\widehat{\psi}_{elecs}$ corresponds to the free energy of a linear isotropic dielectric of permittivity ϵ_r:

$$\widehat{\psi}_{elecs}(\mathbf{P}) := \frac{\rho}{2(\epsilon_r - \epsilon_0)}\mathbf{P} \cdot \mathbf{P}. \tag{2.53}$$

The electronic component $\widehat{\psi}_{elecn}$ of the free energy is related to the densities of electrons and holes. Assuming that the electron and hole gases are in local equilibrium in the conduction and valence bands independently, the expression of the free energy is given by statistical physics (see e.g., Kittel and Kroemer, 1980). Denoting by $E_c(\varepsilon)$ and $E_v(\varepsilon)$ the band edge energy levels of the conduction and valence bands *in the absence of electric potential* ($\varphi = 0$),[10] and by $N_c(\varepsilon)$ and $N_v(\varepsilon)$ the effective densities of state of the conduction and valence bands, respectively (in number of states per unit mass), the specific free energy of the two gases reads[11]

$$\begin{aligned}\widehat{\psi}_{elecn}(\varepsilon, n, p) := n\left[k_B T\left(\ln\left(\frac{n}{N_c(\varepsilon)}\right) - 1\right) + E_c(\varepsilon)\right] \\ + p\left[k_B T\left(\ln\left(\frac{p}{N_v(\varepsilon)}\right) - 1\right) - E_v(\varepsilon)\right],\end{aligned} \tag{2.54}$$

where k_B is the Boltzmann constant. The dependence of E_c, E_v, N_c and N_v on ε is due to the fact that the band structure of a semiconductor results from its atomic lattice configuration, itself modified by strain. These dependences have been investigated in the solid-state physics literature as discussed in Chapter 1.

10 Note that with this definition of E_c and E_v, the electrostatic potential energy of free charges does not appear in the free energy. This is consistent with our definition of the total energy which does not include the electrostatic potential energy of free charges (see footnote Section 2.1.6).

11 The constitutive relation (2.54) corresponds to the free energy of an ideal gas of electrons and holes. It is valid for non-degenerate semiconductors, i.e., semiconductors whose free-carrier concentration is not to high, which is the case for most electronic devices. An extension of our model to degenerate semiconductors would require replacing (2.54) with the free energy of a Fermi gas of electrons and holes.

By (2.34) and (2.51), we have:

$$\begin{cases} \boldsymbol{\sigma}(\varepsilon,\mathbf{P},n,p) = \underbrace{\mathbf{c}:\varepsilon}_{\boldsymbol{\sigma}_{mech}} + \underbrace{\rho\Big(\mathbf{P}\mathbf{e}+\mathbf{e}\mathbf{P}\Big)+\epsilon_0\Big(\mathbf{e}\mathbf{e}-\frac{1}{2}(\mathbf{e}\cdot\mathbf{e})\mathbf{I}\Big)}_{\boldsymbol{\sigma}_{maxw}} \\ \qquad\qquad + \underbrace{\rho n\Big(-k_BT\frac{\partial\ln(N_c)}{\partial\varepsilon}+\frac{\partial E_c}{\partial\varepsilon}\Big)+\rho p\Big(-k_BT\frac{\partial\ln(N_v)}{\partial\varepsilon}-\frac{\partial E_v}{\partial\varepsilon}\Big)}_{\boldsymbol{\sigma}_{elecn}}, \\ \mathbf{e}(\mathbf{P}) = \dfrac{\rho\mathbf{P}}{\epsilon_r-\epsilon_0}, \\ \mu_n(\varepsilon,n) = E_c(\varepsilon)+k_BT\ln\Big(\dfrac{n}{N_c(\varepsilon)}\Big), \\ \mu_p(\varepsilon,p) = -E_v(\varepsilon)+k_BT\ln\Big(\dfrac{p}{N_v(\varepsilon)}\Big). \end{cases} \tag{2.55}$$

Note that the total stress tensor $\boldsymbol{\sigma}$ not only consists of a purely mechanical component ($\boldsymbol{\sigma}_{mech}$) and a Maxwell component ($\boldsymbol{\sigma}_{maxw}$) but contains also an electronic contribution ($\boldsymbol{\sigma}_{elecn}$) which depends on electron and hole densities. As seen in $(2.55)_1$, the dependence of $\widehat{\psi}_{elecn}$ on strain results in an *electronic* contribution to the stress tensor, one that has not been accounted for previously. Regardless of the specific form of $\boldsymbol{\sigma}_{elecn}$, which follows from the constitutive assumptions (2.51) and (2.54), the existence of an electronic stress is the consequence of the dependence on strain of the effective densities of states as well as the energy levels of the valence and conduction bands.

In view of the constitutive relations $(2.55)_{3,4}$ for the chemical potentials, we rewrite $(2.36)_{1,2}$ in the form of generalized current-density relations:

$$\begin{cases} \boldsymbol{\jmath}_n = -k_BT\Big(\dfrac{\rho}{q}\mathbf{M}_n(\varepsilon)\Big)\cdot\nabla n \\ \qquad\qquad + n\Big(\dfrac{\rho}{q}\mathbf{M}_n(\varepsilon)\Big)\cdot\Big[q\nabla\varphi-\nabla E_c(\varepsilon)+k_BT\nabla\big(\ln(N_c(\varepsilon))\big)\Big], \\ \boldsymbol{\jmath}_p = -k_BT\Big(\dfrac{\rho}{q}\mathbf{M}_p(\varepsilon)\Big)\cdot\nabla p \\ \qquad\qquad + p\Big(\dfrac{\rho}{q}\mathbf{M}_p(\varepsilon)\Big)\cdot\Big[-q\nabla\varphi+\nabla E_v(\varepsilon)+k_BT\nabla\big(\ln(N_v(\varepsilon))\big)\Big]. \end{cases} \tag{2.56}$$

We note that Equations (2.56) appear in the physics literature pertaining to the transport of electrons and holes in nonuniform semiconductors, where they are derived from Boltzmann transport equation (see Marshak and Vliet, 1978; Marshak and Vliet, 1984; Manku and Nathan, 1993 and also Nelson, 2003, Chapter 3; Fonash, 2012, Chapter 2).

2.3.3 *Recombination-generation*

In the absence of photogeneration, the dominant mechanism of recombination-generation of electrons and holes in indirect band-gap semiconductors (such as

silicon) is via bulk traps (Pierret, 1987; Sze and Ng, 2006). With the usual approximation that effective recombination-generation centers are traps lying near the mid-gap, the transition rate is described by the simplified Read-Shockley-Hall model (Pierret, 1987, Chapter 5):

$$R(n,p,\varepsilon) = \frac{\rho(pn - n_i^2(\varepsilon))}{\tau_p(n + n_i(\varepsilon)) + \tau_n(p + n_i(\varepsilon))}, \tag{2.57}$$

where

$$n_i(\varepsilon) = \sqrt{N_c(\varepsilon)N_v(\varepsilon)}\exp\left(\frac{-(E_c(\varepsilon) - E_v(\varepsilon))}{2k_BT}\right), \tag{2.58}$$

is the intrinsic concentration of electrons and holes and τ_n and τ_p are two positive constants interpreted as the electron and hole lifetimes, respectively.

To check the thermodynamic consistency of (2.57), we invert $(2.55)_{3,4}$ to express n and p as functions of μ_n and μ_p, and rewrite the numerator of R:

$$\rho(pn - n_i^2) = \rho N_c N_v \exp\left(\frac{-(E_c - E_v)}{k_BT}\right)\Big(\exp\left(\mu_n + \mu_p\right) - 1\Big). \tag{2.59}$$

It follows that $R(\mu_n + \mu_p)$ has the sign of $\left(\mu_n + \mu_p\right)\left(\exp\left(\mu_n + \mu_p\right) - 1\right)$ which is positive for all μ_n and μ_p as required by (2.37).

2.3.4 *Summary of the governing equations for a deformable semiconductor*

At this point, it is useful to summarize the governing equations for the boundary value problem of a deformable semiconductor. Since strains in a crystalline semiconductor are small, the problem is written in the reference configuration of the semiconductor $\mathcal{B}$. The unknown fields are: n, p and $\boldsymbol{u}$ inside the semiconductor, while the electric potential φ has to be determined for the entire space $\mathbb{R}^3$.

i) Field equations

For simplicity, it is assumed that the deformable semiconductor is either in contact with a conductor (electrode) or surrounded by free space. As depicted in Figure 2.2, the deformable semiconductor is in contact with N conductors occupying disjoined regions $\mathcal{C}_i$ with $i = 1...N$. Since the electric field vanishes inside a conductor, φ is constant in each $\mathcal{C}_i$. The surrounding free space is $\mathcal{V} := \mathbb{R}^3 \setminus \{\mathcal{B} \cup \mathcal{C}_1 \cup ... \cup \mathcal{C}_N\}$, where the electric potential φ must also be computed. The field equations are

$$\begin{cases} \epsilon_r \Delta\varphi = q\rho(n - p - C), \\ \rho\dot{n} = -R - \nabla\cdot\boldsymbol{\jmath}_n, \\ \rho\dot{p} = -R - \nabla\cdot\boldsymbol{\jmath}_p, \\ \rho\ddot{\mathbf{u}} = \nabla\cdot\boldsymbol{\sigma} + \rho\mathbf{f}, \end{cases} \quad \text{in } \mathcal{B}, \tag{2.60}$$

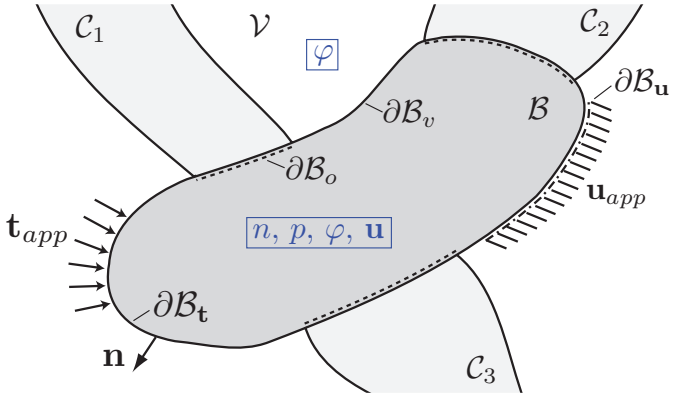

Figure 2.2: Schematic of the boundary-value problem of a deformable semiconductor in contact with three electrodes.

where

$$
\begin{cases}
\jmath_n = -k_B T\left(\dfrac{\rho}{q}\mathbf{M}_n(\varepsilon)\right)\cdot\nabla n \\
\qquad\qquad + n\left(\dfrac{\rho}{q}\mathbf{M}_n(\varepsilon)\right)\cdot\Big[q\nabla\varphi - \nabla E_c(\varepsilon) + k_B T\nabla\big(\ln(N_c(\varepsilon))\big)\Big], \\
\jmath_p = -k_B T\left(\dfrac{\rho}{q}\mathbf{M}_p(\varepsilon)\right)\cdot\nabla p \\
\qquad\qquad + p\left(\dfrac{\rho}{q}\mathbf{M}_p(\varepsilon)\right)\cdot\Big[-q\nabla\varphi + \nabla E_v(\varepsilon) + k_B T\nabla\big(\ln(N_v(\varepsilon))\big)\Big], \\
R = \dfrac{\rho(pn - n_i^2(\varepsilon))}{\tau_p(n + n_i(\varepsilon)) + \tau_n(p + n_i(\varepsilon))}, \\
\boldsymbol{\sigma} = \mathbf{c} : \varepsilon + \rho n\left(-k_B T\dfrac{\partial\ln(N_c)}{\partial\varepsilon} + \dfrac{\partial E_c}{\partial\varepsilon}\right) \\
\qquad\qquad + \rho p\left(-k_B T\dfrac{\partial\ln(N_v)}{\partial\varepsilon} - \dfrac{\partial E_v}{\partial\varepsilon}\right) \\
\qquad\qquad + (2\epsilon_r - \epsilon_0)(\nabla\varphi)(\nabla\varphi) - \dfrac{\epsilon_0}{2}(\nabla\varphi\cdot\nabla\varphi)\mathbf{I}, \\
\varepsilon = \dfrac{1}{2}(\mathbf{u}\nabla + \nabla\mathbf{u}),
\end{cases}
\tag{2.61}
$$

along with Laplace's equation for the electric potential in free space:

$$
\Delta\varphi = 0 \quad \text{in } \mathcal{V}. \tag{2.62}
$$

The boundary $\partial\mathcal{B}$ is split as follows. With respect to the electronic part, let $\partial\mathcal{B}_o$ be the union of contact surfaces with the conductors $\mathcal{C}_i$ and $\partial\mathcal{B}_v$ the interfaces with the free space $\mathcal{V}$. With respect to mechanics, we distinguish between $\partial\mathcal{B}_{\mathbf{u}}$ where a displacement $\mathbf{u}_{app}$ is prescribed and $\partial\mathcal{B}_{\mathbf{t}}$ where an external mechanical traction $\mathbf{t}_{app}$ is applied. From these definitions follows that $\partial\mathcal{B}_o \cup \partial\mathcal{B}_v = \partial\mathcal{B}$ and $\partial\mathcal{B}_{\mathbf{u}} \cup \partial\mathcal{B}_{\mathbf{t}} = \partial\mathcal{B}$. Depending on the problem, the electronic and mechanical parts of the boundary can overlap.

iia) Electronic boundary conditions

Assuming voltage-controlled ohmic contacts with the conductors, conditions are (Selberherr, 1984):

$$\begin{cases} \varphi = \varphi_{bin} + \varphi_{app}, \\ n - p - C = 0, \\ np - n_i^2 = 0, \end{cases} \qquad \text{on } \partial\mathcal{B}_o, \tag{2.63}$$

where φ_{bin} is the built-in potential and φ_{app} the externally applied bias. The built-in potential is obtained by computing the steady-state solution of (2.60) in the mechanical equilibrium case and in the absence of externally applied bias ($\varphi_{app} = 0$ on $\partial\mathcal{B}_o$). Further, $(2.63)_2$ and $(2.63)_3$ correspond to the common assumptions of vanishing space charge and thermal equilibrium (absence of surface recombination) at ohmic contacts (Selberherr, 1984). Their resolution yields Dirichlet boundary conditions for the concentrations of electrons and holes.

Along the interface $\partial\mathcal{B}_v$ with free space, jump conditions for the electric potential φ and the normal component of its gradient must be satisfied. Moreover, in the absence of surface recombination, the flows of electrons and holes must vanish at $\partial\mathcal{B}_v$. We therefore have

$$\begin{cases} [\![\epsilon\nabla\varphi]\!] \cdot \mathbf{n} = 0, \\ [\![\varphi]\!] = 0, \\ \jmath_n \cdot \mathbf{n} = 0, \\ \jmath_p \cdot \mathbf{n} = 0. \end{cases} \qquad \text{on } \partial\mathcal{B}_v, \tag{2.64}$$

where $\mathbf{n}$ is the unit outward normal to $\partial\mathcal{B}_v$ and $[\![f]\!] := f_{vac} - f_{sem}$ denotes the jump of the field quantity f at the interface.[12]

iib) Mechanical boundary conditions

Denoting by $\mathbf{u}_{app}$ the prescribed displacement on $\partial\mathcal{B}_{\mathbf{u}}$, the displacement boundary condition reads

$$\mathbf{u} = \mathbf{u}_{app} \quad \text{on } \partial\mathcal{B}_{\mathbf{u}}. \tag{2.65}$$

Finally, on $\partial\mathcal{B}_{\mathbf{t}}$ where a mechanical traction is prescribed, the localization of linear momentum balance (2.15) on a volume surrounding $\partial\mathcal{B}_{\mathbf{t}}$ yields [13]

$$\mathbf{n} \cdot [\![\boldsymbol{\sigma}]\!] = \mathbf{t}_{app} \quad \text{on } \partial\mathcal{B}_{\mathbf{t}}. \tag{2.66}$$

2.3.5 *Stress in silicon*

Here, we consider silicon to compare the relative magnitudes of the different components of the total stress tensor $(2.55)_1$. We show that, in the case of non-degenerate[14] silicon, the influence of electric field and electronic distribution

12 Note that in the absence of interface charge, $(2.64)_1$ results from the localization at the semiconductor/free space interface of the integral forms of Gauss's law (2.5).

13 Note that in free space, the total stress tensor reduces to Maxwell stress $\boldsymbol{\sigma} = \epsilon_0[(\nabla\varphi)(\nabla\varphi)\big|_{vac} - (1/2)(\nabla\varphi\cdot\nabla\varphi)\big|_{vac}\mathbf{I}]$.

14 In practice, a semiconductor is non-degenerate when its dopant concentrations are not too high and becomes degenerate when the doping overpass some limit, see e.g., Sze and Ng (2006).

on the stress is negligible, which reduces the couplings to the influence of strain on the electronic transport. However, in the high doping regime (e.g., in degenerate silicon), the new electronic contribution to the stress could become important.

We first evaluate the purely mechanical part of the stress $\boldsymbol{\sigma}_{mech}$ from $(2.55)_1$. Given the Young modulus of silicon ($E = 130$ GPa) and considering that the operating strains range between 10^{-4} and 10^{-2} , the corresponding mechanical contribution to stress ranges from 10 MPa to 1 GPa.

To compute an upper bound of the electronic contribution $\boldsymbol{\sigma}_{elecn}$ to the stress, we consider the maximum carrier density in non-degenerate semiconductors (10^{18} atoms/cm^3) and the typical energetic variations per unit strain of the conduction and valence band levels and effective densities of states at room temperature (1 to 3 eV) (cf. Appendix A). Thus, the electronic contribution to stress is no more than 0.5 MPa.

The last contribution is the Maxwell stress $\boldsymbol{\sigma}_{maxw}$ related to the electric field and polarization. As an upper bound again, we consider the maximum electric field observed at the p-n interface in the space charge region of a highly doped p-n junction: 10^7 V/m. With the dielectric constant of silicon $\epsilon_r = 11.9\epsilon_0$, we obtain that the Maxwell contribution to stress does not exceed 100 kPa.

We observe that the electronic and Maxwell contributions to the stress are at least one order of magnitude lower than the smallest operating purely mechanical stress. As a result, for non-degenerate silicon, there is no significant influence of the electronics and the electric field on the mechanics, thus the mechanical problem can be solved independently of the electronic state.

We remark however that for high doping such as 5×10^{19} atoms/cm^3 the electronic contribution to stress is of the order of 25 MPa, which is significant. Besides, the Young modulus of a semiconductor (which is nothing but the derivative of $\boldsymbol{\sigma}$ with respect to $\boldsymbol{\varepsilon}$ evaluated at zero strain) is expected to depend on the electron and hole concentrations in proportion to the second derivative of the band energy levels and density of states with $\boldsymbol{\varepsilon}$. This could contribute to the unusual values of the Young modulus measured for heavily doped semiconductors which have so far been explained by the changes induced by the presence of the dopant nuclei (Najafi and Suzuki, 1989; Ding et al., 1990; Ericson and Schweitz, 1990).

3

BENDING OF A p-n JUNCTION

In this section, we make use of the governing field equations derived in Chapter 2 to compute $\jmath(V)$, the *current-voltage characteristic* (or *characteristic* for short), of a p-n junction undergoing nonuniform strains as a result of the bending of the device. In Section 3.1 the inherently three-dimensional problem is reduced to its one-dimensional counterpart. By means of asymptotics, $\jmath(V)$ is computed in Section 3.2 as a function of the applied strain and curvature. Finally, the result of Section 3.2 is applied in Section 3.3 to compute the strain-induced changes in the characteristic of a typical monocrystalline silicon solar cell subjected to bending. Changes in $\jmath(V)$ of the order 20% are predicted for strains of about 0.2%.

3.1 MOTIVATION AND PROBLEM SETTING

We consider a p-n junction parallel to the mid-plane of a plate made of a crystalline semiconductor, see Figure 3.1(a), whose Helmholtz free-energy is given by (2.51). The simplifications derived in Section 2.3.5 for silicon remain valid for the material considered. Indeed, this is likely to be the case for the centrosymmetric crystalline semiconductors used in practical applications.

The junction occupies the space between the planes $x = 0$ and $x = l$ with the p-n interface located at the plane $x = x_0$. Without loss of generality, we consider that the p region contains only acceptors while the n region contains only donors. Hence, (2.1) specializes to

$$C(x,y,z) = \begin{cases} -N_a & \text{for } x \in (0, x_0), \\ N_d & \text{for } x \in (x_0, l), \end{cases} \tag{3.1}$$

where N_a and N_d are the constant numbers of acceptors and donors per unit mass in the regions p and n, respectively.

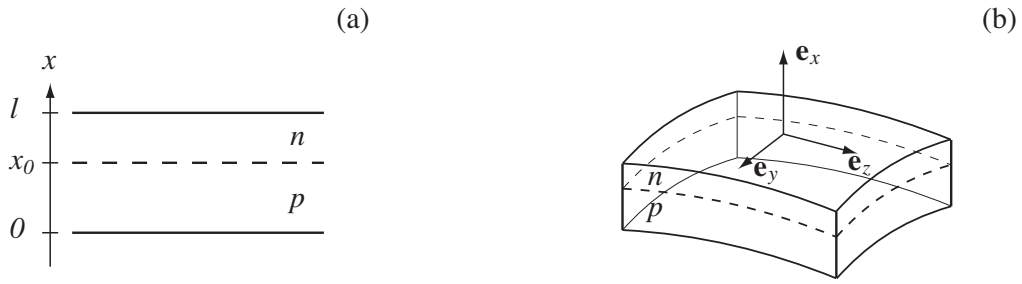

Figure 3.1: Schematic of an in plane p-n junction. (a) Reference configuration $\mathcal{B}_0$, n and p denote the n-doped and p-doped regions, respectively. (b) Deformed configuration bent about the directions $\mathbf{e}_y$ and $\mathbf{e}_z$.

The electric current $\jmath := q(\jmath_p - \jmath_n)$, which results from the external voltage V applied between the surfaces $x = 0$ and $x = l$, is affected by the bending of the junction. Existing studies of the strain effect on the p-n junction (piezojunction effect) consider *uniform strain* whose effect on the electric current is computed by simply substituting, in the classical current-voltage characteristic of Shockley, the values under strain of the electronic parameters. In contrast, the bending of the device results in *nonuniform strains* across the junction, thus modifying the boundary-value problem whose solution is used to compute the current-voltage characteristic, as detailed in what follows.

3.1.1 *Strain field*

We start by describing the equilibrium strain field in the junction. The plate is bent about the directions $\mathbf{e}_y$ and $\mathbf{e}_z$, so that the yy- and zz-components of the small-strain tensor are given by

$$\begin{cases} \varepsilon_{yy}(x,y,z) = \kappa_y(x - x_0) + \varepsilon^0_{yy}, \\ \varepsilon_{zz}(x,y,z) = \kappa_z(x - x_0) + \varepsilon^0_{zz}, \end{cases} \tag{3.2}$$

where κ_y and κ_z are the curvatures associated with the principal strain directions $\mathbf{e}_y$ and $\mathbf{e}_z$, and ε^0_{yy} and ε^0_{zz} are the strain components at $x = x_0$. Let $\kappa := max(\kappa_y, \kappa_z)$ be a characteristic curvature. We introduce the dimensionless coefficients

$$\alpha_y := \frac{\kappa_y}{\kappa}, \qquad \alpha_z := \frac{\kappa_z}{\kappa}. \tag{3.3}$$

Although the displacements and rotations may be large, the strains remain small. The surfaces $x = \texttt{constant}$ that are planar in the reference configuration are mapped into curved surfaces in the deformed configuration. However these surfaces can be locally approximated by their tangent planes and the problem reduces to a planar one. Since we neglect the influence of the boundaries in the directions y and z, the problem is invariant under y- and z-translations. In addition, we consider the stationary problem in the absence of body force. In view of the simplifications introduced in Section 2.3.5, the total stress is approximated by the mechanical part of the stress,

$$\boldsymbol{\sigma} = \mathbf{c} : \boldsymbol{\varepsilon}, \tag{3.4}$$

where $\mathbf{c}$ is the elasticity tensor of the semiconductor. For cubic symmetry crystalline semiconductors, such as silicon, and assuming that the symmetry axes align with the coordinates, the mechanical equilibrium (2.16) combined with the traction-free boundary conditions on the surfaces $x = 0$ and $x = l$, yields $\sigma_{xx} = \sigma_{xy} = \sigma_{xz} = 0$ everywhere in the junction. It follows from (3.4) that

$$\begin{aligned} \varepsilon_{xx}(x,y,z) &= -\frac{c_{xxyy}}{c_{xxxx}}\Big[\varepsilon_{yy}(x,y,z) + \varepsilon_{zz}(x,y,z)\Big] \\ &= -\frac{c_{xxyy}}{c_{xxxx}}\Big[\kappa(\alpha_y + \alpha_z)(x - x_0) + \varepsilon^0_{yy} + \varepsilon^0_{zz}\Big], \end{aligned} \tag{3.5}$$

and the shear components of $\boldsymbol{\varepsilon}$ vanish.

3.1.2 *Strain dependence of the electronic parameters*

Next, we present the dependence of the electronic parameters E_c, E_v, N_c, N_v, $\mathbf{M}_n$ and $\mathbf{M}_p$ on $\boldsymbol{\varepsilon}$ and deduce their spatial variation in x using the strain field equations (3.2) and (3.5). In view of the small-strain assumption, linear relationships in the small-strain tensor $\boldsymbol{\varepsilon}$ are considered. The strain dependence of the band edges E_c and E_v and of the effective densities of states N_c and N_v of the conduction and valence bands is given by:[1]

$$\begin{cases} E_c(\boldsymbol{\varepsilon}) = E_c^r + \widetilde{\mathbf{E}}_c : \boldsymbol{\varepsilon}, & E_v(\boldsymbol{\varepsilon}) = E_v^r + \widetilde{\mathbf{E}}_v : \boldsymbol{\varepsilon}, \\ N_c(\boldsymbol{\varepsilon}) = N_c^r + \widetilde{\mathbf{N}}_c : \boldsymbol{\varepsilon}, & N_v(\boldsymbol{\varepsilon}) = N_v^r + \widetilde{\mathbf{N}}_v : \boldsymbol{\varepsilon}, \end{cases} \tag{3.6}$$

where the superscript r denotes the value of the parameter in the relaxed state ($\boldsymbol{\varepsilon} = \mathbf{0}$) and where the rank-2 tensors $\widetilde{\mathbf{E}}_c$, $\widetilde{\mathbf{E}}_v$, $\widetilde{\mathbf{N}}_c$ and $\widetilde{\mathbf{N}}_v$ account for first-order strain-induced changes in the corresponding quantities.

Similarly, the mobilities of electrons and holes are expressed as

$$\mathbf{M}_n(\boldsymbol{\varepsilon}) = \mathbf{M}_n^r + \widetilde{\mathbf{M}}_n : \boldsymbol{\varepsilon}, \qquad \mathbf{M}_p(\boldsymbol{\varepsilon}) = \mathbf{M}_p^r + \widetilde{\mathbf{M}}_p : \boldsymbol{\varepsilon}, \tag{3.7}$$

where $\widetilde{\mathbf{M}}_n$ and $\widetilde{\mathbf{M}}_p$ are rank-4 tensors. All the tilde coefficients that account for change per unit strain of the electronic parameters are material properties.

The spatial variations of the electronic parameters E_c, E_v, N_c, N_v, $\mathbf{M}_n$ and $\mathbf{M}_p$ are obtained by substituting the strain field (3.2) and (3.5) in (3.6)–(3.7), thus yielding

$$\begin{cases} E_c(x,y,z) = E_c^0 + \kappa \widehat{E}_c(x - x_0), & E_v(x,y,z) = E_v^0 + \kappa \widehat{E}_v(x - x_0), \\ N_c(x,y,z) = N_c^0 + \kappa \widehat{N}_c(x - x_0), & N_v(x,y,z) = N_v^0 + \kappa \widehat{N}_v(x - x_0), \\ m_n(x,y,z) = m_n^0 + \kappa \widehat{m}_n(x - x_0), & m_p(x,y,z) = m_p^0 + \kappa \widehat{m}_p(x - x_0), \end{cases} \tag{3.8}$$

where m_n and m_p are the xx-components of the rank-2 mobility tensors $\mathbf{M}_n$ and $\mathbf{M}_p$. The constants E_c^0, E_v^0, N_c^0, N_v^0, m_n^0, and m_p^0, as well as the coefficients $\widehat{E}_c$, $\widehat{E}_v$, $\widehat{N}_c$, $\widehat{N}_v$, $\widehat{m}_n$, and $\widehat{m}_p$ are calculated in Appendix A for a linearly elastic material with cubic symmetry, subjected to the strain state considered. As a result, electrons and holes evolve in spatially nonuniform conduction and valence bands as illustrated in Figure 3.2.

3.1.3 *Governing equations of the one-dimensional model*

We consider either a polycrystalline material or an orthotropic crystalline material whose x-direction is a principal crystallographic direction. In either case, the mobility tensors $\mathbf{M}_n(\boldsymbol{\varepsilon})$ and $\mathbf{M}_p(\boldsymbol{\varepsilon})$ in the deformed configuration are diagonal when written in the (x,y,z) coordinate system. Hence, by (2.56) and the y- and z-translations invariance, the currents of electrons and holes

1 Note that in (3.6) we assume that these electronic parameters depend linearly on the strain directions. This might not always be the case, e.g., the valence band of silicon E_v is not a linear function of the components ε_{ij} (Appendix A). However, the developments that follow still hold at first order in $\boldsymbol{\varepsilon}$.

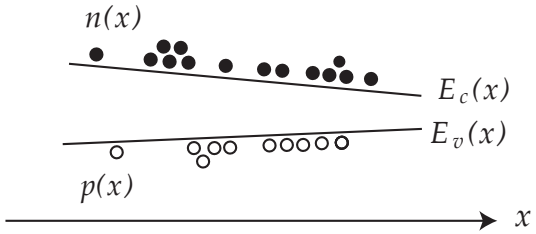

Figure 3.2: As a result of nonuniform strains, the band edge energies of the conduction and valence bands, as well as the densities of states and the charge-carrier mobilities depend on position.

have no components along these directions, i.e., $\boldsymbol{\jmath}_n = \jmath_n(x)\mathbf{e}_x$ and $\boldsymbol{\jmath}_p = \jmath_p(x)\mathbf{e}_x$. In addition we consider only the steady-state regime, i.e., all variables are independent of time.

Under these assumptions, the electronic transport problem (2.5), (2.12), (2.13) and (2.56) reduces to a one-dimensional system of equations whose unknowns are the fields $\varphi(x)$, $n(x)$, and $p(x)$. With the prime denoting the x-derivative, we obtain

$$\begin{cases} \epsilon_r \varphi'' = q\rho\big(n - p - C(x)\big), \\ \quad \jmath_n' = -R, \qquad \jmath_p' = -R, \end{cases} \tag{3.9}$$

where,

$$\begin{cases} \jmath_n = -\dfrac{k_B T \rho}{q} m_n(x) n' + \dfrac{\rho}{q} m_n(x) n \Big[q\varphi' - E_c'(x) + k_B T \big(\ln(N_c(x)) \big)' \Big], \\ \jmath_p = -\dfrac{k_B T \rho}{q} m_p(x) p' + \dfrac{\rho}{q} m_p(x) p \Big[-q\varphi' + E_v'(x) + k_B T \big(\ln(N_v(x)) \big)' \Big]. \end{cases} \tag{3.10}$$

In $(3.9)_{2,3}$, the recombination-generation R and intrinsic concentration n_i given by (2.57) and (2.58) are written as functions of x:

$$R(x) = \frac{\rho(pn - n_i^2(x))}{\tau_p(n + n_i(x)) + \tau_n(p + n_i(x))}, \tag{3.11}$$

where,

$$n_i^2(x) = N_c(x) N_v(x) \exp\left[\frac{-(E_c(x) - E_v(x))}{k_B T} \right]. \tag{3.12}$$

The system of field equations (3.9), (3.11) is supplemented by the boundary conditions at the ohmic contact $x = 0$ and $x = l$ encapsulated in (2.63):

$$\begin{cases} n - p - C = 0, \\ np = n_i^2, \\ \varphi = \varphi_{bin} + \varphi_{app}. \end{cases} \tag{3.13}$$

The reader can refer to Section 2.3.4 for the physical meaning of these boundary conditions. Recall that (3.13) is the decomposition of the electric potential at

each end into the built-in potential φ_{bin} and the externally applied voltage φ_{app}. The difference in the built-in electric potential $\varphi_{bin}(l) - \varphi_{bin}(0)$ corresponds to the voltage drop that exists naturally at equilibrium, i.e., in absence of external voltage bias.

Finally, at the interface $x = x_0$, in the absence of surface charges, the fields n, p and φ are continuous.

Table 3.1: Scaling of the variables for the electronic boundary-value problem.

Scaling factor	Related variable	physical meaning
l	x	space variable
$1/l$	κ	curvature
$k_B T$	E_c, E_v, $\widehat{E}_c$, $\widehat{E}_v$	band edge energy
$U_T := k_B T/q$	φ, V	electric potential, voltage
$\overline{C} := \max(N_a, N_d)$	n, p, C, n_i, N_c, N_v, $\widehat{N}_c$, $\widehat{N}_v$	particles per unit mass
$\overline{m} := \max(m_n^r, m_p^r)$	m_n, m_p, $\widehat{m}_n$, $\widehat{m}_p$	mobility
$\bar{\jmath} := \dfrac{U_T \overline{m} \rho \overline{C}}{l}$	$\jmath_n$, $\jmath_p$	current of particles
$\bar{\jmath}_e := q\bar{\jmath}$	$\jmath$	total electric current
$\overline{\tau} := \dfrac{l^2}{U_T \overline{m}}$	τ_n, τ_p	electron and hole lifetimes
$\overline{R} := \rho \overline{C}/\overline{\tau}$	R	recombination rate

3.2 ASYMPTOTIC ANALYSIS

In this section, we solve the one-dimensional electronic boundary-value problem (3.9), (3.11), and (3.13) by means of asymptotic analysis.

3.2.1 *Non-dimensionalization*

We introduce non-dimensional variables (Markowich, 1986) in Table 3.1. Three small dimensionless parameters are identified for the ensuing asymptotic analysis of the problem. The first parameter, $\lambda := \left(\epsilon_r U_T/q\rho\overline{C}l^2\right)^{1/2}$, is the scaled *Debye length*, which measures the width of the space charge layer that exists at the p-n interface; it is typically of the order of 10^{-5}. The second parameter, $\delta := \left(n_i^0/\overline{C}\right)^{1/2}$, is the dimensionless number that gives the *doping strength* relative to the intrinsic concentration $n_i^0 := \sqrt{N_c^0 N_v^0}\exp[-(E_c^0 - E_v^0)/2k_B T]$ at the interface $x = x_0$. For the problem at hand, this number is of order 10^{-4} to 10^{-3}. Finally, κ is the *dimensionless curvature*, which for the application of interest is of order 10^{-3}.

3.2.2 *Asymptotics with respect to curvature and doping*

We will approximate the equations (3.9), (3.11) and the boundary conditions (3.13) by neglecting all terms that are second order in κ and δ. To alleviate an already cumbersome notation, each dimensionless variable is denoted by the same symbol as its dimensional counterpart. In addition, the prime now corresponds to the derivative with respect to the dimensionless space variable x.

Starting with the spatial variations of the electronic parameters $(3.8)_{3,4}$ we have the following first-order approximation in κ:

$$\big(\ln(N_c(x))\big)' = \frac{\widehat{N}_c}{N_c^0}\kappa + O(\kappa^2), \qquad \big(\ln(N_v(x))\big)' = \frac{\widehat{N}_v}{N_v^0}\kappa + O(\kappa^2). \tag{3.14}$$

Appealing to $(3.8)_{1,2}$ and $(3.11)_2$ in conjunction with the approximation $1+\epsilon = \exp(\epsilon) + O(\epsilon^2)$ for $|\epsilon| < 1$, we approximate $n_i^2(x)$ by

$$\begin{aligned} n_i^2(x) &= N_c^0 N_v^0 \mathrm{e}^{-(E_c^0 - E_v^0)} \exp\left[-\kappa\left(\widehat{E}_c - \widehat{E}_v - \frac{\widehat{N}_c}{N_c^0} - \frac{\widehat{N}_v}{N_v^0}\right)(x - x_0)\right] \\ &\qquad\qquad + O(\kappa^2) \\ &= \delta^4 \exp\big[-\kappa(\underbrace{\widehat{E}_c^e - \widehat{E}_v^e}_{\widehat{E}_g^e})(x - x_0)\big] + O(\kappa^2), \end{aligned} \tag{3.15}$$

where $\widehat{E}_g^e := \widehat{E}_c^e - \widehat{E}_v^e$ is the *effective band gap coefficient*, and $\widehat{E}_c^e := \widehat{E}_c - \widehat{N}_c/N_c^0$ and $\widehat{E}_v^e := \widehat{E}_v + \widehat{N}_v/N_v^0$ are the *effective band edge coefficients*, which combine the effect of band edge level and effective density of states.

With these approximations, the governing equations (3.9) can be recast as

$$\begin{cases} \lambda^2 \varphi'' = n - p - C(x), \\ \quad j_n' = -R, \qquad j_p' = -R, \end{cases} \tag{3.16}$$

with,

$$\begin{cases} \quad j_n = \big(m_n^0 + \kappa \widehat{m}_n (x - x_0)\big)\big[-n' + n(\varphi' - \kappa \widehat{E}_c^e)\big] + O(\kappa^2), \\ j_p = \big(m_p^0 + \kappa \widehat{m}_p (x - x_0)\big)\big[-p' + p(-\varphi' + \kappa \widehat{E}_v^e)\big] + O(\kappa^2), \end{cases} \tag{3.17}$$

and where, in view of (3.11),

$$\begin{cases} R(x) = \dfrac{pn - n_i^2(x)}{\tau_p(n + n_i(x)) + \tau_n(p + n_i(x))}, \\ n_i^2(x) = \delta^4 \exp\big[-\kappa \widehat{E}_g^e (x - x_0)\big] + O(\kappa^2). \end{cases} \tag{3.18}$$

The boundary conditions $(3.13)_{1,2}$ constitute an algebraic system of two equations for two unknowns $n(0)$ and $p(0)$ when evaluated at $x = 0$, and $n(1)$ and $p(1)$ when evaluated at $x = 1$. We write the solution for n and p up to leading order in κ and δ, and complete these boundary conditions with those pertaining to φ:

$$\begin{cases} n(0) = \dfrac{\delta^4}{N_a} \exp[\kappa \widehat{E}_g^e x_0] + O(\delta^4 \kappa^2) + O(\delta^8), \\ p(0) = N_a + O(\delta^4), \\ \varphi(0) = \varphi_{bin}(0) + \varphi_{app}(0), \\ n(1) = N_d + O(\delta^4), \\ p(1) = \dfrac{\delta^4}{N_d} \exp[-\kappa \widehat{E}_g^e (1 - x_0)] + O(\delta^4 \kappa^2) + O(\delta^8), \\ \varphi(1) = \varphi_{bin}(1) + \varphi_{app}(1). \end{cases} \tag{3.19}$$

3.2.3 *In the absence of external voltage: built-in potential*

The equilibrium case, in which no external voltage is applied, i.e., $\varphi_{app}(0) = \varphi_{app}(1) = 0$, is considered for the sole purpose of deriving the voltage drop $\varphi_{bin}(1) - \varphi_{bin}(0)$ across the junction, which allows the specification of the values of $\varphi_{bin}(0)$ and $\varphi_{bin}(1)$ in the boundary conditions on φ. Under equilibrium, we have $\jmath_n(x) = \jmath_p(x) = 0$ for the entire domain $(0,1)$, which, by $(3.16)_2$, yields

$$-n'(x) + n(x)\big(\varphi'_{bin}(x) - \kappa \widehat{E}_c^e\big) = 0 \tag{3.20}$$

Integrating (3.20) between $x = 0$ and $x = 1$ yields the voltage drop across the junction:

$$\varphi_{bin}(1) - \varphi_{bin}(0) = \ln\left(\frac{N_d N_a}{\delta^4}\right) + \kappa\big(\widehat{E}_v^e x_0 + \widehat{E}_c^e(1 - x_0)\big). \tag{3.21}$$

The reference value of the electric potential being arbitrary, $\varphi_{bin}(0)$ and $\varphi_{bin}(1)$ are only required to satisfy (3.21). We hence set the following boundary conditions:

$$\varphi_{bin}(0) = -\ln\left(\frac{N_a}{\delta^2}\right) - \kappa \widehat{E}_v^e x_0, \qquad \varphi_{bin}(1) = \ln\left(\frac{N_d}{\delta^2}\right) + \kappa \widehat{E}_c^e (1 - x_0). \tag{3.22}$$

The full expressions of $n(x), p(x), \varphi_{bin}(x)$ in the absence of external voltage could be derived from the system (3.16), however, they are not needed here.

3.2.4 *Under external voltage: current-voltage characteristic*

We set for the externally applied potential at the extremities of the p-n junction:

$$\varphi_{app}(0) = 0, \qquad \varphi_{app}(1) = -V. \tag{3.23}$$

The computation of $\jmath(V)$ is simplified by replacing the variables n and p with new ones, u and v, defined as

$$u := \delta^{-2} n \exp\big[-\varphi + \kappa \widehat{E}_c^e (x - x_0)\big], \qquad v := \delta^{-2} p \exp\big[\varphi - \kappa \widehat{E}_v^e (x - x_0)\big]. \tag{3.24}$$

Next, the governing equations (3.16) are rewritten in terms of u and v to leading order in κ and δ:

$$\begin{cases} \lambda^2 \varphi'' = \delta^2 \Big(u \exp\big[\varphi - \kappa \widehat{E}_c^e (x - x_0)\big] \\ \qquad\qquad\qquad\qquad - v \exp\big[-\varphi + \kappa \widehat{E}_v^e (x - x_0)\big] \Big) - C(x), \\ \jmath_n' = -R, \qquad \jmath_p' = -R, \end{cases} \tag{3.25}$$

with,

$$\begin{cases} \jmath_n = -\delta^2 \big(m_n^0 + \kappa \widehat{m}_n (x - x_0)\big) u' \exp\big[\varphi - \kappa \widehat{E}_c^e (x - x_0)\big], \\ \jmath_p = -\delta^2 \big(m_p^0 + \kappa \widehat{m}_p (x - x_0)\big) v' \exp\big[-\varphi + \kappa \widehat{E}_v^e (x - x_0)\big], \end{cases} \tag{3.26}$$

where, in light of (3.18) and (3.24),

$$\begin{aligned} R(x) &= A/B\,, \text{ where} \\ A &:= \delta^2(uv-1)\exp\big[-\kappa\widehat{E}_g^e(x-x_0)\big], \\ B &:= \tau_p\Big(u\exp\big[\varphi-\kappa\widehat{E}_c^e(x-x_0)\big]+\exp\big[-\frac{\kappa}{2}\widehat{E}_g^e(x-x_0)\big]\Big) \\ &\quad+\tau_n\Big(v\exp\big[-\varphi+\kappa\widehat{E}_v^e(x-x_0)\big]+\exp\big[-\frac{\kappa}{2}\widehat{E}_g^e(x-x_0)\big]\Big). \end{aligned} \tag{3.27}$$

By (3.22), (3.23) and (3.24), the boundary conditions (3.19) take the form

$$\begin{cases} u(0) &= 1, \\ v(0) &= 1, \\ \varphi(0) &= -\ln\left(\dfrac{N_a}{\delta^2}\right)-\kappa\widehat{E}_v^e x_0, \end{cases} \qquad \begin{cases} u(1) &= \exp[V], \\ v(1) &= \exp[-V], \\ \varphi(1) &= \ln\left(\dfrac{N_d}{\delta^2}\right)+\kappa\widehat{E}_c^e(1-x_0)-V. \end{cases} \tag{3.28}$$

In the system of equations (3.25), (3.27) and (3.28), the small parameter λ multiplies the highest derivative of φ, which implies the existence of a boundary layer at $x = x_0$, where $C(x)$ is discontinuous. In what follows, we outline the main steps of the matched asymptotic expansion analysis used to solve the singular perturbation problem associated with the small parameters λ and δ and refer the reader to Markowich (1986) for further details. The small parameter κ, which embeds strain effects, introduces a regular perturbation of the case $\kappa = 0$. We solve the resulting problem by means of the Poincaré asymptotic expansion.

In the boundary layer, we introduce the fast variable $\widehat{x}$:

$$\widehat{x} = \frac{x-x_0}{\lambda}. \tag{3.29}$$

Away from the boundary layer, we expect u, v and φ to vary on the slow x-scale. We thus introduce the *outer expansions*:

$$\begin{cases} u(x;\lambda,\delta,\kappa) = \overline{u}(x;\delta,\kappa)+O(\lambda), \\ v(x;\lambda,\delta,\kappa) = \overline{v}(x;\delta,\kappa)+O(\lambda), \\ \varphi(x;\lambda,\delta,\kappa) = \overline{\varphi}(x;\delta,\kappa)+O(\lambda). \end{cases} \tag{3.30}$$

In the boundary layer, we write down the *inner expansions*:

$$\begin{cases} u(x;\lambda,\delta,\kappa) = \overline{u}(x;\delta,\kappa)+\widehat{u}(\widehat{x};\delta,\kappa)+O(\lambda), \\ v(x;\lambda,\delta,\kappa) = \overline{v}(x;\delta,\kappa)+\widehat{v}(\widehat{x};\delta,\kappa)+O(\lambda), \\ \varphi(x;\lambda,\delta,\kappa) = \overline{\varphi}(x;\delta,\kappa)+\widehat{\varphi}(\widehat{x};\delta,\kappa)+O(\lambda). \end{cases} \tag{3.31}$$

The matching condition reads

$$\lim_{\widehat{x}\to\pm\infty}[\widehat{u},\widehat{v},\widehat{\varphi}](\widehat{x};\delta,\kappa) = [0,0,0]. \tag{3.32}$$

In the case $\kappa = 0$, Markowich (1986) shows that $\widehat{u}$ and $\widehat{v}$ are identically zero for all $\widehat{x}\in\mathbb{R}$ and establishes the continuity of $\overline{u}$ and $\overline{v}$ at $x = x_0$. It can be shown that these results hold true in the case $\kappa \neq 0$.

We now consider the outer problem for $\kappa \neq 0$. Inserting the outer expansions (3.30) in the system (3.25) and equating the zeroth-order terms in λ, $(3.25)_1$ yields

$$0 = \delta^2 \Big(\overline{u} \exp\left[\overline{\varphi} - \kappa \widehat{E}_c^e (x - x_0)\right] - \overline{v} \exp\left[-\overline{\varphi} + \kappa \widehat{E}_v^e (x - x_0)\right] \Big) - C(x). \quad (3.33)$$

The remaining equations, $(3.25)_{2,3}$, (3.27) and (3.28) are unchanged but apply now to the overlined variables (i.e., to the outer expansions).

The solution of the outer problem on the intervals $(0, x_0)$ and $(x_0, 1)$ is detailed in Appendix B. To find the $j(V)$ relation, we need the currents $j_n(x)$ and $j_p(x)$, which are computed on $(0, x_0)$ and $(x_0, 1)$, respectively, and are evaluated at $x = x_0$:

$$\begin{cases} j_n(x_0) = -\dfrac{\delta^4 m_n^0 \big(\exp[V] - 1\big)}{N_a L_n^0} \left[\coth\left(\dfrac{x_0}{L_n^0}\right) \right. \\ \qquad\qquad \left. + \kappa \left(\dfrac{\widehat{E}_g^e L_n^0}{2} - \dfrac{\widehat{m}_n}{4 m_n^0} \left(L_n^0 + \dfrac{x_0^2}{L_n^0 \sinh^2\left(\dfrac{x_0}{L_n^0}\right)} \right) \right) \right], \\ j_p(x_0) = \dfrac{\delta^4 m_p^0 \big(\exp[V] - 1\big)}{N_d L_p^0} \left[\coth\left(\dfrac{1 - x_0}{L_p^0}\right) \right. \\ \qquad\qquad \left. - \kappa \left(\dfrac{\widehat{E}_g^e L_p^0}{2} - \dfrac{\widehat{m}_p}{4 m_p^0} \left(L_p^0 + \dfrac{(1 - x_0)^2}{L_p^0 \sinh^2\left(\dfrac{1 - x_0}{L_p^0}\right)} \right) \right) \right], \end{cases} \quad (3.34)$$

where the diffusion lengths of electrons and holes are given by $L_n^0 := \sqrt{\tau_n m_n^0}$ and $L_p^0 := \sqrt{\tau_p m_p^0}$. Subtracting $(3.25)_2$ from $(3.25)_3$ and integrating over x, we establish that the total electric current

$$j(x) := j_p(x) - j_n(x) \quad (3.35)$$

is uniform on $(0, 1)$. We denote it with the constant j and evaluate (3.35) at $x = x_0$ which is the only point where both j_n and j_p are known. We therefore have

$$j = \big(\exp[V] - 1\big) j_s, \quad (3.36)$$

where the saturation current j_s is given by

$$\begin{aligned} j_s =& \frac{\delta^4 m_n^0}{N_a L_n^0} \coth\left(\frac{x_0}{L_n^0}\right) + \frac{\delta^4 m_p^0}{N_d L_p^0} \coth\left(\frac{1-x_0}{L_p^0}\right) \\ &+\kappa \left\{ \frac{\delta^4 m_n^0}{N_a} \left[\frac{\widehat{E}_g^e}{2} - \frac{\widehat{m}_n}{4m_n^0} \left(1 + \frac{x_0^2}{(L_n^0)^2 \sinh^2\left(\frac{x_0}{L_n^0}\right)} \right) \right] \right. \\ &\left. - \frac{\delta^4 m_p^0}{N_d} \left[\frac{\widehat{E}_g^e}{2} - \frac{\widehat{m}_p}{4m_p^0} \left(1 + \frac{(1-x_0)^2}{(L_p^0)^2 \sinh^2\left(\frac{1-x_0}{L_p^0}\right)} \right) \right] \right\}. \end{aligned} \tag{3.37}$$

The above equations (3.36) and (3.37) give the $j(V)$ characteristic for a strained p-n junction. Note that, at zeroth-order in κ, (3.37) reduces to the Shockley equation of a rigid p-n junction (see e.g., Markowich et al., 1990, Section 4.2).

Figure 3.3 shows the solution on the outer domain of the original dimensionless problem (3.16), (3.18), and (3.19), in terms of the carrier concentrations n and p, and the currents j_n, j_p and j of electrons, holes and electric current, respectively. Note the presence of a boundary layer at the p-n interface $x = x_0$ for the carrier concentrations whereas the currents remain continuous.

Finally, we rewrite j_s in terms of dimensional variables:

$$\begin{aligned} \frac{j_s}{qU_T(\rho n_i^0)^2} =& \frac{m_n^0}{(\rho N_a) L_n^0} \coth\left(\frac{x_0}{L_n^0}\right) + \frac{m_p^0}{(\rho N_d) L_p^0} \coth\left(\frac{l-x_0}{L_p^0}\right) \\ &+\kappa \left\{ \frac{m_n^0}{(\rho N_a)} \left[\frac{\widehat{E}_g^e}{2k_B T} - \frac{\widehat{m}_n}{4m_n^0} \left(1 + \frac{x_0^2}{(L_n^0)^2 \sinh^2\left(\frac{x_0}{L_n^0}\right)} \right) \right] \right. \\ &\left. - \frac{m_p^0}{(\rho N_d)} \left[\frac{\widehat{E}_g^e}{2k_B T} - \frac{\widehat{m}_p}{4m_p^0} \left(1 + \frac{(l-x_0)^2}{(L_p^0)^2 \sinh^2\left(\frac{l-x_0}{L_p^0}\right)} \right) \right] \right\}, \end{aligned} \tag{3.38}$$

with the dimensional diffusion lengths defined as $L_n^0 := \sqrt{U_T \tau_n m_n^0}$ and $L_p^0 := \sqrt{U_T \tau_p m_p^0}$.

We can understand the different physical processes underlying the macroscopic strain-induced changes in current by considering each strain-related coefficient in (3.38). The effect of the strain-dependent mobilities appears in the coefficients m_n^0, m_p^0, L_n^0, L_p^0, $\widehat{m}_n$ and $\widehat{m}_p$, whereas n_i^0 and $\widehat{E}_g^e$ account for the strain dependence of band energy levels and densities of states together. Depending on the material and the directions of strain, these microscopic effects can either sum up or compensate each other, resulting in a small or large strain effect on the current. For each one of these effects we can distinguish in (3.38) between the change in current that exists if the junction is uniformly strained with strain

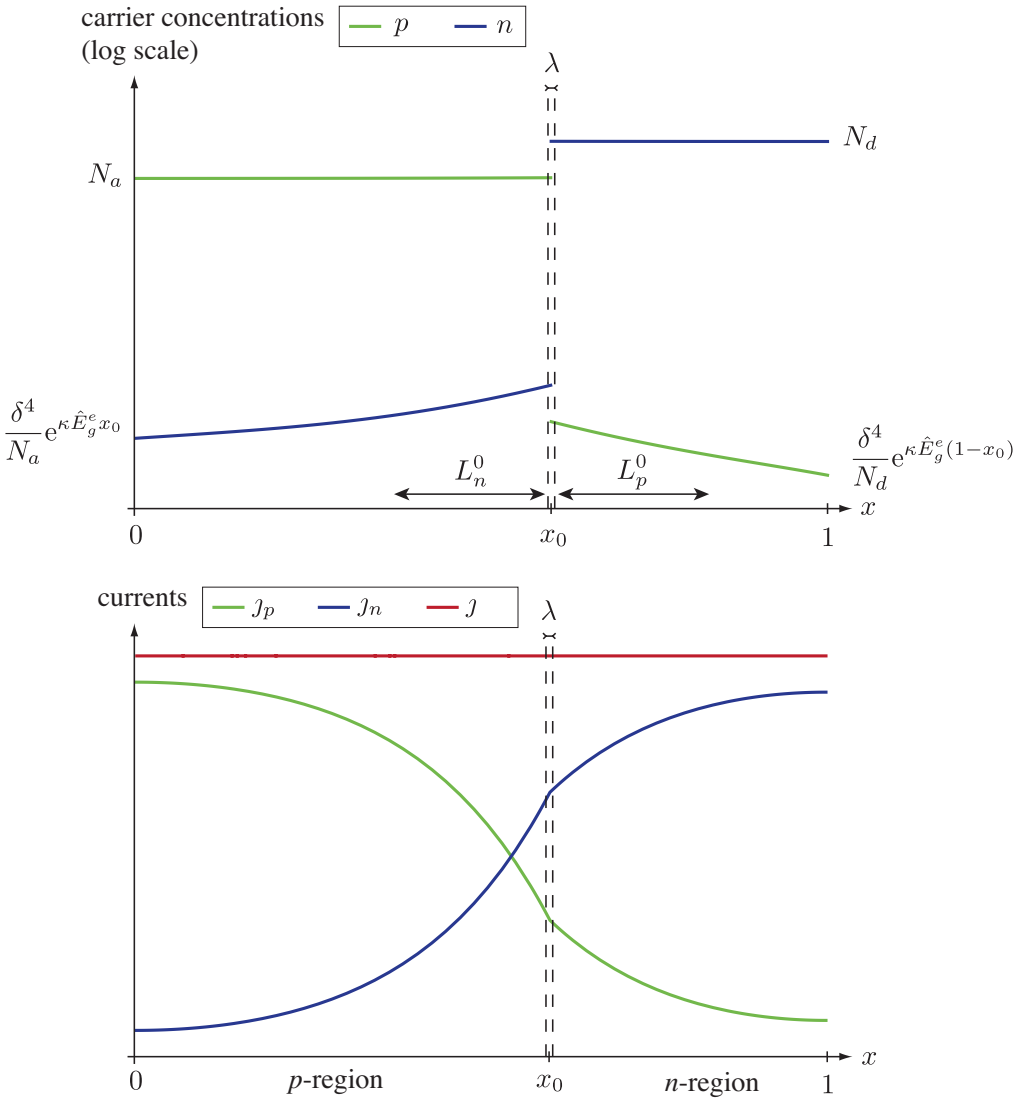

Figure 3.3: Electron and hole densities and currents in the p-n junction, solution of the problem (3.16), (3.18) and (3.19) on the outer domain $(0, x_0) \cup (x_0, 1)$. The explicit forms of the functions n and p are obtained from the relation (3.25) combined with (B.2), (B.5), (B.7), (B.9), (B.11), (B.15), (B.14) and (B.18). The expressions of the current j_n, j_p and j can also be made explicit by combining the same set of equations with (B.4) and (3.35).

ε^0 (accounted for by parameters with superscript 0) and the change due to bending with curvature κ.

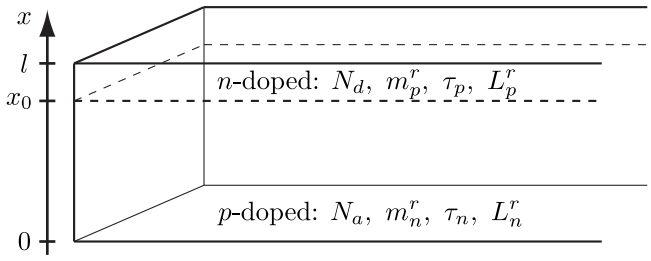

Figure 3.4: Typical crystalline silicon solar cell geometry with a thin n-doped emitter and a thick p-doped base.

3.3 MONOCRYSTALLINE SILICON SOLAR CELL

We now consider a typical monocrystalline silicon solar cell subjected to bending and apply the results of Section 3.2 to investigate the effect of strain on its characteristic $\jmath(V)$. The current $\jmath(V)$ given by (3.36) corresponds to what is called in photovoltaics, the *dark current* of the solar cell. It is the current that circulates through the cell under external voltage V and in the absence of illumination. We show in Section 3.3.1 how the change in dark current can be computed from the asymptotic solution of Section 3.2 and, in Section 3.3.2, we calculate and discuss this strain-effect for some typical strain states.

3.3.1 *Strain-induced changes of the dark current*

Consider the diamond lattice structure of silicon, assume that the principal crystallographic directions $\langle 100\rangle$ are aligned with the (x, y, z) directions (Figure 3.4). The cell consists of a pn^+-junction (i.e., asymmetrically doped: $N_d \gg N_a$) whose characteristics are given in Table 3.2. Note that the thickness of the n^+-region (the *emitter*) is about one thousand times smaller than the thickness of the p-doped region (the *base*), the junction interface is thus effectively located at the boundary plane $x = l$.

As an application of the previous theory, we aim at computing the change in dark current when the cell is under bending about the z-direction. Notice that Equation(3.36) has been derived under the assumption of Dirichlet boundary conditions (3.19) expressing that the densities of electrons and holes at the boundaries $x = 0$ and $x = l$ are the corresponding equilibrium densities. In practice, at the boundaries of a solar cell there is an inevitable surface recombination proportional to the deviation of the densities from their equilibrium values. For reasons to be explained below, the surface recombination can be neglected in the problem considered.

Starting with the dimensional version of (3.35), we evaluate the current at $x = x_0$,

$$\jmath = q\big(\jmath_p(x_0) - \jmath_n(x_0)\big). \tag{3.39}$$

From (3.34), we conclude that the doping strength asymmetry between the regions n^+ and p ($N_d \gg N_a$), results in a current $\jmath_p(x_0)$ (associated to diffusion

Table 3.2: Typical properties of the monocrystalline silicon solar cell (see Nelson, 2003)

property	base p-Si	emitter n^+-Si
Width (μm)	$x_0 = 300$	$l - x_0 = 0.5$
Doping (cm^{-3})	$N_a = 1 \times 10^{16}$	$N_d = 1 \times 10^{19}$
Mobility (cm^2.V^{-1}.s^{-1})	$m_n^r = 1544$	$m_p^r = 77$
Carrier lifetime (s)	$\tau_n = 5 \times 10^{-6}$	$\tau_p = 1 \times 10^{-6}$
Diffusion length (μm)	$L_n^r = 140$	$L_p^r = 14$

of holes in the emitter n^+) which is at least two orders of magnitude smaller than the current $\jmath_n(x_0)$ (associated to diffusion of electrons in the base p), i.e., $\jmath_p(x_0) \ll \jmath_n(x_0)$. This holds even in presence of surface recombination. Further, since $L_n^0 \ll x_0$, surface recombination for $\jmath_n(x_0)$ can be safely ignored, given that it only affects the negligible hole-diffusion current $\jmath_p(x_0)$. It follows from (3.38) that the saturation current of the junction reduces to the contribution of $\jmath_n(x_0)$. Since $L_n^0/x_0 \ll 1$, we obtain the simplified expression:

$$\jmath_s = qU_T(\rho n_i^0)^2 \left[\frac{m_n^0}{(\rho N_a) L_n^0} + \kappa \left\{ \frac{m_n^0}{(\rho N_a)} \left(\frac{\widehat{E}_g^e}{2k_B T} - \frac{\widehat{m}_n}{4m_n^0} \right) \right\} \right] + O\left(\exp\left[\frac{-2x_0}{L_n^0} \right] \right). \quad (3.40)$$

We now define the relative strain-induced change in dark current $\Delta\jmath$, where we also linearize the contribution due to ε^0. As a result, we only keep first-order perturbations in κ and in the amplitude of ε^0 (represented by the yy-component ε_{yy}^0), in which case (3.40) yields

$$\Delta\jmath := \frac{\jmath_s(\varepsilon_{yy}^0, \kappa) - \jmath_s^r}{\jmath_s^r} = \left(\frac{\widehat{m}_n}{2m_n^r} - \frac{\widehat{E}_g^e}{k_B T} \right) \left(\varepsilon_{yy}^0 - \frac{\kappa L_n^r}{2} \right), \quad (3.41)$$

where $\widehat{E}_g^e$, defined in (3.15), is approximated by:

$$\widehat{E}_g^e = \widehat{E}_c - \widehat{E}_v - k_B T \left(\frac{\widehat{N}_c}{N_c^r} + \frac{\widehat{N}_v}{N_v^r} \right). \quad (3.42)$$

3.3.2 *Results for typical strain states and discussion*

Six different cases of strained solar cells are considered as depicted in Figure 3.5. The values of the applied strain and the curvature are summarized in Table 3.3 and have been chosen such that the highest strain in the cell remains lower than 0.2% in compression and in tension, i.e., the typical strains that silicon can sustain without failing.

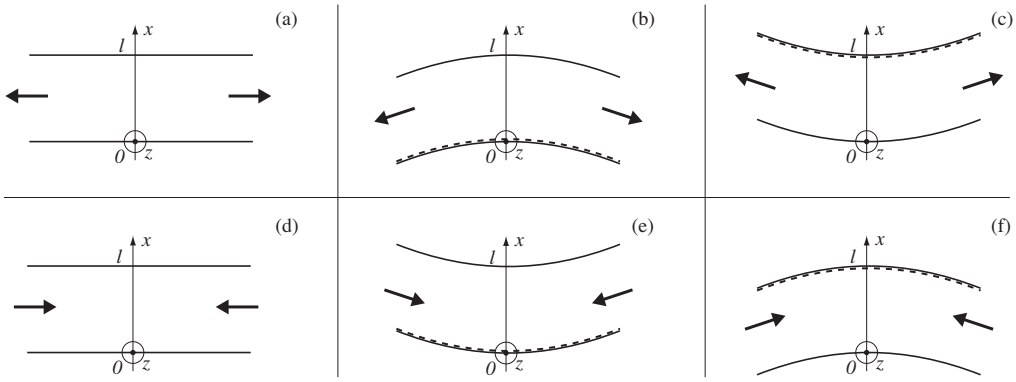

Figure 3.5: Six strain states of the solar cell. Cases (a) and (d) correspond to homogeneous strain states, while cases (b), (c), (e) and (f) correspond to nonuniform strain states due to the bending about the z-axis. Cases (a), (b), (c) correspond to tensile states, whereas cases (d), (e), (f), are compressive states. The dashed line indicates the neutral plane where $\boldsymbol{\varepsilon} = \mathbf{0}$.

Table 3.3: Applied radius of curvature $\mathcal{R} = 1/\kappa$ and yy-component of the strain at the interface $x = x_0$ for the strain states depicted in Figure 3.5. The cell, described in Table 3.2, has a thickness $l = 0.3$ mm.

Case	(a)	(b)	(c)	(d)	(e)	(f)
$\mathcal{R} = 1/\kappa$ (mm)	∞	150	-150	∞	-150	150
ε^0_{yy} $(\times 10^{-3})$	2.0	2.0	0	-2.0	-2.0	0

The coefficients entering the yy-component of the strain are given in Table 3.3, while the remaining strain components are deduced, in the same way as in Section 8.2.3, using the linear constitutive law of silicon in (3.4):

$$\varepsilon_{yy}(x) = \varepsilon^0_{yy} + \kappa x, \quad \varepsilon_{zz}(x) = 0, \quad \varepsilon_{xx}(x) = -\frac{c_{xxyy}}{c_{xxxx}}\varepsilon_{yy}(x), \tag{3.43}$$

where $c_{xxxx} = 166$ GPa and $c_{xxyy} = 64$ GPa (Wortman and Evans, 1965). Since the principal axes of the cubic-symmetry crystal are assumed to be the coordinate axes, the off-diagonal components of $\boldsymbol{\varepsilon}$ vanish.

Using the strain state (3.43), the x-dependence of the six electronic parameters E_c, E_v, N_c, N_v, m_n, m_p in silicon is derived in the Appendix A. We obtain $\widehat{m}_n/2m^r_n = -48$. Further, given the tension-compression asymmetry for the strain dependence of the valence band edge energy and effective density of states (see equations (A.9) and (A.10)) we have for the effective band gap: $\widehat{E}^e_g/k_BT = 46$ for tension ($\varepsilon_{yy} \geq 0$) and 73 for compression ($\varepsilon_{yy} < 0$).

The strain-induced changes in dark current ΔJ are summarized in Table 3.4 for the six strain states considered. They show a decrease (resp. increase) in dark current in tension (resp. compression) that can reach 24%.

By comparing values of $\widehat{m}_n/2m^r_n$ and $\widehat{E}^e_g/k_BT$, we observe that the strain-induced change due to mobility is of the same order as the one due to the

Table 3.4: Strain-induced changes in dark current for the six strain states depicted in Figure 3.5.

Case	(a)	(b)	(c)	(d)	(e)	(f)
ΔJ (%)	-19	-14	-4	24	19	6

energy gap and effective density of states (both included in $\widehat{E}_g^e$). As expected the largest changes correspond to a uniform straining of the cell. The presence of bending is equivalent to a uniform strain change, with the strain at midpoint $x = x_0 - L_n^r/2$ as can be seen from (3.41). Hence, the strain influence is maximal when the strain at the midpoint is maximized.

4

EXPERIMENTAL STRAINING OF A SOLAR CELL

In this chapter, we measure the strain-induced changes in the dark current-voltage characteristic of Silicon HeteroJunction (SHJ) solar cells loaded under uniaxial tension. We choose this type of cells for two reasons. First, SHJ solar cells are made of a crystalline silicon base for which, unlike amorphous silicon or other crystalline materials, the strain dependence of the electronic parameters (band edge energies, densities of states, and mobilities) are relatively well known. Second, we have the possibility at the Laboratory of Physics of Interfaces and Thin Films (*Laboratoire de Physique des Interfaces et des Couches Minces*, LPICM) of École polytechnique to fabricate such cells from commercial crystalline wafers by deposition of the amorphous layers—unlike crystalline silicon solar cells made by dopant diffusion, a method not available at LPICM.

Specializing the analysis of Chapter 3 to the case of uniform strains, the measurements are discussed using a model that involves the strain-induced changes of the electronic properties of the semiconductor.

4.1 DESCRIPTION OF THE SOLAR CELL

4.1.1 *Structure of the solar cell*

The SHJ solar cells are made of crystalline silicon (c-Si) and amorphous silicon (a-Si:H), two materials that have different band gaps (1.12 eV for c-Si at 20°C and about 1.7 eV to 1.8 eV for a-Si:H), hence the appelation *heterojunction*. The solar cells are produced from commercial crystalline silicon wafers by depositing the amorphous layers (see Figure 4.1) in a Plasma Enhanced Chemical Vapor Deposition (PECVD) reactor.

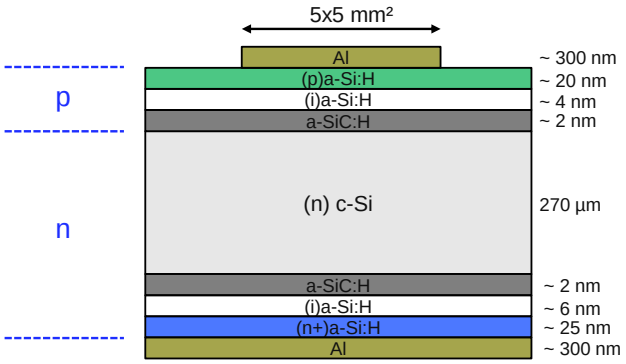

Figure 4.1: Structure of the silicon heterojunction solar cell.

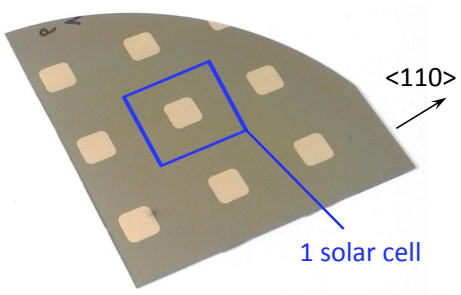

Figure 4.2: A quarter of a 4″ (102 mm) diameter wafer at the end of the fabrication process. Each square corresponds to a 5×5 mm^2 solar cell, the 15×15 mm^2 blue square depicts the area cut out to separate the cells.

Recall that n-doped corresponds to doping with electron donors (phosphorus) and p-doped to doping with electron acceptors (boron).

As shown on Figure 4.1, the structure of the solar cell is composed of a n-doped crystalline silicon wafer [(n)c-Si] of thickness 270 μm, and a p-doped amorphous silicon thin layer [(p)a-Si:H] of a few tens of nanometers which together form the *p-n* heterojunction. Between these two principal layers, are deposited two thin *buffer layers* of silicon carbide [a-SiC:H] and amorphous intrinsic silicon [(i)a-Si:H] whose role is to reduce the density of defects at the crystalline/amorphous interface. On the back side of the stack the three layers of a-SiC:H, (i)a-Si:H, and n^+-doped amorphous silicon [(n+)a-Si:H] have a passivating function, i. e., they reduce the surface recombination. Ultimately, aluminum electrodes are evaporated on each side of the stack. Note that, because we focus on the *dark* current-voltage characteristic, no transparent conductive layer (such as indium tin oxide) is deposited on top of the (p)a-Si:H layer.

4.1.2 *Fabrication of the solar cell*

The SHJ solar cells are fabricated starting from a commercial p-doped c-Si wafer with the surface having a (100) crystallographic orientation and with a resistivity of 2.6 Ω.cm. After dipping the wafer for 30 s in a solution of hydrofluoric acid to eliminate the native silicon oxide layer, the various a-SiC:H and a:Si-H layers are deposited by PECVD at 175°C. The thicknesses of the amorphous layers on Figure 4.1 are estimated from the deposition time in the plasma chamber and using an ellipsometry data analysis of the deposited layers.

The aluminum electrodes are subsequently deposited by thermal evaporation in vacuum and the resulting cells are annealed at 180°C for 15 min to improve the carrier lifetime. For the evaporation of the top electrode, we use a home-made mask with square cell sections of 5×5 mm^2 and spacing between each cell of 10 mm (see Figure 4.2 showing a quarter of a 4″ diameter wafer).

After fabrication, the cells are separated by cutting 15×15 mm^2 squares, as shown on Figure 4.2, providing space around each cell for gripping it as needed for the mechanical loading. Note that the square pattern is deposited parallel

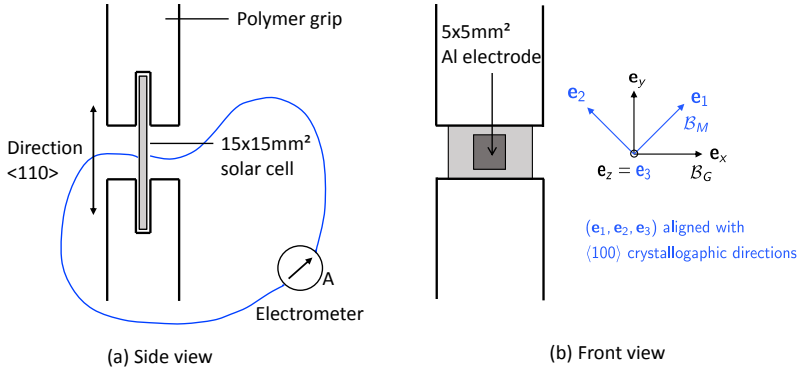

Figure 4.3: Schematic (not to scale) of the experimental set-up. the 15×15 mm^2 solar cell is glued inside the grooves of the 3D printed polymer grips and an electrometer is connected to the front and back electrodes for the measurement of the current-voltage characteristic. $\mathcal{B}_M = (\mathbf{e}_1, \mathbf{e}_2, \mathbf{e}_2)$ is an orthonormal basis (M for material) aligned with the $\langle 100 \rangle$ directions of the crystal and $\mathcal{B}_G = (\mathbf{e}_x, \mathbf{e}_y, \mathbf{e}_z)$ (G for grips) obtained by rotating $\mathcal{B}_M$ by $\pi/4$ in the clockwise direction has its vector $\mathbf{e}_y$ aligned with the loading direction.

to the flat of the wafer so that the side of the cells—which correspond to the loading direction in the mechanical testing—are along the $\langle 110 \rangle$ directions.

4.2 MEASUREMENT OF THE DARK CURRENT UNDER MECHANICAL LOADING

In this section we describe the experimental set-up developed to measure the effect of mechanical loading on the dark current-voltage characteristic and report the experimental results that we obtain.

4.2.1 *Experimental set-up*

To load mechanically the solar cells, we use an Instron 3366 electromechanical testing machine with home made, three-dimensional (3D) printed, grips. As depicted in Figure 4.3, for each experiment, we 3D print two polymer grips with grooves of thickness 500 μm within which the 15×15 mm^2 270 μm thick solar cell is glued (with Araldite standard epoxy glue). Note that the sample is glued inside the grooves after the grips have been set inside the testing machine (cf. Figure 4.4). In that way, we avoid exerting pre-stress on the silicon wafer as it is put inside the testing machine. In such a configuration, the silicon sample carries all the load of the testing machine, unlike situations where the wafer is glued on top of a supporting plate on which the loading is applied. Moreover, given that the stiffness of the polymer grips (Young's modulus about 2.4 GPa) is much smaller than that of silicon (elastic coefficients of the order of 100 GPa), we can assume the silicon wafer to be in a state of uniaxial stress. Using the

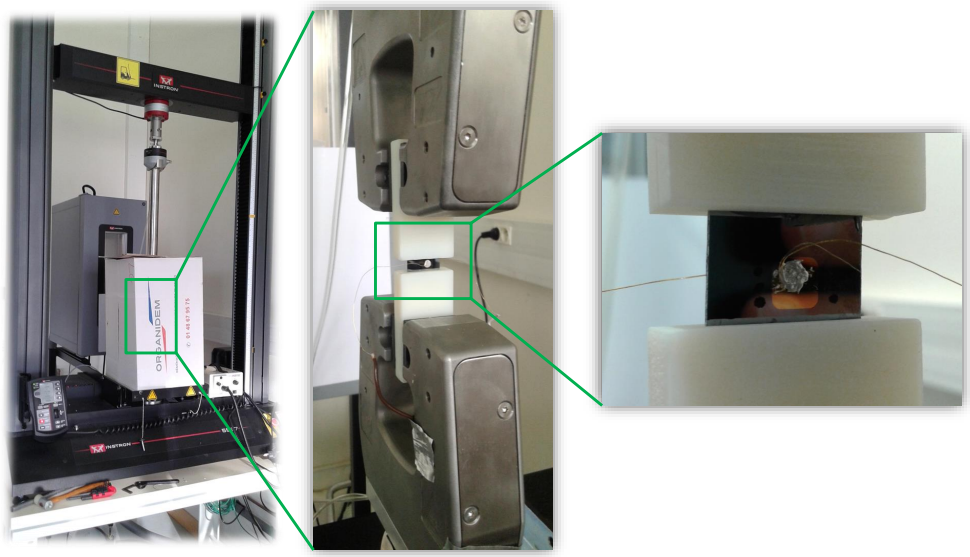

Figure 4.4: Picture of the experimental setting. The 15×15 mm^2 solar cell is glued inside the polymer grips themselves held by the machine grips. The two copper wires are connected to the front and back electrodes with silver paste.

elastic properties of silicon (described by the elasticity tensor $\mathbf{c}$ of silicon) and the knowledge of the stress state of the sample, we can derive its strain state (described by the small strain tensor $\boldsymbol{\varepsilon}$) from the load F measured by the load cell of the testing machine with

$$\boldsymbol{\varepsilon} = \mathbf{c}^{-1} : \boldsymbol{\sigma}, \tag{4.1}$$

where the stress state $\boldsymbol{\sigma}$ is approximately given by

$$\boldsymbol{\sigma} = \frac{F}{S} \mathbf{e}_y \otimes \mathbf{e}_y, \tag{4.2}$$

with $\mathbf{e}_y$ the loading direction (cf. Figure 4.3) and S the section area of the silicon sample in the $(\mathbf{e}_x, \mathbf{e}_z)$ plane.

For the electric measurement, using monofilament copper wires contacted with silver paste to the front and back electrodes, the solar cell is connected to a sourcemeter Keithley 2460. With this set-up, the current-voltage characteristic of the solar cell is measured for different loading forces: $F = 200$ N ($\varepsilon_{yy} = 2.7 \times 10^{-4}$), $F = 300$ N ($\varepsilon_{yy} = 4.1 \times 10^{-4}$), $F = 400$ N ($\varepsilon_{yy} = 5.4 \times 10^{-4}$) and $F = 500$ N ($\varepsilon_{yy} = 6.8 \times 10^{-4}$), which is the last level of loading before the failure of the sample. At the different load levels, the displacement of the grips is maintained fixed for about one minute, time necessary to perform a measurement of the J-V characteristic. Note that we also return to zero load ($F = 0$) between the different loading levels and measure again, in these relaxed states, the J-V characteristics in order to check the reversibility with deformation of the change in the characteristic.

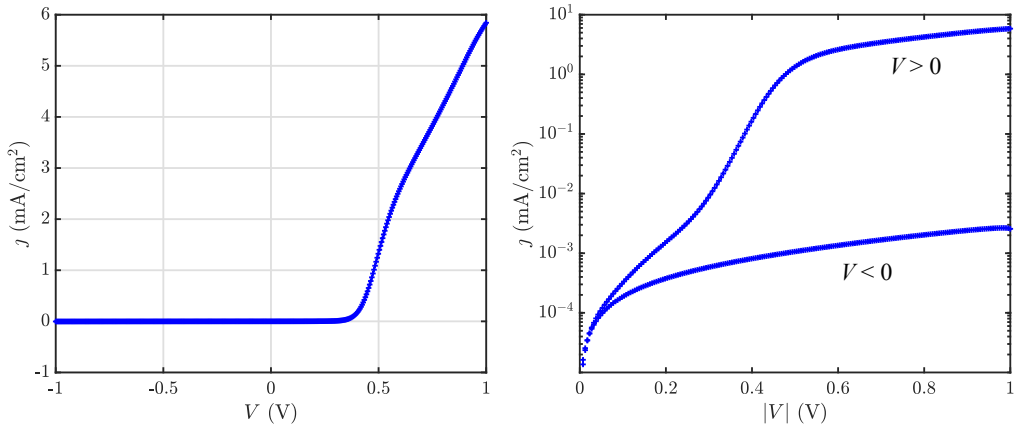

Figure 4.5: Experimental dark current-voltage characteristic of cell 1 at zero load in a linear plot (a) and in semilogarithmic plot (b). Note that in (b) the current is plotted as a function of $|V|$ as usual for diode characteristics. Obviously, the reverse current ($V < 0$) corresponds to the curve with lower current.

4.2.2 *Experimental strain dependence of the current-voltage characteristics*

In this section, we first introduce the two-exponential model that allows us to fit properly the current-voltage characteristics and extract the parameters describing the solar cells (diffusion saturation current, recombination-generation saturation current, parallel and series resistances). Secondly, using this model, we obtain from the measurements under mechanical loading, the experimental strain dependence of the cell parameters.

4.2.2.1 *Two-exponential model for experimental current-voltage characteristics*

We show on Figure 4.5 an example of experimental dark current-voltage characteristic (J-V characteristic). Actually, on the same wafer, the J-V characteristics of the different cells show a large variability as can be seen on Figure 4.6. This variability is likely due to inhomogeneities in the deposition processes and in the contamination from the environment. For the measurements under mechanical load, we select the solar cells with the characteristics closest to the ideal one, with criteria explained below. Recall that the dark current-voltage characteristic of an ideal diode under strain is given by (3.36), which we recall:

$$J = J_s(\varepsilon)\left(\exp\left(\frac{qV}{k_B T}\right) - 1\right), \tag{4.3}$$

where $J_s(\varepsilon)$ is the diffusion saturation current which, in the present setting, depends on the spatially uniform small strain tensor ε. However, as can been seen on Figure 4.5, the shape of an experimental J-V characteristic notably differs from the ideal Shockley relation (4.3).

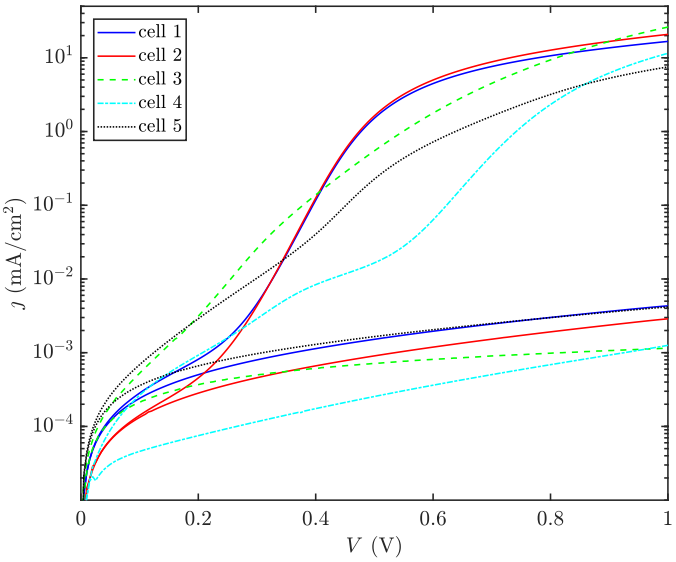

Figure 4.6: Disparity in the current-voltage characteristics of different solar cells deposited on the same wafer (ARCAM Deposition identifier: 1706271).

Indeed, actual solar cells are not ideal diodes and other phenomena than those accounted for in the ideal model are involved (e.g. recombination-generation of carriers inside the space-charge zone (Sah et al., 1957) and resistive effects).

TWO-EXPONENTIAL MODEL With the goal of obtaining the saturation current J_s from the experimental characteristics—and more specifically its relative change with strain—we use, for fitting the dark J-V characteristic, a two exponential model (Wolf et al., 1977; Suckow et al., 2012) with effective series resistance R_s and parallel resistance R_p,

$$J = \underbrace{J_s(\varepsilon)\left(\exp\left(\frac{q\big(V - JR_s(\varepsilon)\big)}{k_B T}\right) - 1\right)}_{\text{Diffusion current}} + \underbrace{J_r(\varepsilon)\left(\exp\left(\frac{q\big(V - JR_s(\varepsilon)\big)}{2k_B T}\right) - 1\right)}_{\text{Recombination-generation current}} + \underbrace{\frac{V - JR_s(\varepsilon)}{R_p(\varepsilon)}}_{\substack{\text{Parallel resistance} \\ \text{current}}}, \quad (4.4)$$

where $J_r(\varepsilon)$ denotes the saturation current of the Recombination-Generation (RG) current whose expression, with a factor $1/2$ in the exponential, comes from a modeling of the recombination-generation phenomena inside the space charge zone (see, e. g., Sze and Ng, 2006). The equivalent electric circuit corresponding to the two-exponential model (4.4) is shown on Figure 4.7 (a).

Note that, while we introduce, *a priori*, a dependence on strain for j_r, R_s and R_p, we do not have, unlike for j_s, a physical model for these dependences. Indeed, R_s and R_p are phenomenological quantities introduced to account for the parasitic resistances of various physical origins (e. g., contact resistance,

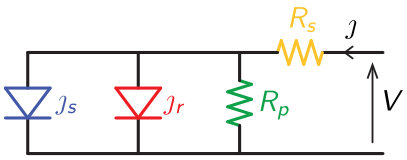

(a)

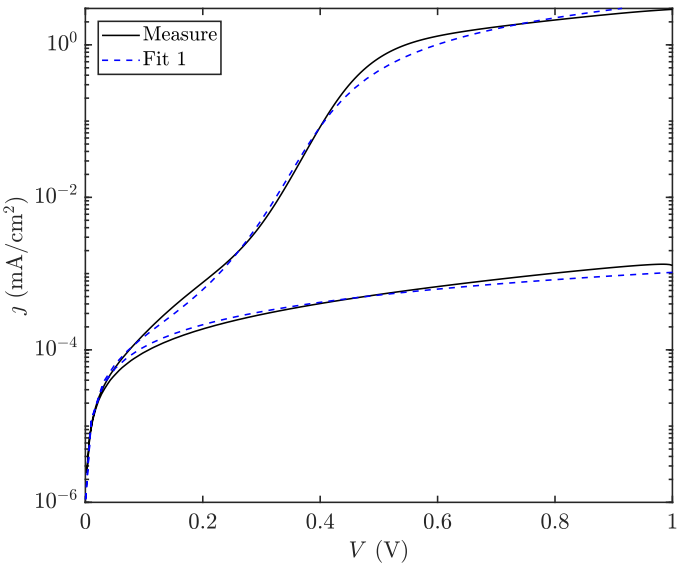

(b)

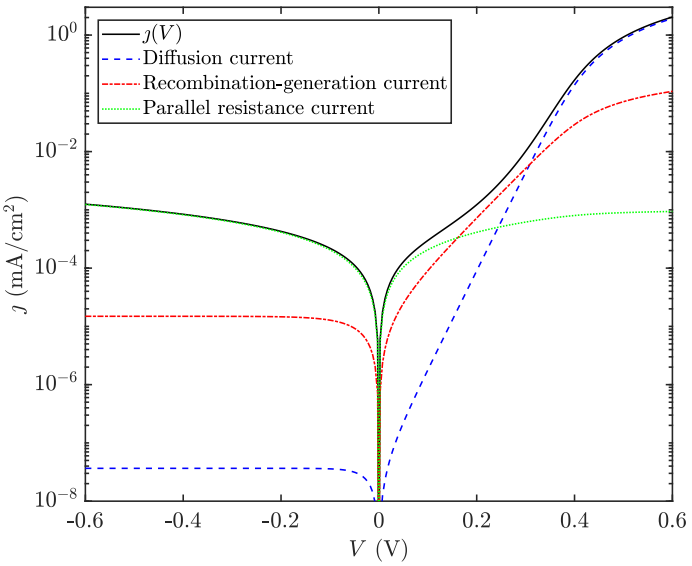

(c)

Figure 4.7: (a) Equivalent electric circuit for the two-exponential model with j-V expression (4.4). (b) Best fit of (4.4) to the experimental j-V characteristic of cell 1 in the absence of mechanical loading. Fit 1 corresponds to a fit over the whole range $(-1\ \text{V}, 1\ \text{V})$. (c) Decomposition of the analytical j-V characteristic (4.4) into its different contributions. Note that the series resistance only affects the j-V curve at high direct voltage $(V > 0.4\ \text{V})$ and causes the decrease in current in this region.

j_s (mA/cm^2)	j_r (mA/cm^2)	R_s ($\Omega \cdot$ cm^2)	R_p ($\Omega \cdot$ cm^2)
3.7×10^{-8}	1.5×10^{-5}	71	4.9×10^5

Table 4.1: Best fit parameters of (4.4) with the experimental j-V characteristic of cell 1 for a fit over the range $(-1\text{ V}, 1\text{ V})$.

resistance of the semiconductor layers, shunts). Likewise, j_r being associated to recombination inside the space charge region, it involves electronic properties of both the crystalline and amorphous silicon whose, for the latter, strain dependence is not known.

FITTING PROCESS AND ANALYSIS OF THE CONTRIBUTIONS TO j

To determine the four model parameters j_s, j_r, R_s and R_p from the experimental j-V characteristics, we use the algorithm developed by Suckow (2014) (see also Suckow et al., 2012) based on a least-square fit of the analytical expression (4.4) to the experimental data. The parameters obtained for cell 1 are summarized in Table 4.1 and the corresponding best fit curve is shown on Figure 4.7 (b). Figure 4.7 (c) showing the decomposition of the current j into its different components displays the following features:

1. The current of the parallel resistance determines the total current under reverse bias ($V < 0$) and is predominant for small direct bias ($0 < V < 0.15$ V).
2. The recombination-generation current is predominant in the intermediate voltage range $0.15\text{ V} < V < 0.3$ V.
3. At higher voltage ($0.3\text{ V} < V < 0.5$ V) the diffusion current is predominant with an increasing influence of the series resistance at the end of the range and above 0.5 V.

Hence, for measuring j_s and its strain dependence with best possible precision, a "good cell" is a cell for which the domain where the diffusion current prevails is the largest possible (i. e., a cell with low j_r and R_s and high R_p). Furthermore, one should choose a cell for which the slope in that range is the highest possible (as the slope essentially results from the combination of slope 1 for the diffusion current and 1/2 for the RG current, a high slope indicates a stronger predominance of the diffusion current). With these criteria, it is clear that among the experimental j-V curves shown on Figure 4.6, the cells suitable for a study of the strain dependence of j_s are cells 1 and 2.

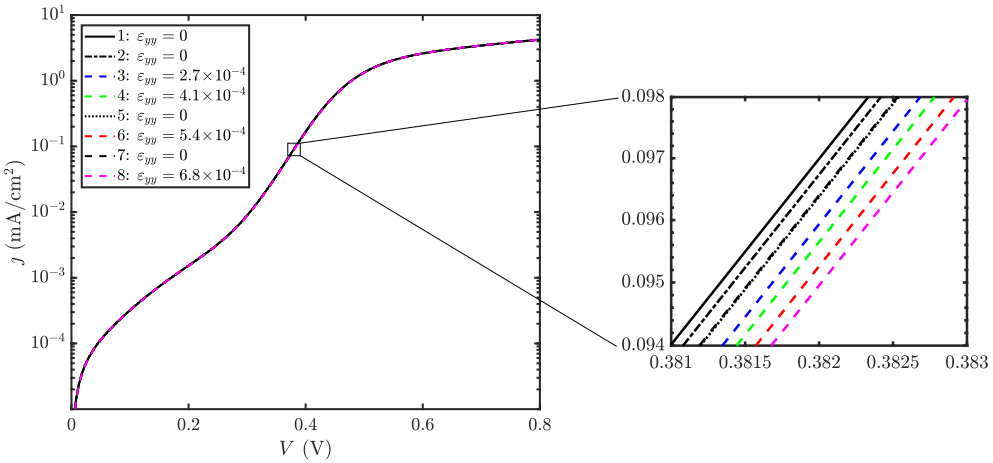

Figure 4.8: Change with strain of the current-voltage characteristic of cell 1. Only the direct current ($V > 0$) is shown. Numbers 1 to 8 indicate the chronological order of mechanical loading and unloading.

4.2.2.2 *Strain dependence of the cell parameters*

The change with strain of the j-V curve of cell 1 is shown on Figure 4.8 where the chronological steps of loading and unloading of the cell are numbered from 1 to 8. One can see that, while the two first loadings induce a residual irreversible change in the characteristic (curve 5 differs from 1 and 2), the characteristic at zero load seems stabilized after the unloading of step 5 (curves 5 and 7 overlap). To obtain the strain-dependence of the cell parameters, we apply the fitting procedure described above at the different loading steps in two ways:

1. *Fit 1*: In the first procedure, the fit is performed over the range $(-1\text{ V}, 1\text{ V})$ with respect to the four parameters j_s, j_r, R_s and R_p, for all the loading levels.

2. *Fit 2*: For comparison, we use a second fitting procedure restricted to the range $(0.2\text{ V}, 0.5\text{ V})$. Indeed, as discussed previously, this corresponds to the region where there is most of the information on j_s, which, in this range, either contributes significantly or predominantly to the total current. However, as very little information on R_s and R_p are available in that range, these parameters are kept fixed across the fit at different loading levels.

The results of the relative change in j_s for the two fitting procedures are shown on Figure 4.9. One can see on Figure 4.9 (a) a relative change in the diffusion saturation current of about -3% for a strain of $\sim 7 \times 10^{-4}$. The difference between the two methods gives an idea of the uncertainty on that measurement, which is about 1% in absolute value. The residual change (i. e., at zero strain) between 0.5% and 1% is difficult to interpret. Indeed, the good alignment of the measurement points on the eye-guide line rather suggest that the reference value of j_s at zero strain is the value of point 2. In addition, the very small

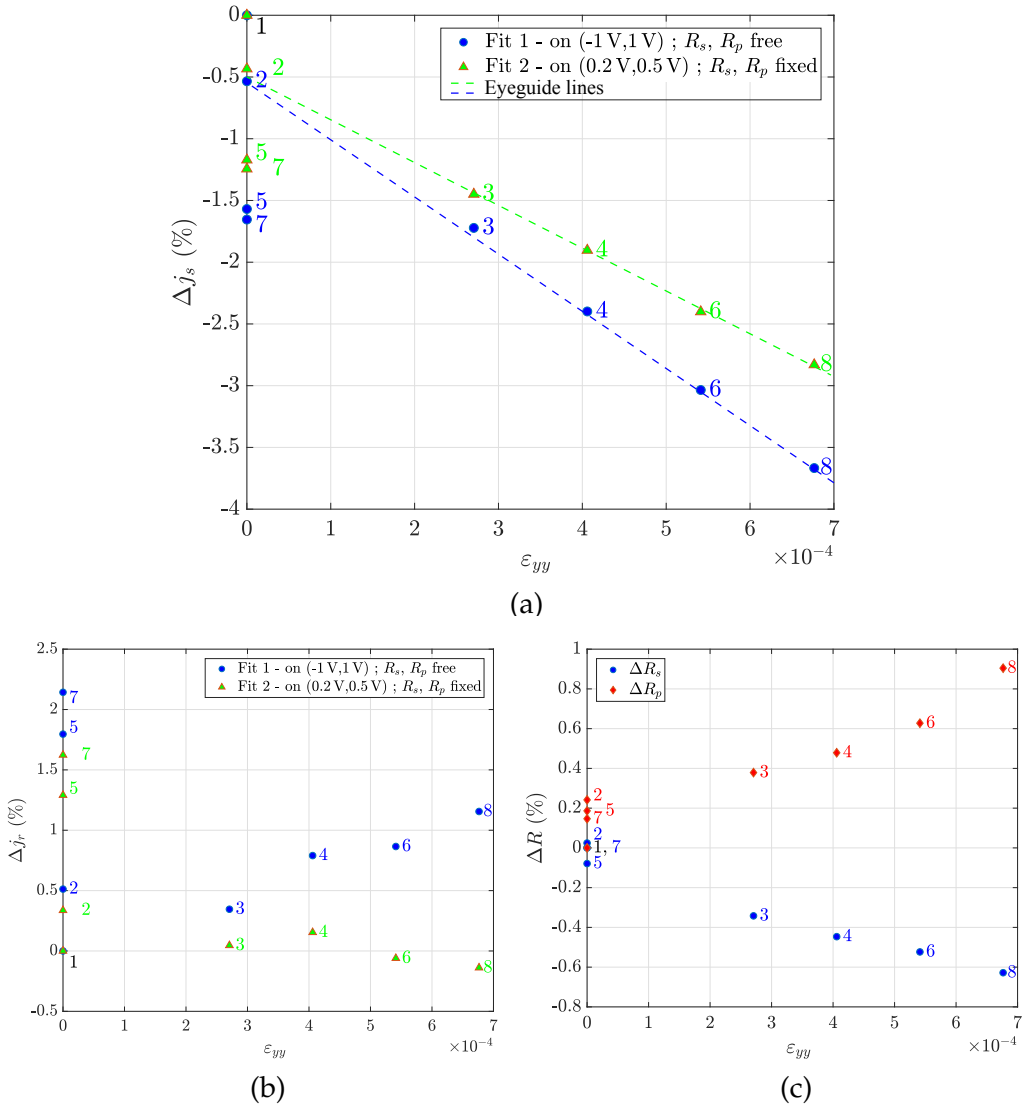

Figure 4.9: Relative change with strain in cell 1 for: (a) The diffusion saturation current j_s with the two fitting procedures Fit 1 and Fit 2; (b) The recombination-generation saturation current j_r with procedure Fit 1 and Fit 2; (c) The series and parallel resistances R_s and R_p with procedure Fit 1.

change of j_r with strain shown on Figure 4.9 (b), except for points 5 and 7, also suggests that a spurious effect is observed here and that the Δj_s of points 5 and 7 are not physical but correspond to a compensation of the spurious Δj_r at these points. For comparison, the predictions of the theory for Δj_s are given in Section 4.3.

Regarding the series and parallel resistance, we observe a decrease of about 0.6% for the first one and an increase of about 1% for the second one. Recalling that for an ideal solar cell $R_s = 0$ and $R_p \to \infty$, this interestingly indicates that the parasitic resistive effect are less important as the cell undergoes uniaxial tensile loading. Given the phenomenological character of these quantities, we have no interpretation for that evolution.

4.3 PREDICTION OF THE STRAIN EFFECT ON THE DIFFUSION SATURATION CURRENT

4.3.1 *Diffusion saturation current*

The expression of the diffusion saturation current $j_s(\varepsilon)$ of Section 3.2.4 shall be modified to account for the heterojunction architecture of the solar cell and the existence of surface recombination on both sides of the cell. Since in our experiments strains are uniform, the strain change in j_s is simply computed algebraically by considering the strain dependence of the electronic parameters. The diffusion saturation current in presence of surface recombination is a well known extension of the Shockley relation (see e.g. Nelson, 2003; Fonash, 2012). Denoting by S_n and S_p the surface recombination on the front side (top of (p)a-Si:H layer) and on the back side (bottom of (n)c-Si layer) of the solar cell, the diffusion current reads,

$$j_s = j_{sn} + j_{sp}, \tag{4.5}$$

where j_{sn} and j_{sp} are the contributions to the diffusion saturation current from the layers (p)a-Si:H and (n)c-Si, respectively, with expressions,

$$\begin{aligned} j_{sn} &= q(\rho^a n_i^a)^2 \frac{U_T m_n}{\rho^a N_a L_n} \frac{\frac{L_n S_n}{U_T m_n}\cosh\left(x_0/L_n\right) + \sinh\left(x_0/L_n\right)}{\frac{L_n S_n}{U_T m_n}\sinh\left(x_0/L_n\right) + \cosh\left(x_0/L_n\right)}, \\ j_{sp} &= q(\rho^c n_i^c)^2 \frac{U_T m_p}{\rho^c N_d L_p} \frac{\frac{L_p S_p}{U_T m_p}\cosh\left((l-x_0)/L_p\right) + \sinh\left((l-x_0)/L_p\right)}{\frac{L_p S_p}{U_T m_p}\sinh\left((l-x_0)/L_p\right) + \cosh\left((l-x_0)/L_p\right)}, \end{aligned} \tag{4.6}$$

Recall that $L_n = \sqrt{U_T m_n \tau_n}$ and $L_p = \sqrt{U_T m_p \tau_p}$ are the diffusion lengths of the minority carriers.

where ρ^a and n_i^a are the mass density and intrinsic concentration in the (p)a-Si:H layer and ρ^c and n_i^c are the same quantities in the (n)c-Si wafer. While other quantities have been previously defined, simply note that the subscript n pertain to the minority carriers (electrons) in the amorphous layer (p)a-Si:H and the subscript p refers to the minority carriers (holes) in the crystalline wafer (n)c-Si. Note also that the intrinsic volume concentration $\rho^a n_i^a$ in amorphous silicon and $\rho^c n_i^c$ in crystalline silicon involve the density of states and band gap of amorphous and crystalline silicon, respectively:

Mobilities are simply related to the diffusion coefficients with $D_n = U_T m_n$ and $D_p = U_T m_p$ (Einstein relation).

$$\begin{aligned} (\rho^a n_i^a)^2 &= (\rho^a)^2 N_c^a N_v^a \exp\left[-E_{gap}^a/k_B T\right], \\ (\rho^c n_i^c)^2 &= (\rho^c)^2 N_c^c N_v^c \exp\left[-E_{gap}^c/k_B T\right]. \end{aligned} \tag{4.7}$$

Experiments measuring the temperature dependence of j_s in silicon heterojunction solar cells similar to ours (Taguchi et al., 2008) find an exponential dependence with $-1/T$ with an activation energy of 1.13 eV. This value, that corresponds to the band gap of crystalline silicon indicates that the component j_{sp} coming from the crystalline wafer is predominant in the sum (4.5). To check independently that j_{sp} dominates in the sum (4.5), we estimate the ratio j_{sn}/j_{sp} with values summarized in Table 4.2 and find $j_{sn}/j_{sp} \sim 10^{-5}$.

Amorphous silicon		Crystalline silicon	
$\rho^a N_c^a$ (cm^{-3})	2×10^{20}	$\rho^c N_c^c$ (cm^{-3})	2.8×10^{19}
$\rho^a N_v^a$ (cm^{-3})	2×10^{20}	$\rho^c N_v^c$ (cm^{-3})	1×10^{19}
$\rho^a N_a$ (cm^{-3})	1×10^{18}	$\rho^c N_d$ (cm^{-3})	1×10^{16}
E_{gap}^a (eV)	1.7	E_{gap}^c (eV)	1.13
m_n ($cm^2/(V{\cdot}s)$)	20	m_p ($cm^2/(V{\cdot}s)$)	450
L_n (nm)	2	L_p (μm)	900
S_n (cm/s)	100	S_p (cm/s)	100
x_0 (nm)	20	$l - x_0$ (μm)	270

Table 4.2: Estimation of the parameters of the silicon heterojunction solar cell. Values from Datta et al. (2008) and Sobkowicz (2014). For the diffusion length of electrons in the amorphous layer L_n, the value of 2 nm is a lower bound (Ritter et al., 1987) which furnishes an upper bound for j_{sn}.

4.3.2 *Strain dependence of the saturation current*

It has been shown that the saturation current is determined by mechanisms taking place in the crystalline silicon, whereby (4.5) reduces to

$$j_s(\varepsilon) \approx j_{sp}(\varepsilon), \tag{4.8}$$

where from $(4.6)_2$, the strain dependence comes from—abandoning the superscript c for crystalline—$N_c(\varepsilon)$, $N_v(\varepsilon)$, $E_{gap}(\varepsilon) = E_c(\varepsilon) - E_v(\varepsilon)$, and through $m_p(\varepsilon)$ which also appears in $L_p(\varepsilon)$.

It turns out that for the particular crystallographic directions chosen in the experiments (uniaxial stress along direction $\langle 110 \rangle$ and current and voltage along direction $\langle 100 \rangle$, see Figure 4.3) the strain dependence in the hole mobility can be neglected. Indeed, using the basis defined in Figure 4.3, the component of the mobility tensor involved in hole transport is $m_p := M_{p,zz}$. The change with strain of that component can be computed using the strain dependence of the electronic parameters detailed in Appendix C, which yields by taking the component ε_{yy} for the amplitude of strain:

$$\frac{\Delta m_p}{m_p} = -\frac{4c_{11}^2 c_{44} + 4c_{11}c_{12}c_{44} - 8c_{12}^2 c_{44}}{c_{11}^2 + c_{11}c_{12} + 2c_{11}c_{44} - 2c_{12}^2} \Pi_{12}^p \varepsilon_{yy}, \tag{4.9}$$

where the c_{ij} are the coefficients of the elasticity tensor and Π_{12}^p is a piezoresistive coefficient of silicon. Numerically, for $\varepsilon_{yy} = 1 \times 10^{-3}$ (upper bound in the experiments), the relative change in mobility is only of 0.2% which is very small compared to the changes due to the other phenomena. Hence, the influence of mobility can be neglected and through a linearization, we can simply express the relative change in saturation current as,

As detailed in Appendix C the dependence of N_c on ε is negligible.

$$\frac{\Delta j_s(\varepsilon)}{j_s} = -\frac{\Delta E_c(\varepsilon)}{k_B T} + \frac{\Delta E_v(\varepsilon)}{k_B T} + \frac{\Delta N_v(\varepsilon)}{N_v}. \tag{4.10}$$

Numerically, using the strain dependences given in Appendix C, we obtain for a strain of $\varepsilon_{yy} = 6.8 \times 10^{-4}$, which corresponds to the maximum strain reached in the experiments,

$$\frac{\Delta J_S}{J_S} = \underbrace{-7\%}_{-\frac{\Delta E_c}{k_B T}} \underbrace{+7\%}_{\frac{\Delta E_v}{k_B T}} \underbrace{-6\%}_{\frac{\Delta N_v}{N_v}} = -6\%. \tag{4.11}$$

The change in saturation current of -6% predicted by the theory is about twice what we have measured. From the decomposition (4.11), we can see that the variation of -6% results from the combination of the positive and negative effects of the various parameters among which the strain effect on the density of states of the valence band. As detailed in Appendix C the uncertainty in the prediction of that effect is quite large, so that it is not surprising to find a difference of a factor two between the measurements and the modeling.

A better quantitative understanding of the effect of strain on the current-voltage characteristic would require both more comprehensive experimental investigations (repeated measurements of the effect of strain for strain states along different crystallographic directions) and better modeling of the effect of strain on the electronic band structure, in particular on the density of states of the valence band.

5 CONCLUSION

In summary, we have derived a theory for the effect of strain on semiconductors in a manner consistent with the laws of thermodynamics, and applied the resulting model to the study of a *p-n* junction device under bending. The predictions have been compared with measurements of the effect of strain on the current-voltage characteristic of a solar cell under uniaxial stress.

In the first chapter, the interactions between mechanics, electrostatics, and electronics are accounted for in a fully coupled continuum model of deformable semiconductors under finite strain. We find that, for the specific case of crystalline semiconductors, the dominant effect is the influence of strain on the electronic transport properties. Further, in this case, electrostatic and electronic contributions to the total stress are negligible. As a result, the mechanical equilibrium can be solved separately to compute the strain field, which subsequently enters the electronic problem through the strain-dependent electronic parameters (i.e., the band edge energies, the densities of states, and the mobilities). Nonetheless, the fully coupled formulation shows the existence of an electronic contribution to the stress which, to the best of our knowledge, has not been mentioned in the literature. Notwithstanding the small magnitude of this electronic-induced stress for non-degenerate crystalline semiconductors, it is an order of magnitude larger than the electrostatic (Maxwell) stress.

In the second chapter, we apply the general theory to determine the effect of bending on the current-voltage characteristic of a *p-n* junction. To this end, we solve the generalized drift-diffusion equations in a inhomogeneous linear strain field. This provides, at first order in the applied curvature, the change induced in the current. While it is well known in the literature that the inhomogeneous character of a semiconductor requires the use of the generalized form of the drift-diffusion equations, they are rarely solved in practical device problems. By computing the characteristic of a *p-n* junction subjected to bending, strain nonuniformities are systematically accounted for in a drift-diffusion framework for the first time. We apply our result to the case of a monocrystalline silicon solar cell subjected to bending and find that changes in dark current are up to 20% for strains of 0.2%. Finally, by comparing various uniform and nonuniform strain fields, we find that the largest dark current changes are expected for the uniform strain loadings.

Finally, in the third chapter we adopt an experimental approach where the effect of uniaxial stress on the current-voltage characteristic of silicon heterojunction solar cell is measured. For that purpose, we use a two exponential model which includes resistive effects to analyze the experimental characteristic of the solar cell . The solar cell is loaded up to a longitudinal strain of 6.8×10^{-4} and we measure a reversible decrease of the diffusion saturation current of about 3%. Given the crystallographic orientation of the silicon sample in the

experiments, this corresponds to half of the variation predicted by the model. Noting a good agreement in order of magnitude between the experiment and theory, the quantitative difference is explained by the insufficient *a priori* knowledge on the effect of strain on the density of states of the valence band.

Part II

STEP DYNAMICS AND INSTABILITIES IN CRYSTAL GROWTH

6 INTRODUCTION

Crystal epitaxy is the process whereby a crystalline layer is deposited on top of a crystalline substrate, which imposes its order. One distinguishes between *homoepitaxy*, which refers to a deposited layer made of the same material as the substrate and *heteroepitaxy*, when the two materials are different. In heteroepitaxy, as a consequence of the lattice mismatch between the overlayer and the substrate, the deposited layer is subject to mechanical strains, which impact the resulting surface morphology.

Epitaxy comes from the Greek roots `epi` *(above) and* `taxis` *(order).*

Practically, different processes can be used for epitaxial growth, among which:

1. *Vapor Phase Epitaxy (VPE)*, where the layer is grown from a vapor composed of volatile precursors that decompose on the surface of the substrate. This covers many different techniques such as, e. g., chemical vapor deposition, plasma-enhanced chemical vapor deposition and metalorganic chemical vapor deposition.

2. *Molecular Beam Epitaxy (MBE)* unlike vapor phase epitaxy takes place in a ultra-high vacuum environment where a beam of evaporated atoms originated from a solid source heated at high temperature directly impacts the substrate.

There exists also liquid-phase epitaxy and solid-phase epitaxy, not considered in this work.

In particular, the situations of epitaxial growth we are concerned with are crystalline thin film depositions and crystal evaporation not only governed by the energetics of the crystal but also by the kinetics of deposition/evaporation. Indeed, when the epitaxy is taking place sufficiently far from thermodynamic equilibrium, the kinetics of the underlying atomic processes plays an important role in the evolution of the surface morphology. The reader might refer to Michely and Krug (2012) for an interesting clarification between situations of epitaxial growth essentially determined by thermodynamic considerations and the situations, of interest for us, where the kinetics is also involved.

When epitaxy is realized on high-symmetry crystal surfaces [e. g., Si(001) or Si(111)], different growth morphologies can be observed. In particular one distinguishes between a three-dimensional growth, whereby islands of several atomic layers grow independently on the surface before coalescing and a layer-by-layer two-dimensional growth, where atomic layers grow successively on top of each other.

The latter, which leads to better crystal quality, can be promoted by performing the epitaxy on crystal surfaces deliberately misoriented from the high-symmetry surfaces: the *vicinal surfaces*. As shown on Figure 6.1, such surfaces present a high density of atomic steps (atomic terrace widths are typically between 20 nm and 200 nm), which by propagating forward achieve a layer-by-layer growth called the *step flow regime*.

Misorientation angles of vicinal surfaces typically range from 0.1° to 2°.

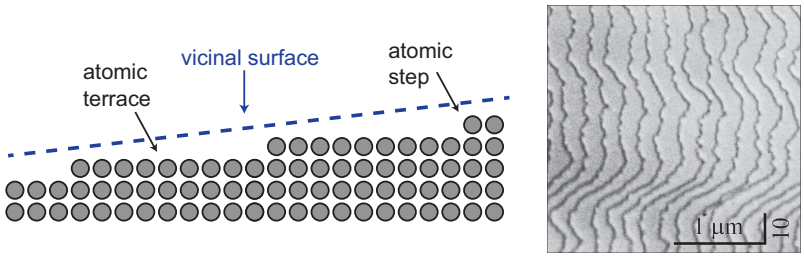

(a) (b)

Figure 6.1: (a) Schematic of a crystal cut forming a vicinal surface. (b) Reflection electron microscopy image of an array of monoatomic steps on Si(111). (b) is reprinted from Latyshev et al. (2017) with permission from Elsevier.

THE PHYSICS OF STEP FLOW Moving towards a quantitative modeling of the dynamics of the atomic steps, we give an overview, illustrated on Figure 6.2, of the microscopic processes today accepted as the underlying physics of step dynamics:

__adatom__ is a portmanteau for "adsorbed atom".

1. *Deposition/evaporation:* As atoms arrive on the surface from the vapor phase (or the MBE beam), some of them are adsorbed on the atomic terraces—where they are called *adatoms* —from which they can possibly re-evaporate to the gas phase.

   By the term epitaxy, we encompass the two situations of crystal growth and crystal sublimation. It is the balance between the deposition and evaporation rates that determines the net evolution of the crystal. In the situations where the crystal is in presence of its element in vapor phase, deposition occurs when the vapor pressure of that element is larger than the equilibrium vapor pressure (supersaturation) while evaporation takes place when the vapor pressure is lower (undersaturation).

   Note that, when the temperature of deposition is low enough, the evaporation probability is so low that pure deposition without evaporation can be assumed. Conversely, experiments of crystal annealing in vacuum correspond to pure evaporation.

2. *Diffusion on terraces:* The adatoms move by diffusion on the terraces.

3. *Attachment/detachment to steps:* As adatoms encounter a step, they have some probability to attach to it, whereby contributing to the progression of the step. Under a more refined viewpoint, adatoms attach to (and detach from) steps at kink sites (see Figure 6.2) after diffusing along the step edges. If the step edge diffusion process is sufficiently fast, it is not considered and adatoms are assumed to attach at any location along the step. Indeed, the overall transport of adatoms being uniquely determined by the limiting kinetic mechanisms, the step edge diffusion process plays no role when steps present a high enough density of kink sites and diffusion along steps is much faster than other kinetic processes.

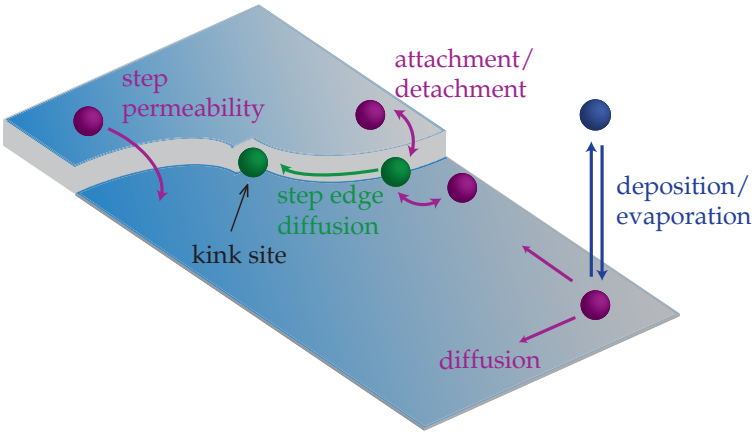

Figure 6.2: Microscopic processes underlying atomic step dynamics. Adatoms are shown in purple, step atoms in green and the vapor atom in blue.

4. *Permeability:* It has been recently proposed that, if the kink density is too low, adatoms can also cross a step without attaching to it (Liu, 1996; Stoyanov, 1998). Such steps are called in the literature *permeable* or *transparent*.

5. *Electromigration:* Electromigration, a phenomenon whereby adatoms experience a drift due to an electric field, is involved in the experimental situations where the substrate is heated by circulating through it a direct electric current of typically a few amperes. Indeed, because a dependence of the step morphology on the current direction was early observed (Latyshev et al., 1989), it has been proposed that adatoms present an effective charge q_e which makes them subject to an electrostatic force (Stoyanov, 1990). To account microscopically for this effective charge, Kandel and Kaxiras (1996) introduced the idea that, as an adatom diffuses on the surface, there is an electric charge transfer between adsorption sites. Based on observations of the step dynamics, it has been estimated that this effective charge lies in the range of one hundredth to one tenth of the elementary charge (Fu et al., 1997; Liu and Weeks, 1998; Thürmer et al., 1999; Homma and Aizawa, 2000; Pierre-Louis and Métois, 2004).

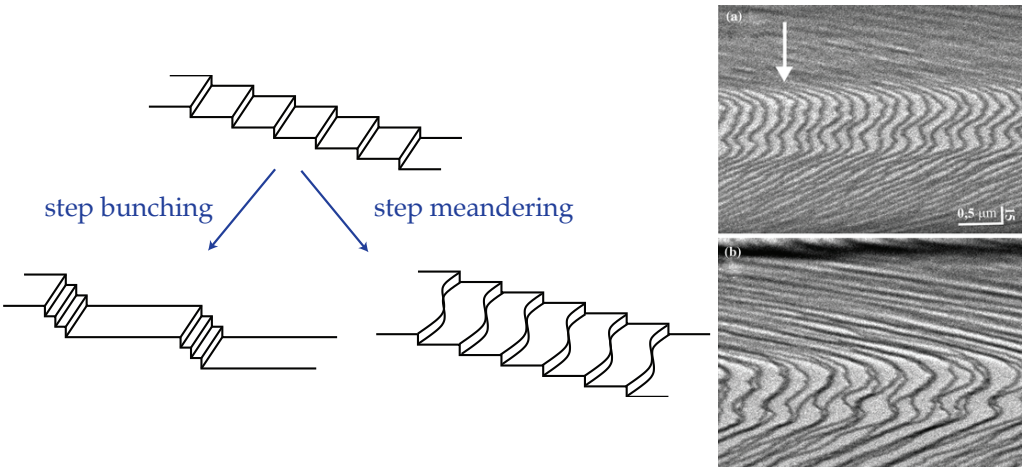

Figure 6.3: (a) Schematic for the two principal step instabilities. Adapted from Krug (2005) with permission from Springer. (b) Reflection electron microscope image of Si(111) at 900°C with regular atomic steps (top) and initial stage of step bunches (bottom). Note that the aspect ratio of 30:1 between vertical and horizontal directions makes the steps appear wavy while they are essentially straight. Reprinted from Kosolobov and Latyshev (2010) with permission from Springer.

OBSERVATIONS OF STEP INSTABILITIES With the advent in the 80's of atomic scale imaging—such as scanning tunneling microscopy and reflection electron microscopy—direct observations of the surfaces after growth and annealing clearly showed irregularities in the spatial arrangement of steps. While in some situations (e. g., MBE growth of Si(111)-7×7 at 650°C, see Omi et al. 2005), the initially straight and equidistant steps propagate without change in their organization, there are cases where this regular pattern is broken. In a first global picture, as illustrated on Figure 6.3, two kinds of instabilities are observed:

1. *Step bunching*, whereby the straight atomic steps propagating at different velocities bunch together. This results in an alternating pattern of wide atomic terraces and step bunches[1] (see an example on Figure 6.3).

2. *Step meandering*, which corresponds to the evolution of the atomic steps from straight lines towards wavy lines.

In this thesis we are particularly concerned with the occurrence, in the step flow regime of the *step bunching* instability.

1 A step bunch consists of a group of closely spaced steps (e. g., in the observations of Pond (1994) on MBE grown GaAs(001), the steps within bunches are distant by 4 nm).

TWO APPROACHES FOR STEP DYNAMICS MODELING An important issue in the field of step flow epitaxy is to *understand the microscopic mechanisms at the origin of step bunching and meandering*. Indeed, the occurrence of one of these instabilities depends on the conditions of epitaxy (deposition/evaporation rates, temperature, homoepitaxy or heteroepitaxy) and the crystal surfaces and material employed. Not only of fundamental interest, understanding the physical processes at stake in the development of instabilities could allow to control the surface morphology that results from crystal growth and use the self-organized surface as patterned template (Teichert et al., 1998; Ronda and Berbezier, 2004).

For that purpose, two main approaches exist, the *Kinetic Monte Carlo (KMC) simulations* of step propagation and the *continuum step flow model*.

There exists also phase field models, which are sometimes a regularization of some version of the continuum model.

In the *KMC simulations*, the motion and exchange of adatoms (on the terrace, with the vapor and the steps) is decomposed in kinetic processes with corresponding hopping rates. These simulations have the advantage to include non-trivial aspects of the modeling such as anisotropy in step diffusion or complex step roughness. With such details, there are cases where this method gives very good account of the pattern of steps observed in experiments (see e. g., Šmilauer and Vvedensky, 1995; Mysliveček et al., 2002).

The second approach uses a *continuum formulation of the step dynamics*, where adatoms are described, on the atomic terraces, through an adatom density ρ (number of adatom per unit area), and the steps are seen as moving interfaces across which, the adatom density encounters discontinuities. This approach is complementary to the KMC simulations in that it provides a more synthetic view of the microscopic processes (the adatoms are not modeled individually); it is computationally less expensive and gives, when the comparison is relevant, good agreement with the KMC results (Misbah et al., 2010). While detailed reviewed of these two approaches can be found in Jeong and Williams (1999), Krug (2005), Misbah et al. (2010), and Michely and Krug (2012), we focus in the present work on the second one, the *continuum step model*.

THE CONTINUUM STEP MODEL In the continuum approach, the step dynamics is obtained by solving the diffusion equation for adatoms on the terraces (with deposition and evaporation as source/sink terms) along with boundary conditions at steps. With that model, the understanding of the occurrence of instabilities involves two levels of modeling and analysis.

1. First, *the set of governing equations* that model the step dynamics with a particular importance of the boundary conditions. These equations are established by translating in mathematical terms the microscopic mechanisms wanted in the modeling. Depending on the point of view, these equations can be proposed using physically sensible phenomenological arguments or derived, using as consistently as possible, general principles and constitutive relations. In the latter case, constitutive relations are written with the help of thermodynamic principles. Following the spirit of the second approach, we intend to develop a consistent derivation of

the governing equations in Section 7.1, which we use as the basis for the next step of the analysis.

2. The second step for understanding step instabilities is to *analyze the stability* of the step governing equations against perturbations of a regular solution (principal solution). As developed in the following, several approaches can be used for performing the stability analysis with different levels of simplifications. Among all possibilities, we present two approaches to the stability analysis in Chapter 8 with an increasing refinement in the physics accounted for.

STEP GOVERNING EQUATIONS The form of the diffusion equation for adatoms on the terraces is not much object of discussions[2] and we derive it in Section 7.1. By contrast, as the boundary conditions at steps may take very different forms in the literature—in particular because they depend on physical assumptions of the mechanisms included in the model—we give below a brief history of the evolution of their expressions.

In their first formulation, by Burton et al. (1951), the boundary conditions expressed the equilibrium of the adatom layer with the reservoir of atoms constituted by the steps:

$$\rho = \rho^*_{eq}, \tag{6.1}$$

along the steps, where ρ^*_{eq} is the equilibrium adatom density. Soon after, these boundary conditions where modified by Chernov (1961) and Schwoebel (1969) to account for the finite kinetics of incorporation of adatoms at steps and the asymmetry of attachment/detachment from the upper and lower terraces. In a one-dimensional setting, where steps are straight lines, letting x the directions perpendicular to the steps, the boundary conditions were proposed by Schwoebel (1969) as

$$-D\partial_x\rho = \kappa_\pm(\rho_\pm - \rho^*_{eq}), \tag{6.2}$$

where D is the coefficient of diffusion on terraces and κ_- (κ_+) are the kinetic coefficients for the attachment/detachment of adatoms from the upper (lower) terraces and ρ_- (ρ_+) the limit values of adatom density at the upper and lower sides of the step. These conditions, expressing microscopic mechanisms were further refined by introducing elastic interactions between steps (see Section 7.2.1 for details), permeability and electromigration.

Recently Jabbour (2005) and Cermelli and Jabbour (2005) developed another approach to derive the step governing equations. Using continuum thermodynamics, they clearly distinguish between general principles and constitutive relations. This method, reviewed in details in Chapter 7, leads to modified boundary conditions with a term accounting for the energetic cost of the step motion for the system formed by the adatom layer. This effect, which we call *adatom jump effect* and takes the form $a^2\rho^*_{eq}[\![\rho]\!]$ in the governing equations, with

The name adatom jump effect *refers to form of the associated term.*

2 Note however that in Section 7.1 we distinguish between the diffusion equation for far-from-equilibrium crystal growth and for near-equilibrium crystal growth. The second version, deriving

a the lattice parameter and $[\![\rho]\!] = \rho_+ - \rho_-$ the jump in adatom density across the step has an impact on the stability of the vicinal surface. While it was shown on a simplified 2-periodic model of steps (Cermelli and Jabbour, 2007) that this term may lead to step bunching under deposition, one of the objectives of this work is to determine its effect on stability both under deposition and evaporation for instabilities involving arbitrarily many steps. This leads us to the second important aspect of step dynamics which is the stability analysis of the governing equations.

STABILITY ANALYSES OF THE STEP FLOW MODEL Studying the stability consists in addressing on the one hand, the linear stability of the system—indicating the onset of instabilities—and on the other hand, the long-term evolution of the surface morphology—i. e., the computation of the bifurcated solution. In this work, we focus on the linear stability analysis, which already has much to teach. In most of the literature, the stability analysis is performed under the so-called quasistatic approximation given in details in Section 8.1. The prevailing idea behind this approximation is that some terms (the dynamics terms) can be neglected in the stability analysis under the condition of low deposition/evaporation rates.

We develop in Section 8.2 such an analysis which has the advantage of providing analytical expressions for the instability criteria. In particular, this allows us to clarify the effect of each mechanism—including the adatom jump effect—and their interplay. We also investigate the effect of the long-range elastic interactions, whereby completing the previous studies developed for nearest-neighbor interactions.

However, as we show in Section 8.1, the quasistatic approximation is not well justified even in the regimes of low deposition/evaporation rates and misses what can be seen as another stabilizing/destabilizing mechanism: *the dynamics effect*. As a result, we develop in Section 8.3 a linear stability analysis of the general equations without resorting to the quasistatic approximation. It turns out that the general stability problem is similar to an hydrodynamic stability problem. In addition the moving steps are moving interfaces and we adopt a method analogous to the *Arbitrary Lagrangian-Eulerian* formulation existing in the stability analysis of fluid-structure interaction problems. These similarities have been pointed out by Léopold Shaabani Ardali (doctoral student at the Fluid Mechanics Laboratory of École polytechnique – LadHyX and French Aerospace Lab – ONERA) who has contributed to the formulation (Section 8.3.2) and numerical resolution (Section 8.3.3) of the linear stability problem. With the general stability results, we develop in Section 8.3.4 a detailed analysis of the issues of the quasistatic approximation from a theoretical viewpoint and show in Section 8.4 that the dynamics effect provides possible explanations for step bunching observed on Si(111)-7×7 and GaAs(001).

With the new phenomena that we bring out in the stability of vicinal surfaces (adatom jump effect and dynamics effect), we revisit in Chapter 9 the prob-

from a linearization of the more general first version, has been used as it is in most of the literature without noticing the underlying near-equilibrium assumption.

lem of step bunching under electromigration, a mechanism specific to some experiments and absent of the analysis of Chapter 8. Our original motivation in reconsidering this problem—for which the underlying destabilizing mechanisms are not yet clear—is to see if the adatom jump effect and dynamics effect can help understand the observations. Isolating the effect of the electromigration force, we show that the adatom jump and dynamics effects do not affect the electromigration-induced step bunching and, as a result, do not provide any new possible explanation. In addition, we discuss the relation between high step kinetics and permeability, two explanations that have been proposed to explain the observed instabilities under electromigration. In doing so, we show that the non-monotonous evolution of the step kinetics or step permeability with temperature—previously considered necessary to account for the experiments—is actually not required. This provides an interesting new element on that problem as the non-monotonous temperature dependence of the surface parameters has justifiably raised many doubts in the literature (Métois and Stoyanov, 1999; Krug, 2005; Misbah et al., 2010).

In sum, we provide in this part a comprehensive linear stability analysis of the major issues of the step flow growth putting the emphasis and bringing new results with the adatom jump effect and the dynamics effect.

OUTLINE This part is organized as follows: We present in Chapter 7 the step governing equations by reviewing in Section 7.1 their derivation from continuum thermodynamics. In Section 7.2, these equations are subsequently specialized to the one-dimensional case of straight steps, the setting relevant for the study of step bunching.

The step bunching analyses are developed in Chapter 8. After introducing the quasistatic approximation in Section 8.1, we discuss the effect of each mechanism through a quasistatic linear stability analysis in Section 8.2. In Section 8.3, we develop a general linear stability analysis which reveals the importance of the *dynamics effect* and show the inadequacies of the quasistatic approximation. While some mathematical details of this stability analysis are given in Appendix D, its consequences on the interpretations of the experimental observations of step bunching are detailed in Section 8.4. For that purpose, we estimate in Appendix E, the values of the parameters of the problem using results of the experimental literature.

The last Chapter 9 is devoted to the problem of electromigration. After introducing that problem in Section 9.1, we present in Section 9.2 the new results brought by our stability analysis and in light of these findings discuss some of the mechanisms proposed in the literature to explain the stability reversals.

7

STEP DYNAMICS GOVERNING EQUATIONS

7.1 DERIVATION OF THE GOVERNING EQUATIONS

In this section, the governing equations for step dynamics are derived using principles of continuum thermodynamics. This derivation is a review of the work of Jabbour (2005) and Cermelli and Jabbour (2005) where, in addition, we include

1. Electromigration,
2. Step permeability.

It is based on the separation of balance laws on the one hand (adatom balance, energy balance, entropy imbalance) and constitutive relations on the other hand.

Consider an atomic step modeled as a time dependent curve $\mathcal{S}(t)$ separating the crystal surface Ω into the upper atomic terrace $\Omega_-(t)$ and the lower one $\Omega_+(t)$ (cf. Figure 7.1).

The curve $\mathcal{S}(t)$ is parametrized with $\mathbf{x} = \mathbf{x}_\mathcal{S}(s,t)$ where s is the arclength parameter oriented such that the lower terrace Ω_+ is locally on the left of $\mathcal{S}$. Denote by $\mathbf{t}$ the unit tangent to $\mathcal{S}$ and $\mathbf{n}$ the unit normal obtained by a counterclockwise rotation of $\mathbf{t}$ by $\pi/2$. The curvature κ of $\mathcal{S}$ is defined by the following Frénet relation: $\partial_s \mathbf{t} = \kappa \mathbf{n}$. Let the velocity of the step $\mathbf{v} := \partial_t \mathbf{x}_\mathcal{S}$ and denote by $v_n := \mathbf{v} \cdot \mathbf{n}$ and $v_t := \mathbf{v} \cdot \mathbf{t}$ its normal and tangential components.

7.1.1 *Balance laws*

Consider a fixed control area $\mathcal{R}$ (independent of time) intersected by the step curve $\mathcal{S}$ and let $\Sigma(t) := \mathcal{S}(t) \cap \mathcal{R}$, $\mathcal{R}_-(t) := \mathcal{R} \cap \Omega_-(t)$ and $\mathcal{R}_+(t) := \mathcal{R} \cap \Omega_+(t)$. The boundaries of $\mathcal{R}_-$ and $\mathcal{R}_+$ are decomposed as $(\partial\mathcal{R})_- \cup \Sigma$ and $(\partial\mathcal{R})_+ \cup \Sigma$, respectively. The end points of Σ (intersection with $\partial\mathcal{R}$) are denoted A and B, chosen such that the arc parameters $S_A(t)$ and $S_B(t)$ of A and B defined by $\mathbf{x}_A(t) = \mathbf{x}_\mathcal{S}(S_A(t), t)$ and $\mathbf{x}_B(t) = \mathbf{x}_\mathcal{S}(S_B(t), t)$ satisfy $S_A \leq S_B$.

7.1.1.1 *Transport theorems*

SURFACE INTEGRAL Let $\varphi(\mathbf{x}, t)$ be a scalar field defined on Ω which experiences a discontinuity as crossing $\mathcal{S}$. For $\mathbf{x} \in \mathcal{S}$, we denote by $\varphi_-(\mathbf{x}, t)$ and $\varphi_+(\mathbf{x}, t)$ the limit values of φ approaching $\mathcal{S}$ from Ω_- and Ω_+, respectively. Moreover the jump of φ as crossing $\mathcal{S}$ is written $[\![\varphi(\mathbf{x}, t)]\!] := \varphi_+(\mathbf{x}, t) - \varphi_-(\mathbf{x}, t)$.

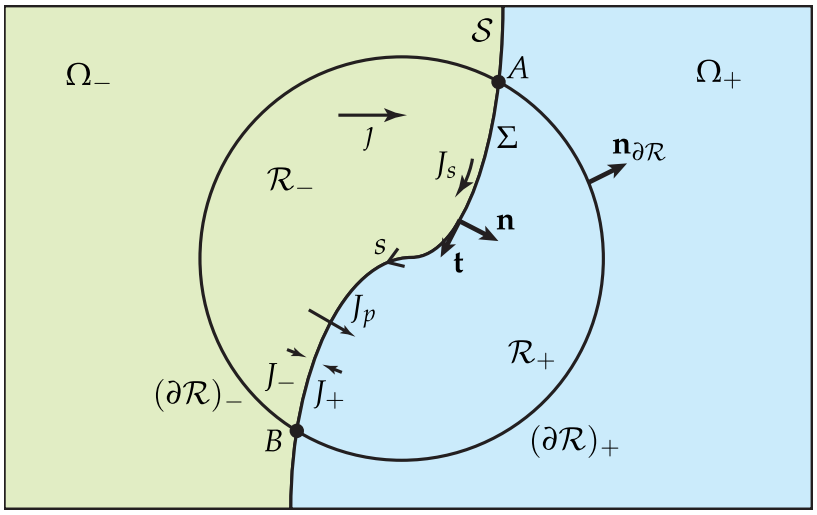

Figure 7.1: Schematic top view of atomic terraces $\Omega_+ \cup \Omega_-$ separated by an atomic step $\mathcal{S}$.

We recall the Reynolds transport theorems (Gurtin, 1993) for $\mathcal{R}$ (i.e., a fixed domain with a moving discontinuity),

$$\frac{\mathrm{d}}{\mathrm{d}t}\int_{\mathcal{R}} \varphi \,\mathrm{d}a = \int_{\mathcal{R}} \partial_t \varphi \,\mathrm{d}a - \int_{\Sigma} [\![\varphi]\!] v_n \,\mathrm{d}s, \tag{7.1}$$

and for $\mathcal{R}_-$ and $\mathcal{R}_+$ taken independently (i. e., time-dependent domains),

$$\frac{\mathrm{d}}{\mathrm{d}t}\int_{\mathcal{R}_\pm} \varphi \,\mathrm{d}a = \int_{\mathcal{R}_\pm} \partial_t \varphi \,\mathrm{d}a \mp \int_{\Sigma} \varphi_\pm v_n \,\mathrm{d}s. \tag{7.2}$$

LINE INTEGRAL As $\mathcal{S}$ evolves, the endpoints of Σ move with velocity

$$\mathbf{V}_\alpha(t) := \dot{\mathbf{x}}_\alpha(t) = \mathbf{t}_\alpha(t)\dot{S}_\alpha(t) + \mathbf{v}(S_\alpha(t), t) \quad \text{for } \alpha = A, B, \tag{7.3}$$

where dot denote the time derivative and $\mathbf{t}_\alpha(t) := \mathbf{t}(S_\alpha(t), t)$ with $\alpha = A, B$ are the tangents at the endpoints. Denote by $V^t_\alpha(t) := \mathbf{V}_\alpha(t) \cdot \mathbf{t}_\alpha(t)$ the tangential velocities for $\alpha = A, B$, which by (7.3) can be rewritten

$$V^t_\alpha(t) = \dot{S}_\alpha(t) + v_t(S_\alpha(t), t). \tag{7.4}$$

Let $\xi(s, t)$ a scalar field defined along $\mathcal{S}$. Introducing the normal time derivative of ξ defined by

$$\overset{\square}{\xi} := \partial_t \xi - v_t \partial_s \xi, \tag{7.5}$$

the transport theorem for a line integral on a portion Σ of $\mathcal{S}$ reads

$$\frac{\mathrm{d}}{\mathrm{d}t}\int_{\Sigma} \xi \,\mathrm{d}s = \int_{\Sigma} (\overset{\square}{\xi} - \xi\kappa v_n) \,\mathrm{d}s + \int_{\partial\Sigma} \xi V^t_{\partial\Sigma}. \tag{7.6}$$

where the boundary term denotes

$$\int_{\partial\Sigma} \xi V^t_{\partial\Sigma} = \xi(S_B(t), t) V^t_B(t) - \xi(S_A(t), t) V^t_A(t). \tag{7.7}$$

7.1.1.2 *Mass balance*

Let $\rho(\mathbf{x},t)$ the adatom density and $\boldsymbol{\jmath}(\mathbf{x},t)$ the adatom surface diffusion flux on the atomic terraces, and denote by $r(\mathbf{x},t)$ the net evaporation/deposition flux of adatoms on the terraces.

ADATOM BALANCE ON UPPER AND LOWER TERRACES The balance of adatoms written on the regions $\mathcal{R}_-$ and $\mathcal{R}_+$ independently reads

$$\frac{\mathrm{d}}{\mathrm{d}t}\int_{\mathcal{R}_\pm}\rho\,\mathrm{d}a=\int_{\mathcal{R}_\pm}r\,\mathrm{d}a-\int_{\partial\mathcal{R}_\pm}\boldsymbol{\jmath}\cdot\mathbf{n}_{\partial\mathcal{R}}\,\mathrm{d}s+\int_\Sigma\left(\pm J_p-J_\pm\right)\mathrm{d}s, \tag{7.8}$$

where $J_-(s,t)$ and $J_+(s,t)$ are the net attachment rate of adatoms to the step from the upper and lower terraces, respectively, and $J_p(s,t)$ is the scalar permeability current of adatoms crossing the step ($J_p>0$ for adatoms crossing in the downward direction). Using the Reynolds transport theorem (7.2) along with the divergence theorem, (7.8) is rewritten

$$\int_{\mathcal{R}_\pm}\left(\partial_t\rho-r+\nabla\cdot\boldsymbol{\jmath}\right)\mathrm{d}a+\int_\Sigma\left(\mp\rho_\pm v_n+J_\pm\pm J_p\pm\boldsymbol{\jmath}_\pm\cdot\mathbf{n}\right)\mathrm{d}s=0, \tag{7.9}$$

Localization of (7.9) on the terraces yields the diffusion equation,

$$\partial_t\rho=r-\nabla\cdot\boldsymbol{\jmath}\quad\text{on }\Omega_-\cup\Omega_+, \tag{7.10}$$

while localization at the step provides the local mass balances,

$$\begin{cases}J_-+J_p=\boldsymbol{\jmath}_-\cdot\mathbf{n}-\rho_-v_n & \text{along }\mathcal{S}_-,\\ J_+-J_p=-\boldsymbol{\jmath}_+\cdot\mathbf{n}+\rho_+v_n & \text{along }\mathcal{S}_+.\end{cases} \tag{7.11}$$

$\pm\rho_\pm v_n$ can be seen as an advection current in the referential of the step.

GLOBAL ATOMIC BALANCE In the above adatom balances, the step is seen as an exterior sink/source term of adatoms for the lower and upper terraces. We now write a global balance of atoms over $\mathcal{R}$, which accounts for the fact that adatoms attaching to the step contribute to the extension of the top crystal layer of the upper terrace. In addition, we introduce a diffusion current of adatoms along the step but neglect the contribution of the step linear density of adatoms to the total number of atoms. Let $J_s(s,t)$ the scalar adatom diffusion flux along the step (see Figure 7.1, J_s is oriented such that $\mathbf{J}_s=J_s\mathbf{t}$) and a the lattice parameter of the crystal, the global balance reads

$$\frac{\mathrm{d}}{\mathrm{d}t}\left\{\int_{\mathcal{R}}\rho\,\mathrm{d}a+\int_{\mathcal{R}_-}\frac{1}{a^2}\,\mathrm{d}a'\right\}=\int_{\mathcal{R}}r\,\mathrm{d}a-\int_{\partial\mathcal{R}}\boldsymbol{\jmath}\cdot\mathbf{n}_{\partial\mathcal{R}}\,\mathrm{d}s-\int_{\partial\Sigma}J_s, \tag{7.12}$$

where,

$$\int_{\partial\Sigma}J_s=J_s(S_B(t),t)-J_s(S_A(t),t). \tag{7.13}$$

Appealing to the Reynolds transport theorems (7.1) and (7.2) and the divergence theorem in the presence of a discontinuity, specifically,

$$\int_{\partial\mathcal{R}}\boldsymbol{\jmath}\cdot\mathbf{n}_{\partial\mathcal{R}}\,\mathrm{d}s=\int_{\mathcal{R}}\nabla\cdot\boldsymbol{\jmath}\,\mathrm{d}a+\int_\Sigma[\![\boldsymbol{\jmath}]\!]\cdot\mathbf{n}\,\mathrm{d}s, \tag{7.14}$$

Equation 7.12, combined with Equation 7.8, yields

$$\int_{\mathcal{R}_\pm} \left(\partial_t \rho - r + \nabla\cdot \jmath\right) \mathrm{d}a - \int_\Sigma \left([\![\rho]\!] v_n - \frac{v_n}{a^2} - [\![\jmath]\!]\cdot \mathbf{n} - \frac{\partial J_s}{\partial s}\right) \mathrm{d}s. \tag{7.15}$$

With the help of (7.11), localization of (7.15) along the step provides the following step velocity equation:

$$\frac{v_n}{a^2} = J_- + J_+ - \frac{\partial J_s}{\partial s} \quad \text{along } \mathcal{S}. \tag{7.16}$$

7.1.1.3 *Free-energy imbalance*

Assuming an isothermal setting, denote by $\psi(\mathbf{x}, t)$ the surface free-energy density of adatoms on the terraces, ψ_c the surface free-energy density of a monoatomic crystal layer and ψ_s the line free-energy density of the step[1]. Let $\mu(\mathbf{x}, t)$, $\mu_v(\mathbf{x}, t)$ and $\mu_s(s, t)$ the atomic chemical potentials when atoms are in the terrace adatom layers, in the vapor phase and attached to the step, respectively. The free-energy imbalance expresses that the rate of change of free-energy in $\mathcal{R}$ is lower than the sum of the chemical energy income from the boudary and the work of the Lorentz force, specifically,

$$\underbrace{\frac{\mathrm{d}}{\mathrm{d}t}\left\{ \int_{\mathcal{R}} \left(\psi + \mathbb{1}_{\mathcal{R}_-}\psi_c\right) \mathrm{d}a + \int_\Sigma \psi_s \,\mathrm{d}s\right\}}_{\text{Rate of change of the free-energy}} \leq \underbrace{\int_{\mathcal{R}} \mu_v r \,\mathrm{d}a - \int_{\partial\mathcal{R}} \mu \jmath\cdot\mathbf{n}\,\mathrm{d}s - \int_{\partial\Sigma} \left(\mu_s J_s - \psi_s V^t_{\partial\Sigma}\right)}_{\text{Incoming energy with atoms inflow}} \tag{7.17}$$

$$\underbrace{- \int_{\mathcal{R}} q_e(\nabla\phi)\cdot\jmath\,\mathrm{d}a - \int_\Sigma q_e(\nabla\phi)\cdot\mathbf{J}_s\,\mathrm{d}s}_{\text{Work of the Lorentz force}},$$

where $\mathbb{1}_{\mathcal{R}_-}$ is the characteristic function of $\mathcal{R}_-$, q_e the adatom effective charge and ϕ the electric potential related to the electromigration electric field $\mathbf{e} = -\nabla\phi$. By the transport theorems (7.1), (7.2), (7.6) and the divergence theorem, (7.17) is rewritten

$$\begin{aligned}&\int_{\mathcal{R}} \left(\partial_t\psi - \mu_v r + \nabla\cdot(\mu\jmath) + q_e(\nabla\phi)\cdot\jmath\right)\mathrm{d}a\\ &+ \int_\Sigma \left((\psi_c - [\![\psi]\!] - \kappa\psi_s)v_n + [\![\mu\jmath]\!]\cdot\mathbf{n} + \partial_s(\mu_s J_s) + q_e J_s(\nabla\phi)\cdot\mathbf{t}\right)\mathrm{d}s \leq 0.\end{aligned} \tag{7.18}$$

Using the adatom balance (7.10), localization of (7.18) on the terraces yields

$$\partial_t\psi - \mu\partial_t\rho + (\mu - \mu_v)r + \nabla\mu_e\cdot\jmath \leq 0 \quad \text{on } \Omega_-\cup\Omega_+, \tag{7.19}$$

1 Note that under the isothermal assumption and neglecting the adatom density along the step, ψ_c and ψ_s are assumed constant. In addition, although we work here in an isotropic framework, one could consider, for a more general modeling, a dependence of ψ_s on the orientation of the step with respect to a reference direction of the crystal (see, e. g., Cermelli and Jabbour, 2005).

where $\mu_e = \mu + q_e\phi$ is the electrochemical potential of adatoms. Likewise, using (7.11) to recast $[\![\mu \boldsymbol{\jmath}]\!] \cdot \mathbf{n}$ as

$$[\![\mu \boldsymbol{\jmath}]\!] \cdot \mathbf{n} = [\![\mu\rho]\!] v_n - (\mu_+ J_+ + \mu_- J_-) + [\![\mu]\!] J_p, \tag{7.20}$$

and appealing to (7.16), localization of (7.18) along the step furnishes

$$\begin{aligned} &\Big(\psi_c - [\![\psi - \mu\rho]\!] - \kappa\psi_s - \frac{\mu_s}{a^2}\Big) v_n \\ &\quad - (\mu_+ - \mu_s) J_+ - (\mu_- - \mu_s) J_- + [\![\mu]\!] J_p + J_s \partial_s \mu_{es} \leq 0 \quad \text{along } \mathcal{S}, \end{aligned} \tag{7.21}$$

where $\mu_{es} := \mu_s + q_e\phi$ is the electrochemical potential of step adatoms.[2]

7.1.2 *Constitutive relations*

7.1.2.1 *Thermodynamic restrictions*

Following the Coleman-Noll procedure (Coleman and Noll, 1963), the dissipation inequalities (7.19) and (7.21), valid for any admissible process, furnish restrictions on the constitutive relations. Assume ψ to be a function of ρ, $\psi := \psi(\rho)$, by (7.19) the adatom chemical potential reads

$$\mu = \partial_\rho \psi. \tag{7.22}$$

Moreover, with (7.19) and (7.21) as guides, we assume the dissipative fluxes to depend linearly on the corresponding thermodynamic forces, namely

$$\begin{cases} r = -\omega(\mu - \mu_v), & \boldsymbol{\jmath} = -\rho M(\nabla \mu_e), & J_s = -M_s \partial_s \mu_{es}, \\ J_+ = \gamma_+(\mu_+ - \mu_s), & J_- = \gamma_-(\mu_- - \mu_s), & J_p = -\gamma_p [\![\mu]\!], \end{cases} \tag{7.23}$$

where, by (7.19) and (7.21), ω, M, M_s, $\gamma_\pm$, γ_p are all scalar positive coefficients. Lastly (7.21) provides the *kinetic relation*,

$$v_n = b \underbrace{\Big(\frac{\mu_s}{a^2} + \kappa\psi_s - \psi_c + [\![\psi - \mu\rho]\!]\Big)}_{\mathcal{F}_d}, \tag{7.24}$$

where $b \geq 0$ and $\mathcal{F}_d$ is the *step driving force* resulting from the adatom diffusion.

Note that appears here the term $[\![\psi - \mu\rho]\!]$ which corresponds to what we call the *adatom jump effect*. This term is not included in other forms of governing equations not derived from continuum thermodynamics (see, e. g., Pierre-Louis, 2003b). It precisely accounts for the free-energy cost associated to the fact that, as the step moves forward the adatom layer on the lower terrace (to which corresponds a specific thermodynamic state) is replaced by the adatom layer on the upper terrace (in another thermodynamic state). A mention of this term can be found in Jeong and Williams (1999), Section 3.3.3, but it was not included in the step dynamics models before Jabbour (2005) and Cermelli and Jabbour (2005). Importantly, as already sketched by Cermelli and Jabbour (2007) and as we investigate in details in Chapter 8, this *adatom jump term* has a strong influence on the stability of steps.

2 Here it has been assumed, by default, that step adatoms have the same effective charge as terrace adatoms. Note however that we have no information from experiments on step adatom effective charge. Nevertheless, these details do not affect the stability analysis, as the latter is subsequently carried out assuming that gradients in J_s are negligible in (7.16).

7.1.2.2 *Step chemical potential*

As the step velocity is already prescribed by (7.16), Equation 7.34 can be seen as a generalized Gibbs-Thomson relation furnishing the step chemical potential,

$$\mu_s = \mu_c - a^2\left(\kappa\psi_s + [\![\psi - \mu\rho]\!] - \frac{v_n}{b}\right), \tag{7.25}$$

where we have introduced the notation $\mu_c := a^2\psi_c$ since $a^2\psi_c$ has the dimension of an energy per unit atom, like a chemical potential. Note however that μ_c does not have the signification of a chemical potential as an income of an atom from another phase to the crystal phase necessarily occurs through the step (hence involving μ_s).

Aside: Variational definition of the chemical potential

Equation 7.25 is called generalized Gibbs-Thomson relation in comparison with the classical derivation of the step chemical potential with variational approach (see, e. g., Krug, 2005; Jeong and Williams, 1999) which we recall below. With the regions defined in Figure 7.1, consider inside the region $\mathcal{R}$ the total free-energy Ψ of the upper terrace (we disregard here the adatom layers) which is the sum of the free energies of the crystal monoatomic layer in $\mathcal{R}_-$ and of the step along Σ,

$$\Psi = \int_{\mathcal{R}_-} \psi_c \, \mathrm{d}a + \int_\Sigma \psi_s \, \mathrm{d}s \tag{7.26}$$

In the variational approach, the step chemical potential $\mu_s(s)$ is defined as the increase in Ψ upon the addition of one atom at the abscissa s of the step. Let $\delta u(s)$, be an elementary normal displacement of the step —i. e., after displacement step, the step curve is parametrized by $\mathbf{x} = \mathbf{x}_S(s) + \delta u(s)\mathbf{n}$— such that $\delta u(S_1) = \delta_u(S_2) = 0$, the definition of μ_s reads

$$\delta\Psi = \int_\Sigma \mu_s \frac{\delta u}{a^2} \, \mathrm{d}s. \tag{7.27}$$

By applying the transport theorems for surface and line integrals (7.2) and (7.6) to (7.26), the variation $\delta\Psi$ is obtained as

$$\delta\Psi = \int_\Sigma (\psi_c - \kappa\psi_s)\delta u \, \mathrm{d}s, \tag{7.28}$$

which combined with (7.27) yields the classical Gibbs-Thomson relation,

$$\mu_s = \mu_c - a^2\kappa\psi_s. \tag{7.29}$$

By comparing (7.29) and (7.25), one can see that with the non-equilibrium thermodynamic approach developed in the present work, full account is taken of firstly, the energetics of the global system {crystal monolayer+step+adatom layer} and secondly, the dissipation related to the finite velocity of the step.

7.1.2.3 *Choice of a free energy*

The restrictions on the constitutive relations derived in Section 7.1.2.1 need to be completed by a constitutive assumption for the adatom free-energy density. Assume the adatom layer over terraces to be an ideal gas, its free energy reads

$$\psi(\rho) = \rho\left[k_B T\left(\ln\left(\frac{\rho}{\rho^*_{eq}}\right) - 1\right) + \mu_c\right], \tag{7.30}$$

where ρ^*_{eq} is the equilibrium adatom density, whose physical meaning is further explained below. By (7.22), we have

$$\mu(\rho) = k_B T \ln\left(\frac{\rho}{\rho^*_{eq}}\right) + \mu_c. \tag{7.31}$$

Noting that $\mu(\rho^*_{eq}) = \mu_c$, it appears that ρ^*_{eq} is the *adatom density in equilibrium with a straight isolated step*. Indeed, in such a situation, by (7.25), the step chemical potential reduces to μ_c (cf. $\kappa = 0$, $[\![\psi - \mu\rho]\!] = 0$ since in equilibrium $\rho = \rho^*_{eq}$ over all Ω, and $v_n = 0$ at equilibrium) and $\mu(\rho^*_{eq}) = \mu_c$ is then the expression of equilibrium of the adatom layer with the step reservoir.

Using the free energy assumption, we explicit some of the constitutive relations (7.23) and (7.25). Noting that $[\![\psi - \mu\rho]\!] = -k_B T[\![\rho]\!]$ and letting $D = k_B T M$, these constitutive relations are rewritten as

$$\begin{cases} \jmath = D\left(-\nabla\rho + \dfrac{q_e\rho}{k_B T}\mathbf{e}\right), \qquad r = \omega\left[\mu_v - \mu_c - k_B T \ln\left(\dfrac{\rho}{\rho^*_{eq}}\right)\right], \\ \mu_s = \mu_c - a^2\left(\kappa\psi_s - k_B T[\![\rho]\!] - \dfrac{v_n}{b}\right), \\ J_\pm = \gamma_\pm\left[k_B T \ln\left(\dfrac{\rho_\pm}{\rho^*_{eq}}\right) + a^2\left(\kappa\psi_s - k_B T[\![\rho]\!] - \dfrac{v_n}{b}\right)\right], \\ J_p = \gamma_p \ln\left(\dfrac{\rho_-}{\rho_+}\right). \end{cases} \tag{7.32}$$

7.1.3 *Step dynamic governing equations*

Neglecting the adatom step diffusion J_s (acceptable for a high enough density of kinks), we combine (7.10), (7.11), (7.16) and (7.32) to write the step dynamics governing equations as a partial differential system for ρ over $\Omega_- \cup \Omega_+$ with boundary conditions along $\mathcal{S}$ and a condition on v_n for the computation of the motion of $\mathcal{S}$.

$$\begin{cases} \partial_t\rho = D\,\nabla\cdot\left(\nabla\rho - \dfrac{q_e\rho}{k_B T}\mathbf{e}\right) + \omega\left[\mu_v - \mu_c - k_B T \ln\left(\dfrac{\rho}{\rho^*_{eq}}\right)\right], \\ -\rho_- v_n - D\left(\nabla\rho|_- - \dfrac{q_e\rho_-}{k_B T}\mathbf{e}\right)\cdot\mathbf{n} = J_- + \gamma_p \ln\left(\dfrac{\rho_-}{\rho_+}\right), \\ \rho_+ v_n + D\left(\nabla\rho|_+ - \dfrac{q_e\rho_+}{k_B T}\mathbf{e}\right)\cdot\mathbf{n} = J_+ - \gamma_p \ln\left(\dfrac{\rho_-}{\rho_+}\right), \\ v_n = a^2[J_- + J_+], \end{cases} \tag{7.33}$$

with J_- and J_+ given in $(7.32)_4$.

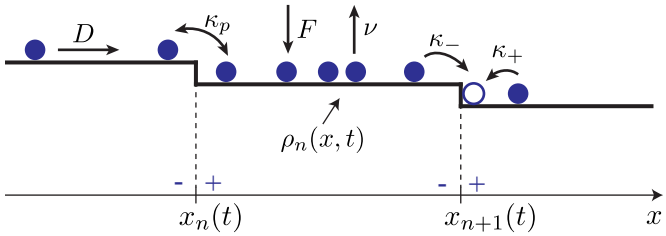

Figure 7.2: Schematic of two successive atomic steps depicting the microscopic processing involved in step flow.

7.2 ONE DIMENSIONAL STEP DYNAMICS MODEL

The stability analysis of Chapter 8 addresses the problem of step bunching for which a one-dimensional model of the vicinal surface, modeled as a sequence of straight parallel steps is suitable.

In this setting, as shown on Figure 7.2, we denote by $x_n(t)$ the position of the n^{th} step and by $\rho_n(x,t)$ the adatom density on the terrace n (between steps n and $n+1$).

7.2.1 *Elastic interactions between straight steps*

In the free-energy imbalance (7.17), we have neglected the work of any possible mechanical force acting on the system considered (Ω comprised of the adatom layer, the crystal monoatomic layer of the upper terrace and the step).

In fact, at the atomistic level, a step constitutes a crystal defect which generates a displacement of the atoms in the underlying bulk (see e.g., the atomistic simulations of the displacement generated by a step in nickel and gold by Shilkrot and Srolovitz 1996). In a continuum picture, this displacement field is associated to a stress field, both being singular at the step. As known from Eshelby (1951) a mobile elastic singularity (e. g., a crystal defect such as a vacancy) is subject to an *elastic configurational force*.

A configurational *force works against the displacement of a singularity relative to the material (i. e., its motion in the reference configuration).*

7.2.1.1 *Introduction of the elastic interactions in the step dynamics equations*

As we do not have a theory that accounts, from the outset, for the contribution of the stress field to the energetics of the step-terrace system[3], we include, *a posteriori*, the contribution of elasticity to the step driving force, by introducing it in (7.24), as it has been done in previous works (Natori, 1994; Tersoff et al., 1995; Pierre-Louis, 2003b).

We denote by f_n the elastic driving force exerting per unit length of the n^{th} atomic step (working against the step velocity $\dot{x}_n$).

3 Considering that mechanical tractions are not well defined on the lower boundary of the surface of the crystal, such a theory would likely require to take as a system the union of the crystal surface and part of the bulk underneath.

The inclusion of the elastic interactions between steps modifies the kinetic relation (7.24)—specialized to the 1D setting—as follows:

$$\dot{x}_n = b\Big(\frac{\mu_s}{a^2} - \psi_c + [\![\psi - \mu\rho]\!]_{x_n} + f_n\Big), \tag{7.34}$$

and in turn, the step chemical potential $(\mu_s)_n$ of the n^{th} step, contains the elastic interactions through,

$$(\mu_s)_n = \mu_c - a^2\Big([\![\psi - \mu\rho]\!]_{x_n} + f_n + \frac{\dot{x}_n}{b}\Big), \tag{7.35}$$

7.2.1.2 *Expression of the elastic configurational force*

With the assumption of straight and parallel steps, the elastic configurational force f_n can be explicitly computed. In a continuum picture, where the crystal can be assimilated to a semi-infinite medium, the elastic field generated by a step is obtained by replacing it by a line density of dipoles and/or monopoles. In the case of homoepitaxy, the step is modeled by a line density of force dipoles with tangential and normal dipole moments d_x and d_z, respectively. Likewise, for heteroepitaxy, a combination of a line density of force monopoles m and dipoles is used to account for the surface step elastic field (Marchenko and Parshin, 1980; Stewart et al., 1994; Tersoff et al., 1995). As a result, the n^{th} step is subject to the configurational force f_n resulting from the interaction of its elastic field, with the elastic field of all other steps. Letting $R \in \mathbb{N}$ the arbitrary range of the step-step elastic interactions beyond which they are neglected, we show below that the configurational force f_n exerting on the n^{th} step reads

$$f_n = \sum_{\substack{r\in\{-R,\dots,R\}\\ r\neq 0}} \left(\frac{\beta}{x_{n+r} - x_n} - \frac{\alpha}{(x_{n+r} - x_n)^3}\right), \tag{7.36}$$

where the coefficients $\alpha > 0$ and $\beta \geq 0$ accounting for the dipole-dipole and monopole-monopole interactions between steps, respectively, are computed in Section 7.2.1.3.

7.2.1.3 *Derivation of the step-step configurational force*

In this section, in a first part, reviewing the work of Stewart et al. (1994), we give the arguments leading to a representation of the steps through force dipoles and the combination of dipoles and monopoles in the absence and presence of a far field stress, respectively. In a second part, we use the work of Eshelby on the elastic interactions between defects to derive the configurational force exerted on a step.

HALF-PLANE MULTIPOLE MODEL OF STEPS. A simple continuum representation of the elastic field generated by a step consists in replacing the stepped surface by an elastic half plane undergoing a surface distribution of forces $\mathbf{f}^s(x)$ exerted by the step system on the bulk (Stewart et al., 1994). As shown on Figure 7.3, this distribution of forces is assumed localized on a surface domain $\mathcal{L}$ around the step.

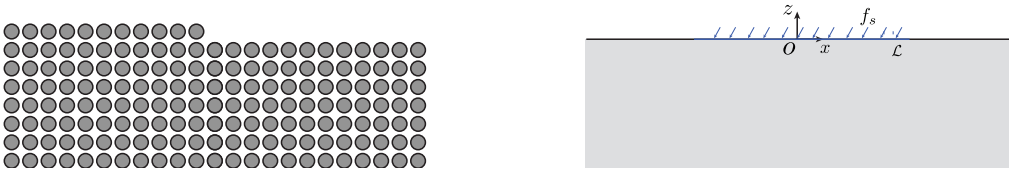

Figure 7.3: Representation in a continuum picture of the effect of a step on the bulk through a surface distribution of forces $\mathbf{f}^s(x)$

The displacement field $\mathbf{u}(x,z)$ generated by this distribution of forces can be described as a convolution with the appropriate Green's function:

$$u_i(x,z) = \int_{\mathcal{L}} G_{ij}(x-x',z) f_j^s(x') \mathrm{d}x', \tag{7.37}$$

with G_{ij} the four components of the tensor Green's function where indices i and j span x and z with the implicit summation on repeated indices. Using a Taylor expansion of the Green's function around x,

$$G_{ij}(x-x',z) = \sum_n \frac{(-1)^n (x')^n}{n!} \frac{\partial^n G_{ij}(x,z)}{\partial x^n}, \tag{7.38}$$

Stewart et al. (1994) shows that the distribution of forces $\mathbf{f}^s(x)$ can be represented by its multipole moments, whose order n reads

$$d_i^n = \int_{\mathcal{L}} f_i^s(x) x^n \mathrm{d}x. \tag{7.39}$$

This allows to rewrite the displacement field in the bulk as

$$u_i(x,z) = \sum_n D_{ij}^n(x,z) d_j^n, \tag{7.40}$$

with D_{ij}^n the n^{th} order multipole Green's function, which reads

$$D_{ij}^n(x,z) = \frac{(-1)^n}{n!} \frac{\partial^n G_{ij}(x,z)}{\partial x^n}. \tag{7.41}$$

With arguments relative to the balance of forces and balance of angular momentum on the step system, it can be shown (Stewart et al., 1994; Muller, 2004) that $d_z^0 = 0$. In addition, in the absence of far field stress, it is shown that the x-monopole moment $m := d_x^0$ (per unit length of step) vanishes whereas for a stressed crystal, it is equal to

$$m = \sigma h, \tag{7.42}$$

with σ the xx-component of the far-field bulk stress and h the step height. For the dipole moments (d_x^1, d_z^1), its components can be obtained by comparing the displacement field of the continuum model with experimental atomic scale imaging or atomistic computations (see e.g. Stewart et al., 1994). Higher order moment multipoles, which have smaller contributions to the displacement field far enough from the steps, are usually neglected. It has been checked, with atomistic simulations, that this monopole and dipole model of steps provides

good representations of the step elastic field (Muller, 2004). Note that more refined continuum model (Kukta and Bhattacharya, 2002; Kukta et al., 2002) have been developed, which take into account the geometry of the stepped surface—also called the roughness correction—and better model the step elastic field, in particular close to the step. These works confirm that the classical multipole expansion works well for like-oriented parallel straight steps, as it is the case for our subsequent study of step bunching.

FROM THE MULTIPOLE MODEL TO THE CONFIGURATIONAL FORCE We derive now the elastic interaction between steps using, instead of the usual energetic based method (Marchenko and Parshin, 1980), the general expression of the configurational force on an elastic singularity derived by Eshelby (1951). In the present setting, the configurational force on a step is the scalar force working against a step displacement along the x-axis (see Figure 7.4).

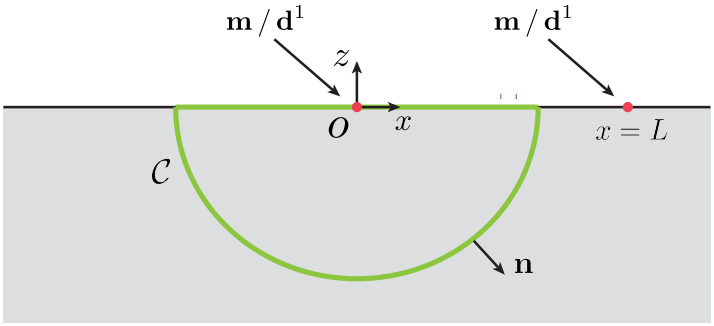

Figure 7.4: Schematic of steps located at the origin and at $x = L$ interacting through their elastic fields. Both steps are represented by elastic dipole $\mathbf{d}^1$ and/or monopole m.

Written in a 2D setting where steps are assumed straight, the configurational force per unit length of step reads

$$f = \mathbf{e}_x \cdot \int_{\mathcal{C}} \mathbf{P}\mathbf{n}\mathrm{d}l, \tag{7.43}$$

where $\mathcal{C}$ is a contour that contains the step—and no other elastic singularity—with outward unit normal $\mathbf{n}$ and $\mathbf{P}$ is the energy-momentum tensor defined in the present framework of linear elasticity as

$$\mathbf{P} := \psi_b \mathbf{I} - \nabla \mathbf{u}^T \cdot \boldsymbol{\sigma}, \tag{7.44}$$

with ψ_b the elastic energy density of the bulk, and $\boldsymbol{\sigma}$ the Cauchy stress tensor. To compute explicitly f with (7.43) we use the fact that it is independent of the integration contour $\mathcal{C}$ and take it to be a half circle of arbitrary radius. In addition, we work in plane strain deformation and assume the bulk to be made of a linear isotropic elastic material with Young's modulus E and Poisson ratio δ.

In that framework, analytical expressions of the Green's function defined in (7.37) are known (Love, 2013; Stewart et al., 1994) and the displacement

field resulting from a line distribution of monopole $\mathbf{m} = m\mathbf{e}_x$ located on the (Oy)-axis reads

$$\mathbf{u}^m(x) = \frac{m}{\pi E_2}\Big(-2\ln(r) - (1+\delta_2)\frac{z^2}{r^2}\Big)\mathbf{e}_x + \frac{m}{\pi E_2}\Big((1-\delta_2)\sin^{-1}\Big(\frac{x}{r}\Big) + (1+\delta_2)\frac{xz}{r^2}\Big)\mathbf{e}_z, \quad (7.45)$$

where $r = \sqrt{x^2+z^2}$, $E_2 = E/(1-\delta^2)$ and $\delta_2 = \delta/(1-\delta)$. Likewise, the displacement field associated to a line distribution of dipoles (d_x^1, d_z^1) is derived using the dipole displacement tensor (7.41) ($n=1$) and reads:

$$\mathbf{u}^{d^1}(x,z) = \frac{2}{\pi E_2 r^4}\Big[\Big(d_x^1(x^3 - \delta_2 xz^2) + d_z^1(zx^2 - \delta_2 z^3)\Big)\mathbf{e}_x + \Big(d_x^1(-z^3 + \delta_2 zx^2) + d_z^1(x^3 + (2+\delta_2)xz^2)\Big)\mathbf{e}_z\Big]. \quad (7.46)$$

In view of (7.45) and (7.46) and using the constitutive relation of a linear isotropic elastic material, one can explicitly compute the configurational force (7.43). We obtain that the configurational force exerted by:

1. A dipole line (d_x^1, d_z^1) at $x = L$ on the same dipole line on the (Oy)-axis reads:
$$f^{dd} = -\frac{\alpha}{L^3} \quad \text{with} \quad \alpha = \frac{4(1-\delta^2)\big((d_x^1)^2 + (d_z^1)^2\big)}{\pi E}, \quad (7.47)$$
2. A monopole line m at $x = L$ on the same monopole line on the (Oy)-axis reads:
$$f^{mm} = \frac{\beta}{L} \quad \text{with} \quad \beta = \frac{2(1-\delta^2)m^2}{\pi E}. \quad (7.48)$$

7.2.2 *One-dimensional governing equations*

The governing equation (7.33) are specialized to the one-dimensional case and elastic interactions between steps are included. In addition, assuming small departures of the adatom density from its equilibrium value ($|\rho - \rho_{eq}^*| \ll \rho_{eq}^*$), we linearize $\ln(\rho/\rho_{eq}^*) \approx (\rho - \rho_{eq}^*)/\rho_{eq}^*$.

Identifying $\nu := k_B T\omega/\rho_{eq}^*$ with the evaporation probability, $F := \omega(\mu_v - \mu_c + k_B T)$ with the deposition flux, defining $\kappa_\pm = k_B T\gamma_\pm/\rho_{eq}^*$ and $\kappa_p = k_B T\gamma_p/\rho_{eq}^*$ as the attachment/detachment and permeability kinetic coefficients, and denoting by e the x-component of the electric field $\mathbf{e}$, the 1D governing equations read for all $n \in \mathbb{Z}$

$$\begin{cases} \partial_t \rho_n = D\Big(\partial_{xx}^2\rho_n - \dfrac{q_e e}{k_B T}\partial_x\rho_n\Big) + F - \nu\rho_n \quad \text{on} \quad (x_n, x_{n+1}), \\ -\rho_n^- \dot{x}_{n+1} - D\Big((\partial_x\rho_n)^- - \dfrac{q_e e\rho_n^-}{k_B T}\Big) = J_{n+1}^- - \kappa_p[\![\rho]\!]_{x_{n+1}} \quad \text{at} \quad x_{n+1}, \\ \rho_n^+ \dot{x}_n + D\Big((\partial_x\rho_n)^+ - \dfrac{q_e e\rho_n^+}{k_B T}\Big) = J_n^+ + \kappa_p[\![\rho]\!]_{x_n} \quad \text{at} \quad x_n, \\ \dot{x}_n = a^2(J_n^- + J_n^+), \end{cases} \quad (7.49)$$

with

$$\begin{cases} J_n^- = \kappa_- \left[\rho_{n-1}^- - \rho_{eq}^* - a^2 \rho_{eq}^* \left(\chi [\![\rho]\!]_{x_n} - \dfrac{f_n}{k_B T} - \dfrac{\dot{x}_n}{k_B T b} \right) \right] \\ J_n^+ = \kappa_+ \left[\rho_n^+ - \rho_{eq}^* - a^2 \rho_{eq}^* \left(\chi [\![\rho]\!]_{x_n} - \dfrac{f_n}{k_B T} - \dfrac{\dot{x}_n}{k_B T b} \right) \right], \end{cases} \tag{7.50}$$

where we have used the following notations $\rho_n^- := \rho_n(x_{n+1}, t)$, $\rho_n^+ := \rho_n(x_n, t)$, $(\partial_x \rho_n)^- := \partial_x \rho_n(x_{n+1}, t)$, $(\partial_x \rho_n)^+ := \partial_x \rho_n(x_n, t)$ and $[\![\rho]\!]_{x_n} = \rho_n(x_n, t) - \rho_{n-1}(x_n, t)$.

$\chi = 1$ is a parameter allowing to track the adatom jump effect. Throughout subsequent analyses, χ will temporarily be set to 0 for the purpose of isolating that effect from the other ones.

7.2.3 *Nondimensionalization*

We nondimensionalize the free-boundary value problem (7.49) and (7.50) with the initial terrace width L_0 as a characteristic length, ρ_{eq}^* for the adatom density and L_0^2/D as a characteristic time, and consequently identify nine dimensionless parameters in the dimensionless formulation of the problem. The equilibrium adatom coverage is described by

$$\Theta := a^2 \rho_{eq}^*. \tag{7.51}$$

As a fraction of the available lattice sites, clearly $0 \leq \Theta \leq 1$. The deposition and evaporation of adatoms are characterized by the dimensionless counterpart of F and ν:

$$\overline{F} := \frac{F L_0^2}{\rho_{eq}^* D} = \frac{L_0^2}{\left(L_d^{dep}\right)^2}, \tag{7.52}$$

which quantifies the ratio of the initial terrace width to the diffusion length under deposition and

$$\overline{\nu} := \frac{\nu L_0^2}{D} = \frac{L_0^2}{\left(L_d^{eva}\right)^2}, \tag{7.53}$$

that similarly gives the ratio of the initial terrace width to the diffusion length under evaporation. Note that the natural requirement that $\rho \leq 1/a^2$ and the more compelling assumption that ρ deviates little from ρ_{eq}^* implies upper bounds on the values of $\overline{F}$ and $\overline{\nu}$ discussed in Appendix E. The electromigration force is given by its dimensionless counterpart,

$$\overline{e} = \frac{q_e e L_0}{k_B T}. \tag{7.54}$$

Given that the adatom attachment/detachment (a/d) from above and below are related to similar atomistic mechanisms, they shall have comparable orders of magnitude, hence the kinetic coefficients are rewritten in terms of

$$\overline{\kappa} = \frac{\kappa_- L_0}{D}, \tag{7.55}$$

expressing the ratio of the initial terrace width to the attachment/detachment kinetic length D/κ_- associated to the upper terrace (Krug, 2005). $\overline{\kappa}$ is an important parameter that allows to distinguish between the *attachment/detachment limited regime* and the *diffusion limited regime*. These notions refer to the two kinetic processes: a/d at steps and diffusion on terraces. $\overline{\kappa}$ can be seen as the ratio of a characteristic step a/d velocity κ_- to a characteristic diffusion velocity D/L_0. Then, $\overline{\kappa} \ll 1$ corresponds to situations where it is the a/d which is the limiting kinetic process and $\overline{\kappa} \gg 1$ is associated to cases where it is the diffusion which is limiting.

To quantify the asymmetry of attachment/detachment at steps from the upper and lower terraces, we introduce

$$S = \frac{\kappa_+}{\kappa_-}, \tag{7.56}$$

giving the strength of the Ehrlich-Schwoebel (ES) effect. The case $0 < S < 1$ ($S > 1$) correspond to an inverse (direct) ES effect, while $S = 1$ is for a symmetric a/d. Similarly, the importance of adatom hopping between terraces is given by the dimensionless permeability kinetic coefficient,

$$\overline{\kappa}_p = \frac{\kappa_p L_0}{D}. \tag{7.57}$$

The strength of the elastic interactions is represented by the dimensionless counterparts of α and β,

$$\overline{\alpha} = \frac{a^2\alpha}{k_B T L_0^3} \qquad \text{and} \qquad \overline{\beta} = \frac{a^2\beta}{k_B T L_0}, \tag{7.58}$$

while the kinetic coefficient b is rewritten in dimensionless form

$$\overline{b} = \frac{L_0 k_B T b}{a^2 D}. \tag{7.59}$$

Without relabeling the dimensionless variables, the governing equations for the adatom diffusion problem (7.49) and (7.50) read in their dimensionless form

$$\begin{cases} \partial_t \rho_n = \partial^2_{xx}\rho_n - \overline{e}\partial_x\rho_n - \overline{\nu}\rho_n + \overline{F}, \\ -\rho_n^-(\dot{x}_{n+1} - \overline{e}) - (\partial_x\rho_n)^- = J_{n+1}^- - \overline{\kappa}_p[\![\rho]\!]_{x_{n+1}}, \\ \rho_n^+(\dot{x}_n - \overline{e}) + (\partial_x\rho_n)^+ = J_n^+ + \overline{\kappa}_p[\![\rho]\!]_{x_n}, \\ \dot{x}_n = \Omega(J_n^+ + J_n^-), \end{cases} \tag{7.60}$$

where,

$$\begin{cases} J_n^- = \overline{\kappa}(\rho_{n-1}^- - 1 - \chi\Omega[\![\rho]\!]_{x_n} + f_n + \dot{x}_{n-1}/\overline{b}), \\ J_n^+ = \overline{\kappa}S(\rho_n^+ - 1 - \chi\Omega[\![\rho]\!]_{x_n} + f_n + \dot{x}_n/\overline{b}), \end{cases} \tag{7.61}$$

and f_n is rewritten as a dimensionless quantity,

$$f_n = \sum_{\substack{r\in\{-R,\dots,R\} \\ r\neq 0}} \left(\frac{\overline{\beta}}{x_{n+r} - x_n} - \frac{\overline{\alpha}}{(x_{n+r} - x_n)^3} \right). \tag{7.62}$$

Note that the term in $1/\overline{b}$ in (7.61) accounts for the dissipation related to the non-equilibrium processes underlying the propagation of the step. While, with the experimental data available, we have no way to estimate b and $\overline{b}$, the fact that we aim at studying situations not too far from equilibrium (consistently with the near-equilibrium assumption of Section 7.2.2) suggests that the contribution of $\overline{b}$ to the step governing equation should be small. Hence, for the remaining of this work, we neglect this effect by taking the limit $\overline{b} \to \infty$.

8

STEP BUNCHING LINEAR STABILITY ANALYSES

In this chapter, we analyze the step bunching instability with the governing equations (7.60)-(7.62) specialized to the case without electromigration[1] ($\bar{e} = 0$).

The so-called quasistatic approximation is presented in Section 8.1 and the corresponding linear stability analysis is performed in Section 8.2. The stability analysis is then extended to the general case in Section 8.3. Throughout these sections, the effect of each physical mechanism on stability is discussed with particular emphasis on the new *adatom jump effect* and *dynamics effect*. We show the consequences of these new mechanisms on the interpretation of experiments where step bunching is observed in Section 8.4.

8.1 THE QUASISTATIC APPROXIMATION

8.1.1 *Definition of the quasistatic approximation*

Throughout the following sections, the step bunching phenomenon is investigated by computing the stability of the steady-state solution ($\overset{o}{x}_n(t) = n + \overset{o}{V}t$ and $\overset{o}{\rho}_n(x,t) = \overset{o}{\tilde{\rho}}(x - \overset{o}{x}_n(t))$, for all $n \in \mathbb{Z}$) against perturbations in the step positions and adatom densities.

Stability analyses of step dynamics on systems like (7.60)-(7.62) have been carried out in numerous works (see, e.g., Bales and Zangwill, 1990; Pimpinelli et al., 1994; Pierre-Louis and Misbah, 1998; Pierre-Louis, 2003b). However, with a few exceptions (Ghez et al., 1993; Keller et al., 1993; Gillet, 2000; Ranguelov and Stoyanov, 2007; Dufay et al., 2007) these analyses have been performed under the so-called *quasistatic approximation*. This approximation, which consists in neglecting the dynamics terms: $\partial_t \rho_n$ in $(7.60)_1$, $\rho_n^- \dot{x}_{n+1}$ in $(7.60)_2$ and $\rho_n^+ \dot{x}_n$ in $(7.60)_3$ considerably simplifies the stability analysis. This simplification is classically assumed appropriate in the regimes of slow deposition/evaporation rates (Krug, 2005; Michely and Krug, 2012) quantified by

$$\overline{F}\Theta \ll 1 \qquad \text{and} \qquad \overline{\nu}\Theta \ll 1, \tag{8.1}$$

for pure deposition and pure evaporation, respectively. The derivation of the conditions (8.1) for the quasistatic approximation is presented in the following. However, by comparing in Section 8.3.4 the stability results with and without the quasistatic approximation we will show that this is an inadequate approximation even in the regime (8.1). In addition, discussing in Section 8.1.2 the classical justification for the approximation under consideration, we also explain *a priori* why it cannot be used for the stability analysis.

1 The case with electromigration, which corresponds to a specific class of experiments is presented in Chapter 9.

8.1.2 *Prevailing justification for the quasistatic approximation*

In this section, we introduce the justification given in the literature for the quasistatic approximation and distinguish between its use for the computation of the steady-state solution and for the stability analysis.

There are two distinct problems to be considered in step dynamics, the first problem is the computation of the steady-state solution of (7.60) (i.e., find the step velocity $\overset{o}{V}$ and the adatom density profile $\overset{o}{\tilde{\rho}}$ of the equidistant step solution: $\overset{o}{x}_n(t) = n + \overset{o}{V}t$ and $\overset{o}{\rho}_n(x,t) = \overset{o}{\tilde{\rho}}(x - \overset{o}{x}_n(t)))$, while the second problem concerns the stability of the steady-state solution with respect to step bunching. Whereas the first problem is governed by the system (7.60)-(7.62), the second one is ruled, as far as the linear stability is concerned, by the linear perturbation equations, derived in Section 8.2.2 and Section 8.3.2.

Recall that the dynamics terms are $\partial_t \rho_n$, $\rho_n^- \dot{x}_{n+1}$ and $\rho_n^+ \dot{x}_n$ in (7.60)

QUASISTATIC APPROXIMATION FOR THE STEADY-STATE SOLUTION The idea for neglecting the dynamics terms is to estimate their order of magnitude, and we do this in the dimensional governing equations (7.49) and (7.50). For the steady-state solution, the term $\partial_t \rho_n$ in (7.49) can be rewritten $\overset{o}{V}\partial_x \overset{o}{\tilde{\rho}}$ which, noting that $\overset{o}{\tilde{\rho}}$ is of order ρ^*_{eq} and typically varies over L_0, is of order $\overset{o}{V}\rho^*_{eq}/L_0$. The question is whether this non-equilibrium term is small compared to the diffusive adatom source $D\partial^2_{xx}\rho_n$ which is of order $D\rho^*_{eq}/L_0^2$. Hence, we define the ratio $\mathcal{P} := \overset{o}{V}L_0/D$ of the dynamics term over its diffusive counterpart. Similarly the terms $-\rho_n^- \dot{x}_{n+1}$ and $\rho_n^+ \dot{x}_n$ are both of order $\rho^*_{eq}\overset{o}{V}$, to be compared to the diffusion currents $D(\partial_x \rho_n)^{\pm}$ of order $D\rho^*_{eq}/L_0$. Again the ratio of these two term is the same dimensionless parameter $\mathcal{P}$.

The quantity $\mathcal{P} := \overset{o}{V}L_0/D$ is called *Péclet number* and can be seen as the ratio of the step velocity $\overset{o}{V}$ over a characteristic diffusion velocity D/L_0. Such an analysis suggests that a computation of the steady-state solution under the quasistatic approximation is justified in the regime were $\mathcal{P}$ is small compared to one.

For situations where deposition prevails over evaporation (i.e., $F \gg \nu\rho^*_{eq}$)—which is often the case for MBE or CVD at sufficiently low temperature—the steady-state step velocity is given by $\overset{o}{V} = Fa^2L_0$. Conversely, when evaporation prevails—typical examples are the numerous experiments of pure evaporation without deposition—the step velocity is not explicit, but one can show that its absolute value is bounded above by its limit in the slow evaporation regime ($\nu \to 0$): $\overset{o}{V}_{SE} = \nu\rho^*_{eq}L_0a^2$.

This provides *a priori* estimates of the Péclet number in the two limit regimes where deposition or evaporation prevail, which we rewrite in terms of the dimensionless coefficients of Section 7.2.3:

$$\mathcal{P}^{dep} = \frac{Fa^2L_0^2}{D} = \overline{F}\Theta, \tag{8.2}$$

for deposition (see Krug 2005; Michely and Krug 2012) and

$$\mathcal{P}^{eva} = \frac{\nu\rho_{eq}^* L_0^2 a^2}{D} = \overline{\nu}\Theta, \tag{8.3}$$

for evaporation.

QUASISTATIC APPROXIMATION FOR THE STABILITY ANALYSIS Note that, in this discussion, we have estimated the order of magnitude of the dynamics terms in the governing equations of the particular steady-state solution. In the existing literature, it has been assumed that the smallness of the dynamics terms in the system (7.60)-(7.62) is sufficient for neglecting them in the computation of the stability of the steady-state solution. However, this is not the case and, as shown in details in Section 8.3.2 below, the contribution of the dynamics terms to the linear perturbation equations—which furnishes the stability—does not vanishes as $\mathcal{P} \to 0$. This shortcut, which consists in assuming that the smallness of the dynamics terms in (7.60) allows to neglect them in the stability analysis is at the origin of the quasi-absence of discussion in the literature of what we call the *dynamics effect* on the stability of steps.

INTEREST OF A QUASISTATIC ANALYSIS While the quasistatic approximation is not valid simply under the slow deposition/evaporation condition (8.1), as discussed in Section 8.3.4 below, there are still particular cases where the stability results with and without the quasistatic approximation converge.[2] The quasistatic approximation remains of interest, as a provisional approach, because it provides stability results in analytical form (unlike the general stability analysis, which is numerical). This allows to understand in a simplified setting the effects of the various physical mechanisms on the stability of step dynamics, stability that should be subsequently reinterpreted to account for the effect of dynamics.

2 For instance, under deposition, the effect of dynamics on stability becomes negligible compared to the effect of elasticity as the deposition rate goes to zero (and with it, the Péclet number $\mathcal{P} = \overline{F}\Theta$). While, in this particular situation, this amounts to recover the results derived under the quasistatic approximation, actually it has its origin in the contingent fact that stabilization and destabilization caused by step-step elastic interactions are independent of the deposition rate while all other stabilizing/destabilizing mechanisms—including the dynamics effect—are kinetic mechanisms whose strength is proportional to the deposition rate.

8.1.3 *Review of the works beyond the quasistatic approximation*

The mathematical method to treat the linear stability of (7.60)-(7.62) with all dynamics terms is more intricate than that which resorts to the quasistatic approximation. A few works (Ghez et al., 1993; Gillet, 2000; Pierre-Louis, 2003b; Ranguelov and Stoyanov, 2007; Dufay et al., 2007) have addressed such a problem on systems[3] like (7.60).

Importantly, the motivation in above cited works for going beyond the quasistatic approximation is to investigate the stability in the high deposition/evaporation regime where the condition (8.1) is violated. By contrast, our motivation for addressing the stability of the system with dynamics terms concerns the lack of validity of the quasistatic approach in the very regime (8.1) ($\overline{F}\Theta \ll 1$ under deposition and $\overline{\nu}\Theta \ll 1$ under evaporation) where it is supposedly valid.

Of course, our analysis can also be used in the regime beyond (8.1), however, it is physically doubtful that for these high deposition/evaporation rates the crystal growth takes place through step flow and can be modeled by (7.60)-(7.62). First, when deposition (resp. evaporation) rates are so high that (8.1) is not satisfied, it has been pointed out that the high (resp. low) density of adatoms on terraces induces island (resp. holes) nucleation, i. e., the growth mode changes from 2D step flow regime to 3D growth (Pierre-Louis and Misbah, 1998; Michely and Krug, 2012). This 3D growth regime corresponds to a different class of problems, both from the experimental and modeling point of view. Second even though in the regime beyond (8.1), the crystal were growing in the step flow regime, the near-equilibrium assumption—which underlies the governing equations (7.60)-(7.62)—is not satisfied and one would need to consider the diffusion equation and boundary conditions prior to the linearization of the chemical potential (see Section 7.1.3). Hence in that case one should consider a different set of governing equations than those used in the literature.

We briefly review the different existing works addressing the effects of dynamics on the stability of steps. As we will see, some works focus on the method to compute the stability (Ghez et al., 1993) and others discuss some consequences of the dynamics on stability (Gillet, 2000). However none of them develop a mathematically consistent treatment of the step stability on the general equations (7.60)-(7.62), together with a comprehensive discussion of the dynamics effect on stability both in a general setting (i. e., not concerned by a given material) and on specific examples (by assessing the importance of the dynamics effect in some experiments showing step bunching). It is precisely this combination we would like to develop in the following sections of the present chapter.

3 The governing equations in these works lightly differs from (7.60)-(7.62), essentially because some mechanisms (Schwoebel effect, elastic interactions, permeability, adatom jump effect) are neglected in one work or the other, but are not fundamentally different from (7.60)-(7.62). Note also that in the early work of Ghez et al. (1993) and Keller et al. (1993), the dynamics terms are absent of the boundary conditions $(7.60)_{2,3}$ and only included in the step velocity equation $(7.60)_4$.

As an illustration of the recent interest for the dynamics effect, Ranguelov and Stoyanov (2007) addressed the problem of step dynamics in the simplified framework of infinitely fast terrace diffusion ($D \to \infty$) and slow attachment/detachment kinetics (κ_- and κ_+ small but finite) which, as they say, "provides a relatively simple way to study the linear stability of a step train beyond the quasistatic approximation". They discuss the effect of the dynamics on the problem of step bunching under electromigration (Ranguelov and Stoyanov, 2008) and in another work, show experimental evidence that the dynamics effect may induce step bunching for sufficiently high deposition rate (Ranguelov et al., 2017). In terms of theoretical analysis, with the assumptions for terrace diffusion and step kinetics, the problem they consider takes a very different form from the general step governing equations (7.60)-(7.62) which makes the comparison of their analysis with our work difficult. Note that the limit considered in these works is motivated by the search for a mathematically simplified model. In contrast, in the following, by not focusing on any limit case *a priori*, we analyze, in Section 8.3, the effects of dynamics on the general problem. In particular, we find, in agreement with experimental works presented in Ranguelov et al. (2017) that, when accounting for step-step elastic stabilizing interaction and the dynamics effect, there is a critical deposition rate beyond which the step bunching instability develops (cf. Figure 8.9). While Ranguelov and Stoyanov (2007) noticed the same instability in the limit case they consider, our work shows that such a behavior exists irrespective of the terrace diffusion and attachment/detachment velocities and quantifies their influence on the critical deposition rate. This constitutes a valuable contribution to understand the experimental evidence in Ranguelov et al. (2017).

In the same decade, other works have considered (Gillet, 2000; Pierre-Louis, 2003b; Dufay et al., 2007) the possible influence of the dynamics terms. In works by Pierre-Louis (2003b) and Dufay et al. (2007), avoiding the mathematical difficulty that the term $\partial_t \rho_n$ in $(7.60)_1$ introduces in the stability analysis, the idea is to solely account for the advection part of the dynamics terms[4]. While we have checked that this approach might provide the good stability results in specific cases, we have found several situations in the regime $\mathcal{P} \ll 1$, where the stability results derived with that simplification are not valid. By contrast, in Section 8.3, accounting for all the dynamics terms, we are sure that the stability results are valid for any set of parameters.

While Pierre-Louis (2003b) simply mentioned the advective approach without discussing the consequences on the stability results, the work of Dufay et al. (2007) is devoted, through such an analysis, to the effect of advection on the electromigration-induced step bunching problem. The main result of this work

What is called the advection effect is the effect of the advective terms neglecting some contributions of the dynamics terms as detailed in footnote 4.

4 More precisely note that the term $\partial_t \rho_n$ can be decomposed in a convective component and a transient component by doing the change of variable $\tilde{x} := x - (n + \overset{o}{V} t)$. Letting $\tilde{\rho}_n(\tilde{x}, t) := \rho_n(\tilde{x} + n + \overset{o}{V} t, t)$ the time derivative of ρ_n is rewritten $\partial_t \rho_n = \partial_t \tilde{\rho}_n - \overset{o}{V} \partial_x \tilde{\rho}_n$. In the work mentioned here, only the advective term $-\overset{o}{V} \partial_x \tilde{\rho}_n$ is conserved while the time derivative $\partial_t \tilde{\rho}_n$ is neglected in $(7.60)_1$. Similarly, for the boundary conditions $(7.60)_{2,3}$, the terms $-\rho_n^- \dot{x}_{n+1}$ and $\rho_n^+ \dot{x}_n$ are replaced by $-\rho_n^- \overset{o}{V}$ and $\rho_n^+ \overset{o}{V}$ whereby neglecting there the perturbations in the step positions about the principal velocity $\overset{o}{V}$.

is that the advection effect could allow to better understand the stability inversions in the electromigration problem. In contrast, in Chapter 9, we develop an analytical approach, which consists in separating the electromigration effect from the other mechanisms and conclude that the dynamics effect cannot explain the stability reversals observed in electromigration-induced step bunching experiments.

An earlier treatment of the effect of dynamics on the step stability problem is given by Ghez et al. (1990, 1993) and Keller et al. (1993) with a method relatively close to ours (developed below in Section 8.3.2). Indeed, the particularity of that stability problem is that the equations shall be perturbed both with respect to the function (the adatom density on terraces) and the domain of definition of the functions (given by the step positions) without *a priori* relation between both perturbations. To address that particularity, Ghez et al. (1990) write the perturbation equations on the domain of the steady-state solutions and correct the inadequacy of the domain of definition by performing Taylor expansions of the boundary conditions about the steady-state position of the interface. To better understand this approach, we make the relation with stability problems in fluid-structure interaction where the position of the solid/fluid interface is, in addition to velocity and pressure fields, a quantity subject to perturbations. Works on these stability problems teach us that two methods are possible to treat a stability problem with freely moving domain. The first one is known as *the transpiration method* and correspond to the approach used by Ghez, Keller and coworkers without specification of the name of that method. A second method, *the arbitrary Lagrangian-Eulerian formulation* consists in rewriting the differential equation on a fixed domain using a Lagrangian space variable[5]. This is one of the elements of the method we develop in Section 8.3.2[6]. While Ghez et al. (1990, 1993) and Keller et al. (1993) have developed a proper mathematical method to address the general stability problem, in the formulation of the step governing equations the dynamics terms are missing from the boundary conditions $(7.60)_{2,3}$ (cf. footnote 3). While, this important details derives from the use of phenomenological constitutive relations for the attachment/detachment of adatoms at steps (see Ghez and Iyer 1988), the derivation of Section 7.1 shows that thermodynamic consistency requires to include the dynamics terms in $(7.60)_{2,3}$, as has been done in more recent works (Pierre-Louis, 2003b; Ranguelov and Stoyanov, 2007; Dufay et al., 2007). Furthermore, in Ghez et al. (1990, 1993) and Keller et al. (1993), the results of the stability analysis are discussed by using inadequate dimensionless parameters. For instance, lengths are nondimensionalized with the evaporation diffusion length $\sqrt{D/\nu}$, which is not relevant for discussing deposition cases. In our opinion, this renders their discussion of the effects of dynamics intractable.

With a mathematical method analogous to the one of of Ghez et al. (1993), as part of his thesis Gillet (2000) analyze the stability of steps while properly

5 The Lagrangian space variable is *arbitrary* in the sense that the mapping between Eulerian and Lagrangian formulations has no physical meaning (unlike in solid mechanics) and several choices are possible.

6 Note that we have secondarily checked that the results of the transpiration method coincides with the arbitrary Lagrangian-Eulerian formulation presented here.

including all the dynamics terms. Again, it is the transpiration method which is adopted unlike the arbitrary Lagrangian-Eulerian formulation that we develop. However, the resulting stability of steps with dynamics effect is not discussed much in this work. While Gillet (2000) simply notes that the dynamics effect may destabilize the steps under deposition, we provide, in Section 8.3.4, a detailed discussion which includes other stabilizing/destabilizing mechanisms. In particular, we point out, in Section 8.3.4 the fundamental role of $\overline{\kappa}$ for understanding the effect of the dynamics.[7]

In view of all these previous works, our objective is to clarify the consequences on stability of the dynamics effect and their importance in many situations. In this respect, it is important to highlight the generality of the results presented in Section 8.3.4 on the effects of the dynamics and on the inadequacies of the quasistatic approximation. Indeed these results are based on the stability analysis developed in Section 8.3.1 which fully accounts for the dynamics terms whereby covering all possible regimes and sets of parameters. Furthermore, in Appendix E, with the aim of completing the general and theoretical analysis, we estimate for particular materials, values and ranges for the physical parameters of the model. To this end, we combine for each parameter the results of several experimental works. On that basis, we show quantitatively in Section 8.4 that the dynamics effect is likely to be important for some illustrative examples.

7 The parameter $\overline{\kappa}$ is as an important parameter of the step dynamics problem which allows to distinguish between attachment/detachment (a/d) limited regime ($\overline{\kappa} \ll 1$) and diffusion limited regime ($\overline{\kappa} \gg 1$). In the former case the a/d velocity being smaller than the diffusion velocity D/L_0, it is the limiting kinetic mechanism while in the latter case it is the diffusion on terraces which is the limiting factor. See for instance Chung and Altman (2002) for a discussion on these two regimes.

8.2 QUASISTATIC APPROXIMATION STABILITY ANALYSIS

In this section, we perform a linear stability analysis of the steady-state solution under the quasistatic approximation. We derive analytical expressions of λ, the growth rate of a perturbation, which allows us to discuss the effect of each physical mechanism on the stability. Under the quasisatic approximation, the dynamics terms are neglected, which reduces (7.60) to

Recall that in this chapter $\bar{e} = 0$.

$$\begin{cases} 0 = \partial^2_{xx}\rho_n - \overline{\nu}\rho_n + \overline{F}, \\ -(\partial_x\rho_n)^- = \overline{\kappa}(\rho_n^- - 1 - \chi\Theta(\rho_{n+1}^+ - \rho_n^-) + f_n) - \overline{\kappa}_p(\rho_{n+1}^+ - \rho_n^-), \\ (\partial_x\rho_n)^+ = \overline{\kappa}S(\rho_n^+ - 1 - \chi\Theta(\rho_n^+ - \rho_{n-1}^-) + f_n) + \overline{\kappa}_p(\rho_n^+ - \rho_{n-1}^-), \\ \dot{x}_n = \Theta(J_n^+ + J_n^-). \end{cases} \tag{8.4}$$

8.2.1 *Steady-state solution*

Consider an infinite sequence of atomic steps, assumed equidistant at $t = 0$, and let their initial position be $x_n(0) = n$ for all $n \in \mathbb{Z}$.

The principal solution of (8.4), denoted by $\left(\overset{o}{\rho}(x,t), \overset{o}{V}\right)$, with $\overset{o}{\rho} : \mathbb{R} \times \mathbb{R}^+ \to \mathbb{R}$ is the solution where all the steps propagate at the same speed (i.e., $\overset{o}{x}_n(t) = n + \overset{o}{V}t$ for all $n \in \mathbb{Z}$) and the adatom density profile is the same on all terraces. The function $\overset{o}{\rho}(x,t)$ can be written as the piecewise function

$$\overset{o}{\rho}(x,t) = \overset{o}{\tilde{\rho}}(x - \overset{o}{x}_n(t)) \quad \text{for} \quad x \in \left(\overset{o}{x}_n(t), \overset{o}{x}_n(t) + 1\right), \tag{8.5}$$

where $\tilde{x} \mapsto \overset{o}{\tilde{\rho}}(\tilde{x})$ is defined on $(0,1)$.

Denoting by $\overset{o}{\rho}^+$ and $\overset{o}{\rho}^-$, the limit values of $\overset{o}{\tilde{\rho}}$ at 0^+ and 1^-, respectively, integration of $(8.4)_1$ on any terrace yields the function $\overset{o}{\tilde{\rho}}$ up to the two unknown integration constants $\overset{o}{\rho}^+$ and $\overset{o}{\rho}^-$. These are obtained with the two boundary conditions $(8.4)_{2,3}$, hence completely determining $\overset{o}{\tilde{\rho}}$, that is the adatom density over all the terraces. Finally, the velocity $\overset{o}{V}$ of the steps is obtained with $(8.4)_4$. Note that because of the conservation of equidistance between steps, $f_n = 0$ when one solves for the principal solution.

Although $\overset{o}{\tilde{\rho}}(x)$ and $\overset{o}{V}$ have analytical expressions, they are quite lengthy in the general case and we prefer not to report them. For understanding the spirit of the method, we only write the expressions of $\overset{o}{\tilde{\rho}}(x)$ and $\overset{o}{V}$ in the particular case without evaporation ($\overline{\nu} = 0$):

$$\overset{o}{\tilde{\rho}}(x) = -\frac{1}{2}\overline{F}x(x-1) + (\overset{o}{\rho}^- - \overset{o}{\rho}^+)x + \overset{o}{\rho}^+, \tag{8.6}$$

where

$$\overset{o}{\rho}^+ = 1 + \frac{\overline{F}\left(\overline{\kappa}(1 - \chi\Theta A) + 2\overline{\kappa}_p + 2\right)}{2\overline{\kappa}B} \quad \text{and} \quad \overset{o}{\rho}^- = 1 + \frac{\overline{F}\left(\overline{\kappa}(S - \chi\Theta A) + 2\overline{\kappa}_p + 2\right)}{2\overline{\kappa}B},$$

(8.7)

with $A := S - 1$ and $B := \overline{\kappa}S + \overline{\kappa}_p S + \overline{\kappa}_p + S + 1 > 0$. The resulting velocity of steps is

$$\overset{o}{V} = \overline{F}\Theta. \tag{8.8}$$

Note that in the absence of Schwoebel effect ($S = 1$), $\overset{o}{\rho}$ is symmetric with respect to $x = 1/2$, i.e., $\overset{o}{\rho}^+ = \overset{o}{\rho}^-$.

8.2.2 *Linear stability analysis*

To address the stability of the uniform step propagation against step bunching, we describe the position of the steps relative to the principal solution with $\zeta_n(t) := x_n(t) - \overset{o}{x}_n(t)$.

The first step of the stability analysis consists in integrating $(8.4)_1$ to express the adatom density profile $\rho_n(x,t)$ on the terraces as a function of the step positions and the limit values of the adatom densities at the steps. In that way, the problem of the time evolution of the step positions and adatom densities involving space and time derivatives is reduced to a dynamical system involving three scalar quantities per steps: the step position and the limit values of the adatom densities on each side of the step.

Write the adatom density on terrace n,

$$\rho_n(x,t) = \tilde{\rho}_n(x - x_n(t), t) \quad \text{for} \quad x \in \big(x_n(t), x_{n+1}(t)\big)\,, \tag{8.9}$$

where for all $n \in \mathbb{Z}$, the functions $\tilde{x} \mapsto \tilde{\rho}_n(\tilde{x},t)$ are defined on the intervals $\big(\zeta_n(t), 1 + \zeta_{n+1}(t)\big)$. The integration of $(8.4)_1$ on terrace n yields the x-dependence of the functions $\tilde{\rho}_n$, where the two time-dependent, integration constants are the (unknown) limit values $\rho_n^+(t) := \tilde{\rho}_n\big(\zeta_n(t), t\big)$ and $\rho_n^-(t) := \tilde{\rho}_n\big(1 + \zeta_{n+1}(t), t\big)$. Hence, $\tilde{\rho}_n(\tilde{x},t)$ can be formally written as

$$\tilde{\rho}_n(\tilde{x},t) = \check{\rho}\big[\rho_n^-(t), \rho_n^+(t), \zeta_n(t), \zeta_{n+1}(t)\big]\big(\tilde{x}\big), \tag{8.10}$$

where $\check{\rho}$ is a known function with analytical expression which we do not write explicitly for conciseness. Again, in the particular case without evaporation $\overline{\nu} = 0$, note that $\check{\rho}$ reads

$$\begin{aligned}\check{\rho}\big[\rho_n^-(t), \rho_n^+(t), \zeta_n(t), \zeta_{n+1}(t)\big]\big(\tilde{x}\big) = &-\frac{\overline{F}}{2}\big(\tilde{x} - \zeta_n(t)\big)\big(\tilde{x} - \zeta_{n+1}(t) - 1\big) \\ &+ \frac{\rho_n^-(t)\big(\tilde{x} - \zeta_n(t)\big) - \rho_n^+(t)\big(\tilde{x} - \zeta_{n+1}(t) - 1\big)\big)}{\zeta_{n+1}(t) + 1 - \zeta_n(t)}.\end{aligned} \tag{8.11}$$

The three remaining equations of (8.4), written at each step, yields a dynamical system of three equations per terrace for the three scalar unknowns associated to the n$^{\text{th}}$ terrace: $\rho_n^-(t)$, $\rho_n^+(t)$ and $\zeta_n(t)$ which, letting $\mathbf{p}_n(t) = \big(\rho_n^-(t), \rho_n^+(t), \zeta_n(t)\big)$ can be formally written as

$$\mathbf{M}\dot{\mathbf{p}}_n = \boldsymbol{\mathcal{F}}\big(\mathbf{p}_{n-R}, ..., \mathbf{p}_{n+R+1}\big), \tag{8.12}$$

where

$$\mathbf{M} = \begin{pmatrix} 0 & 0 & 0 \\ 0 & 0 & 0 \\ 0 & 0 & 1 \end{pmatrix}, \tag{8.13}$$

and $\boldsymbol{\mathcal{F}}$ is a vectorial function, whose three components derive from (8.4)$_{2,3,4}$:

$$\begin{cases} \mathcal{F}_1(\mathbf{p}_{n-R},\dots,\mathbf{p}_{n+R+1}) = \dfrac{\mathrm{d}\check{\rho}}{\mathrm{d}\tilde{x}}\Big|_{\tilde{x}=\zeta_n} + J^-_{n+1} - \overline{\kappa}_p(\rho^+_{n+1} - \rho^-_n), \\ \mathcal{F}_2(\mathbf{p}_{n-R},\dots,\mathbf{p}_{n+R+1}) = \dfrac{\mathrm{d}\check{\rho}}{\mathrm{d}\tilde{x}}\Big|_{\tilde{x}=1+\zeta_{n+1}} - J^+_n - \overline{\kappa}_p(\rho^+_n - \rho^-_{n-1}), \\ \mathcal{F}_3(\mathbf{p}_{n-R},\dots,\mathbf{p}_{n+R+1}) = \Theta(J^n_- + J^n_+) - \overset{o}{V}, \end{cases} \tag{8.14}$$

where

$$\begin{aligned} J^-_n &= \overline{\kappa}(\rho^-_{n-1} - 1 - \chi\Theta(\rho^+_n - \rho^-_{n-1}) + f_n), \\ J^+_n &= \overline{\kappa}S(\rho^+_n - 1 - \chi\Theta(\rho^+_n - \rho^-_{n-1}) + f_n), \end{aligned} \tag{8.15}$$

and f_n is rewritten with the step relative displacements:

$$f_n = \sum_{\substack{r\in\{-R,\dots,R\} \\ r\neq 0}} \left(\frac{\overline{\beta}}{\zeta_{n+r} - \zeta_n + r} - \frac{\overline{\alpha}}{(\zeta_{n+r} - \zeta_n + r)^3} \right). \tag{8.16}$$

The system (8.12)-(8.16) is linearized near the principal solution $\overset{o}{\mathbf{p}}_n = (\overset{o}{\rho}{}^-, \overset{o}{\rho}{}^+, 0)$ yielding the linear perturbation equation for $\delta\mathbf{p}_n(t) = \big(\delta\rho^-_n(t), \delta\rho^+_n(t), \delta\zeta_n(t)\big)$,

$$\mathbf{M}\delta\dot{\mathbf{p}}_n = \sum_{r=-R}^{R+1} \frac{\partial\boldsymbol{\mathcal{F}}}{\partial\mathbf{p}_{n+r}}\Big|_{\overset{o}{\mathbf{p}}} \delta\mathbf{p}_{n+r}. \tag{8.17}$$

Equation 8.17 is diagonalized using the spatial Fourier transform of $\big(\delta\mathbf{p}_n\big)_{n\in\mathbb{Z}}$:

$$\widehat{\delta\mathbf{p}}_k(t) = \sum_{n=-\infty}^{+\infty} \delta\mathbf{p}_n(t)\mathrm{e}^{ikn}, \tag{8.18}$$

where k is the wavenumber indexing the Fourier mode (with associated dimensionless wavelength $2\pi/k$) and i denotes the imaginary unit. Note that modes of all possible wavelengths are described by taking k in the first Brioullin zone $[-\pi,\pi]$ and an arbitrary perturbation $\delta\mathbf{p}_n(t)$ can be written as,

$$\delta\mathbf{p}_n(t) = \frac{1}{2\pi}\int_{-\pi}^{\pi} \widehat{\delta\mathbf{p}}_k(t)\mathrm{e}^{-ikn}\,\mathrm{d}k. \tag{8.19}$$

The Fourier transform of (8.17) reads[8]

$$\mathbf{M}\widehat{\dot{\delta\mathbf{p}}}_k = \underbrace{\left(\sum_{r=-R}^{R+1} \frac{\partial \boldsymbol{\mathcal{F}}}{\partial \mathbf{p}_{n+r}}\bigg|_{\overset{o}{\mathbf{p}}} \mathrm{e}^{ikr}\right)}_{\mathbf{C}_k} \widehat{\delta\mathbf{p}}_k, \tag{8.20}$$

where $\mathbf{C}_k$ denotes the 3×3 matrix associated to the Fourier mode k. Under the condition that the determinant of the upper-left 2×2 submatrix of $\mathbf{C}_k$ is not zero—which can be shown to be the case for $\Theta < 0.5$—the linear system comprised of the two first rows of (8.20) can be solved to express $\widehat{\delta\rho}_k^-$ and $\widehat{\delta\rho}_k^+$ in terms of $\widehat{\delta\zeta}_k$, thereupon allowing to rewrite the third row of (8.20) as an equation on $\widehat{\delta\zeta}_k$:

$$\dot{\widehat{\delta\zeta}}_k = \lambda(k)\widehat{\delta\zeta}_k. \tag{8.21}$$

where $\lambda(k)$ is the sought-after dispersion relation. The time evolution of an initial perturbation containing the sole mode of wavenumber k, with shape $\delta\zeta_n(0) = \widehat{\delta\zeta}_k(0)\mathrm{e}^{-ikn}$, is

$$\delta\zeta_n(t) = \widehat{\delta\zeta}_k(0) \exp\Big[i\left(\mathrm{Im}(\lambda(k))t - kn\right) + \mathrm{Re}(\lambda(k))t\Big], \tag{8.22}$$

where Re and Im denote the real and imaginary parts, respectively. Clearly, the linear stability of the equidistant train of step is given by the condition $\mathrm{Re}\big(\lambda(k)\big) < 0$ for all $k \in [-\pi, \pi]$. Note that $\lambda(-k) = \overline{\lambda(k)}$, so that for stability, $\mathrm{Re}\big(\lambda(k)\big)$ needs only to be studied on $[0, \pi]$.

The dispersion relation $\mathrm{Re}\big(\lambda(k)\big)$, which furnishes the stability against perturbation of wavelength $2\pi/k$ is very important as it constitutes the basis of all the discussion that follows.

In conclusion, following the approach presented above, one obtains an analytical expression of the dispersion relation $\lambda(k)$ whose real part provides the stability of the steady-state solution. While we do not report the lengthy expression of $\mathrm{Re}\big(\lambda(k)\big)$ in the general case, in Section 8.2.3 analytical and numerical treatment for special cases are combined to interpret the effects of the various physical factors on stability.

8.2.3 *Results*

In this section, we use an analytical approach to understand how the physics of the problem determines the stability of steps. To this end, as sketched on Figure 8.1, we shall distinguish between:

1. *The mechanisms*: physical processes that tend to stabilize or destabilize the step dynamics. These are dipole-dipole and monopole-monopole *elastic interactions*, *Ehrlich-Schwoebel effect* and the *adatom jump effect*. Note that, in the analysis beyond the quasistatic approximation developed in Section 8.3, another mechanism, the *dynamics effect*, is exhibited.

8 To give a different perspective, note that we could consider the linear perturbation problem for a finite number of steps N with periodic boundary conditions. In that case the right hand side of (8.17) written for $n = 0, \ldots, N-1$ is a linear system for the $3N$ vector variable $\big(\delta\rho_0^-(t), \delta\rho_0^+(t), \delta\zeta_0(t), \ldots, \delta\rho_{N-1}^-(t), \delta\rho_{N-1}^+(t), \delta\zeta_{N-1}(t)\big)$. The $3N \times 3N$ matrix obtained from (8.17) has a block circulant architecture and $\mathbf{C}_k$ in (8.20) correspond to the matrix eigenvalue of the block-diagonalization of the matrix underlying (8.17).

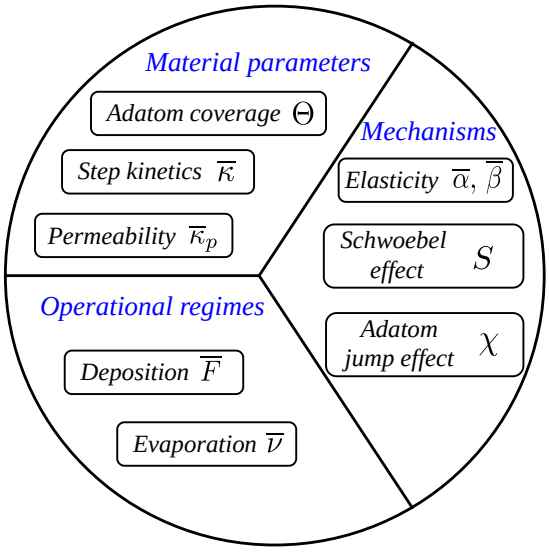

Figure 8.1: Diagram of the physical factors that determine the stability of steps. One should distinguish between the mechanisms that are intrinsically stabilizing/destabilizing and the parameters (material and operational) that govern the relative importance of the mechanisms involved.

2. *The operational regimes*: these regimes are those of deposition and evaporation and are considered independently. We will show that two classes of mechanisms can be distinguished, on the one hand elasticity which has an influence on stability independent, at first order, of the deposition/evaporation rates, this is an *energetic* mechanism. On the other hand, the other mechanisms, whose influence on stability grows, at first order, linearly with the deposition/evaporation rates, are called *kinetic*.

3. *The material parameters*: these parameters, which determine the relative influence on stability of the different mechanisms involved, are the adatom coverage Θ and the dimensionless parameters for step kinetics $\overline{\kappa}$ and permeability $\overline{\kappa}_p$. When simultaneous stabilizing and destabilizing mechanisms are present, the dominant ones depend on the set of material parameters.

First, the effect (stabilizing or destabilizing) of each mechanism taken independently is determined by studying the dispersion relation $\mathrm{Re}(\lambda(k))$ both with analytical and numerical approaches.[9] Without specific mention, we assume nearest-neighbor elastic interactions ($R = 1$).

A typical dispersion curve is given in Figure 8.2. While the sign of $\lim_{k\to 0} \mathrm{Re}(\lambda(k))$ and $\mathrm{Re}(\lambda(\pi))$ give the stability against long wavelength perturbations and step pairing, respectively, $\mathrm{Re}(\lambda(k))$ for an arbitrary value of k in the interval $(0, \pi)$ gives the stability for perturbation with intermediate wavelength $2\pi/k$ (in dimensionless space variable).

9 The numerical approach requires some typical numerical values of the eight dimensionless parameters of Section 7.2.3. These are estimated, in Appendix E, on the basis of the experimental literature on GaAs(001) and Si(111) for homoepitaxy and SiGe on Si(001) for heteroepitaxy.

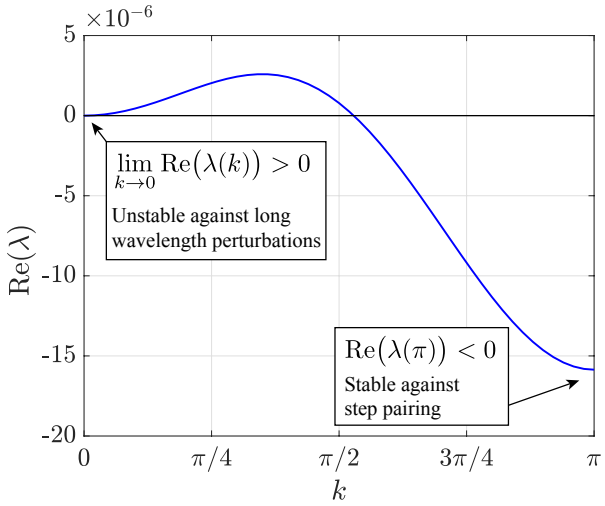

Figure 8.2: An example of dispersion curve under deposition for $\overline{F} = 10^{-1}$, $\overline{\nu} = 0$, $S = 0.4$, $\overline{\kappa} = 20$, $\Theta = 0.01$, $\overline{\alpha} = 10^{-4}$, $\overline{\beta} = 0$ under the quasistatic approximation. On that example, steps are unstable against long wavelength perturbations ($k \to 0$) and stable with respect to step pairing ($k = \pi$).

REDUCTION OF THE STABILITY STUDY TO LONG WAVELENGTHS AND STEP PAIRING A numerical study of the dispersion curves for the physically relevant dimensionless parameters allows to derive the following conjecture:[10]

Conjecture 1 *If* $\lim_{k\to 0} Re(\lambda(k)) < 0$ *and* $Re(\lambda(\pi)) < 0$, *then* $Re(\lambda(k)) < 0$ *for all* $k \in (0, \pi)$.

In other words, it is enough to check the stability against both long wavelength perturbations and step pairing to ensure the stability for all wavelengths. Conversely, it is clear that instability of either of the two limit cases is enough for the step flow to be unstable.

ASIDE: PROOF OF CONJECTURE 1 FOR THE CASE $\chi = 0$

While Conjecture 1 is based on numerical observations, it can be proven analytically in the simplified case of (8.4) without the adatom jump effect ($\chi = 0$) [a] and with nearest-neighbor elastic interactions ($R = 1$). In this case the dispersion relation reads

$$\mathrm{Re}\big(\lambda(k)\big) = \frac{2\overline{\kappa}\Theta\big(-A\overline{F}(1+S)\sin^2(k/2) + 8C(\overline{\beta} - 3\overline{\alpha})\sin^4(k/2)\big)}{B(4\overline{\kappa}_p \sin^2(k/2) + \overline{\kappa}B)}, \quad (8.23)$$

where we recall that $A := S - 1$, $B := \overline{\kappa}S + \overline{\kappa}_p S + S + \overline{\kappa}_p + 1$ and we define $C := \overline{\kappa}_p(S+1)(2\overline{\kappa}S + S + 1) + \overline{\kappa}S(\overline{\kappa}S + S + 1) + \overline{\kappa}_p^2(S+1)^2$.

10 As an exception, Conjecture 1 is not valid for the very particular case where there are both attractive and repulsive elastic interactions with comparable magnitudes and the range R of these interactions is strictly larger than 1 (i.e., elastic interactions further than nearest neighbors are considered). In this case instabilities at finite wavelength may happen while long wavelength and step pairing perturbations are both stable.

Noting that the denominator of (8.23) is a strictly positive number, the sign of $\mathrm{Re}\big(\lambda(k)\big)$ is studied by considering its numerator only. The latter can be written $a\sin^2(k/2) + b\sin^4(k/2)$ with $a := -2\overline{\kappa}\Theta A\overline{F}(1+S)$ and $b := 16\overline{\kappa}\Theta C(\overline{\beta} - 3\overline{\alpha})$. The assumption that both long wavelength and step pairing instabilities are stable implies that $a < 0$ and $a + b < 0$, respectively, which are sufficient conditions ensuring that $a\sin^2(k/2) + b\sin^4(k/2)$ and consequently $\mathrm{Re}\big(\lambda(k)\big)$ are negative for all $k \in (0, \pi)$, hence proving Proposition 1 for that particular case.

[a] This simplification has no physical justification for our thermodynamically derived governing equation and it is only performed here for obtaining a tractable analytical expression. Note however that taking $\chi = 0$ in (7.60)-(7.62) amounts to the step dynamics governing equations as written in Pierre-Louis (2003b)

8.2.3.1 *Effect of the mechanisms under deposition*

For better readability of the analytical expressions, let

$$A := S - 1, \tag{8.24}$$

whose sign gives the direct or inverse character of the Schwoebel effect and introduce

$$\begin{aligned} B &:= \overline{\kappa}S + \overline{\kappa}_p S + S + \overline{\kappa}_p + 1 \quad \text{and} \\ C &:= \overline{\kappa}_p(S+1)(2\overline{\kappa}S + S + 1) + \overline{\kappa}S(\overline{\kappa}S + S + 1) + \overline{\kappa}_p^2(S+1)^2, \end{aligned} \tag{8.25}$$

two strictly positive expressions. Consider pure deposition ($\overline{\nu} = 0$) and nearest-neighbor elastic interactions, the growth rate $\mathrm{Re}(\lambda_{SP}^{dep})$ associated to step pairing ($k = \pi$) reads

$$\mathrm{Re}(\lambda_{SP}^{dep}) = \frac{\Theta\overline{\kappa}\big(2\overline{F}(S+1)(2B\chi\Theta - A) + 16C(\overline{\beta} - 3\overline{\alpha})\big)}{B\big(\overline{\kappa}(B - 2\chi\Theta A) + 4\overline{\kappa}_p\big)}, \tag{8.26}$$

while for long wavelength perturbations, performing a series expansion of $\mathrm{Re}\big(\lambda(k)\big)$ about $k = 0$ yields:

1. for $S \neq 1$,

$$\mathrm{Re}\big(\lambda(k)\big) = -\frac{\overline{F}\Theta(S+1)A}{2B^2}k^2 + o(k^2), \tag{8.27}$$

2. for $S = 1$,

$$\mathrm{Re}\big(\lambda(k)\big) = \frac{\Theta(\overline{\kappa} + 2\overline{\kappa}_p)\big((\overline{\kappa}+2)\overline{F}\chi\Theta - 2\overline{\kappa}(\overline{\kappa} + 2\overline{\kappa}_p + 2)(3\overline{\alpha} - \overline{\beta})\big)}{2\overline{\kappa}(\overline{\kappa} + 2\overline{\kappa}_p + 2)^2}k^4 + o(k^4). \tag{8.28}$$

Eqs. (8.26)-(8.28) allow us to determine directly the effect of each mechanism on the stability under deposition. Note that under the condition that $\Theta < 0.5$ (satisfied in practice), the denominator of (8.26) remains positive. Analyzing the sign of the terms of the numerator shows that: the Schwoebel effect—appearing in $A = S - 1$—is stabilizing when it is direct and destabilizing when it is

inverse; the monopole-monopole ($\overline{\beta}$) and dipole-dipole ($\overline{\alpha}$) elastic interactions are respectively destabilizing and stabilizing, the adatom jump effect (χ terms in the numerator) is destabilizing. All these conclusions are derived for the step pairing instability.

Regarding long wavelength instabilities, (8.27) and (8.28) show that, if any, the Schwoebel effect determine their stability while in its absence, the stability results from the combined effects of elastic and adatom jump effect which are qualitatively the same as for step pairing (i. e., stabilizing and destabilizing in the same way as for step pairing).

Note in particular, from (8.26)-(8.28), that the permeability is not itself a stabilizing or destabilizing mechanism in the sense that if other mechanisms are disabled ($S = 1$, $\chi = 0$, $\overline{\alpha} = 0$ and $\overline{\beta} = 0$) the permeability has no effect on stability. In contrast, permeability appears as a parameter that changes the relative weight of the stabilizing or destabilizing effects of the various mechanisms. For example, by taking $\overline{\kappa}_p \to \infty$ (i. e., steps are very permeable), it can be seen from the numerator of (8.26) and (8.28) that the effect of elasticity becomes predominant over the Schwoebel and adatom jump effects. Indeed, both in (8.26) and (8.28), elasticity has, as a factor term, a larger power of $\overline{\kappa}_p$ than the two other effects have. The result physically makes sense because having very permeable steps amounts to shunt the asymmetry of step attachment/detachment and equalize the adatom density on both sides of the steps, whereby minimizing the influence of the Schwoebel and adatom jump effects.

In addition, an interesting conclusion that can be drawn from (8.26)-(8.28) is that the different mechanisms do not exhibit a complex interplay in the sense that for any set of parameters the influence on stability of each mechanism remains in the same direction. Indeed, the effects of the various mechanisms are essentially additive up to modifications, by changing the parameters, of their relative weight but not of the signs of their factors.

8.2.3.2 *Effect of the mechanisms under evaporation*

Considering now evaporation ($\overline{F} = 0$), an analytical study is done for step pairing instabilities while for long wavelength perturbations, given the complexity of the analytical expressions, a numerical study confirms that each mechanism has qualitatively the same effect on stability as for step pairing. The step pairing instabilities growth rate reads

$$\mathrm{Re}(\lambda_{SP}^{dep}) = \frac{8\sqrt{\overline{\nu}}e^{2\sqrt{\overline{\nu}}}\overline{\kappa}\Theta\Big(N_1 + (\overline{\beta} - 3\overline{\alpha})N_2\Big)}{D_1}, \tag{8.29}$$

where the denominator D_1 has the following expression:

$$\begin{aligned} D_1 :=& 4\mathrm{e}^{2\sqrt{\overline{\nu}}}\Big[\sqrt{\overline{\nu}}\Big(-2\overline{\kappa}_p + \overline{\kappa}(S-1)\chi\Theta \\ &+ \Big(2\overline{\kappa}_p + \overline{\kappa}(S[1-\chi\Theta]+1+\chi\Theta)\Big)\cosh\left(\sqrt{\overline{\nu}}\right)\Big) \\ &+ \Big(\overline{\nu}+\overline{\kappa}D\Big)\sinh\left(\sqrt{\overline{\nu}}\right)\Big]\times \\ &\Big[\sqrt{\overline{\nu}}\Big(2\overline{\kappa}_p + \overline{\kappa}(1-S)\chi\Theta + \Big(2\overline{\kappa}_p + \overline{\kappa}(S[1-\chi\Theta]+1+\chi\Theta)\Big)\cosh\left(\sqrt{\overline{\nu}}\right)\Big) \\ &+ \Big(\overline{\nu}+\overline{\kappa}D\Big)\sinh\left(\sqrt{\overline{\nu}}\right)\Big], \end{aligned} \tag{8.30}$$

with $D := \overline{\kappa}_p + (\overline{\kappa}+\overline{\kappa}_p)S$. Using that $\Theta < 0.5$ and $\cosh\left(\sqrt{\overline{\nu}}\right) > 1$ one can easily show that $D_1 > 0$.

The kinetic part N_1 of the numerator reads

$$N_1 := (1+S)\overline{\kappa}\Big(\overline{\nu}^{\frac{3}{2}}A - \chi\Theta\nu\Big(\sqrt{\overline{\nu}}(1+S)\left(1+\cosh\left(\sqrt{\overline{\nu}}\right)\right) + 2D\sinh\left(\sqrt{\overline{\nu}}\right)\Big)\Big), \tag{8.31}$$

while its energetic contribution N_2 reads:

$$\begin{aligned} N_2 := 8\sqrt{\overline{\nu}}\mathrm{e}^{2\sqrt{\overline{\nu}}}\overline{\kappa}\Theta\big(&N_{21} + N_{22}\cosh(\sqrt{\overline{\nu}}) + N_{23}\cosh(2\sqrt{\overline{\nu}}) + N_{24}\sinh(\sqrt{\overline{\nu}}) \\ &+ N_{25}\sinh(2\sqrt{\overline{\nu}})\big), \end{aligned} \tag{8.32}$$

where

$$\begin{cases} N_{21} := -\Big(\sqrt{\overline{\nu}}D\Big(4\overline{\kappa}_p - \overline{\kappa}(2\chi\Theta A + S + 1)\Big) + \sqrt{\overline{\nu}\overline{\nu}}(S+1)\Big), \\ N_{22} := 4\sqrt{\overline{\nu}\overline{\kappa}}(1+S)D, \\ N_{23} := \sqrt{\overline{\nu}}\Big(D\big(4\overline{\kappa}_p + \overline{\kappa}(3+3S+2(1-S)\chi\Theta)\big) + (1+S)\overline{\nu}\Big), \\ N_{24} := 2\overline{\kappa}\big(2D^2 + 2S\overline{\nu} + (S^2-1)\chi\Theta\overline{\nu}\big), \\ N_{25} := \Big(4\overline{\nu\kappa}_p(1+S) + 2\overline{\kappa}D^2 + \overline{\kappa}\big(1+\chi\Theta + S(4+S-S\chi\Theta)\big)\overline{\nu}\Big). \end{cases} \tag{8.33}$$

It can be shown using again the assumption $\Theta < 0.5$ that $N_2 > 0$.

As a result, for the step pairing instability, the elastic interaction terms have the same effect on stability as under deposition (as $N_2 > 0$). Contrariwise, the kinetic mechanisms see their effect on stability opposite to the one under deposition, i. e., the direct (resp. inverse) Schwoebel effect is destabilizing (resp. stabilizing) (see the terms factor of A in (8.31)) and the adatom jump effect is stabilizing (see the terms factor of χ in (8.31)).

Note, as under deposition, that there is no complex interplay between the mechanisms and that permeability again is not a stabilizing or destabilizing mechanism in itself.

Table 8.1: Effect on stability of the elementary mechanisms. ES effect: Ehrlich-Schwoebel effect; AJ effect: Adatom Jump effect; DD Elas.: Dipole-dipole elastic interactions; MM Elas.: Monopole-monopole elastic interactions. $\mathcal{S}$: Stabilizing; $\mathcal{D}$: Destabilizing.

	Direct ES	Inverse ES	AJ effect	DD Elas.	MM Elas.
	$S > 1$	$S < 1$	χ	$\overline{\alpha}$	$\overline{\beta}$
Deposition	$\mathcal{S}$	$\mathcal{D}$	$\mathcal{D}$	$\mathcal{S}$	$\mathcal{D}$
Evaporation	$\mathcal{D}$	$\mathcal{S}$	$\mathcal{S}$	$\mathcal{S}$	$\mathcal{D}$

In summary, after showing that the stability analysis can be reduced to considering the step pairing and long wavelengths instabilities, we have used as much as possible an analytical approach to clarify the effect of each mechanism in these two limits both under pure deposition and pure evaporation. This analysis provides the effect of each of these mechanisms on stability as summarized in Table 8.1.

An important point to note for each of the three mechanisms studied here, is that when the mechanism is stabilizing (resp. destabilizing) for either step pairing or long wavelength perturbations, it is actually stabilizing (resp. destabilizing) for all wavelengths (i. e., for all $k \in (0, \pi)$). Anticipating a little bit on the study of stability with dynamics terms in Section 8.3, we can already note that it is not the case for the dynamics effect (introduced in Section 8.3), which for a given set of parameters, may be destabilizing for some wavelengths and stabilizing for others.

8.2.3.3 *Influence of the operational and material parameters*

The stability of step flow in the presence of several simultaneous mechanisms results from the interplay between the effects of each mechanism. We discuss here, on the basis of the expression of $\mathrm{Re}(\lambda)$ (8.26)-(8.29), how the parameters affect the relative weight of the different mechanisms. For clarity, we distinguish between the parameters that quantify the strength of a mechanism (S for the Schwoebel effect, $\overline{\alpha}$ and $\overline{\beta}$ for the dipole-dipole and monopole-monopole elastic interactions respectively) and the parameters that rule the interplay between the mechanisms: these are either operational ($\overline{F}$ and $\overline{\nu}$) or material (Θ, $\overline{\kappa}$ and $\overline{\kappa}_p$) parameters.

Recall that $\mathrm{Re}(\lambda(k))$ is the growth rate of a perturbation of wavelength $2\pi/k$.

First, the deposition/evaporation parameters $\overline{F}$ and $\overline{\nu}$ allows to distinguish between the *kinetic* mechanisms and the *energetic* ones. As seen in (8.26)-(8.28), under deposition, $\mathrm{Re}(\lambda)$ associated with the Schwoebel effect and the adatom jump effect are linear in $\overline{F}$ (those mechanisms are called kinetic) unlike the contribution of the elastic interactions which is independent of $\overline{F}$ (elasticity is an energetic mechanism). Similarly, under evaporation, a Taylor expansion of (8.29) in the domain $\overline{\nu} \ll 1$ provides dependencies on $\overline{\nu}$ identical to those on $\overline{F}$ under deposition. Hence as the deposition/evaporation rates increase, the

Table 8.2: Scaling of the contribution of the mechanisms to the growth rate with the control and material parameters $\overline{F}$, $\overline{v}$ and Θ. Decompose $\mathrm{Re}(\lambda) = \sum_{mech} \mathrm{Re}(\lambda_{mech})$ where *mech* spans the three mechanisms ES: Ehrlich-Schwoebel effect; AJ effect: Adatom jump effect; Elas.: elastic interactions. The contribution of each mechanism scales as $\mathrm{Re}(\lambda_{mech}) \propto \overline{F}^a \Theta^b$ under deposition and $\mathrm{Re}(\lambda_{mech}) \propto \overline{v}^a \Theta^b$ under evaporation with the exponents a and b given in the table.

	ES effect	AJ effect	Elas.
	S	χ	$\overline{\alpha}$, $\overline{\beta}$
a (for $\overline{F}$, $\overline{v}$)	1	1	0
b (for Θ)	1	2	1

effects of the kinetic mechanisms become more prominent compared to the effect of elasticity.

Secondly, the adatom coverage Θ provide a distinction between the adatom jump effect whose contribution to $\mathrm{Re}(\lambda)$ is quadratic in Θ and the other mechanisms whose contribution is linear in Θ. This implies that adatom jump effect becomes more important for materials with high Θ (relatively high adatom coverage, $\Theta = 0.2$ has been observed on GaAs(001) and on Si(111)-1×1 (see Appendix E). The influences of $\overline{F}$, $\overline{v}$ and Θ are summarized in Table 8.2.

Last $\overline{\kappa}$ and $\overline{\kappa}_p$ both accounting for kinetic processes at steps play comparable roles. In particular, as noted by Pierre-Louis (2003b) (see also Sato et al., 2000), transparency can be understood as a mechanism in parallel—in the sense of an electric circuit analogy—with the attachment/detachment of adatoms at steps. Recalling that $\overline{\kappa}$ and $\overline{\kappa}_p$ are dimensionless velocities associated to a/d and permeability, respectively, $\overline{\kappa}_p$ has a sensible effect on stability only when $\overline{\kappa}_p \gtrsim \overline{\kappa}$. This clearly appears in the expressions (8.26)-(8.29) where $\overline{\kappa}_p$ appears in weighted sums with $\overline{\kappa}$. Whereas the scaling of the growth rate by $\overline{\kappa}$ and $\overline{\kappa}_p$ is not trivial in general, it can be seen in particular cases—where the magnitudes of $\overline{\kappa}$, $\overline{\kappa}_p$ and 1 are clearly separated—that the largest power of $\overline{\kappa}$ and $\overline{\kappa}_p$ is for the contribution of elasticity to $\mathrm{Re}(\lambda)$, then comes the contribution of the adatom jump effect with a smaller exponent and finally the exponent of the Schwoebel effect which is the smallest. This is consistent with the fact that the Schwoebel effect has more influence as the a/d kinetic is slower ($\overline{\kappa} \searrow$) and in absence of permeability ($\overline{\kappa}_p = 0$). By contrast, a faster a/d kinetics ($\overline{\kappa} \nearrow$) or a more efficient permeability ($\overline{\kappa}_p \nearrow$) increases the influence of the energetic effect (elasticity) to the detriment of the kinetic ones (Schwoebel effect and adatom jump effect).

8.2.4 *Quasistatic analysis of long range elasticity*

As developed in Section 7.2.1.3 the configurational force f_n exerted on the n^{th} step results from the interaction of its elastic field with the elastic field of all other steps. However, in Section 8.2.3 as well as in all the literature accounting for elastic interaction between steps (Tersoff et al., 1995; Pierre-Louis, 2003b),

Table 8.3: Dependence of the dispersion curve on the range R of elastic interactions considered for steps stabilized and destabilized solely through dipole-dipole and monopole-monopole elastic interactions. The following idealizations are applied $S = 1$, $\chi = 0$, $\overline{\kappa}_p = 0$ and $\overline{\nu} = 0$. DDEI: Dipole-dipole elastic interactions; MMEI: Monopole-monopole elastic interactions. We introduce $a(k)$, common factor to DDEI and MMEI dispersion relations $a(k) := \left(16\overline{\kappa}\Theta \sin^4(k/2)\right)/\left(2+\overline{\kappa}\right)$.

	$R=1$	$R=2$	$R=3$
(DDEI): $\frac{\mathrm{Re}(\lambda(k))}{a(k)}$	$-3\overline{\alpha}$	$-\frac{(9+\cos(k))3\overline{\alpha}}{8}$	$-\frac{(753+113\cos(k)+16\cos(2k))3\overline{\alpha}}{648}$
(MMEI): $\frac{\mathrm{Re}(\lambda(k))}{a(k)}$	$\overline{\beta}$	$\frac{(3+\cos(k))\overline{\beta}}{2}$	$\frac{(33+17\cos(k)+4\cos(2k))\overline{\beta}}{18}$

the stability with respect to step bunching is analyzed under the assumption of nearest-neighbor interactions, which only considers elastic interaction of a step with its adjacent neighbors. The point of this section is to quantify both for the dipole-dipole and monopole-monopole elastic interactions the consequences of this approximation on the stability predictions.

For this purpose, using the linear stability analysis of Section 8.2.2—developed for elastic interactions of arbitrary range R—we study the R-dependence of the stability dispersion curve for a system of steps where elasticity is the unique stabilizing/destabilizing mechanism (i.e. the other mechanisms: Schwoebel effect and adatom jump effect discussed in Section 8.2.3 are disabled by setting $S = 1$ and $\chi = 0$). In addition, for simplicity in the analytical expressions, steps are assumed impermeable ($\overline{\kappa}_p = 0$) and evaporation is neglected ($\overline{\nu} = 0$). As detailed in footnote 11, these assumptions do not restrict the generality of the discussion as the R-dependence of the elastic contribution to the stability is not modified when elasticity is combined with other mechanisms.[11] For both dipole-dipole and monopole-monopole elastic interactions taken independently, the R-dependence of the dispersion curve is shown analytically in Table 8.3 and graphically on Figure 8.3. As can be seen on Figure 8.3, the further nearest neighbors have a negligible effect for the dipole-dipole elastic interactions

11 Indeed, when the step dynamics involves the other mechanisms or when including evaporation, the ratio of the contribution of elasticity to the growth rate for range R to the same quantity for range 1 remains the same as the one presented in Table 8.3 and Figure 8.3. For instance, for a non-zero evaporation rate, the growth rate for dipole-dipole interactions with $R = 1$ reads

$$\mathrm{Re}\left(\lambda^{R=1}(k)\right) = \frac{24\overline{\kappa}\Theta\overline{\alpha}\sqrt{\overline{\nu}}\sin^4\left(\frac{k}{2}\right)\left(\overline{\kappa}\cos(k) - \overline{\kappa}\cosh\left(\sqrt{\overline{\nu}}\right) - \sqrt{\overline{\nu}}\sinh\left(\sqrt{\overline{\nu}}\right)\right)}{2\overline{\kappa}\cosh\left(\sqrt{\overline{\nu}}\right) + \left(\overline{\kappa}^2+\overline{\nu}\right)\sinh\left(\sqrt{\overline{\nu}}\right)}, \tag{8.34}$$

and is modified for second-nearest-neighbor interactions in the proportion

$$\mathrm{Re}\left(\lambda^{R=2}(k)\right)\Big/\mathrm{Re}\left(\lambda^{R=1}(k)\right) = \frac{9+\cos(k)}{8}, \tag{8.35}$$

which corresponds to the same ratio as the one displayed in Table 8.3. The same range dependency in the elastic part of the growth rate is observed when other phenomena (transparency, Schwoebel effect, adatom jump effect) are also included.

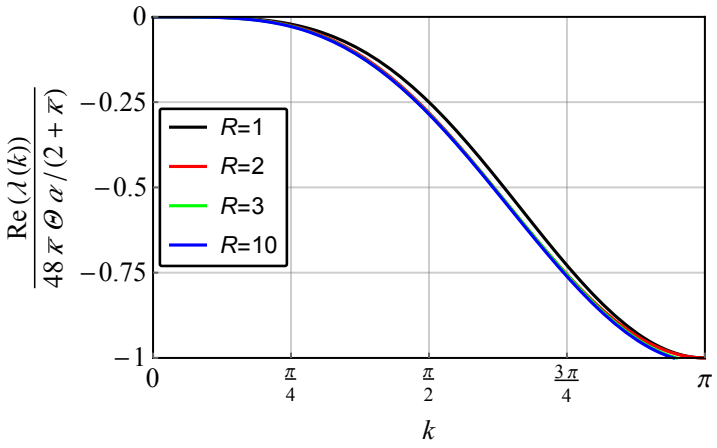

(a) Dipole-dipole

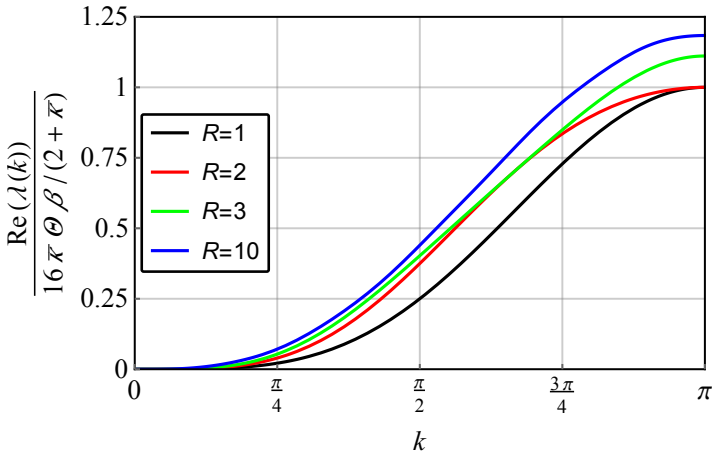

(b) Monopole-monopole

Figure 8.3: Dispersion curves associated with the step dynamics problem described in Table 8.3, which shows the dependence on the range R of elastic interactions. (a) Dipole-dipole and (b) Monopole-monopole elastic interactions.

and convergence of the dispersion curves is reached within less than 1% at $R = 3$. By contrast, they induce changes of the order of 20% in the case of monopole-monopole elastic interactions. In conclusion, while for the analysis developed here, where the parameters are simply known in order of magnitude, the assumption of nearest-neighbor interactions is largely acceptable, the modification caused by long range elastic interactions shall be taken into account for an accurate quantitative theory with monopole-monopole elastic interactions.

8.3 GENERAL STABILITY ANALYSIS INCLUDING DYNAMICS TERMS

The quasistatic stability analysis of Section 8.2 provides analytical expressions for the growth rate of perturbations, which are very helpful to understand the effect of each mechanism. However as discussed in Section 8.1, these results rely on an approximation whose scope of validity is not clear, *a priori*, which explains we go beyond that approximation to get a complete picture of step stability. In this section we develop a linear stability analysis for the general system (7.60) (rewritten below in (8.36)) and use its results to discuss the validity of the quasistatic approximation.

Recalling that we have taken $\overline{b} \to \infty$ since Section 7.2.3 and that for the present Chapter 8, we are not concerned with the effect of electromigration ($\overline{e} = 0$), (7.60)-(7.62) is rewritten

$$\begin{cases} \partial_t \rho_n = \partial^2_{xx}\rho_n - \overline{v}\rho_n + \overline{F}, \\ -\rho_n^- \dot{x}_{n+1} - (\partial_x \rho_n)^- = \overline{\kappa}(\rho_n^- - 1 - \chi\Theta[\![\rho]\!]_{x_{n+1}} + f_{n+1}) - \overline{\kappa}_p[\![\rho]\!]_{x_{n+1}}, \\ \rho_n^+ \dot{x}_n + (\partial_x \rho_n)^+ = \overline{\kappa}S(\rho_n^+ - 1 - \chi\Theta[\![\rho]\!]_{x_n} + f_n) + \overline{\kappa}_p[\![\rho]\!]_{x_n}, \\ \dot{x}_n = \Theta(J_n^+ + J_n^-), \end{cases} \tag{8.36}$$

where,

$$f_n = \sum_{\substack{r\in\{-R,\dots,R\} \\ r\neq 0}} \left(\frac{\overline{\beta}}{x_{n+r} - x_n} - \frac{\overline{\alpha}}{(x_{n+r} - x_n)^3} \right). \tag{8.37}$$

For simplicity, lying on the results of Section 8.2.4, we assume nearest-neighbor interactions, i.e. take $R = 1$.

For the clarity of the discussion developed throughout this section,the reader should note that we call *the dynamics terms* the three terms $\partial_t\rho$, $-\rho_n^-\dot{x}_{n+1}$ and $\rho_n^+\dot{x}_n$ in $(8.36)_1$, $(8.36)_2$ and $(8.36)_3$ respectively. These are the terms neglected in the quasistatic linear stability analysis of Section 8.2 while conserved in the present chapter.

8.3.1 *Steady-state solution*

As in Section 8.2.1, the steady-state solution is written $\overset{o}{x}_n(t) = n + \overset{o}{V}t$ for all $n \in \mathbb{Z}$ and $\overset{o}{\rho}(x,t) = \overset{o}{\tilde{\rho}}(x - \overset{o}{x}_n(t))$ for $x \in \left(\overset{o}{x}_n(t), \overset{o}{x}_n(t) + 1\right)$. Inserting these expressions in (8.36), one can obtain, by solving $(8.36)_{1-3}$, an analytical expression of $\overset{o}{\tilde{\rho}}$ which nevertheless involves the unknown step velocity $\overset{o}{V}$. As a second step, inserting the currents J_n^- and J_n^+ in $(8.36)_4$ yields an equation for $\overset{o}{V}$. In the particular case of pure deposition ($\overline{v} = 0$), this equation can be solved analytically and, as it turns out, one recovers the quasistatic steady-state velocity $\overset{o}{V} = \overline{F}\Theta$. However, in the general case ($\overline{v} \neq 0$), this is a transcendental equation with a unique physically sound solution computed numerically by starting from the quasistatic solution of Section 8.2.1.

8.3.2 *Linear stability analysis*

In this section, we develop a method to investigate the linear stability of the steady-state solution of (8.36).

LAGRANGIAN FORMULATION The problem under consideration being a free-boundary problem, the perturbation of the adatom density is not defined on the same domain as the steady-state solution. Thus, the partial differential system $(8.36)_{1-3}$ is rewritten on a fixed domain by introducing the *Lagrangian* space variable u related to x on (x_n, x_{n+1}) by the diffeomorphism g_n defined by

$$u = g_n(x,t) := \frac{x - x_n(t)}{x_{n+1}(t) - x_n(t)}. \tag{8.38}$$

Denoting by g_n^{-1} its reciprocal function, let for all $n \in \mathbb{Z}$, $\tilde{\rho}_n$ be the *Lagrangian adatom density* defined on $(0,1) \times \mathbb{R}^+$ by

$$\tilde{\rho}_n(u,t) := \rho_n(g_n^{-1}(u,t),t). \tag{8.39}$$

Using the relations between the partial derivatives of ρ_n and of $\tilde{\rho}_n$,[12] (8.36) is rewritten with Lagrangian variables

$$\begin{cases} s_n^2 \partial_t \tilde{\rho}_n = \partial_{uu}\tilde{\rho}_n + s_n\big[\dot{x}_n + [\dot{x}_{n+1} - \dot{x}_n]u\big]\partial_u\tilde{\rho}_n \\ \qquad\qquad + s_n^2\big[-\overline{\nu}\tilde{\rho}_n + \overline{F}\big], \\ -s_n\tilde{\rho}_n^-\dot{x}_{n+1} - (\partial_u\tilde{\rho}_n)^- = s_n\Big[\underbrace{\overline{\kappa}\Big(\tilde{\rho}_n^- - 1 - \chi\Theta(\tilde{\rho}_{n+1}^+ - \tilde{\rho}_n^-) + f_{n+1}\Big)}_{\tilde{J}_{n+1}^-} \\ \qquad\qquad - \overline{\kappa}_p(\tilde{\rho}_{n+1}^+ - \tilde{\rho}_n^-)\Big], \\ s_n\tilde{\rho}_n^+\dot{x}_n + (\partial_u\tilde{\rho}_n)^+ = s_n\Big[\underbrace{\overline{\kappa}S\Big(\tilde{\rho}_n^+ - 1 - \chi\Theta(\tilde{\rho}_n^+ - \tilde{\rho}_{n-1}^-) + f_n\Big)}_{\tilde{J}_n^+} \\ \qquad\qquad + \overline{\kappa}_p(\tilde{\rho}_n^+ - \tilde{\rho}_{n-1}^-)\Big], \\ \dot{x}_n = \Theta(\tilde{J}_n^+ + \tilde{J}_n^-), \end{cases} \tag{8.40}$$

where $s_n = x_{n+1} - x_n$ and the superscripts plus and minus denote evaluations at 0 and 1, respectively: $\tilde{\rho}_n^+ := \tilde{\rho}_n(0,t)$, $\tilde{\rho}_n^- := \tilde{\rho}_n(1,t)$, $(\partial_u\tilde{\rho}_n)^+ := \partial_u\tilde{\rho}_n(0,t)$ and $(\partial_u\tilde{\rho}_n)^- := \partial_u\tilde{\rho}_n(1,t)$. Note that the differential equation $(8.40)_1$ is defined on $(0,1)$.

12 These relations, directly deriving from (8.38) and (8.39) are:

$$\begin{aligned} \partial_t\tilde{\rho}_n &= \big(\dot{x}_n + (\dot{x}_{n+1} - \dot{x}_n)u\big)\partial_x\rho_n + \partial_t\rho_n, \\ \partial_u\tilde{\rho}_n &= (x_{n+1} - x_n)\partial_x\rho_n \quad \text{and} \\ \partial_{uu}\tilde{\rho}_n &= (x_{n+1} - x_n)^2\partial_{xx}\rho_n. \end{aligned}$$

LINEAR PERTURBATION EQUATION Noting that, for the steady-state solution the variable u coincides with the variable $x - \overset{o}{x}_n(t)$, the Lagrangian form of the principal solution reads $\overset{o}{\tilde{\rho}}(u)$. To derive the linear perturbation equation, consider the perturbed state

$$\begin{cases} x_n(t) = n + \overset{o}{V}t + \varepsilon\delta x_n(t) + o(\varepsilon), \\ \tilde{\rho}_n(u,t) = \overset{o}{\tilde{\rho}}(u) + \varepsilon\delta\tilde{\rho}_n(u,t) + o(\varepsilon), \end{cases} \tag{8.41}$$

where ε is a small parameter, and let the perturbation,

$$\mathbf{q}_n(u,t) := \big(\delta x_n(t), \delta\tilde{\rho}_n(u,t)\big). \tag{8.42}$$

Inserting (8.41) in (8.40) and collecting terms of order ε yields a linear system for $\mathbf{q}_n$, which reads in abstract form

$$\mathcal{A}\big(\mathbf{q}_{n-1}, \mathbf{q}_n, \mathbf{q}_{n+1}, \mathbf{q}_{n+2}\big) = \mathcal{B}\big(\partial_t\mathbf{q}_n, \partial_t\mathbf{q}_{n+1}\big), \tag{8.43}$$

where and $\mathcal{A}$ and $\mathcal{B}$ denote linear operators involving u-derivatives of $\delta\tilde{\rho}_n$ with complete expressions given in Appendix D.

BLOCH-WAVE ANALYSIS Following the stability method of hydrodynamics (Chandrasekhar, 1981), an arbitrary perturbation $\mathbf{q}$ is written as a combination of normal modes and the stability of the system is obtained by checking the stability with respect to each of these modes. Using the linearity of (8.43) and noting that the operators $\mathcal{A}$ and $\mathcal{B}$ are time independent and independent of n (i.e., invariant under 1-terrace translation), the perturbations, solutions of (8.43), can be written as a combination of the normal modes given by the *Bloch waves*[13],

$$\begin{cases} \delta x_n(t) = \delta\hat{x}\exp(ikn + \lambda t), \\ \delta\tilde{\rho}_n(u,t) = \delta\hat{\rho}(u)\exp(ikn + \lambda t), \end{cases} \tag{8.44}$$

where $k \in (-\pi, \pi)$ is the wavenumber and λ the associated growth rate.

Inserting (8.44) in (8.43) yields for a given wavenumber k, a generalized eigenvalue problem of the form:

$$\hat{\mathcal{A}}_k\hat{\mathbf{q}} = \lambda\hat{\mathcal{B}}_k\hat{\mathbf{q}}, \tag{8.45}$$

where $\hat{\mathbf{q}}(u) := \big(\delta\hat{x}, \delta\hat{\rho}(u)\big)$ and $\hat{\mathcal{A}}_k$ and $\hat{\mathcal{B}}_k$ are linear operators deriving from $\mathcal{A}$ and $\mathcal{B}$ with complete expressions given in Appendix D.

13 The Bloch wave decomposition of $\tilde{\rho}_n$ (or Floquet mode decomposition in 1D) is based on the Bloch's theorem and the resort to that theorem can be seen more explicitly by introducing the global variable $v = u + n \in \mathbb{R}$ where $u \in (0,1)$ is the local variable and $n \in \mathbb{Z}$. Letting $\delta\tilde{\rho}(v,t)$ defined on $\mathbb{R}\times\mathbb{R}^+$ by $\delta\tilde{\rho}(v,t) := \delta\tilde{\rho}_n(v-n,t)$ when $v \in (n, n+1)$, the operators $\mathcal{A}$ and $\mathcal{B}$ rewritten as acting on $(\delta x_n, \delta\tilde{\rho})$ satisfy $\mathcal{A}[n+1, v+1, t] = \mathcal{A}[n, v, t]$ and a similar relation for $\mathcal{B}$. This makes explicit the space periodicity of the differential operators allowing to write the solutions of (8.43) as a combinations of Bloch waves reading for $\delta\tilde{\rho}$: $\delta\tilde{\rho}(v,t) = \delta\check{\rho}(v)\exp(ikv + \lambda t)$ where $\delta\check{\rho}$ is a 1-periodic function. $\delta\hat{\rho}$ is related to $\check{\rho}$ by $\delta\hat{\rho}(u) = \delta\check{\rho}(u)\exp(iku)$ on $(0,1)$.

The numerical resolution of (8.45) for a given k provides a set of eigenvalues (whose number depends on the numerical mesh resolution). The eigenvalue corresponding to the most unstable mode is the one with largest real part. Taking for a set of values of k in $(0,\pi)$ the real part of the most critical eigenvalue $\lambda(k)$, we can plot numerically the dispersion relation $\mathrm{Re}\big(\lambda(k)\big)$, which, unlike the analytical dispersion relation of Section 8.2 accounts for the dynamics effect.[14]

In the explicit expressions of $\hat{\mathcal{A}}_k$ and $\hat{\mathcal{B}}_k$ of Appendix D, we show in red the terms coming from the dynamics terms in (8.36). Among these terms, we can see that, in addition to terms proportional to $\overset{o}{V}$, which are of the order of the Péclet number $\mathcal{P}$ [15], there are also terms of order 0 (with respect to the Péclet number). Hence, even for $\mathcal{P}\to 0$, this makes the generalized eigenvalue problem with dynamics terms different from the corresponding problem where the dynamics terms have been neglected at the beginning. Consequently, the stability results obtained from the quasistatic approximation are not expected to be valid even in the regime of small Péclet number. This supports our discussion of Section 8.1.2 where we were explaining that the smallness of the dynamics terms does not necessarily allows to neglect them when analyzing the stability.

8.3.3 *Numerical method*

The eigenvalue problem (8.45) involves two operators $\hat{\mathcal{A}}_k$ and $\hat{\mathcal{B}}_k$ acting on the scalar variable $\delta\hat{x}$ and on the function $\delta\hat{\rho}:\ (0,1)\to\mathbb{C}$ and its derivatives. This problem is solved numerically, using the Chebyshev collocation method (Peyret, 2002), a spectral method adapted to nonperidic problems such as (8.45).

Consider a complex valued function f defined on $(0,1)$ and let its Chebychev series approximation f_N truncated at order N,

$$f_N := \sum_{n=0}^{N} \check{f}_n \check{T}_n, \tag{8.46}$$

where $\check{f}_n$ are the Chebychev coefficients and $\check{T}_n$ denote the Chebyshev polynomials[16] represented on Figure 8.4 and defined on (0,1) by

$$\check{T}_0(u) = 1, \quad \check{T}_1(u) = 2u-1, \tag{8.48}$$

14 Note that as the operators $\hat{\mathcal{A}}_{-k}$ and $\hat{\mathcal{B}}_{-k}$ are the complex conjugates of the $\hat{\mathcal{A}}_k$ and $\hat{\mathcal{B}}_k$, respectively, the eigenvalues associated to the wavelength $-k$ are complex conjugate to those of wavelength k. As a result, the set of eigenvalues of wavelength $-k$ and k have the same real part, which allows us to reduce the computation of the growth rate $mathrmRe\big(\lambda(k)\big)$ on $k\in(0,\pi)$, domain where the dispersion relation are displayed.

15 Indeed under deposition $\mathcal{P}=\overline{F}\Theta=\overset{o}{V}$ while under evaporation $\mathcal{P}\approx\overset{o}{V}$ because $\mathcal{P}=\overline{v}\Theta$ and $\overset{o}{V}\approx\overline{v}\Theta+o(\overline{v})$

16 Note that the Chebychev polynomials $\check{T}_n$ defined on $(0,1)$ that we used here are obtained by rescaling the traditional Chebyshev polynomials T_n defined on $(-1,1)$ (see e.g., Peyret, 2002) with

$$\check{T}_n(u) = T_n\left(2u-1\right), \text{ for } u\in(0,1). \tag{8.47}$$

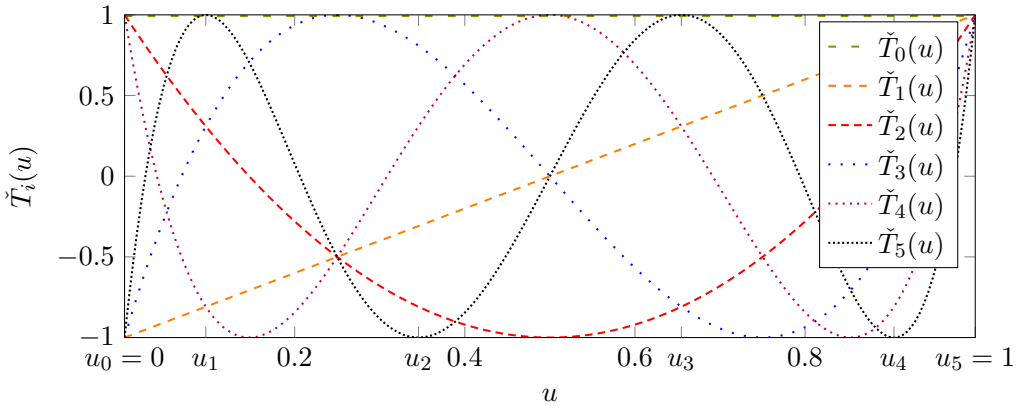

Figure 8.4: Representation of the first six Chebyshev polynomials $\check{T}_n$ along with the six Gauss-Lobatto points for $N = 5$.

and the recurrence relationship

$$\check{T}_n - (4u - 2)\check{T}_{n-1} + \check{T}_{n-2} = 0 \quad \text{for } n \leq 2. \tag{8.49}$$

To compute the Chebychev coefficients $\check{f}_n$, two main methods are available. First, the *tau*-method, whereby the coefficients $\check{f}_n$ are obtained by projection of f on the basis $(\check{T}_n)_{0\leq n\leq N}$,

$$\check{f}_n = \int_0^1 \frac{f(u)\check{T}_n(x)}{\sqrt{u(1-u)}}\,\mathrm{d}u. \tag{8.50}$$

Second, the *collocation* method where the coefficients $\check{f}_n$ are obtained from the $N+1$ equation deriving from the interpolation of f on the Gauss-Lobatto points $(u_0, \ldots, u_N)$,

$$f_N(u_n) = \sum_{j=0}^{N} \check{f}_j \check{T}_j(u_n) = f(u_n), \tag{8.51}$$

where the Gauss-Lobatto mesh is composed of the $N+1$ points defined by

$$u_n = \frac{1}{2}\left(\cos\left(\frac{\pi(N-n)}{N}\right) + 1\right), \text{ for } n = 0 \ldots N, \tag{8.52}$$

illustrated on Figure 8.4 for $N = 5$. Note that the points are not uniformly distributed on $(0, 1)$ but denser close to the edges.

These two methods, although leading to different discretizations, have the same rate of convergence in the approximation (Peyret, 2002). In the present case as (8.45) involves another function (the steady-state solution $\overset{o}{\rho}$), its evaluation on the points u_i is straightforward while its projection on the functions T_i requires more work. Hence, we use the collocation method.

With the Chebychev approximation, the first and second derivatives of f are approximated by

$$f'_N = \sum_{n=0}^{N} \check{f}_n \check{T}'_n \quad \text{and} \quad f''_N = \sum_{n=0}^{N} \check{f}_n \check{T}''_n. \tag{8.53}$$

In addition, using the collocation technique, the values of f'_N and f''_N can be obtained without resorting to the $\check{f}_n$. Indeed it is possible to define a differentiation matrix $\check{\mathbf{D}}$, that directly relates the values, on the Gauss-Lobatto points, of the function and its first derivative through[17]

$$f'_N(u_n) = \check{D}_{n,j} f_N(u_j). \tag{8.54}$$

Note that, with the Chebyshev method, the derivative at one point does not only depend on the neighboring points but on all the points of the domain. As a result, $\check{\mathbf{D}}$ is a full matrix. Similarly, the second-order derivative is approximated using $(\check{\mathbf{D}})^2$.

To derive the discrete form of (8.45), the operators $\hat{\mathcal{A}}_k$ and $\hat{\mathcal{B}}_k$ are decomposed as a sum of operators acting separately on $\delta\hat{x}$, $\delta\hat{\rho}$ and its derivatives:

$$\begin{aligned}\hat{\mathcal{A}}_k(\delta\hat{x}, \delta\hat{\rho}) &= \hat{\mathcal{A}}^1_k \delta\hat{x} + \hat{\mathcal{A}}^2_k \delta\hat{\rho} + \hat{\mathcal{A}}^3_k \delta\hat{\rho}' + \hat{\mathcal{A}}^4_k \delta\hat{\rho}'' \\ \hat{\mathcal{B}}_k(\delta\hat{x}, \delta\hat{\rho}) &= \hat{\mathcal{B}}^1_k \delta\hat{x} + \hat{\mathcal{B}}^2_k \delta\hat{\rho},\end{aligned} \tag{8.55}$$

where the full expressions of the $\hat{\mathcal{A}}^p_k$, $p = 1 \dots 4$ and $\hat{\mathcal{B}}^m_k$, $m = 1, 2$ are given in Appendix D.

Using the decomposition (8.55), the operators $\hat{\mathcal{A}}_k$ and $\hat{\mathcal{B}}_k$ are approximated using the $(N+2) \times (N+2)$ matrices $\check{\mathbf{A}}^k$ and $\check{\mathbf{B}}^k$ written as

$$\begin{aligned}\check{\mathbf{A}}_k \check{\mathbf{q}} &= \check{\mathbf{A}}^1_k (\check{\mathbf{D}})^2 \delta\check{\boldsymbol{\rho}} + \check{\mathbf{A}}^2_k \check{\mathbf{D}} \delta\check{\boldsymbol{\rho}} + \check{\mathbf{A}}^3_k \delta\check{\boldsymbol{\rho}} + \check{\mathbf{A}}^4_k \delta\hat{x}, \\ \check{\mathbf{B}}_k \check{\mathbf{q}} &= \check{\mathbf{B}}^1_k \delta\check{\boldsymbol{\rho}} + \check{\mathbf{B}}^2_k \delta\hat{x},\end{aligned} \tag{8.56}$$

where $\delta\check{\boldsymbol{\rho}} = \big(\delta\hat{\rho}(u_0), \dots, \delta\hat{\rho}(u_N)\big)$, $\check{\mathbf{q}} = (\delta\hat{x}, \delta\check{\boldsymbol{\rho}})$ and $\check{\mathbf{A}}^p_k$, $p = 1 \dots 4$ and $\check{\mathbf{B}}^m_k$, $m = 1, 2$ are the discretization of the corresponding operators $\hat{\mathcal{A}}^p_k$ and $\hat{\mathcal{B}}^m_k$ on the Gauss-Lobatto mesh $\{u_i,\, 0 \le i \le N\}$.

This allows to write (8.45) as a $(N+2) \times (N+2)$ generalized eigenvalue problem: For a given $k \in (0, \pi)$, find $(\lambda, \check{\mathbf{q}}) \in \mathbb{C} \times \mathbb{C}^{N+2}$ with $\check{\mathbf{q}} \neq \mathbf{0}$ such that

$$\check{\mathbf{A}}_k \check{\mathbf{q}} = \lambda \check{\mathbf{B}}_k \check{\mathbf{q}}. \tag{8.57}$$

After solving (8.57) numerically, we consider the leading eigenvalue λ (the eigenvalue with largest real part), which corresponds to the most critical growth rate.

Note that as $\check{\mathbf{B}}_k$ is not invertible, (8.45) has less than $N+2$ solutions. Indeed as can be seen from (D.5) in Appendix D, the last three rows of $\check{\mathbf{B}}_k$ being linearly dependent, its kernel is of dimension 2. As a result, and noting that $\check{\mathbf{A}}_k$ is invertible, (8.57) has only N solutions.

17 For being accurate, note that the coefficients of the $\check{\mathbf{D}}$ are obtained by adapting the differentiation matrix $\mathbf{D}$ found in Peyret (2002)—which corresponds to Chebychev polynomials defined on $(-1, 1)$—to the Chebychev method reformulated on $(0, 1)$.

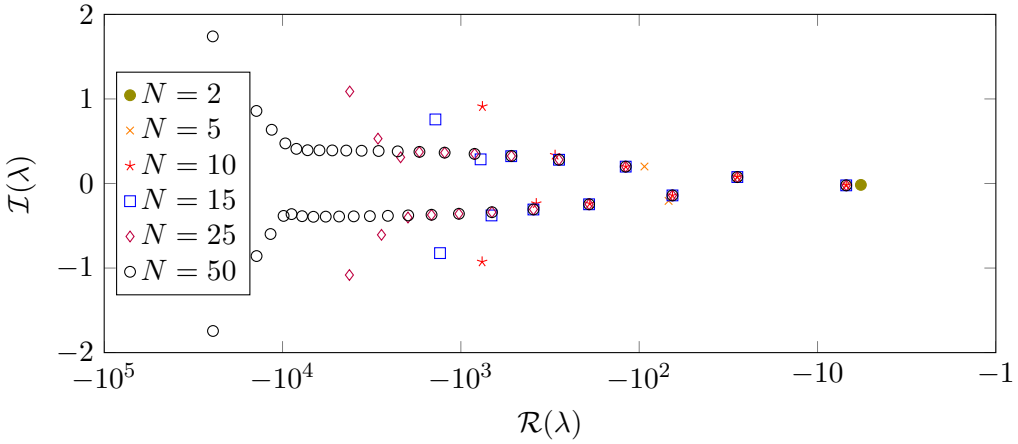

Figure 8.5: Evolution of the eigenvalue spectrum of (8.57) with the number N of discretization points for the set of parameters $\overline{F} = 10^{-2}$, $\overline{v} = 0$, $S = 1$, $\overline{\kappa} = 10$, $\overline{\kappa}_p = 0$, $\Theta = 0.01$, $\overline{\alpha} = 0$, $\overline{\beta} = 0$ and $k = \pi/2$. The logarithmic scale used on the abscissa is not wide enough to include the leading eigenvalue $-1.1271 \times 10^{-7} + 1.0000 \times 10^{-4} i$.

CONVERGENCE We evaluate the convergence of the numerical method by considering the leading eigenvalue, and determine a satisfactory number of discretization points $N + 1$.

For a given set of parameters ($\overline{F} = 10^{-2}$, $\overline{v} = 0$, $S = 1$, $\overline{\kappa} = 10$, $\overline{\kappa}_p = 0$, $\Theta = 0.01$, $\overline{\alpha} = 0$, $\overline{\beta} = 0$ and $k = \pi/2$), the leading eigenvalue with $N = 50$ is $-1.1271 \times 10^{-7} + 1.0000 \times 10^{-4} i$. Because of the spectral convergence properties of the Chebyshev method (Peyret, 2002), full convergence with five significant digits of the leading eigenvalue is achieved with N as low as 5. This fast convergence has been verified for various set of parameters and we select the value $N = 10$ for the subsequent analysis.

A superposition of the eigenvalue spectra for different values of N is shown in Figure 8.5. On top of the leading eigenvalue previously discussed, we observe the progressive formation of two branches of constant imaginary part in the stable spectral plane. Note that, although these branches are not of particular interest for the linear stability analysis, as expected for a consistent numerical method they get more and more resolved as N increases.

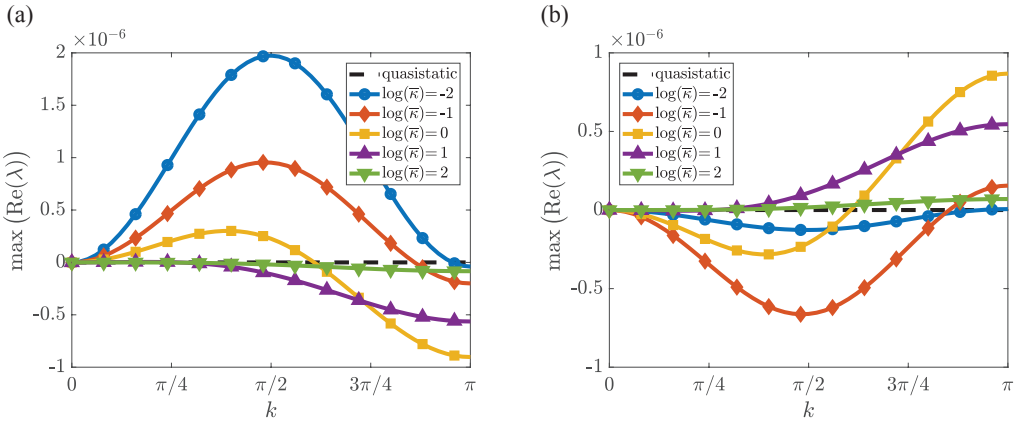

Figure 8.6: Dispersion curves corresponding to the dynamics effect only (the other mechanisms are disabled, $S = 1$, $\overline{\alpha} = 0$, $\overline{\beta} = 0$, $\chi = 0$, $\Theta = 0.01$). (a) Deposition ($\overline{F} = 0.01$, $\overline{\nu} = 0$). (b) Evaporation ($\overline{\nu} = 0.01$, $\overline{F} = 0$).

8.3.4 *Results*

8.3.4.1 *Influence of the dynamics effect under deposition and evaporation*

In line with the analysis of Section 8.2.3, we aim at understanding the influence on stability of the *dynamics effect* as a stabilizing or destabilizing mechanism. To this end, all other mechanisms are disabled ($S = 1$, $\overline{\alpha} = 0$, $\overline{\beta} = 0$, $\chi = 0$) and the dispersion curves, resulting from the sole effect of dynamics are studied as function of the remaining parameters: $\overline{F}$, $\overline{\nu}$, Θ, $\overline{\kappa}$ and $\overline{\kappa}_p$.

THE DETERMINANT PARAMETER $\overline{\kappa}$ First, the case without permeability ($\overline{\kappa}_p = 0$) is considered and it appears, as shown on Figure 8.6 that $\overline{\kappa}$ is the parameter that determines the influence on stability of the dynamics effect.

Qualitatively, the dynamics terms have, under deposition, a destabilizing effect for low values of $\overline{\kappa}$ ($\overline{\kappa} \leq 1$, tend to the attachment/detachment limited regime[18]) and a stabilizing effect for high value of $\overline{\kappa}$ ($\overline{\kappa} > 1$, tend to the diffusion limited regime). The effect of $\overline{\kappa}$ is reversed for evaporation where low values of $\overline{\kappa}$ ($\overline{\kappa} \ll 1$) correspond to a stabilizing effect while intermediate and high values of $\overline{\kappa}$ ($\overline{\kappa} \gtrsim 1$) are destabilizing regimes.

These results, summarized in Table 8.4, complete Table 8.1 and the diagram Figure 8.1 is now modified to include the dynamics effect as shown on Figure 8.7.

18 Recall from Section 7.2.3 that the notion of attachment/detachment limited regime and diffusion limited regime refer to the two kinetic processes: a/d at steps and diffusion on terraces. $\overline{\kappa} := \kappa_- L_0/D$ can be seen as the ratio of a characteristic step a/d velocity κ_- to a characteristic diffusion velocity D/L_0. Then, $\overline{\kappa} \ll 1$ corresponds to situations where it is the a/d which is the limiting kinetic process and $\overline{\kappa} \gg 1$ is associated to cases where it is the diffusion which is limiting.

Table 8.4: Effect on the stability against step bunching of the dynamics terms. $\mathcal{S}$: Stabilizing; $\mathcal{D}$: Destabilizing. This complete Table 8.1.

	Dynamic effect	
	$\overline{\kappa} \ll 1$	$\overline{\kappa} \gg 1$
Deposition	$\mathcal{D}$	$\mathcal{S}$
Evaporation	$\mathcal{S}$	$\mathcal{D}$

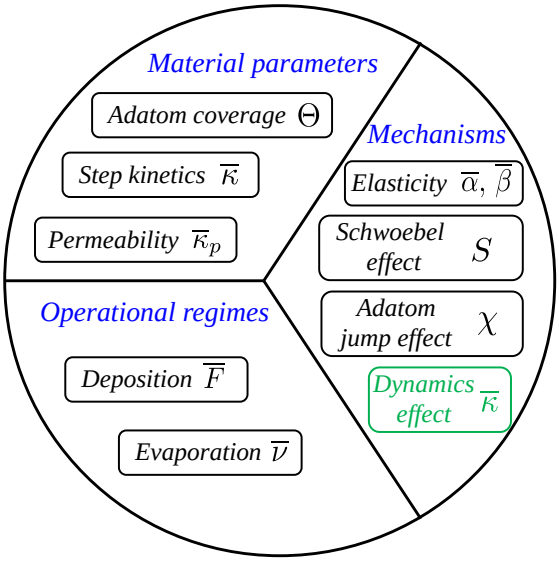

Figure 8.7: Modification of the diagram Figure 8.1, which shows the positioning of the dynamics effect as a stabilizing/destabilizing mechanism.

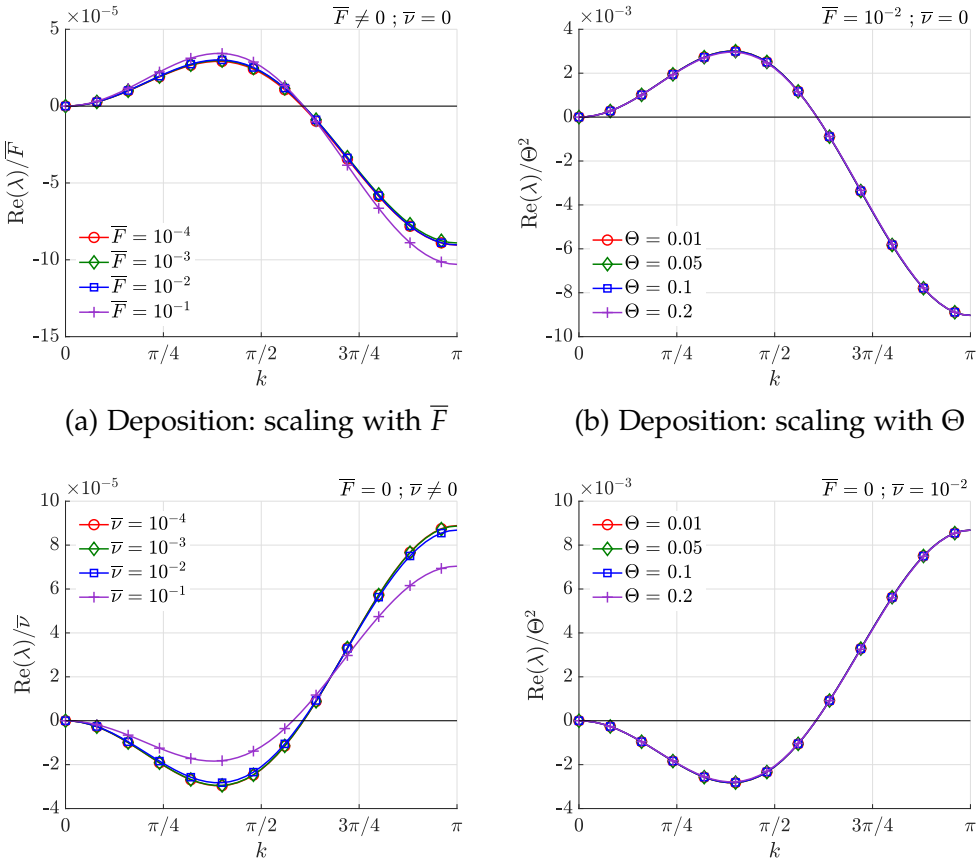

(a) Deposition: scaling with $\overline{F}$

(b) Deposition: scaling with Θ

(c) Evaporation: scaling with $\overline{\nu}$

(d) Evaporation: scaling with Θ

Figure 8.8: Scaling of the dispersion curves with $\overline{F}$, $\overline{\nu}$ and Θ ($\overline{\kappa} = 1$, $S = 1$, $\overline{\alpha} = 0$, $\overline{\beta} = 0$, $\chi = 0$). Deposition ($\overline{\nu} = 0$) with $\Theta = 0.01$ for (a) and $\overline{F} = 10^{-2}$ for (b). Evaporation ($\overline{F} = 0$) with $\Theta = 0.01$ for (c) and $\overline{\nu} = 10^{-2}$ for (d).

8.3.4.2 *Influence of the operational and material parameters*

A parametric study with $\overline{F}$, $\overline{\nu}$ and Θ of the dispersion curves associated to the dynamics effect reveals that these parameters do not affect the shape of the dispersion curve—thereby do not change the effect on stability—but simply act as scaling factors for $\mathrm{Re}(\lambda)$. As can be seen on Figure 8.8, showing the dispersion curves for different values of $\overline{F}$ and Θ—under deposition, (a) and (b)—and of $\overline{\nu}$ and Θ—under evaporation, (c) and (d)—the growth rate scales linearly with the deposition/evaporation rates ($\mathrm{Re}(\lambda) \propto \overline{F}$ and $\mathrm{Re}(\lambda) \propto \nu$) while it scales quadratically with the adatom coverage ($\mathrm{Re}(\lambda) \propto \Theta^2$). Putting this in perspective with the scaling of the other mechanisms (see Table 8.2), the linear dependence with the deposition/evaporation rates associates the dynamics effect to the group of kinetic mechanisms (like Schwoebel effect, adatom jump effect). Furthermore, the Θ^2 dependence of the growth rate of the dynamics effect is common with the adatom jump effect (by contrast with a linear dependence on Θ for the other mechanisms), and indicates that these

Table 8.5: Scaling of the dynamics effect contribution to the growth rate with the control and material parameters $\overline{F}$, $\overline{v}$ and Θ. $\mathrm{Re}(\lambda) \propto \overline{F}^a \Theta^b$ under deposition and $\mathrm{Re}(\lambda) \propto \overline{v}^a \Theta^b$ under evaporation. This completes Table 8.2.

	Dynamic effect
a (for $\overline{F}$, $\overline{v}$)	1
b (for Θ)	2

two mechanisms are expected to be particularly prominent at high adatom coverage.

In sum, the scalings of the dynamics contribution to stability with $\overline{F}$, $\overline{v}$ and Θ are summarized in Table 8.5, hence completing the scaling of the other mechanisms of Table 8.2.

8.3.4.3 *Inconsistencies of the quasistatic approximation*

In this section, we analyze the differences between the stability results derived under the quasistatic framework and with dynamics terms and discuss the validity of the quasistatic approximation in the regime (8.1) where it is classically invoked.

We examine successively the modifications caused by the dynamics effect on the stability results of the elastic configurational force, the Schwoebel effect and the adatom jump effect and conclude to the inconsistency of the quasistatic approximation. Recall that the claim of the quasistatic approximation is that the dynamics terms (see Section 8.1.1) can be neglected for computing the step stability in the regimes (8.1).

To quantify the changes due to the dynamics effect, we define the normalized distance d ($0 \leq d \leq 2$) between the quasistatic and the dynamic dispersion curves by

$$d = \frac{\|\mathrm{Re}(\lambda_D) - \mathrm{Re}(\lambda_{QS})\|}{\max\left(\|\mathrm{Re}(\lambda_D)\|, \|\mathrm{Re}(\lambda_{QS})\|\right)}, \tag{8.58}$$

where λ_D and λ_{QS} are the complex growth rates derived with dynamics terms and under the quasistatic approximation, respectively, and $\|\mathrm{Re}(\lambda)\|$ is the norm of $k \mapsto \mathrm{Re}(\lambda[k])$ defined by

$$\|\mathrm{Re}(\lambda)\| = \max_{k \in (0,\pi)} |\mathrm{Re}(\lambda[k])|. \tag{8.59}$$

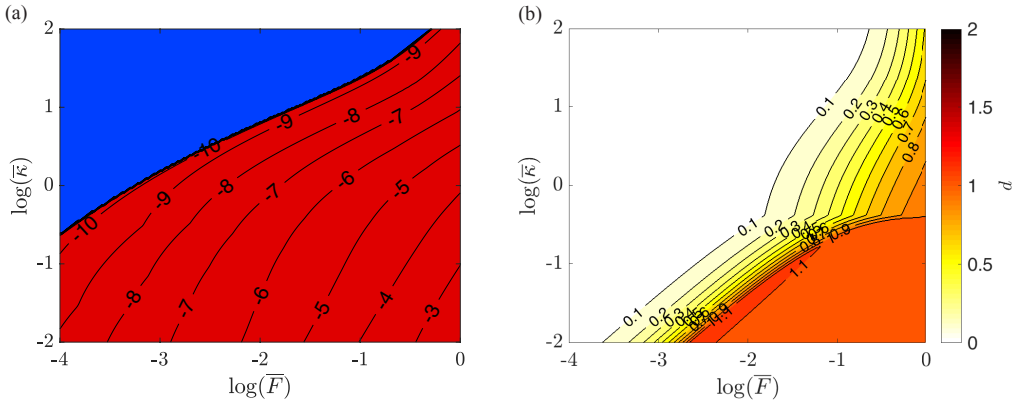

Figure 8.9: Interplay, under deposition, of the dynamics effect with dipole-dipole elastic interactions. Parameters are $\overline{\nu} = 0$, $\Theta = 0.01$, $\overline{\alpha} = 10^{-4}$, $\overline{\beta} = 0$, $S = 1$, $\overline{\kappa}_p = 0$, $\chi = 0$. (a) Stability diagram: blue and red domains correspond to the stable ($\max_{k\in(0,\pi)} \mathrm{Re}(\lambda) < 0$) and unstable ($\max_{k\in(0,\pi)} \mathrm{Re}(\lambda) > 0$) regions, respectively. In the unstable domain, isolines display $\max_{k\in(0,\pi)} \log\left(\mathrm{Re}(\lambda)\right)$, indicating the magnitude of the most critical growth rate. Recall for comparison that the stability diagram corresponding to the classical model (only elastic interaction, no dynamics terms) is stable (blue domain) everywhere. (b) Distance d between dynamics and quasistatic results are defined by (8.58).

DIPOLE-DIPOLE ELASTICITY Consider first the effect of the dynamics terms on steps interacting through dipole-dipole elastic interactions only (i.e. $\overline{\alpha} \neq 0$, $\overline{\beta} = 0$, $S = 1$, $\overline{\kappa}_p = 0$, $\chi = 0$). In the quasistatic case, the discussion of Section 8.2.3 shows that the step propagation is stable both under deposition and evaporation for all parameter values. Figure 8.9 (a) shows the stability diagrams, under deposition, in $(\overline{F}, \overline{\kappa})$ space, when including the dynamics terms. Negative (positive) domains for the most critical growth rate ($\max_{k\in(0,\pi)} \mathrm{Re}(\lambda(k))$) are shown in blue (red) and correspond to stable (unstable) step dynamics against bunching.

With $\overline{\alpha} = 10^{-4}$, the order of magnitude of interaction strength for the typical terrace width of 20 nm, a region appears where the step dynamics is unstable. Note that this destabilizing effect is observed although Θ has the low value of 0.01. A first manifestation of the breakdown of the quasistatic approximation is that, although we are in the regime (8.1), the dynamics terms have a non-negligible effect on stability. Nevertheless, as seen on Figure 8.9 (b), the effect of the dynamics terms vanishes as $\overline{F} \to 0$ and we will see that it is particular to the interplay of the dynamics effect with elasticity. Indeed, as seen in Sections 8.2.3.3 and 8.3.4.2 (summarized in Table 8.2 and Table 8.5) the stabilizing effect of the elastic interactions is independent of $\overline{F}$ (energetic effect) while the contribution of the dynamics effect is proportional to $\overline{F}$ (kinetic effect) and thereby weaken as the deposition/evaporation rate decreases.

Recall that high Θ promotes the effect of dynamics on stability

For evaporation, for the adatom coverage $\Theta = 0.01$, the dynamics effect is too weak to inverse the stability and the step dynamics remains stable everywhere.

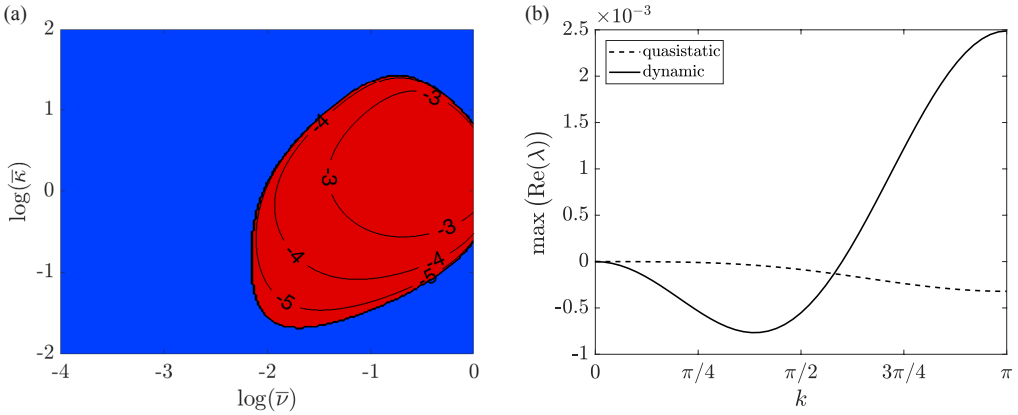

Figure 8.10: Interplay, under evaporation, of the dynamics effect with dipole-dipole elastic interactions. Parameters are $\overline{F} = 0$, $\Theta = 0.2$, $\overline{\alpha} = 10^{-4}$, $\overline{\beta} = 0$, $S = 1$, $\overline{\kappa}_p = 0$, $\chi = 0$. (a) Stability diagram and (b) dispersion curve at the point $(\overline{\nu}, \overline{\kappa}) = (0.1, 1)$. [see color legend on Figure 8.9]

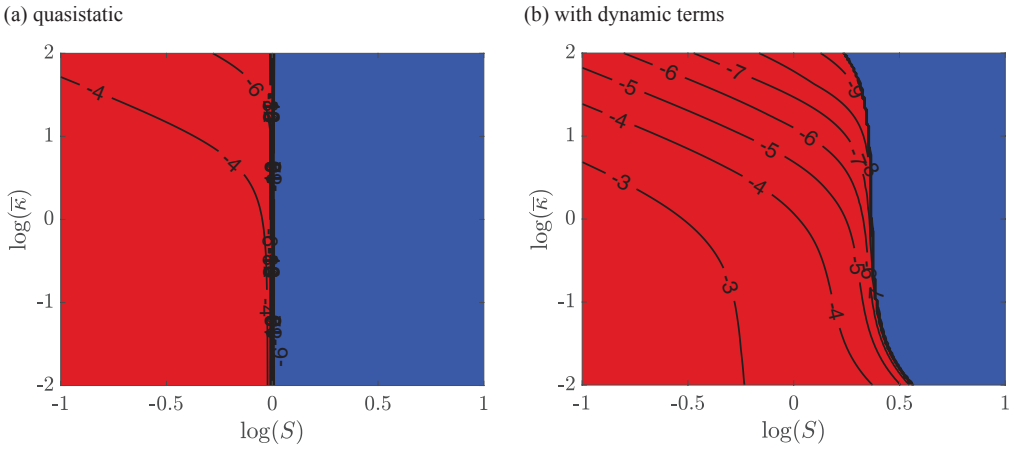

Figure 8.11: Stability diagrams for the Schwoebel effect under deposition. (a) under the quasistatic approximation and (b) with dynamics terms. $\overline{F} = 10^{-2}$, $\Theta = 0.2$, $\overline{\kappa}_p = 0$, $\overline{\alpha} = 0$, $\overline{\beta} = 0$, $\chi = 0$. [see color legend on Figure 8.9]

However for higher values of Θ such as $\Theta = 0.2$, an unstable region in the domain of intermediate values of $\overline{\kappa}$ appears as shown in Figure 8.10.

SCHWOEBEL EFFECT Second, consider the interplay of the dynamics terms with the Schwoebel effect (other mechanisms disabled : $\overline{\alpha} = 0$, $\overline{\beta} = 0$, $\chi = 0$, $\overline{\kappa}_p = 0$). As shown in Section 8.2.3, under deposition, the quasistatic approximation predicts a stable growth for $S > 1$ and unstable one for $S < 1$. The stability diagrams under the quasistatic approximation and with dynamics effect are compared in Figure 8.11.

While it appears that the dynamics terms extend the unstable regime beyond the quasistatic limit $S = 1$, looking, on Figure 8.12, at the dispersion curves at points a, $(\overline{\kappa}, S)_a = (10^1, 10^{0.25})$ and b, $(\overline{\kappa}, S)_b = (10^{-1}, 10^{0.25})$ allows to better

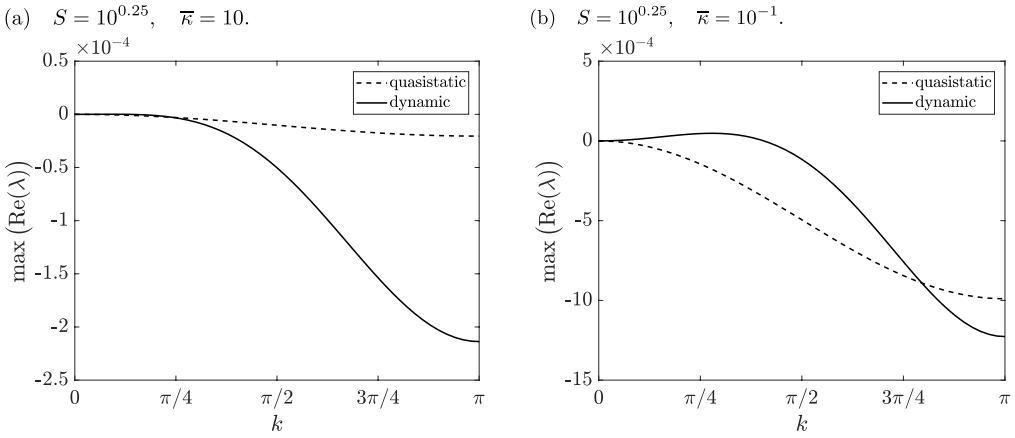

Figure 8.12: Dispersion curves associated to Figure 8.11 at points (a) $(\overline{\kappa}, S)_a = (10^1, 10^{0.25})$ and (b) $(\overline{\kappa}, S)_b = (10^{-1}, 10^{0.25})$.

understand the stability diagram. Figure 8.12 (a) shows that at point a most of the wavelengths are stabilized by the dynamics terms while the long wavelength perturbations are unstable but with a negligible small growth rate. Physically, this instability might not develop in the typical time scale of the deposition. By contrast at point b (see Figure 8.12 (b)) a wider range of wavelengths is unstable with a growth rate several orders of magnitude higher than at point a. This analysis is consistent with the discussion of Section 8.3.4.1 where it has been seen that under deposition the dynamics terms are stabilizing (destabilizing) for high (low) values of $\overline{\kappa}$.

The changes in the stability diagram induced by the dynamics terms, as observed on Figure 8.11, as well as on the more informative dispersion curves of Figure 8.12, illustrate again that there are cases where the stability is inverted by the dynamics terms (in that case in the region $0 < S < 10^{0.5}$ and $\overline{\kappa} > 1$) even though the deposition rate ($\overline{F} = 10^{-2}$) and adatom coverage ($\Theta = 0.2$) are such that the classical condition (8.1) of the quasistatic approximation is satisfied. In addition, the dependence on $\overline{F}$ of the stability limit in S, presented on Figure 8.13, shows that as $\overline{F} \to 0$ the stability limit does not converge to the quasistatic value $S = 1$, whereby suggesting that even as $\overline{F} \to 0$, the effect of the dynamics terms does not vanish. As shown on Figure 8.14 (a), the dynamics terms have also a prominent effect under evaporation where they destabilize the step dynamics for $S < 1$ in the region of high $\overline{\kappa}$. Furthermore, Figure 8.14 (b), where $\overline{\kappa} = 10$, shows that, like under deposition, this effect does not vanishes as $\overline{\nu} \to 0$.

To clarify how the dynamics effect evolves with decreasing $\overline{F}$ and Θ, Figure 8.15 shows the diagram of d for different values of these parameters. Figure 8.15 (a)-(c) reveals that for the high value $\Theta = 0.2$, the large regions in the space $(S, \overline{\kappa})$ where the dispersion curve is significantly modified by the dynamics terms (typically regions where $d > 0.2$) are not reduced as $\overline{F}$ decreases. By contrast, one can see on Figure 8.15 (d)-(f) that d vanishes almost everywhere as Θ decreases down to 0.01. This is consistent with the fact that

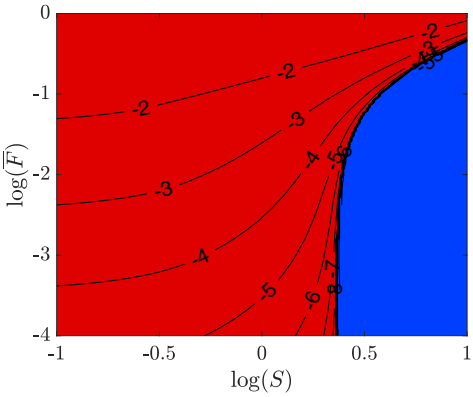

Figure 8.13: Stability diagram under deposition of the Schwoebel effect with dynamics terms for $\Theta = 0.2$, $\overline{\kappa} = 0.1$, $\overline{\kappa}_p = 0$, $\overline{\alpha} = 0$, $\overline{\beta} = 0$, $\chi = 0$. [see color legend on Figure 8.9]

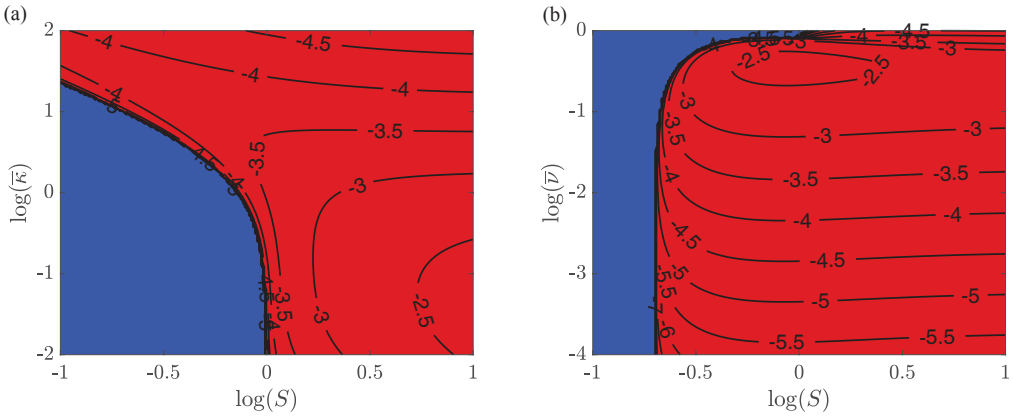

Figure 8.14: Stability diagram under evaporation of the Schwoebel effect with dynamics terms under evaporation for $\Theta = 0.2$, $\overline{\kappa}_p = 0$, $\overline{\alpha} = 0$, $\overline{\beta} = 0$, $\chi = 0$. (a) $\overline{\nu} = 10^{-2}$, (b) $\overline{\kappa} = 10$. [see color legend on Figure 8.9]

these dispersion curves result from the interplay between the Schwoebel effect and dynamics effect which, as discussed in Section 8.2.3 and Section 8.3.4.2, both have growth rate proportional to $\overline{F}$ and a Θ dependence of the growth rate, linear for the Schwoebel effect and quadratic for the dynamics effect (cf. Table 8.2 and Table 8.5). This discussion on the classical Schwoebel effect establishes that the traditional claim that the dynamics terms can be neglected when computing the step stability in the regime (8.1) ($\Theta\overline{F} \ll 1$) is not valid. Indeed, while the cases of Figure 8.15 (a)-(c) all lie well in the regime (8.1), clearly the measure d of the importance of the dynamics terms on stability is not negligible. In the present case of the interplay between Schwoebel and dynamics effects, the stability dispersion curves essentially converge to the quasistatic one as Θ vanishes. However, as the next example shows it, the criterion $\Theta \to 0$ is not a universal condition for neglecting the dynamics effect.

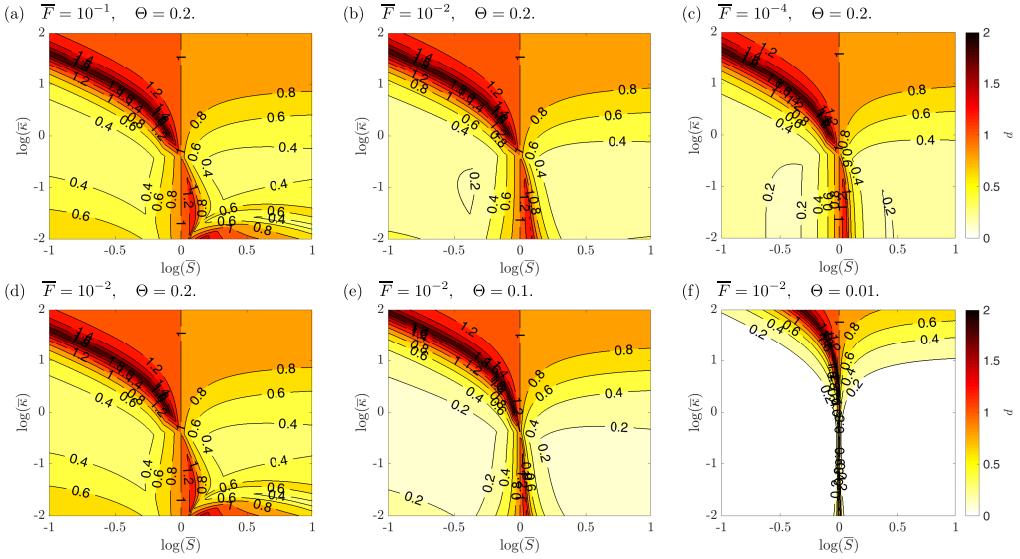

Figure 8.15: Diagrams of the distance d for the effect of the dynamics terms on the Schwoebel effect under deposition. $\overline{\kappa}_p = 0$, $\overline{\alpha} = 0$, $\overline{\beta} = 0$, $\chi = 0$.

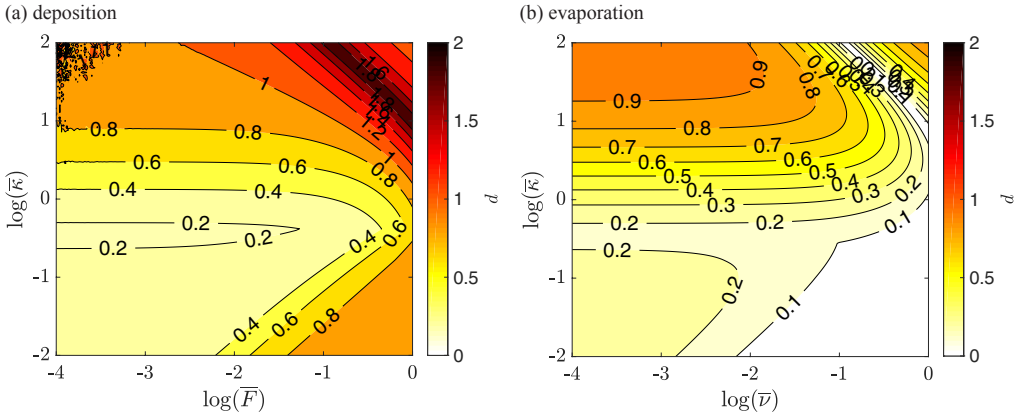

Figure 8.16: Diagrams of the distance d for the effect of dynamics terms on the adatom jump effect. $S = 1$, $\Theta = 0.01$, $\overline{\kappa}_p = 0$, $\overline{\alpha} = 0$, $\overline{\beta} = 0$, $\chi = 1$. (a) deposition; (b) evaporation.

ADATOM JUMP EFFECT The adatom jump effect, which is for the quasistatic approximation, destabilizing (stabilizing) under deposition (evaporation)—see Section 8.2.3—is another example where the modification brought by the dynamics terms does not vanish as $\overline{F}$, $\overline{\nu} \to 0$ but in addition is independent of Θ. This is easily understood since, as these two mechanisms both have a growth rate linear in $\overline{F}$ and quadratic in Θ, none of them become predominant as these parameters vary. Figure 8.16, showing the distance d in the space $(\overline{F}, \overline{\kappa})$ for deposition (a) and evaporation (b), illustrates that for both cases the effect of the dynamics terms is determinant in the region of high $\overline{\kappa}$ for all values of $\overline{F}$. The diagrams of Figure 8.16 which correspond to $\Theta = 0.01$ are unchanged when varying Θ up to 0.2.

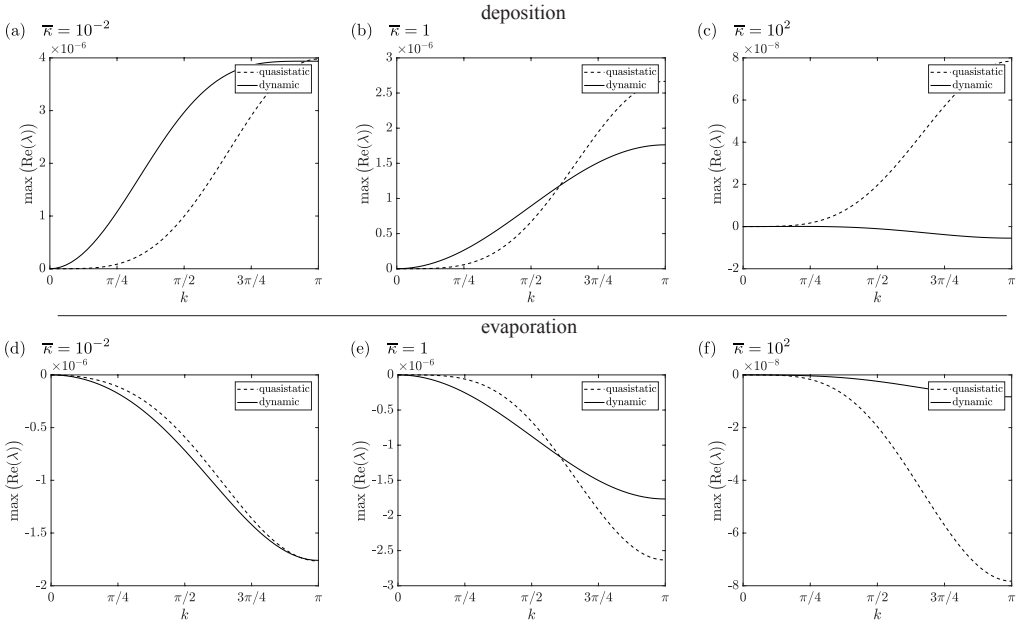

Figure 8.17: Dynamics effects on the dispersion curve of the adatom jump effect with parameters of Figure 8.16. (a)-(c) are deposition cases and correspond to diagram Figure 8.16 (a). (d)-(f) are evaporation cases and correspond to diagram Figure 8.16 (b).

To understand the effect of dynamics on the stability of the adatom jump effect, the change in dispersion curve is reported for three values of $\overline{\kappa}$ for the deposition rate $\overline{F} = 10^{-2}$ on Figure 8.17 (a)-(c) and for the evaporation rate $\overline{\nu} = 10^{-2}$ on Figure 8.17 (d)-(f). This reveals the stabilizing (destabilizing) influence of the dynamics at high values of $\overline{\kappa}$ for deposition (evaporation) is, under deposition, strong enough to reverse the stability and make the system stable, but too weak under evaporation to make the system unstable.

CONCLUSION ON THE QUASISTATIC APPROXIMATION The discussion of the interplay of the dynamics effect with the three fundamental mechanisms of Section 8.2.3 shows that well in the regime (8.1), where the quasistatic approximation has been classically used, and even in the limits of very low $\overline{F}$, Θ—for deposition—and $\overline{\nu}$, Θ—for evaporation—the effect of the dynamics terms are not necessarily negligible. Nevertheless, when combined with some particular mechanisms, the dynamics effect might become small as $\Theta \to 0$ (dynamics effect with the Schwoebel effect, cf. Figure 8.15) or as $\overline{F}$, $\overline{\nu} \to 0$ (dynamics effect with elasticity, cf. Figure 8.9), but this is not general. In echo to the *a priori* analysis of the weaknesses of the quasistatic approximation in Section 8.1.2, this comparison of the stability results with and without this approximation confirms that the classical condition (8.1) ($\overline{F}\Theta \ll 1$ under deposition and $\overline{\nu}\Theta \ll 1$ under evaporation) is not sufficient for neglecting the dynamics effect. In the next section, we show how these new results may help to reinterpret some experimental observations of step bunching.

8.4 REINTERPRETING SOME EXPERIMENTAL RESULTS

The epitaxial growths of GaAs(001) at 600°C-700°C (Hata et al., 1993; Kasu and Fukui, 1992; Ishizaki et al., 1994; Pond, 1994; Ishizaki et al., 1996; Shinohara and Inoue, 1995) and of Si(111)-7×7 around 700°C-780°C (Omi et al., 2005) provide two experimental cases of step bunching under deposition. A quasistatic stability analysis of the classical model of step dynamics[19] predicts that the Schwoebel effect and elastic interactions are both stabilizing (see Section 8.2.3), hence the experimental evidences of step bunching under deposition were first explained by invoking an inverse Schwoebel effect (Ishizaki et al., 1996; Tejedor et al., 1998).

However, as noticed by several authors (Pimpinelli and Videcoq, 2000; Vladimirova et al., 2001; Slanina et al., 2005), an inverse ES barrier—favoring attachment of adatoms from the upper terrace—is difficult to justify microscopically. Indeed, although it is exceptionally conceivable for a given surface, resorting to an inverse ES barrier to account for all experimental situations where step bunching under deposition occurs seems more as an "useful effective description of more complex step bunching mechanisms" (Slanina et al., 2005).

In particular, in GaAs(001) and Si(111)-7×7, the works that intended to measure the ES barrier conclude to the existence of a direct ES barrier in GaAs(001) while they lead to contradictory results in Si(111). Indeed, for GaAs(001) both atomistic simulations with empirical potentials (Salmi et al., 1999) and experimental studies of the formation of islands (Šmilauer and Vvedensky, 1995; Krug, 1997) conclude for a direct ES barrier. On the other hand, for Si(111)-7×7, observations of the denuded zones around the steps (Voigtlander et al., 1995; Rogilo et al., 2013), measurements of the decay rates of islands and holes under evaporation and deposition (Ichimiya et al., 1996), and measurements of the distributions over terraces of the nucleated islands under deposition (Chung and Altman, 2002) are inconclusive, as they lead to a direct (Ichimiya et al., 1996), an inverse (Chung and Altman, 2002; Rogilo et al., 2013), and the absence of ES barrier (Voigtlander et al., 1995).

All these results led theoreticians to consider new mechanisms to account for step bunching under deposition, like the coupling between the diffusing precursors and the adatoms for the vapor phase epitaxy of GaAs(001) (Pimpinelli and Videcoq, 2000) or the fast diffusion of adatoms along steps of Si(111)-7×7 (Politi and Krug, 2000). While these mechanisms are plausible, there is no clear evidence for their implication in the observed step bunching cases. In particular, the step bunching on GaAs(001) is also observed in molecular beam epitaxy deposition experiments (Pond, 1994), which occurs without precursors. Hence the coupling with precursors cannot be invoked for interpreting the latter experiment.

In this section, we show how, without resorting to these more sophisticated mechanisms, a stability analysis of the classical step flow model which includes

19 The "classical" model does not include the adatom jump effect, (see, e. g., Pierre-Louis, 2003b).

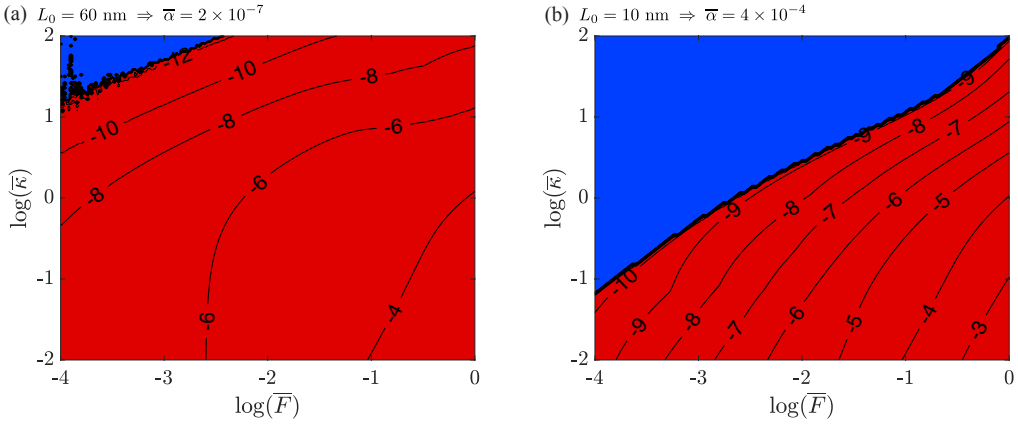

Figure 8.18: Stability diagrams for Si(111)-7×7 under deposition with $S = 1$, $\overline{\kappa}_p = 0$, $\overline{\nu} = 0$, $\overline{\beta} = 0$, $\Theta = 0.01$ for two initial terrace widths L_0: (a) $\overline{\alpha} = 2 \times 10^{-7}$ associated to $L_0 = 60$ nm and (b) $\overline{\alpha} = 4 \times 10^{-4}$ corresponding to $L_0 = 10$ nm. [see color legend on Figure 8.9.] Note that the lower right corner defined by $\overline{F} > \overline{\kappa}$ is not an physically relevant region as it is associated to a dimensionless adatom density larger than 1 (see (8.6)-(8.7)).

the adatom jump effect and the dynamics effect may *naturally* accounts for the existence of step bunching under deposition.

Qualitatively, as we have shown in Sections 8.2.3 and 8.3.4.1, both the adatom jump effect and the dynamics effect are destabilizing under deposition. In the following, we refine the plausibility that these effects may lead to step bunching by comparing them quantitatively with the stabilizing direct ES effect and elastic interactions.

8.4.1 *Si(111)-7×7*

For a quantitative analysis, the specificity of Si(111)-7×7 is that the coefficient of elastic interactions $\overline{\alpha}$ is fairly well known from the work of Stewart et al. (1994) while, as reviewed above, the Schwoebel barrier remains undetermined.

Indeed, as developed in Appendix E, for an initial terrace length $L_0^* = 20$ nm—corresponding to a miscut angle of about 1° (step height is 0.31 nm)—we have $\overline{\alpha}^* = 5 \times 10^{-5}$ and $\overline{\alpha} \propto L_0^{-3}$ for other initial step spacings. In the experiments of Omi et al. (2005), the terrace width typically varies between 10 nm and 60 nm which corresponds to $\overline{\alpha}$ ranging from 2×10^{-7} and 4×10^{-4}. In addition, in the absence of precise information, we consider a low value of adatom coverage $\Theta = 0.01$[20]. The values of $\overline{F}$ and $\overline{\kappa}$ being either difficult to estimate or completely unknown, we discuss in Appendix E, the ranges used for these parameters. Finally, nothing suggests that the steps of Si(111)-7×7 are permeable (Chung and Altman, 2002), hence we take $\overline{\kappa}_p = 0$.

Figure 8.18 shows for the two extreme values of the range of $\overline{\alpha}$ considered, the stability diagrams when including elastic interactions, the adatom jump effect and the dynamics effect.

20 $\Theta = 0.01$ is a conservative value in the sense that it minimizes the influence of the adatom jump effect and dynamics effect: the two effects whose importance we want to show.

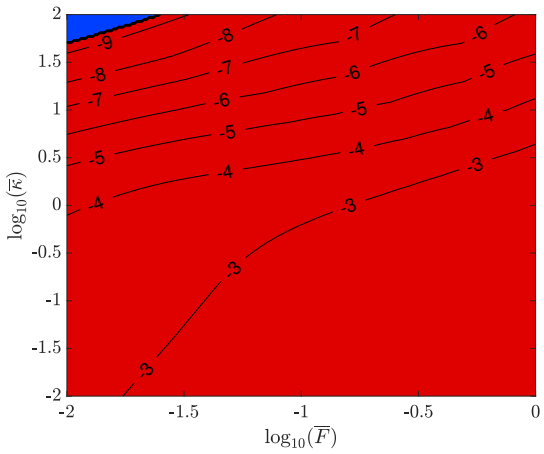

Figure 8.19: Stability diagram for GaAs(001) under deposition with $\overline{\nu} = 0$, $S = 2$, $\overline{\kappa}_p = 0$, $\overline{\alpha} = 5 \times 10^{-6}$, $\overline{\beta} = 0$, $\Theta = 0.2$ [see color legend on Figure 8.9]. Note that the lower right corner defined by $\overline{F} > \overline{\kappa}$ is not an accessible region as it is associated to a dimensionless adatom density larger than 1 (see (8.6)-(8.7).

We can see, for the low value of $\overline{\alpha}$ (large terrace width $L_0 = 60$ nm) almost the entire domain $(\overline{F}, \overline{\kappa})$ is unstable and a large region is unstable for the high value of $\overline{\alpha}$ (small terrace width $L_0 = 10$ nm). Note that similar unstable regions exist when only one of the two effects (adatom jump effect and dynamics effect) are considered, which suggests that both effects are involved in the instability.

Hence, we can see quantitatively that, for all miscut angles there exists a region of the space $(\overline{F}, \overline{\kappa})$ where the combination of the two effects neglected in previous analyses is strong enough to overcome the stabilizing elastic interactions. Thus, these mechanisms appear as plausible explanation for the step bunching observed in the work of Omi et al. (2005). Note that as they observe two different structures of the step bunches depending on the temperature in the range 700°C-780°C, Omi et al. propose that at the origin of the bunching may lie different mechanisms. Those discussed here may likely be involved in one or the other temperature ranges. The problem of associating a particular mechanism to a given temperature range could be achieved by looking at the post bifurcated solution and analyzing the structure of the step bunches.

8.4.2 *GaAs(001)*

Unlike Si(111)-7×7, we find, in the literature, estimates for the Schwoebel barrier of GaAs(001) (see Appendix E) and select the value $S = 2$ at 600°C. In addition, as detailed in Appendix E, the elastic interaction parameter is about $\overline{\alpha} = 5 \times 10^{-6}$ and the equilibrium adatom coverage is rather high, around $\Theta = 0.2$, which implies that the influence of adatom jump and dynamics effects is important. In addition, from the knowledge of the surface diffusion constant, it is shown in Appendix E that $\overline{F}$ is rather high between 0.1 and 1. Finally,

without indication for the existence of permeability for GaAs(001), we take $\overline{\kappa}_p = 0$.

On the basis of these estimates, we can see on Figure 8.19 that within the estimated ranges of $\overline{F}$ and $\overline{\kappa}$, there exists again a region where the destabilization brought by the combination of the adatom jump effect and dynamics effect overcome the stabilization of the elastic interactions and direct Schwoebel effect.

From these two examples, we can see that including the adatom jump effect and the dynamics effect can destabilize the steps more than the other mechanisms (Schwoebel effect and elasticity) stabilize them. In addition, to add a quantitative remark, note that one can estimate the typical number of monolayers for the instability to develop by comparing the time of deposition of one monolayer, $1/\mathcal{P} = 1/(\overline{F}\Theta)$ (in dimensionless time) to the characteristic time for the instability to develop, $1/\mathrm{Re}(\lambda)$ (read on the isolines of the stability diagrams). In that way, we can see that on Figure 8.18 and Figure 8.19 that in the regions of low $\overline{\kappa}$ the instability may develop in 10 to 100 monolayers which is fast enough to account for the observations of the experiments. Hence the observed step bunching previously explained with other mechanisms could actually naturally develop because of these two effects.

9 STEP BUNCHING UNDER ELECTROMIGRATION

Step bunching under electromigration concerns situations of evaporation or deposition where, while an indirect heating of the substrate or a heating through an alternating current results in stable growth, a heating of the same substrate through direct current may, depending on the direction of the current, cause step bunching. The surface for which electromigration induced step bunching has attracted most interest is Si(111) whose behavior, as presented in Section 9.1.1, exhibits an intriguing dependence on temperature.

9.1 THE ELECTROMIGRATION PROBLEM

9.1.1 *Experimental observations*

The first experimental report of step bunching caused by a direct current on Si(111) is due to Latyshev et al. (1989) in the sublimation regime (i. e., pure evaporation). These were later reproduced, further examined and extended to deposition by Yang et al. (1996), Métois and Stoyanov (1999), Stoyanov et al. (2000), Homma and Aizawa (2000), and Gibbons et al. (2005) (for Gibbons' work see also Gibbons et al. 2006; Gibbons 2006).

These experimental results are summarized as follows. Under pure evaporation[1], as temperature increases, three stability regimes are observed. The regime I (low temperature, around $850°C - 950°C$), where step-down electric field causes step bunching while step-up electric field results in stable growth. The regime II (intermediate temperature, around $1040°C - 1190°C$) where, in contrast with regime I, step bunching is observed for step-up electric field while under step-down electric field the step flow is stable. And the regime III (high temperature, around $1200°C - 1300°C$), where the same stability behavior as in regime I is observed[2]. As an illustration of these two stability reversals, we reproduce, on Figure 9.1, the atomic force microscope images of Gibbons et al. (2006) showing, in the three temperature regimes, the organizations of the atomic steps after direct current annealing.

Note that these stability reversals have been consistently observed in all the above cited works, with small variations in the transition temperatures of about 50°C, likely due to a dependence of these on the initial miscut angle (Degawa et al., 2001). Understanding what are the mechanisms behind these two reversals of stability is a first challenge.

1 Pure evaporation is the simplest experimental case corresponding to the conditions of annealing: the substrate is heated with a direct current in the absence of any deposition source.

2 Note that a fourth regime at higher temperatures ($T > 1300°C$) which exhibits the same stability as in regime II has been reported (Homma and Aizawa, 2000), but has been the object of less investigations.

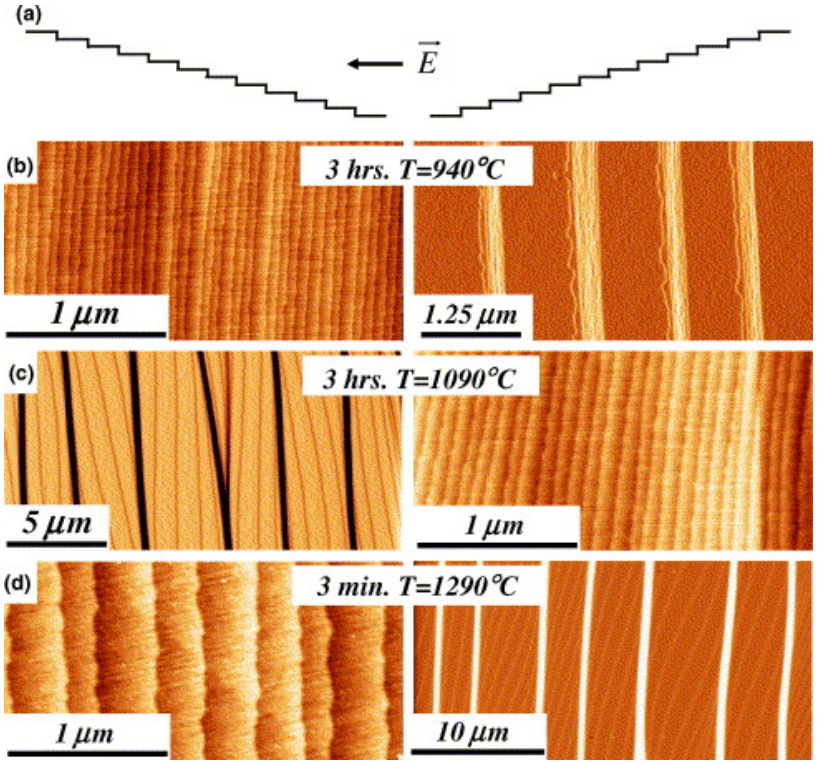

Figure 9.1: (a) Schematic of the vicinal atomic step structure before annealing with the direction of the electric field. (b)-(d) Derivative mode atomic force microscope images after direct current annealing (i. e., pure evaporation) in the three temperature regimes. Images should be viewed as if illuminated from left to right and step bunches can be observed in (b) right, (c) left and (d) right. Reprinted from Gibbons et al. (2006) with permission from Elsevier.

The global picture of experimental results shall be completed by the observations under deposition in the different temperature regimes.[3] While the stability behavior under deposition is the same as under evaporation in regimes I and III, results are less clear in Regime II. On the one hand, Métois and Stoyanov (1999) observe a reversal of stability with respect to evaporation (i. e., stable for step-up current and step bunching for step-down current under net deposition in regime II). On the other hand, Gibbons et al. (2005) report, in Regime II, the same stability behavior under net deposition as under evaporation. These apparently contradictory results for deposition in Regime II could be due to the difference in the net deposition flux between the two authors. Indeed, the net deposition rate in regime II are 0.09 Å/s for Gibbons et al. and 2.1 Å/s for Métois and Stoyanov (1999).There would be no contradiction if there exists a limit deposition rate above which the reversal of stability with respect to evaporation in regime II is observed. All these experimental results are summarized in Table 9.1.

3 Note that, at these temperatures, deposition actually corresponds to the combination of evaporation and deposition (from another heated silicon source), such that the result is net deposition.

	Evaporation		Net deposition	
	Step-down e.f.	Step-up e.f.	Step-down e.f.	Step-up e.f
Regime I $\sim 950°C$	$\mathcal{U}$	$\mathcal{S}$	$\mathcal{U}$	$\mathcal{S}$
Regime II $\sim 1150°C$	$\mathcal{S}$	$\mathcal{U}$	$\mathcal{U}$ (M.S.) $\mathcal{S}$ (G.N.P)	$\mathcal{S}$ (M.S.) $\mathcal{U}$ (G.N.P)
Regime III $\sim 1250°C$	$\mathcal{U}$	$\mathcal{S}$	$\mathcal{U}$	$\mathcal{S}$

Table 9.1: Compilation of the experimental observations of the stability against step bunching for Si(111) under electromigration as observed by Yang et al. (1996), Stoyanov et al. (2000), Métois and Stoyanov (1999) (M.S.) and Gibbons, Noffsinger, and Pelz (2005) (G.N.P.). $\mathcal{S}$ and $\mathcal{U}$ denote stable and unstable domains respectively.

9.1.2 *Review of existing theories*

A theoretical analysis of step bunching under electromigration was first performed for sublimation by Stoyanov (1991) who, by introducing the concept of electromigration force in the step flow model (see (7.49)), showed that for a diffusion length, $\sqrt{D/\nu}$ large compared to the terrace length (which is expected to be the case for Si(111) in all temperature regimes, cf. Yang et al. 1996), a step-down current results in step bunching while a step-up current leads to a stable growth. This provides an explanation for the stability in regime I and III.

Since the work of Stoyanov, it is the unexpected observations in Regime II that have raised many discussions. The possibility of a change in the sign of the adatom effective charge was considered by Kandel and Kaxiras (1996) but ruled out by the experiments of Degawa et al. (2000), which show that the adatom drift direction corresponds to the current direction ($q_e > 0$), irrespective of the temperature. Natori (1994) showed with a step flow model how a fast step kinetics ($\overline{\kappa} \gg 1$) leads to an inversion of stability and Suga et al. (2000) recovered the same result with dynamical Monte Carlo simulation of the terrace-adatom-step-kink model. In these simulations, slow and fast step kinetics are obtained by changing the ratio of the hopping rate between terrace sites to the hopping rate between step and terrace sites.

In the late 90's, it was proposed that the stability reversal in regime II is due to step permeability (Stoyanov, 1998; Métois and Stoyanov, 1999). Indeed, assuming the steps to be sufficiently permeable ($\overline{\kappa}_p$ high enough) makes the steps unstable against step bunching in the step-up direction. However, it is not clear why, as temperature increases, steps change from impermeable to permeable and impermeable again. Pierre-Louis (2003b) relating the mechanisms of Natori (1994) and Stoyanov (1998) highlighted, through a linear stability

analysis, that step permeability ($\overline{\kappa}_p$ high) or fast step kinetic ($\overline{\kappa}$ high) are two possible explanations of the observations in regime II.

Finally, more recently, it was proposed that, as a result of an enhanced surface diffusion near the steps, the step kinetic coefficients ($\overline{\kappa}$, $\overline{\kappa}_p$) may be negative and furnish another explanation to bunching under step-up current (Zhao et al., 2004; Zhao and Weeks, 2005; Pierre-Louis, 2006). The latter, although, *a priori* surprising and not thermodynamically consistent in our setting (but shown to be thermodynamically consistent in Pierre-Louis 2003a using a phase field approach) seems to provide good agreement with the stability diagram of regime II, both under evaporation and net deposition (Pierre-Louis and Métois, 2004)).

9.2 STABILITY RESULTS FOR CURRENT-INDUCED STEP BUNCHING

In this section, we make use of the quasistatic and dynamic stability analyses of Chapter 8 to investigate the current-induced step bunching. In particular, we wonder whether the adatom jump effect or the dynamics effect can provide an explanation for the stability reversals with temperature.

Recall that the stabilizing/destabilizing mechanisms are Schwoebel effect, elasticity, adatom jump effect, dynamics effect and electromigration.

To this end, instead of studying $\mathrm{Re}(\lambda)$ which mixes the contributions of the various mechanisms in presence, we focus on the contribution of electromigration to stability through a Taylor expansion of $\mathrm{Re}(\lambda)$ in the electric field e. This expansion is justified as estimations of the dimensionless electric field ($\overline{e} \sim 10^{-5}$) suggest that its contribution to $\mathrm{Re}(\lambda)$ is essentially linear, which is verified *a posteriori*. Denote by $\Lambda_0(k)$ and $\Lambda_1(k)$ the zeroth and first order coefficients of the Taylor expansion,

$$\mathrm{Re}\big(\lambda(k)\big) = \Lambda_0(k) + \Lambda_1(k)\overline{e} + o(\overline{e}). \tag{9.1}$$

The experimental observations tell us that, in all temperatures and deposition/evaporation regimes, a stability reversal is observed upon a reversal of the electric field. This implies that $|\Lambda_1(k)\overline{e}| > |\Lambda_0(k)|$[4]. In other words, while $\Lambda_0(k)$ determines the stability for $\overline{e} = 0$ (this corresponds to the study of Section 8.2 and Section 8.3), experimental observations indicate that the stability under electromigration is determined by the sign of $\Lambda_1(k)$.

If for all $k \in (0, \pi)$, $\Lambda_1(k) > 0$, a step-down (resp. step-up) electric field results in step bunching (resp. stable step dynamics), as it is observed in regimes I and III. Conversely, if for all $k \in (0, \pi)$, $\Lambda_1(k) < 0$, a step-down (resp. step-up) electric field results in a stable step dynamics (resp. step bunching), as it is observed in regimes II.

On that basis, the adatom jump effect or the dynamics effect can provide explanations for the reversals of stability with temperature if and only if they affect the sign of $\Lambda_1(k)$.

As reviewed in Section 9.1.1, the two stability reversals with increasing temperature under pure evaporation are observed consistently across all studies,

4 A more careful statement would be : let K_- (K_+) the subset of $(0, \pi)$ where $\Lambda_0(k)$ is negative (positive). Then the experimental observation requires that for all $k \in K_+$ $|\Lambda_1(k)\overline{e}| > |\Lambda_0(k)|$ and if $K_+ = \emptyset$, there exist a $k \in K_-$ such that $|\Lambda_1(k)\overline{e}| > |\Lambda_0(k)|$.

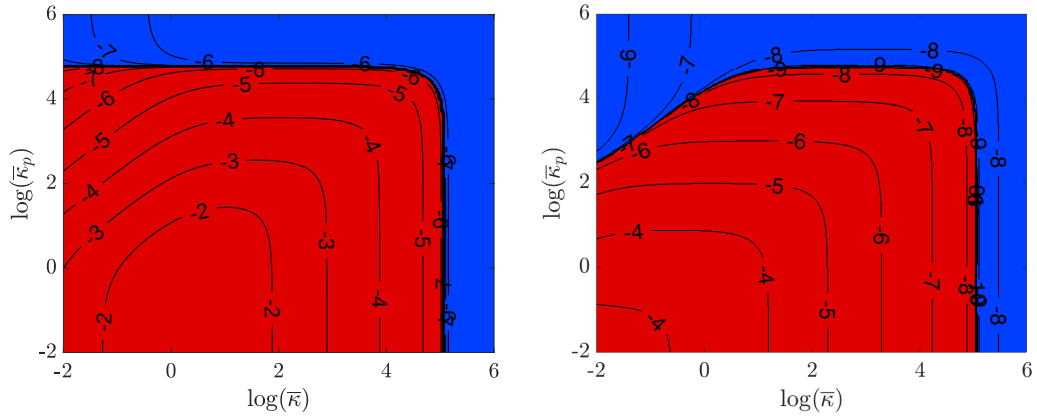

(a) $\overline{\nu} = 10^{-4}$, $k = \pi$ (b) $\overline{\nu} = 10^{-4}$, $k = 0.1$

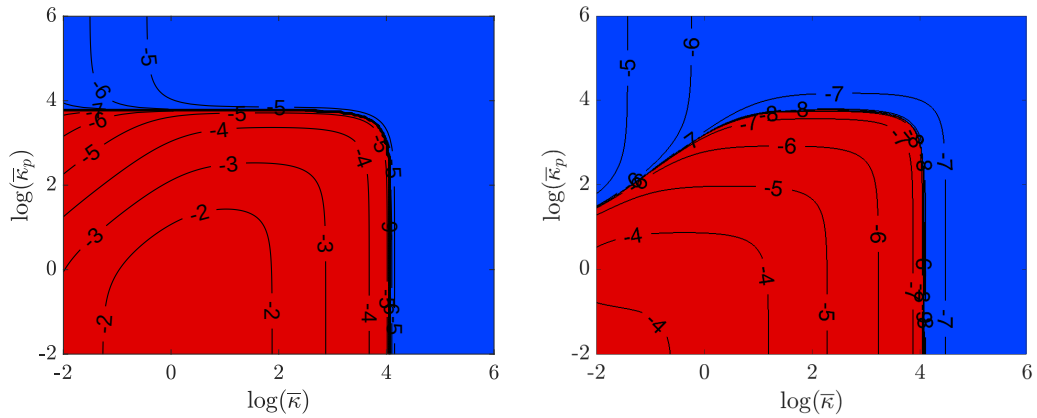

(c) $\overline{\nu} = 10^{-3}$, $k = \pi$ (d) $\overline{\nu} = 10^{-3}$, $k = 0.1$

Figure 9.2: Values of $\Lambda_1(k)$ for pure evaporation and without Schwoebel effect ($S = 1$). Red domains correspond to $\Lambda_1(k) > 0$, i. e., step bunching occurs for step-down electric field ($\overline{e} > 0$). Conversely blue domains correspond to $\Lambda_1(k) < 0$, i. e., step bunching occurs for step-up electric field ($\overline{e} < 0$). Isolines display $\log|\Lambda_1(k)|$. (a) and (c) correspond to the step pairing instability while (b) and (d) show the long wavelength instabilities.

and constitute the first experimental fact to confront with theoretical predictions. In the following, we develop a numerical analysis of $\Lambda_1(k)$ under pure evaporation.

9.2.1 *Effect of step kinetics and permeability under evaporation*

We report in Figure 9.2, the values of $\Lambda_1(k)$ for $k = \pi$ (step pairing) and $k = 0.1$ (long wavelength instability) under pure evaporation in the domain $(\overline{\kappa}, \overline{\kappa}_p)$. No Schwoebel effect is assumed ($S = 1$) and as developed in Section 9.2.3 the presence or absence of the other mechanisms (elasticity, adatom jump effect, dynamics effect) do not affect the value of $\Lambda_1(k)$. Moreover as the evaporation rate $\overline{\nu}$ typically varies from 10^{-6} in regime I to 10^{-3} in regime III, we select two

values in this range (see Appendix E, Section E.2 for estimations of the physical parameters in the electromigration problem).

Before interpreting the values of $\Lambda_1(k)$, note that the study of the dependence of Λ_1 on Θ shows that Λ_1 simply scales linearly with Θ (as it is the case with the contributions of Schwoebel effect and elasticity to Λ_0). Hence the relevant parameters that determine the sign of Λ_1 are really $\overline{\nu}$, $\overline{\kappa}$ and $\overline{\kappa}_p$.

First, by comparing in Figure 9.2, (a) with (b) and (c) with (d), we can see that for almost every point in the domain $(\overline{\kappa}, \overline{\kappa}_p)$ the sign of Λ_1 for long wavelength and step pairing instabilities is the same. There is only a small region ($\overline{\kappa} < 1$ and $\overline{\kappa}_p \in (10^2, 10^4)$ where the sign of Λ_1 changes with k. We do not expect this domain to be encountered in experiments as it would imply that step flow is unstable for both step-down (unstable for long wavelengths) and step-up (unstable for step pairing) current which is not the case. In addition, the work of Gibbons et al. (2006) —who studied the morphology of the step bunches under electromigration— confirms that $\overline{\kappa} < 1$ should not be considered for Si(111) above 900°C. Indeed their main conclusion is that for all three regimes, the adatom transport is diffusion-limited (i. e., $\overline{\kappa} \gg 1$).

One can see from any of the Figure 9.2 that for not too high step kinetics and permeability ($\overline{\kappa} < 10^4$ and $\overline{\kappa}_p < 10^2$), $\Lambda_1(k)$ is positive, i. e., step bunching occurs for step-down current (provided that Λ_1 prevails over Λ_0). This corresponds to the regimes I and III and we recover here the result known since Stoyanov (1991) that normally (i. e., without permeability and without resort to extremely high step kinetics) step-down current induces step bunching.

As either the step kinetics ($\overline{\kappa}$) or the step permeability ($\overline{\kappa}_p$) is increased, at some point, Λ_1 becomes negative which corresponds to step-bunching for step-up current as seen in regime II. Moreover a careful analysis of Figure 9.2 teaches that it is essentially $\max(\overline{\kappa}, \overline{\kappa}_p)$ that determine the point where the sign of Λ_1 changes, irrespective of the magnitude of the lowest of these two parameters.

With this simultaneous analyses of the step kinetics and permeability, we join Pierre-Louis (2003b) in concluding that high step kinetics and fast permeability are equally possible explanations for observations in regime II. To go further, we believe that high step kinetics and fast permeability result in the same behavior because, essentially, they are two ways of modeling the same physical process.

9.2.2 *Reinterpreting fast step kinetics as permeability*

In this section, studying the influence of the Schwoebel effect on Λ_1, we give arguments that support the idea that fast step kinetics and permeability are just two mathematical formulations of the same physical phenomenon. In a microscopic approach, while permeability accounts for a direct jump of an adatom across a step without attaching to it (i. e., at the microscale, without attaching to a kink), if step kinetics is fast ($\overline{\kappa}$ high), then steps are *de facto* permeable: fast kinetics between terrace and step result in fast kinetics also across the step ($\overline{\kappa} \gg 1 \Rightarrow \mu_+ \approx \mu_s$ and $\mu_- \approx \mu_s$ whereby $\mu_+ \approx \mu_-$). At the microscale, an adatom crosses a step by first attaching to the step from one side and detaching from the step on the other side.

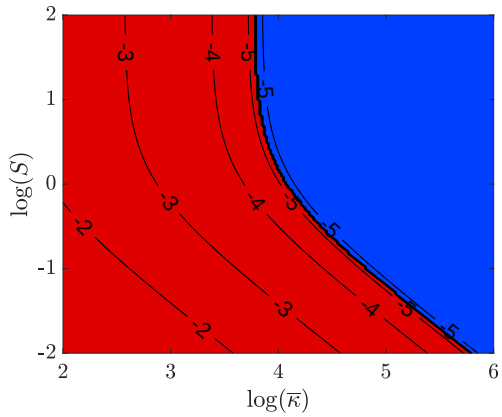

Figure 9.3: Values of $\Lambda_1(\pi)$ for pure evaporation ($\overline{\nu} = 10^{-3}$, $\Theta = 0.1$) and without permeability ($\overline{\kappa}_p = 0$). Red domains: $\Lambda_1(\pi) > 0$, blue domains: $\Lambda_1(\pi) < 0$. Isolines indicate $\log|\Lambda_1(\pi)|$.

This microscopic analysis is confirmed by considering the influence of the Schwoebel effect on Λ_1. Consider the case $\overline{\nu} = 10^{-3}$ and the step pairing instability ($k = \pi$) in the absence of permeability ($\overline{\kappa}_p = 0$). We show on Figure 9.3, how a Schwoebel effect ranging from $S = 10^{-2}$ to $S = 10^2$ shifts the limit in $\overline{\kappa}$ where the sign of $\Lambda_1(\pi)$ changes. One can see that, with respect to the $\overline{\kappa}$-limit at $S = 1$, a decrease of S below one moves the limit to higher $\overline{\kappa}$ while an increase of S above one essentially does not change the critical value of $\overline{\kappa}$. Recalling that $\kappa_- = \overline{\kappa}D/L_0$ and $\kappa_+ = S\overline{\kappa}D/L_0$, one can see that decreasing (resp. increasing) S below (resp. above) $S = 1$ amounts to slow down (resp. speed up) the step kinetics on the lower side of the step.

Physically, the effective permeability —i. e., not related to the $\overline{\kappa}_p$ term but due to the fast attachment/detachment of adatoms at the step— has the kinetics of the slower side of the step. Indeed, a/d from the lower and upper terraces can be considered as two processes in series (in the sense of electric circuits) that result in an effective permeability. This explains that the $\overline{\kappa}$-limit in Figure 9.3 is shifted only in the case $S < 1$, which corresponds to a slowdown of the effective permeability.

With these considerations on the physical meaning of the microscopic processes at steps and the limit of inversion of Λ_1, we can see that a high step kinetics is equivalent, at the level of the physical mechanism and its consequences on stability, to an effective permeability.

9.2.3 *Absence of influence of the other mechanisms*

As an important result, we have noticed that the value of $\Lambda_1(k)$ is not affected by the inclusion, in the step dynamic model, of the adatom jump effect, the dynamics terms and the elastic interactions. Concretely, by including these mechanisms, the stability diagrams of Figure 9.2 are unchanged. This tells us, in particular, that the two new phenomena which we focus on in this

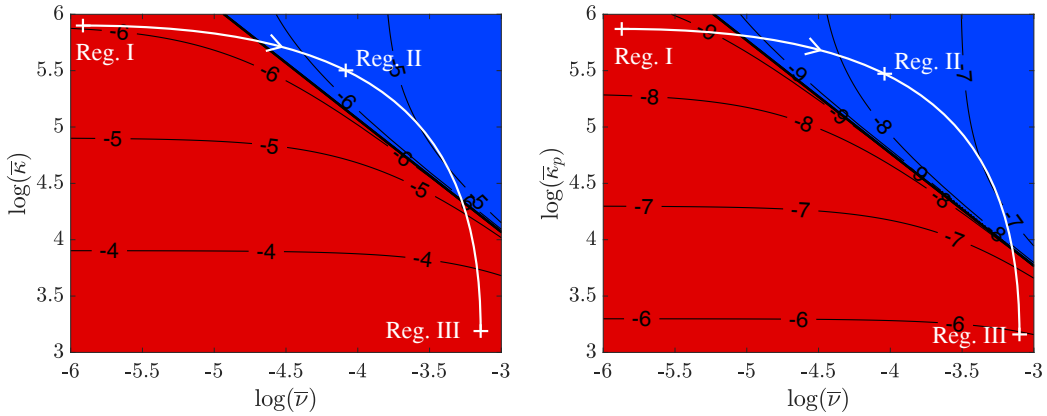

(a) Case $\overline{\kappa} \gg \overline{\kappa}_p$ (b) Case $\overline{\kappa}_p \gg \overline{\kappa}$

Figure 9.4: Values of $\Lambda_1(\pi)$ for pure evaporation and without Schwoebel effect ($S = 1$). Red domains: $\Lambda_1(\pi) > 0$, blue domains: $\Lambda_1(\pi) < 0$. Isolines indicate $\log|\Lambda_1(\pi)|$.

work —adatom jump effect and dynamics effect— do not provide new possible explanations for the observed stability reversals with temperature.

9.2.4 *Stability reversals with temperature under evaporation*

While high step kinetics and permeability provide possible explanations for the observations of electromigration-induced step bunching in regime II, it has been suggested in the literature (Métois and Stoyanov, 1999) that the two stability reversal with increasing temperature are due to a first transition from impermeable to permeable steps and a second transition from permeable to impermeable. Such a non-monotonous evolution of the step permeability with temperature is, *a priori*, surprising and we show in the following that it is not necessary.

Indeed, as can be seen from Figure 9.2, the domain $\Lambda_1 < 0$ gets larger as $\overline{\nu}$ increases. While we have no ideas, from experiments, of the values of $\overline{\kappa}$ and $\overline{\kappa}_p$, on the contrary $\overline{\nu}$ can be estimated and typically evolves from 10^{-6} in regime I to 10^{-4} and 10^{-3} in regimes II and III, respectively (see Section E.2).

Concerning $\overline{\kappa}$, we only know from Gibbons et al. 2006 that in all likelihood $\overline{\kappa} \gg 1$ for all three temperature regimes.

Figure 9.4 shows the value of $\Lambda_1(\pi)$ for the situations were either step kinetics or permeability is dominant. For either of these two cases, based on estimations of $\overline{\nu}$ in the three regimes, we propose three points that would correspond to a monotonous evolution of the step kinetics $\overline{\kappa}$ (Figure 9.4 (a)) or the step permeability $\overline{\kappa}_p$ (Figure 9.4 (b)) that account for the two stability reversals observed in experiments. This is simply to show that it is not necessary to resort to a non-monotonous evolution of step kinetics or permeability to explain the two stability reversals.

Using microscopic models of adatom hopping on terraces and at steps, we further discuss in Section E.2, the range and temperature dependence of $\overline{\kappa}$ and

$\overline{\kappa}_p$, based on surface physics. In particular, from the microscopic meaning of $\overline{\kappa}$ and $\overline{\kappa}_p$, it is not evident that $\overline{\kappa}$ or $\overline{\kappa}_p$ can reach the high values above 10^4 where the stability reversal occurs ($\Lambda_1 < 0$).

Hence, while these mechanisms remain plausible, to clarify their reality, we would need more accurate experimental comparison. In particular, the shape of the step bunches could provide more refined information against which the model prediction could be compared.

9.2.5 *Stability prediction under net deposition*

Experimentally, net deposition is achieved by heating a silicon source on top of the substrate and is identified from a motion of the step in the step-down direction. In terms of modeling, the step velocity of the steady-state solution $\overset{o}{V}$ changes from negative to positive when $\overline{F} > \overline{v}$. In that case, we observe that irrespective of the step kinetics and permeability parameters, $\Lambda_1(k) > 0$ for all k. This implies that for all three temperature regimes, step bunching occurs for step-down current, which is consistent with the observations of Métois and Stoyanov (1999). However, this is in contradiction with the results of Gibbons et al. (2005) that observe step bunching under under step-up current for net deposition in regime II.

A clarification of this point from the experimental standpoint would allow to further discuss the theoretical modeling.

10 CONCLUSION

In conclusion, we have developed a comprehensive linear stability analysis of the step dynamics by putting the emphasis on the poorly studied adatom jump effect and dynamics effect. Our analysis reveals that these two mechanisms provide possible explanations for some occurrences of step bunching in experiments.

After recalling how the adatom jump term and the dynamics terms appear from a derivation of the step dynamics equation based on continuum thermodynamics, we have presented the so-called quasistatic approximation. While this approximation may be valid for the computation of the steady-state solution in the slow deposition/evaporation regimes, we have shown that its use for analyzing the linear stability of steps is not well justified even in the regime of slow deposition/evaporation.

In terms of stability computation method, in addition to the classical linear stability analysis under the quasistatic approximation, we have developed a stability analysis of the general equations with dynamics terms. The specificity lying in that both the function and the domain are subjected to perturbations is treated with an arbitrary Lagrangian-Eulerian formulation and the perturbation problem initially formulated on a periodic system of infinite size is rewritten on a unit cell (one terrace) using Bloch wave decomposition. The stability problem hence takes the form of a generalized eigenvalue problem solved numerically. This new approach to the general stability problem provides an alternative to the works of Ghez et al. (1993) and Gillet (2000).

For interpreting the stability results, we combine analytical and numerical approaches to analyze the influence on stability of all the mechanisms independently (Schwoebel effect, elasticity, adatom jump effect, dynamics effect) as well as their interplay. For the latter, we discuss the influence of the control parameters and material parameters on the relative weight of the different mechanisms on stability which provides a physical interpretation of the stability results.

In doing so, we recover the effect on stability of the classical mechanisms such as the Schwoebel effect and elasticity while extending the latter beyond the assumption of nearest-neighbor interactions. More importantly, we find the effect on stability of the adatom jump effect and the dynamics effect both under deposition and evaporation. The adatom jump effect proves to be destabilizing under deposition and stabilizing under evaporation while the effect on stability of the dynamics depends on the value of $\overline{\kappa}$ (expressing the ratio of step attachment/detachment kinetics to terrace diffusion kinetics). In addition, the adatom jump effect and dynamics effect turn out to be, compared to the other mechanisms, all the more influential as the adatom coverage is high.

We complete the general analysis by assessing quantitatively the importance of the adatom jump effect and dynamics effect in some crystal growth experiments. For that purpose we combine several experimental works to estimate the physical parameters of the problem. The two mechanisms above mentioned provide possible explanations for some cases of step bunching observed in GaAs(001) and Si(111)-7×7. These explanations appear as interesting alternative to the more refined mechanisms invoked previously to account for step bunching.

Finally, we revisit the problem of step bunching under electromigration where the stability reversals with temperature still remain poorly understood. Unfortunately, for this problem, we establish that the adatom jump and dynamics effects do not affect the current-induced step bunching and whereby are of no help to understand the experimental results. Nevertheless, exploring two mechanisms invoked in the literature, fast step kinetics and step permeability, we argue why they are essentially two mathematical formulations of the same physical phenomenon. In addition, we show that it is not necessary to resort to a non-monotonous evolution of the step kinetics/permeability to account for the observed stability reversals. However, we cannot clearly assert that these phenomena are indeed involved in the stability reversals. Indeed, in view of the microscopic meaning of the step kinetics parameters, some doubts exist regarding the possibility that the high values required for the stability inversions are physically acceptable.

The new results brought by the adatom jump effect and dynamics effect, to the theoretical analysis of step bunching constitute a valuable progress to the understanding of step bunching. However, as it is often the case in the field of atomic step dynamics, it is difficult to clearly associate the occurrence of step bunching in an experiment to a given mechanism. Indeed, not only various origins to step bunching are possible but quite little is known on the parameters of the step flow model and for many of them, ranges of possible values crossing several orders of magnitude need to be considered. Furthermore, in any modeling of the step flow, phenomena which, could potentially play an important role are not accounted for. For instance, diffusion of adatoms along the steps is neglected in most approaches, including ours, but also the possibly important role of vacancies. Better confidence towards the involvement of a mechanism in particular cases of step bunching could be achieved by investigating, not only the onset of instabilities, but also the pattern that develops in the long term evolution of the instabilities. As a promising path, recent works (Pimpinelli et al., 2002; Krug, 2005) have undertaken a classification of the step bunches based on some of their characteristics and time evolution constants. In this respect, the important changes brought by the adatom jump effect and dynamics effect to the linear stability suggests that the characteristics of the step bunches will also be modified. Such a work, if able to tackle the difficulties related to the lack of knowledge on the microscopic parameters, could allow to identify more accurately the physical processes at stake for particular occurrences of step bunching.

APPENDICES

A

SPACE-DEPENDENCE OF THE ELECTRONIC PARAMETERS

The first part of this appendix pertains to the derivation of the strain-dependent coefficients for the 1D boundary value problem in Section 3.1.3. The second part gives their numerical values for the *p-n* junction in the monocrystalline silicon solar cell application considered in Section 3.3.

A1. 3D-TO-1D REDUCTION OF THE STRAIN-DEPENDENT ELECTRONIC PARAMETERS

Using the strain field $\varepsilon(x)$ in (3.2) and (3.5) into the three-dimensional version of the strain-dependent electronic parameters (3.6) and (3.7), we obtain for the conduction and valence band edges:

$$E_c(x) = E_c^0 + \kappa \widehat{E}_c(x - x_0), \qquad E_v(x) = E_v^0 + \kappa \widehat{E}_v(x - x_0), \tag{A.1}$$

with

$$\begin{cases} E_c^0 := E_c^r - \dfrac{c_{xxyy}}{c_{xxxx}} \widetilde{E}_{c,xx}(\varepsilon_{yy}^0 + \varepsilon_{zz}^0) + \widetilde{E}_{c,yy}\varepsilon_{yy}^0 + \widetilde{E}_{c,zz}\varepsilon_{zz}^0, \\ \widehat{E}_c := -\dfrac{c_{xxyy}}{c_{xxxx}} \widetilde{E}_{c,xx}(\alpha_y + \alpha_z) + \widetilde{E}_{c,yy}\alpha_y + \widetilde{E}_{c,zz}\alpha_z. \end{cases} \tag{A.2}$$

Here, c_{xxxx} and c_{xxyy} are the normal and transverse components of the elasticity tensor $\mathbf{c}$ and $\widetilde{E}_{c,xx}$, $\widetilde{E}_{c,yy}$, and $\widetilde{E}_{c,zz}$ denote the Cartesian components of the tensor $\widetilde{\mathbf{E}}_c$. For the conduction band edge, E_v^0 and $\widehat{E}_v$ follow relations strictly analogous to (A.2).

We have similar relations for the effective densities of states:

$$N_c(x) = N_c^0 + \kappa \widehat{N}_c(x - x_0), \qquad N_v(x) = N_v^0 + \kappa \widehat{N}_v(x - x_0), \tag{A.3}$$

with N_c^0, N_v^0, $\widehat{N}_c$, $\widehat{N}_v$ defined in strict analogy with (A.2).

For the mobilities, due to the assumed constitutive and loading symmetries, we need the xx-component of the mobility tensors $\mathbf{M}_n$ and $\mathbf{M}_p$ denoted by

$$m_n := M_{n,xx}, \qquad m_p := M_{p,xx}. \tag{A.4}$$

Inserting (3.2) and (3.5) in (3.7) we obtain:

$$m_n(x) = m_n^0 + \kappa \widehat{m}_n(x - x_0), \qquad m_p(x) = m_p^0 + \kappa \widehat{m}_p(x - x_0), \tag{A.5}$$

where

$$\begin{cases} m_n^0 := M_{n,xx}^r - \dfrac{c_{xxyy}}{c_{xxxx}} \widetilde{M}_{n,xxxx}(\varepsilon_{yy}^0 + \varepsilon_{zz}^0) + \widetilde{M}_{n,xxyy}\varepsilon_{yy}^0 + \widetilde{M}_{n,xxzz}\varepsilon_{zz}^0, \\ \widehat{m}_n := -\dfrac{c_{xxyy}}{c_{xxxx}} \widetilde{M}_{n,xxxx}(\alpha_y + \alpha_z) + \widetilde{M}_{n,xxyy}\alpha_y + \widetilde{M}_{n,xxzz}\alpha_z, \end{cases} \tag{A.6}$$

and analogous relations for m_p^0 and $\widehat{m}_p$.

A2. STRAIN-DEPENDENCE OF THE ELECTRONIC PROPERTIES OF SILICON

Next, we select on the basis of the physics literature pertaining to the effect of strain on the electronic properties of silicon the numerical values for the aforementioned electronic parameters needed for the application in Section 3.3.

Although the influence of strain on the electronic properties of monocrystalline silicon has been studied over more than fifty years, it is still an open subject and one can find in the literature constants that vary by more than 30% as seen in Walle (1989), Friedel et al. (1989), and Fischetti and Laux (1996). While in the solid-state physics literature the effect of strain refers to the sub-bands composing the conduction and valence bands, we introduce here, through linearizations, a two-band equivalent description of the conduction and valence bands that combines the effect of strain on their constitutive sub-bands. While below, we simply present the results pertaining to the bending example of Chapter 3, the full derivation is detailed in Appendix C.

Consider first the band edges $E_c(\varepsilon)$ and $E_v(\varepsilon)$ and the effective Densities Of State (DOS) $N_c(\varepsilon)$, $N_v(\varepsilon)$ whose computations are based on the so-called deformation potentials that have been introduced by Bardeen and Shockley (1950) (see e.g., Herring and Vogt, 1956; Bir et al., 1974; Walle, 1989; Friedel et al., 1989; Fischetti and Laux, 1996 and a synthesis in Creemer, 2002, Section 2.2.2).

I. CONDUCTION BAND EDGE ENERGY

The shift of the band edge of the conduction band depends on the strain-induced volume change through (Herring and Vogt, 1956):

$$\Delta E_c(\varepsilon) := E_c(\varepsilon) - E_c^r = \left(\Xi_d + \frac{1}{3}\Xi_u\right) \mathrm{Tr}(\varepsilon). \tag{A.7}$$

In view of the strain triaxiality (3.43) of the problem considered, it reads as a function of x:

$$\Delta E_c(x) = \widehat{E}_c \varepsilon_{yy}(x), \qquad \widehat{E}_c = \left(1 - \frac{c_{xxyy}}{c_{xxxx}}\right)\left(\Xi_d + \frac{1}{3}\Xi_u\right). \tag{A.8}$$

For numerical application, we take the values of Fischetti and Laux (1996): $\Xi_d = 1.1$ eV and $\Xi_u = 10.5$ eV that give $\widehat{E}_c = 2.83$ eV.

II. VALENCE BAND EDGE ENERGY

The strain effect on the valence band edge $E_v(\varepsilon)$ and DOS $N_v(\varepsilon)$ is more complicated and less well understood than for the conduction band. Due to the complex structure of the valence band, the band edge shift, although linear with respect to the strain amplitude, is not linear with respect to the directions of the strain (Kanda, 1967). In addition, the strain effect depends on the sign of the strain components which implies, regarding silicon, that the validity

of (3.40) is restricted to situations where the strain keep the same sign in the whole p-n junction. In view of the stress triaxiality (3.43), we compute $\Delta E_v(x)$:

$$\Delta E_v(x) = E_v(x) - E_v^r = \begin{cases} \widehat{E}_v^+ \varepsilon_{yy}(x) & \text{for } \varepsilon_{yy}(x) \geq 0, \\ \widehat{E}_v^- \varepsilon_{yy}(x) & \text{for } \varepsilon_{yy}(x) < 0, \end{cases} \tag{A.9}$$

with $\widehat{E}_v^+ = 3.26$ eV and $\widehat{E}_v^- = -0.68$ eV obtained from the values of deformation potentials of Fischetti and Laux (1996).

III. EFFECTIVE DENSITIES OF STATE

The DOS N_c of the conduction band is little affected by strain compared to the other parameters so that it can be assumed constant (Kanda, 1967; Creemer and French, 2000). Hence, $\widehat{N}_c = 0$. For the valence band the change in DOS $\Delta N_v(\varepsilon)$ has been the object of fewer studies. However, Creemer (2002) recently pointed that this effect is of the same order as the bands edge shift. For simplicity, we assume a linear dependence of $\Delta N_v(\varepsilon)$ with respect to ε of the type of $(3.6)_2$ and appeal to the computation of Creemer to derive $\widetilde{\mathbf{N}}_v$. Taking into account the stress triaxiality of the problem considered, this leads to spatial variation of N_v of the form

$$\Delta N_v(x) = N_v(x) - N_v^r = \begin{cases} \widehat{N}_v^+ \varepsilon_{yy}(x) & \text{for } \varepsilon_{yy}(x) \geq 0, \\ \widehat{N}_v^- \varepsilon_{yy}(x) & \text{for } \varepsilon_{yy}(x) < 0, \end{cases} \tag{A.10}$$

where $\widehat{N}_v^+ = -63 N_v^r$ and $\widehat{N}_v^- = 63 N_v^r$.

IV. MOBILITIES

Consider now the the strain-induced changes in electron and hole mobilities in silicon. These are at the origin of the piezoresistive effect and have been extensively studied both experimentally and theoretically. A comparison of the data of the literature can be found in Table 2.4 of Creemer (2002). It shows a scattering of about 20%. In light of the strain triaxiality of the problem, the spatial dependence of the xx-component of the mobilities reads

$$\Delta m_n(x) = m_n(x) - m_n^r = \widehat{m}_n \varepsilon_{yy}(x), \qquad \Delta m_p(x) = m_p(x) - m_p^r = \widehat{m}_p \varepsilon_{yy}(x). \tag{A.11}$$

Using the experimental values of Smith (1954), we have $\widehat{m}_n = -96 m_n^r$ and $\widehat{m}_p = 2 m_p^r$.

B

MATCHED ASYMPTOTICS: OUTER PROBLEM

In this appendix we solve, on the domains $(0, x_0)$ and $(x_0, 1)$, for the fields $\overline{u}$, $\overline{v}$ and $\overline{\varphi}$ defined in (3.30), the outer problem $(3.25)_{2,3}$, (3.27) and (3.33) along with boundary conditions (3.28).

Solving (3.33) for $\overline{\varphi}$, we obtain

$$\overline{\varphi} = \ln\left(\frac{C + \sqrt{C^2 + 4\delta^4 \overline{u}\overline{v}\exp\left[-\kappa \widehat{E}_g^e(x - x_0)\right]}}{2\delta^2 \overline{u}\exp\left[-\kappa \widehat{E}_c^e(x - x_0)\right]}\right). \tag{B.1}$$

For later use, on appeal to (B.1), we obtain the following approximations:

$$\begin{aligned}
&\exp\left[\overline{\varphi} - \kappa \widehat{E}_c^e(x - x_0)\right] = \\
&\qquad \begin{cases} \dfrac{\delta^2 \overline{v}}{N_a}\exp\left[-\kappa \widehat{E}_g^e(x - x_0)\right] + O(\delta^6) & \text{for } 0 \le x \le x_0, \\ \dfrac{N_d}{\delta^2 \overline{u}} + O(\delta^2) & \text{for } x_0 \le x \le 1, \end{cases} \\
&\exp\left[-\overline{\varphi} + \kappa \widehat{E}_v^e(x - x_0)\right] = \\
&\qquad \begin{cases} \dfrac{N_a}{\delta^2 \overline{v}} + O(\delta^2) & \text{for } 0 \le x \le x_0, \\ \dfrac{\delta^2 \overline{u}}{N_d}\exp\left[-\kappa \widehat{E}_g^e(x - x_0)\right] + O(\delta^6) & \text{for } x_0 \le x \le 1. \end{cases}
\end{aligned} \tag{B.2}$$

Inserting (B.1) and $(3.18)_2$ in (3.27), we also have an approximation for the recombination-generation rate R:

$$R = \begin{cases} \dfrac{\delta^4}{\tau_n N_a}(uv - 1)\exp\left[-\kappa \widehat{E}_g^e(x - x_0)\right] + O(\delta^6) & \text{for } 0 \le x \le x_0, \\ \dfrac{\delta^4}{\tau_p N_d}(uv - 1)\exp\left[-\kappa \widehat{E}_g^e(x - x_0)\right] + O(\delta^6) & \text{for } x_0 \le x \le 1. \end{cases} \tag{B.3}$$

Using (B.2), we rewrite $(3.25)_{2,4}$ for the currents of electrons and holes at leading order in δ:

$$\begin{aligned}
\overline{j}_n &= \begin{cases} -\left(m_n^0 + \kappa \widehat{m}_n(x - x_0)\right)\dfrac{\delta^4 \overline{v}\overline{u}'}{N_a}\exp\left[-\kappa \widehat{E}_g^e(x - x_0)\right] & \text{for } 0 \le x \le x_0, \\ -\left(m_n^0 + \kappa \widehat{m}_n(x - x_0)\right)\dfrac{N_d \overline{u}'}{\overline{u}} & \text{for } x_0 \le x \le 1, \end{cases} \\
\overline{j}_p &= \begin{cases} -\left(m_p^0 + \kappa \widehat{m}_p(x - x_0)\right)\dfrac{N_a \overline{v}'}{\overline{v}} & \text{for } 0 \le x \le x_0, \\ -\left(m_p^0 + \kappa \widehat{m}_p(x - x_0)\right)\dfrac{\delta^4 \overline{u}\overline{v}'}{N_d}\exp\left[-\kappa \widehat{E}_g^e(x - x_0)\right] & \text{for } x_0 \le x \le 1. \end{cases}
\end{aligned} \tag{B.4}$$

Although not justified *a priori*, we make ours the assumption of Markowich that u and v are well scaled (i.e.,that $\overline{u}, \overline{v}, \overline{u}'$and $\overline{v}'$ are $O(1)$) to show that $\bar{\jmath}_n$ and $\bar{\jmath}_p$ are $O(\delta^4)$ on $(0,1)$. Consider first $\bar{\jmath}_n$. By $(B.4)_1$, $\bar{\jmath}_n$ is $O(\delta^4)$ on $(0, x_0)$. Appealing to the continuity of $\bar{\jmath}_n$ across the junction and noticing that $\bar{\jmath}_n$ satisfies on $(x_0, 1)$ Equation $(3.25)_2$ with R of order $O(\delta^4)$ (see (B.3)), it follows that $\bar{\jmath}_n$ is $O(\delta^4)$ on $(0,1)$. Through a similar reasoning we also derive that $\bar{\jmath}_p$ is $O(\delta^4)$ on $(0,1)$.

In view of the expression $(B.4)_1$ for $\bar{\jmath}_n$ on $(x_0, 1)$ and the fact that $\bar{\jmath}_n$ is $O(\delta^4)$, it follows that $\overline{u}'$ is $O(\delta^4)$ on $(x_0, 1)$. By integration over $(x_0, 1)$ we obtain that $\overline{u}$ is constant up to a term of $O(\delta^4)$ on $(x_0, 1)$. Likewise, $\overline{v}$ is constant up to a term of $O(\delta^4)$ on $(0, x_0)$. Therefore, using the boundary conditions $(3.28)_{2,3}$ we have up to terms of $O(\delta^4)$:

$$\begin{cases} \overline{u}(x) = \overline{u}(1) = \exp[V] & \text{for } x \in (x_0, 1), \\ \overline{v}(x) = \overline{v}(0) = 1 & \text{for } x \in (0, x_0). \end{cases} \tag{B.5}$$

Recall that the variable u is associated to n and the variable v is associated to p. Physically, the fact that $\overline{u}$ and $\overline{v}$ are constant at leading order in δ in the regions $(x_0, 1)$ and $(0, x_0)$, respectively, should be related to the fact that $(x_0, 1)$ is the region where electrons are majority carrier and $(0, x_0)$ is the region where holes are majority carriers. The regions of majority carriers are regions were the concentrations of electrons and holes are governed by the dopant concentration at leading order. At this point, we still need the expressions of the fields $\overline{u}$ and $\overline{v}$ in the domain were electrons and holes are minority carriers, respectively.

Combining $(3.25)_2$, (B.3) and $(B.4)_1$, we obtain that $\overline{u}$ is, on $(0, x_0)$, solution of the differential equation

$$\left(m_n^0 + \kappa \widehat{m}_n (x - x_0)\right)\left(\overline{u}'' - \kappa \widehat{E}_g^e \overline{u}'\right) + \kappa \widehat{m}_n \overline{u}' = \frac{\overline{u}' - 1}{\tau_n}. \tag{B.6}$$

Introducing the diffusion length of electrons $L_n^0 := \sqrt{\tau_n m_n^0}$ and defining the variable

$$y := \overline{u} - 1, \tag{B.7}$$

we rewrite (B.6) as an equation for y on $(0, x_0)$,

$$y'' - \frac{1}{(L_n^0)^2} y + \kappa \left(\frac{\widehat{m}_n}{m_n^0} (x - x_0) y'' + \left(\frac{\widehat{m}_n}{m_n^0} - \widehat{E}_g^e \right) y' \right) + O(\kappa^2) = 0. \tag{B.8}$$

Likewise, we combine $(3.25)_3$, (B.3), and $(B.4)_2$, and introduce the variable

$$z := \overline{v} \exp[V] - 1 \tag{B.9}$$

to write the following equation for z on $(x_0, 1)$:

$$z'' - \frac{1}{(L_p^0)^2} z + \kappa \left(\frac{\widehat{m}_p}{m_p^0} (x - x_0) z'' + \left(\frac{\widehat{m}_p}{m_p^0} - \widehat{E}_g^e \right) z' \right) + O(\kappa^2) = 0, \tag{B.10}$$

where $L_p^0 := \sqrt{\tau_p m_p^0}$ is the diffusion length of holes.

We solve (B.8) by posing the following Poincaré asymptotic expansion:

$$y(x) = y_0(x) + \kappa y_1(x) + O(\kappa^2), \tag{B.11}$$

which we substitute in (B.8). At orders 0 and 1 in κ, we obtain the following equations on $(0, x_0)$:

$$\begin{cases} O(\kappa^0): & y_0'' - \dfrac{1}{(L_n^0)^2} y_0 = 0, \\ O(\kappa^1): & y_1'' - \dfrac{1}{(L_n^0)^2} y_1 = -\left(\dfrac{\widehat{m}_n}{m_n^0}(x - x_0) y_0'' + \left(\dfrac{\widehat{m}_n}{m_n^0} - \widehat{E}_g^e \right) y_0' \right), \end{cases} \tag{B.12}$$

along with the boundary conditions

$$\begin{cases} y_0(0) = 0, & y_0(x_0) = \exp[V] - 1, \\ y_1(0) = 0, & y_1(x_0) = 0. \end{cases} \tag{B.13}$$

The resolution of (B.12) yields, for $x \in (0, x_0)$,

$$\begin{cases} y_0(x) = \left(\exp[V] - 1 \right) \dfrac{\sinh\left(\dfrac{x}{L_n^0} \right)}{\sinh\left(\dfrac{x_0}{L_n^0} \right)}, \\ y_1(x) = -\dfrac{\exp[V] - 1}{8 L_n^0 \sinh\left(\dfrac{x_0}{L_n^0} \right)} \left[\cosh\left(\dfrac{x}{L_n^0} \right) \left(\dfrac{\widehat{m}_n}{m_n^0} 2x(x - 2x_0) \right) \right. \\ \qquad\qquad + \sinh\left(\dfrac{x}{L_n^0} \right) \left(-4 \widehat{E}_g^e L_n^0 (x - x_0) \right. \\ \qquad\qquad \left. \left. + \dfrac{\widehat{m}_n}{m_n^0} \left(2 L_n^0 (x - x_0) + 2 \coth\left(\dfrac{x_0}{L_n^0} \right) x_0^2 \right) \right) \right]. \end{cases} \tag{B.14}$$

Similarly, (B.10) is solved with the asymptotic expansion:

$$z(x) = z_0(x) + \kappa z_1(x) + O(\kappa^2). \tag{B.15}$$

At orders 0 and 1 in κ we obtain the following equations on $(x_0, 1)$:

$$\begin{cases} O(\kappa^0): & z_0'' - \dfrac{1}{(L_p^0)^2} z_0 = 0, \\ O(\kappa^1): & z_1'' - \dfrac{1}{(L_p^0)^2} z_1 = -\left(\dfrac{\widehat{m}_p}{m_p^0}(x - x_0) z_0'' + \left(\dfrac{\widehat{m}_p}{m_p^0} - \widehat{E}_g^e \right) z_0' \right), \end{cases} \tag{B.16}$$

along with the boundary conditions

$$\begin{cases} z_0(x_0) = \exp[V] - 1, & z_0(1) = 0, \\ z_1(x_0) = 0, & z_1(1) = 0. \end{cases} \tag{B.17}$$

The resolution of (B.16) yields, for $x \in (x_0, 1)$,

$$\begin{cases} z_0(x) = \Big(\exp[V] - 1\Big) \dfrac{\sinh\left(\dfrac{1-x}{L_p^0}\right)}{\sinh\left(\dfrac{1-x_0}{L_p^0}\right)}, \\ z_1(x) = \dfrac{\exp[V]-1}{8L_p^0 \sinh\left(\dfrac{1-x_0}{L_p^0}\right)} \Bigg[-\cosh\left(\dfrac{1-x}{L_p^0}\right)\left(\dfrac{\widehat{m}_p}{m_p^0} 2(1-x)(x-2x_0+1)\right) \\ \qquad + \sinh\left(\dfrac{1-x}{L_p^0}\right)\Bigg(4\widehat{E}_g^e L_p^0 (x-x_0) \\ \qquad + \dfrac{\widehat{m}_p}{m_p^0}\left(-2L_p^0(x-x_0) + 2\coth\left(\dfrac{1-x_0}{L_p^0}\right)(1-x_0)^2\right)\Bigg)\Bigg]. \end{cases} \tag{B.18}$$

We now know the functions y and z on $(0, x_0)$ and $(x_0, 1)$, respectively. Hence, combining (B.5), (B.7), (B.9), (B.11), (B.15), (B.14), and (B.18), we obtain an explicit expression for $\overline{u}$ and $\overline{v}$ on $(0, 1)$ (which we do not report here for the sake of brevity). We can combine (B.4) with these expressions of $\overline{u}$ and $\overline{v}$ to compute the currents of electrons and holes in the minority carrier regions. The currents, when evaluated at x_0^- and x_0^+ for j_n and j_p, are given in (3.34).

C

DERIVATION OF THE STRAIN-DEPENDENT ELECTRONIC PARAMETERS WITH FULL GENERALITY OF THE STRAIN TRIAXIALITY

In this appendix, we present the strain dependence of the electronic parameters of silicon, for an arbitrary strain triaxiality. To this end, we use the results from the solid state physics literature on the strain dependence of the properties of the subbands of the conduction and valence bands of silicon and derive an equivalent two-band formulation of the effective strain dependence of the band edges and densities of states. In sum, we compute, in this appendix, the following quantities:

$$\begin{cases} \Delta E_c(\varepsilon) := E_c(\varepsilon) - E_c^r, & \Delta E_v(\varepsilon) := E_v(\varepsilon) - E_v^r, \\ \Delta N_c(\varepsilon) := N_c(\varepsilon) - N_c^r, & \Delta N_v(\varepsilon) := N_v(\varepsilon) - N_v^r, \end{cases} \tag{C.1}$$

as well as the changes in mobilities,

$$\Delta \mathbf{M}_n(\varepsilon) := \mathbf{M}_n(\varepsilon) - \mathbf{M}_n^r, \qquad \Delta \mathbf{M}_p(\varepsilon) = \mathbf{M}_p(\varepsilon) - \mathbf{M}_p^r, \tag{C.2}$$

where the superscript r denotes the relaxed state of the crystal (zero strain).

From a microscopic prospective, the effect of strain on these electronic parameters is originated in the modification of the energy band structure induced by the deformation. More precisely, the conduction and valence bands are composed of subbands whose edges and curvature (directly related to both the effective mass and the effective density of state) are modified by the crystal deformation. Consequently, the mobilities $\mathbf{M}_n$ and $\mathbf{M}_p$ that are related to the distribution of carriers in the different subbands and their effective masses are also affected by strains. The theoretical modeling of the strain dependence using deformation potential theory has been considered under various assumptions by, among others, Bardeen and Shockley (1950), Bir et al. (1974), Kleimann et al. (1998), and Herring and Vogt (1956) and an up-to-date discussion can be found in Kanda (1991) and Creemer et al. (2001), Creemer (2002), Chapter 2.

C.1 REDUCTION OF THE BAND STRUCTURE TO A TWO BANDS DESCRIPTION

The energy band structure of silicon has six subbands in the conduction band and two subbands—called heavy hole band and light hole band—in the valence band (a third subband of the valence band, called spin-orbit band, can be neglected as justified subsequently). Band structure computations performed on the strained crystal allows to quantify the strain-induced changes in each subband. In this section, we shall reduce the multiple bands picture of solid-state physics to a simplified description with one effective conduction band and one effective valence band whose strain-induced changes are equivalent to the compiled effect of the subbands.

C.1.1 *Conduction band*

First, consider the conduction band of silicon. Its six subbands have, in the relaxed state, equal Density Of States (DOS), denoted by $N_{sc,r}$ (the index sc indicates a Subband of the Conduction band and r the Relaxed state $\boldsymbol{\varepsilon} = \mathbf{0}$), and equal edge energy corresponding to the edge energy of the effective conduction band $E_{c,r}$. A general non-isotropic strain changes the edge energy of the m conduction subband by the quantity $\Delta E_{sc}^{m}(\boldsymbol{\varepsilon})$, while the change in effective density of states is much smaller and can be neglected (Creemer, 2002). Note that in terms of edge energy, the degeneracy of the six levels is lifted by a non-isotropic strain. The computation of the change in band edge $\Delta E_{sc}^{m}(\boldsymbol{\varepsilon})$ is treated with the deformation potential theory that was introduced by Bardeen and Shockley (1950) and further developed by Herring and Vogt (1956) and Bir et al. (1974). It is usually modeled with the *dilational deformation potential* Ξ_d and *shear deformation potential* Ξ_u by:

$$\Delta E_{sc}^{m}(\boldsymbol{\varepsilon}) = (\Xi_d \mathbb{1} + \Xi_u \mathbf{k}^m \otimes \mathbf{k}^m) : \boldsymbol{\varepsilon}, \tag{C.3}$$

where $\mathbf{k}^m$ is the unit vector associated to the direction of the band m in the $\mathbf{k}$-space (reciprocal to the physical space).

Let $\mathcal{B}_M = (\mathbf{e}_1, \mathbf{e}_2, \mathbf{e}_3)$, the basis aligned with the principal crystallographic directions $\langle 100 \rangle$ of silicon (index M of $\mathcal{B}_M$ is for material, as it is attached to the directions of the material), the $\mathbf{k}^m$ vectors are $\pm\mathbf{e}_1, \pm\mathbf{e}_2, \pm\mathbf{e}_3$ for the subbands $m = 1, 4$, $m = 2, 5$, and $m = 3, 6$, respectively. Values for Ξ_d and Ξ_u vary in the literature by about 10 %. We take the values of Herring and Vogt (1956): $\Xi_d = 1.1$ eV and $\Xi_u = 10.5$ eV.

We now introduce a unique effective conduction band with DOS N_c and edge energy $E_c(\boldsymbol{\varepsilon})$. Its definition is determined such that this description is equivalent to the multiple-band model. This *equivalence* is translated by the equality, for any strain $\boldsymbol{\varepsilon}$, between the densities of electrons in the one-band description and in the six-subband description.

In the multiple-band description, the density of electrons $n(\boldsymbol{\varepsilon})$ is given by (Wortman et al., 1964)

$$n(\boldsymbol{\varepsilon}) = \sum_{m=1}^{6} N_{sc} \exp\Big[-\big(E_c^r + \Delta E_{sc}^{m}(\boldsymbol{\varepsilon}) - E_{F_n}(\boldsymbol{\varepsilon})\big)/k_B T \Big], \tag{C.4}$$

where $E_{F_n}(\boldsymbol{\varepsilon})$ is the quasi-Fermi level for electrons. Likewise, in the one-band description, the density of electrons reads

$$n(\boldsymbol{\varepsilon}) = N_c \exp\Big[-\big(E_c^r + \Delta E_c(\boldsymbol{\varepsilon}) - E_{F_n}(\boldsymbol{\varepsilon})\big)/k_B T \Big]. \tag{C.5}$$

Letting

$$N_c := 6N_{sc}, \qquad \Delta E_c(\boldsymbol{\varepsilon}) := -k_B T \ln\left(\frac{1}{6} \sum_{m=1}^{6} \exp\big[-\Delta E_{sc}^{m}(\boldsymbol{\varepsilon})/k_B T \big] \right), \tag{C.6}$$

the equality of electron densities in the two descriptions (C.4) and (C.5) is satisfied. Aiming at developing a first order linear theory of the effect of strain on semiconductors, we linearize (C.6) for small strain-induced changes

$$\Delta E_c(\varepsilon) = \frac{1}{6}\sum_{m=1}^{6} \Delta E_{sc}^m(\varepsilon). \tag{C.7}$$

Finally, inserting (C.3) in (C.7) yields

$$\Delta E_c(\varepsilon) = \left(\Xi_d + \frac{1}{3}\Xi_u\right)\mathbb{1} : \varepsilon, \tag{C.8}$$

relation used in (A.7).

C.1.2 *Valence band*

Second, consider the valence band comprised of the heavy hole band and light hole band. While these two bands have the same energy level in the relaxed state, there also exists a third subband, the spin-orbit coupling band, lying at a lower energy level than the two others. As such, this subband contributes much less to the density of holes and can be neglected. In the same way as for the conduction band, we derive an equivalent one-band description with the additional difficulty that the densities of states of the heavy and light hole bands depend significantly on strain.

Denote by $\Delta E_{sv}^l(\varepsilon)$ and $\Delta E_{sv}^h(\varepsilon)$ the changes in band edge energy of the light and heavy hole subbands with respect to their common level in the relaxed state E_v^r and let $\Delta N_{sv}^l(\varepsilon)$ and $\Delta N_{sv}^h(\varepsilon)$ the changes in DOS of these two subbands. In the multiple-band description, the density of holes $p(\varepsilon)$ is given by

$$\begin{aligned} p(\varepsilon) = \Bigg(&\left(N_{sv,r}^l + \Delta N_{sv}^l(\varepsilon)\right)\exp\left[\Delta E_{sv}^l(\varepsilon)/k_BT\right] + \\ &\left(N_{sv,r}^h + \Delta N_{sv}^h(\varepsilon)\right)\exp\left[\Delta E_{sv}^h(\varepsilon)/k_BT\right]\Bigg)\exp\left[\left(E_v^r - E_{F_p}(\varepsilon)\right)/k_BT\right], \end{aligned} \tag{C.9}$$

where $E_{F_p}(\varepsilon)$ is the quasi-Fermi level of holes.

In the one-band description of the valence band, the density of holes reads

$$p(\varepsilon) = \left(N_v^r + \Delta N_v(\varepsilon)\right)\exp\left[\left(E_v^r + \Delta E_v(\varepsilon) - E_{F_p}(\varepsilon)\right)/k_BT\right], \tag{C.10}$$

where $\Delta N_v(\varepsilon)$ and $\Delta E_v(\varepsilon)$ are the effective change of the one-band density of states and energy level to be computed from the knowledge on the subbands. Equalizing (C.9) and (C.10) yields at first order in ε

$$\begin{aligned} \Delta N_v(\varepsilon) &= \Delta N_{sv}^l(\varepsilon) + \Delta N_{sv}^h(\varepsilon), \\ \Delta E_v(\varepsilon) &= \frac{N_{sv,r}^l}{N_v^r}\Delta E_{sv}^l(\varepsilon) + \frac{N_{sv,r}^h}{N_v^r}\Delta E_{sv}^h(\varepsilon). \end{aligned} \tag{C.11}$$

In sum, the strain dependence of the equivalent one-band quantities has been expressed as function of the strain dependence of the subband quantities. The

latter can be found in the solid state physics literature, in particular the change in subband energy level is given by Kanda (1967), for $u = h, l$,

$$\Delta E^u_{sv}(\boldsymbol{\varepsilon}) = a\,\mathbb{1} : \boldsymbol{\varepsilon} \pm \left(\frac{b^2}{2}\left((\varepsilon_{11}-\varepsilon_{22})^2 + (\varepsilon_{11}-\varepsilon_{33})^2 + (\varepsilon_{33}-\varepsilon_{22})^2\right) \right. \\ \left. d^2\left(\varepsilon_{12}^2 + \varepsilon_{13}^2 + \varepsilon_{23}^2\right)\right)^{1/2}, \quad \text{(C.12)}$$

where the the plus sign is for the heavy hole band and the minus sign for the light hole band (see, e. g., Creemer, 2002, Chapter 2) and a, b and d are the valence band deformation potentials for which we retain the most recent values of Fischetti and Laux (1996): $a = 2.1$ eV, $b = -2.33$ eV and $d = -4.75$ eV. For the effective description of the valence band, $\Delta E_v(\boldsymbol{\varepsilon})$ is obtained combining (C.11) and (C.12) with $N^h_{sv,r}/N^r_v = 0.84$ and $N^l_{sv,r}/N^r_v = 0.16$.[1]

While it has been recognized early that, unlike the conduction band, the effective density of states of the valence band depends on strain (Kanda, 1967; Bir et al., 1974; Kleimann et al., 1998) it is only recently that Creemer (2002) pointed out that the change in DOS of the valence band contributes significantly to the piezojunction effect, in particular at relatively moderate strain (a few tenth of percent). We do not have an analytical expression valid for an arbitrary triaxial strain state of that strain dependence and therefore assume an hydrostatic relation, which we calibrate from the band calculations under uniaxial strain of Creemer (2002). In addition, these band calculations reflect a symmetric behavior between tensile and compressive strains, which we account for. The hydrostatic strain dependence is a strong assumption and we should, in the following, keep in mind that the estimated contribution to the change in electric current induced by modification of the valence band density of states is very uncertain. In sum, we write, for each valence subband $u = h, l$,

$$\Delta N^u_{sv}(\boldsymbol{\varepsilon}) = \widetilde{N}^u_{sv}\,|\mathbb{1} : \boldsymbol{\varepsilon}|, \quad \text{(C.15)}$$

where the scalar coefficients $\widetilde{N}^l_{sv} = 240 N^l_{sv,r}$ and $\widetilde{N}^h_{sv} = -240 N^h_{sv,r}$ are computed from Figure 2.16 of Creemer (2002). Combining (C.11) with (C.15), we obtain the strain dependence of the effective valence band density of states:

$$\Delta N_v(\boldsymbol{\varepsilon}) = \widetilde{N}_v\,|\mathbb{1} : \boldsymbol{\varepsilon}|, \quad \text{(C.16)}$$

with $\widetilde{N}_v = -170 N^r_v$. Relation (C.16) is only an approximate estimation of the strain effect on the DOS of the valence band. A detailed band calculation under strain is be required to derive a more exact strain dependence with full account of strain triaxiality.

1 These ratio of density of states are obtained as follows. The effective density of states of each subband is related to the effective mass of each subband m^l and m^h by (Sze and Ng, 2006)

$$N^u_{sv,r} \propto (m^u)^{3/2}, \quad \text{(C.13)}$$

for $u = l, h$ where $m^l = 0.16 m_0$ and $m^h = 0.49 m_0$ with m_0 the free-electron mass. In addition, the density of states of the effective valence band is simply,

$$N^r_v = N^l_{sv,r} + N^h_{sv,r}, \quad \text{(C.14)}$$

which combined with (C.13) yields the ratios of DOS.

C.2 CHANGE IN MOBILITIES

The change with strain of mobility of electrons and holes is equal to the opposite of the change in resistivity. The latter is measured in experiments (Smith, 1954; Creemer, 2002) and, as such, yields the mobility changes of electrons and holes in the effective one-band description. Thus, there is no need to resort to the subband description for mobilities. The changes in resistivity are usually expressed with respect to the stress tensor $\boldsymbol{\sigma}$ with the rank-4 piezoresistive tensors $\boldsymbol{\Pi}_n$ and $\boldsymbol{\Pi}_p$ for electrons and holes (Smith, 1954; Creemer, 2002). Using those tensors and the constitutive relation $\boldsymbol{\sigma} = \mathbf{c} : \varepsilon$ with $\mathbf{c}$ the elasticity tensor, the relative change in the ij-coefficient of the mobility tensor can be expressed with the small strain tensor ε

$$\frac{(\Delta \mathbf{M}_q)_{ij}(\varepsilon)}{(\mathbf{M}_q^r)_{ij}} = -\left(\boldsymbol{\Pi}_q : \mathbf{c} : \varepsilon\right)_{ij}, \tag{C.17}$$

for $q = n, p$ and for every $i, j = 1, 2, 3$, without summation on the repeated indices.

PRACTICAL CALCULATION OF THE EFFECT OF STRAIN ON MOBILITIES

Relation (C.17) can be expressed in matrix form using the Voigt notation. Denote by $[\mathbf{a}]^{\mathcal{B}}$ the matrix of the coefficient of a tensor $\mathbf{a}$ of rank-1 or -2 in the basis $\mathcal{B}$ and $[[\mathbf{A}]]^{\mathcal{B}}$ the matrix of the coefficients, *in Voigt notation*, of a properly symmetric tensor $\mathbf{A}$ of rank-2 or -4 in basis $\mathcal{B}$. For any rank-2 tensor, we have the usual relation between classical and Voigt notations

$$\begin{aligned} &[[\mathbf{A}]]_1 = [\mathbf{A}]_{11}, \quad [[\mathbf{A}]]_2 = [\mathbf{A}]_{22}, \quad [[\mathbf{A}]]_3 = [\mathbf{A}]_{33}, \\ &[[\mathbf{A}]]_4 = [\mathbf{A}]_{23}, \quad [[\mathbf{A}]]_5 = [\mathbf{A}]_{13}, \quad [[\mathbf{A}]]_6 = [\mathbf{A}]_{12}, \end{aligned} \tag{C.18}$$

with an exception for the extradiagonal terms of the strain tensor ε

$$[[\varepsilon]]_4 = 2[\varepsilon]_{23}, \quad [[\varepsilon]]_5 = 2[\varepsilon]_{13}, \quad [[\varepsilon]]_6 = 2[\varepsilon]_{12}. \tag{C.19}$$

This allows us to rewrite (C.17) as

$$\frac{[[\Delta \mathbf{M}_q]]_i(\varepsilon)}{[[\mathbf{M}_q^r]]_i} = -\left([[\boldsymbol{\Pi}]]_q \cdot [[\mathbf{c}]] \cdot [[\varepsilon]]\right)_i, \tag{C.20}$$

for every $i = 1, 2, 3$, where for two rank-2 or -4 tensors $\mathbf{A}$ and $\mathbf{B}$, $[[\mathbf{A}]] \cdot [[\mathbf{B}]]$ denotes the traditional matrix-matrix or matrix-vector product.

In Voigt notations, due to the cubic symmetries of silicon, in the basis $\mathcal{B}_M$ the matrices $[[\boldsymbol{\Pi}_q]]$ for $q = n, p$ read (Smith, 1954; Sun et al., 2010)

Recall that $\mathcal{B}_M$ is aligned with directions $\langle 100 \rangle$ of the crystal.

$$[[\boldsymbol{\Pi}_q]]^{\mathcal{B}_M} = \begin{pmatrix} \Pi_{11}^q & \Pi_{12}^q & \Pi_{12}^q & 0 & 0 & 0 \\ \Pi_{12}^q & \Pi_{11}^q & \Pi_{12}^q & 0 & 0 & 0 \\ \Pi_{12}^q & \Pi_{12}^q & \Pi_{11}^q & 0 & 0 & 0 \\ 0 & 0 & 0 & \Pi_{44}^q & 0 & 0 \\ 0 & 0 & 0 & 0 & \Pi_{44}^q & 0 \\ 0 & 0 & 0 & 0 & 0 & Pi_{44}^q \end{pmatrix}, \tag{C.21}$$

Π_{11}^n	Π_{12}^n	Π_{44}^n	Π_{11}^p	Π_{12}^p	Π_{44}^p
-102.2	53.4	-13.6	6.6	-1.1	138.1

Table C.1: Piezoresistive coefficients in 10^{-11} Pa^{-1} from Smith (1954). For comparison with values obtained by other works see Creemer (2002), Table 2.4.

with the coefficients summarized in Table C.1. Note the variations of two orders of magnitude between the different coefficients of Table C.1, which indicate that the carrier mobilities might be significantly or little affected by the stress depending on:

1. The stress state,
2. The relevant components of the mobility tensor for the particular directions of current and electrochemical potential gradient in the experiment.

We also recall that the elasticity tensor $\mathbf{c}$ of silicon in Voigt notation has the same form as (C.21) with coefficients in the basis $\mathcal{B}_M$, $c_{11} = 166$ GPa, $c_{12} = 64$ GPa and $c_{44} = 80$ GPa (Wortman and Evans, 1965).

D

DETAILS OF THE LINEAR STABILITY ANALYSIS WITH DYNAMICS TERMS

EXPRESSION OF THE OPERATORS $\mathcal{A}$ AND $\mathcal{B}$

In section 8.3.2 the linear operators $\mathcal{A}$ and $\mathcal{B}$ read as follows

$$\begin{aligned}
&\mathcal{A}(\mathbf{q}_{n-1},\mathbf{q}_n,\mathbf{q}_{n+1},\mathbf{q}_{n+2}) = \\
&\begin{pmatrix} A_1^1(u)\,(\delta x_n - \delta x_{n+1}) \\ A_2^1\,\delta x_n + A_2^{1\prime}\,\delta x_{n+1} + A_2^{1\prime\prime}\,\delta x_{n+2} \\ A_3^1\,\delta x_{n-1} + A_3^{1\prime}\,\delta x_n + A_3^{1\prime\prime}\,\delta x_{n+1} \\ A_4^1\,(\delta x_{n-1} - 2\delta x_n + \delta x_{n+1}) \end{pmatrix} + \begin{pmatrix} A_1^2\,\delta\tilde\rho_n(u,t) \\ A_2^2\,\delta\tilde\rho_{n+1}^+ + A_2^{2\prime}\,\delta\tilde\rho_n^- \\ A_3^2\,\delta\tilde\rho_n^+ + A_3^{2\prime}\,\delta\tilde\rho_{n-1}^- \\ A_4^2\,\delta\tilde\rho_n^+ + A_4^{2\prime}\,\delta\tilde\rho_{n-1}^- \end{pmatrix} \\
&\qquad + \begin{pmatrix} A_1^3\,\partial_u\delta\tilde\rho_n(u,t) \\ A_2^3\,(\partial_u\delta\tilde\rho_n)^- \\ A_3^3\,(\partial_u\delta\tilde\rho_n)^+ \\ 0 \end{pmatrix} + \begin{pmatrix} A_1^4\,\partial_{uu}\delta\tilde\rho_n(u,t) \\ 0 \\ 0 \\ 0 \end{pmatrix},
\end{aligned} \tag{D.1}$$

where

$$\left\{\begin{aligned}
A_1^1(u) =& 2\nu\overset{o}{\tilde\rho}(u) - 2F - \overset{o}{V}\overset{o}{\tilde\rho}'(u),\\
A_2^1 =& \overline{\kappa}(1+3\overline{\alpha}-\overline{\beta}) + (\overline{\kappa}_p + \chi\overline{\kappa}\Theta)\overset{o}{\tilde\rho}(0) - \big(\overline{\kappa}(1+\chi\Theta) + \overline{\kappa}_p + \overset{o}{V}\big)\overset{o}{\rho}(1),\\
A_2^{1\prime} =& -\overline{\kappa}(1+6\overline{\alpha}-2\overline{\beta}) - (\overline{\kappa}_p + \chi\overline{\kappa}\Theta)\overset{o}{\tilde\rho}(0)\\
&\qquad + \big(\overline{\kappa}(1+\chi\Theta) + \overline{\kappa}_p + \overset{o}{V}\big)\overset{o}{\rho}(1),\\
A_2^{1\prime\prime} =& \overline{\kappa}(3\overline{\alpha}-\overline{\beta}), \quad A_3^1 = \overline{\kappa}S(3\overline{\alpha}-\overline{\beta}),\\
A_3^{1\prime} =& \overline{\kappa}S(1-6\overline{\alpha}+2\overline{\beta}) + (\overline{\kappa}_p - \chi\overline{\kappa}S\Theta)\overset{o}{\tilde\rho}(1)\\
&\qquad + \big(\overline{\kappa}S + (\chi\Theta-1) - \overline{\kappa}_p + \overset{o}{V}\big)\overset{o}{\rho}(0),\\
A_3^{1\prime\prime} =& -\overline{\kappa}S(1-3\overline{\alpha}+\overline{\beta}) - (\overline{\kappa}_p - \chi\overline{\kappa}S\Theta)\overset{o}{\tilde\rho}(1)\\
&\qquad + \big(\overline{\kappa}S + (1-\chi\Theta) + \overline{\kappa}_p - \overset{o}{V}\big)\overset{o}{\rho}(0),\\
A_4^1 =& \Theta\overline{\kappa}(1+S)(\overline{\beta}-3\overline{\alpha}),\\
A_1^2 =& -\overline{\nu}, \quad A_2^2 = -\chi\overline{\kappa}\Theta - \overline{\kappa}_p, \quad A_2^{2\prime} = \overline{\kappa}(1+\chi\Theta) + \overline{\kappa}_p + \overset{o}{V},\\
A_3^2 =& \overline{\kappa}S(1-\chi\Theta) + \overline{\kappa}_p - \overset{o}{V}, \quad A_3^{2\prime} = \chi\overline{\kappa}S\Theta - \overline{\kappa}_p,\\
A_4^2 =& \overline{\kappa}\Theta\big(\chi\Theta(1+S) - S\big), \quad A_4^{2\prime} = -\overline{\kappa}\Theta\big(\chi\Theta(1+S)+1\big),\\
A_1^3 =& \overset{o}{V}, \quad A_2^3 = 1, \quad A_3^3 = -1, \quad A_1^4 = 1.
\end{aligned}\right. \tag{D.2}$$

and

$$\mathcal{B}\left(\partial_t \mathbf{q}_n, \partial_t \mathbf{q}_{n+1}\right) = \begin{pmatrix} (u-1)\overset{o}{\tilde{\rho}}'(u)\delta\dot{x}_n - u\overset{o}{\tilde{\rho}}'(u)\delta\dot{x}_{n+1} \\ \overset{o}{\tilde{\rho}}(1)\delta\dot{x}_{n+1} \\ \overset{o}{\tilde{\rho}}(0)\delta\dot{x}_n \\ \delta\dot{x}_n \end{pmatrix} + \begin{pmatrix} \partial_t \delta\tilde{\rho}_n(u,t) \\ 0 \\ 0 \\ 0 \end{pmatrix}, \quad \text{(D.3)}$$

EXPRESSION OF THE OPERATORS $\hat{\mathcal{A}}_k$ AND $\hat{\mathcal{B}}_k$

The operators $\hat{\mathcal{A}}_k$ and $\hat{\mathcal{B}}_k$ after the Bloch wave decomposition have the following expressions (we show in red the terms coming from the dynamics terms, see the explanations in Section 8.1):

$$\begin{aligned} \hat{\mathcal{A}}_k \hat{\mathbf{q}} &= \hat{\mathcal{A}}_k^1(u)\delta\hat{x} + \hat{\mathcal{A}}_k^2\delta\hat{\rho}(u) + \hat{\mathcal{A}}_k^3\delta\hat{\rho}'(u) + \hat{\mathcal{A}}_k^4\delta\hat{\rho}''(u) \\ &= \begin{pmatrix} \hat{A}_1^1(u)\delta\hat{x} \\ \hat{A}_2^1\delta\hat{x} \\ \hat{A}_3^1\delta\hat{x} \\ \hat{A}_4^1\delta\hat{x} \end{pmatrix} + \begin{pmatrix} \hat{A}_1^2\delta\hat{\rho}(u) \\ \hat{A}_2^2\delta\hat{\rho}(0) + \hat{A}_2^{2\prime}\delta\hat{\rho}(1) \\ \hat{A}_3^2\delta\hat{\rho}(0) + \hat{A}_3^{2\prime}\delta\hat{\rho}(1) \\ \hat{A}_4^2\delta\hat{\rho}(0) + \hat{A}_4^{2\prime}\delta\hat{\rho}(1) \end{pmatrix} + \begin{pmatrix} \hat{A}_1^3\delta\hat{\rho}'(u) \\ \hat{A}_2^3\delta\hat{\rho}'(1) \\ \hat{A}_3^3\delta\hat{\rho}'(0) \\ 0 \end{pmatrix} + \begin{pmatrix} \hat{A}_1^4\delta\hat{\rho}''(u) \\ 0 \\ 0 \\ 0 \end{pmatrix}, \end{aligned} \quad \text{(D.4)}$$

and

$$\begin{aligned} \hat{\mathcal{B}}_k \hat{\mathbf{q}} &= \hat{\mathcal{B}}_k^1(u)\delta\hat{x} + \hat{\mathcal{B}}_k^2\delta\hat{\rho}(u) \\ &= \begin{pmatrix} \hat{B}_1^1(u)\delta\hat{x} \\ \hat{B}_2^1\delta\hat{x} \\ \hat{B}_3^1\delta\hat{x} \\ \hat{B}_4^1\delta\hat{x} \end{pmatrix} + \begin{pmatrix} \hat{B}_1^2\delta\hat{\rho}(u) \\ 0 \\ 0 \\ 0 \end{pmatrix}, \end{aligned} \quad \text{(D.5)}$$

where

$$
\begin{cases}
\hat{A}_1^1(u) = \left(-1+\mathrm{e}^{ik}\right)\left(2\overline{F} - 2\overline{\nu}\overset{o}{\tilde{\rho}}(u) + \overset{o}{V}\overset{o\prime}{\tilde{\rho}}(u)\right), \\
\hat{A}_2^1 = \left(-1+\mathrm{e}^{ik}\right)\left(\overline{\kappa}\left((\mathrm{e}^{ik}-1)(3\overline{\alpha}-\overline{\beta}) + (\overset{o}{\tilde{\rho}}(1)-\overset{o}{\tilde{\rho}}(0))\chi\Theta + \overset{o}{\tilde{\rho}}(1) - 1\right)\right. \\
\qquad\qquad \left. + \overset{o}{\tilde{\rho}}(1)(\overline{\kappa}_p + \overset{o}{V}) - \overline{\kappa}_p\overset{o}{\tilde{\rho}}(0)\right), \\
\hat{A}_3^1 = \left(-1+\mathrm{e}^{ik}\right)\left(\overline{\kappa}S\left((1-\mathrm{e}^{-ik})(3\overline{\alpha}-\overline{\beta}) - \overset{o}{\tilde{\rho}}(0)(\chi\Theta-1) + \overset{o}{\tilde{\rho}}(1)\chi\Theta - 1\right)\right. \\
\qquad\qquad \left. + \overset{o}{\tilde{\rho}}(0)(\overline{\kappa}_p - \overset{o}{V}) - \overline{\kappa}_p\overset{o}{\tilde{\rho}}(1)\right), \\
\hat{A}_4^1 = -2\overline{\kappa}(S+1)\Theta(3\overline{\alpha}-\overline{\beta})(\cos(k)-1), \\
\hat{A}_1^2 = -\overline{\nu}, \quad \hat{A}_2^2 = -\mathrm{e}^{ik}(\chi\overline{\kappa}\Theta + \overline{\kappa}_p), \quad \hat{A}_2^{2\prime} = \overline{\kappa}_p + \overline{\kappa}(1+\chi\Theta) + \overset{o}{V}, \\
\hat{A}_3^2 = \overline{\kappa}S(1-\chi\Theta) + \overline{\kappa}S + \overline{\kappa}_p - \overset{o}{V}, \quad \hat{A}_3^{2\prime} = \mathrm{e}^{-ik}(\chi\overline{\kappa}S\Theta - \overline{\kappa}_p), \\
\hat{A}_4^2 = \overline{\kappa}\Theta\big((S+1)\chi\Theta - S\big), \quad \hat{A}_4^{2\prime} = -\mathrm{e}^{-ik}\overline{\kappa}\Theta\big((S+1)\chi\Theta + 1\big), \\
\hat{A}_1^3 = \overset{o}{V}, \quad \hat{A}_2^3 = 1, \quad \hat{A}_3^3 = -1, \quad \hat{A}_1^4 = 1, \\
\hat{B}_1^1(u) = -\left(1 + \left(-1+\mathrm{e}^{ik}\right)u\right)\overset{o\prime}{\tilde{\rho}}(u), \quad \hat{B}_2^1 = -\mathrm{e}^{ik}\overset{o}{\tilde{\rho}}(1), \\
\hat{B}_3^1 = \overset{o}{\tilde{\rho}}(0), \quad \hat{B}_4^1 = -1, \quad \hat{B}_1^2 = 1.
\end{cases}
\tag{D.6}
$$

E

SELECTION OF THE MATERIAL PARAMETERS OF CRYSTAL GROWTH

E.1 MATERIAL PARAMETERS FOR SI(111)-7×7 AND GAAS(001)

Based on the material properties of GaAs, Si and SiGe as found in the experimental literature, we discuss the values of the eight dimensionless parameters defined in Section 7.2.3. When estimation of these parameters from material properties appears difficult, we provide ranges, which are physically sensible.

Note that, in addition to a dependence on quantities intrinsic to material properties of the vicinal surfaces, many of the parameters ($\overline{F}$, $\overline{\nu}$, $\overline{\kappa}$, $\overline{\kappa}_p$, $\overline{\alpha}$ and $\overline{\beta}$) involve the initial terrace width L_0, itself related to the experimentally chosen miscut angle of the vicinal surface. Given that typical terrace widths vary between 10 nm and 200 nm (for typical miscut angles between 0.1° and 2°), the parameters are subsequently expressed for a reference terrace width $L_0^* = 20\,\text{nm}$ and denoted by $\overline{F}^*$, $\overline{\nu}^*$, $\overline{\kappa}^*$, $\overline{\kappa}_p^*$, $\overline{\alpha}^*$ and $\overline{\beta}^*$. For each of these parameters, the value at an arbitrary terrace width can be obtained with a relation of the type $\overline{X} = \overline{X}^*(L_0/L_0^*)^p$ with p the power associated to the parameter considered.

Upper bounds on $\overline{F}$ and $\overline{\nu}$

Before referring to experimental evaluations of the parameters, note that, the satisfaction of the "near equilibrium" assumption ($|\rho - \rho_{eq}^*| \ll \rho_{eq}^*$ with dimensional quantities) underlying the derivation of Section 7.2.2 implies upper bounds on $\overline{F}$ and $\overline{\nu}$. Physically, given the finite diffusion speed of adatoms, a high deposition (evaporation) rate involves possibly too high adatom excess (deficit) far from the adatoms sinks (the steps), i.e., around the middle of the terraces.

For estimating these bounds, consider first a situation of pure deposition ($\overline{\nu} = 0$) with equidistant steps, under the assumption of infinite a/d velocities ($\overline{\kappa} \to \infty$). This assumption, conservative in the sense that it tends to underestimate the adatom density on terraces, implies that $\overset{o}{\rho}{}^{\pm} = 1$ and $\overset{o}{\rho}(x) = 1 - 1/2\overline{F}x(x-1)$ with a maximum adatom densities of $\overset{o}{\rho}_{max} = 1 + \overline{F}/8$ at $x = 1/2$. Expressing quantitatively the near equilibrium assumption as a maximum departure from the equilibrium adatom density of, e.g., one fourth of that density, implies a restriction on $\overline{F}$, specifically, $\overline{F} < 2$. A similar reasoning for the case of pure evaporation ($\overline{F} = 0$) implies that $\overline{\nu} < 2.5$.

In sum, the consistency with the near equilibrium assumption requires $\overline{F}$ and $\overline{\nu}$ not to be more, in order of magnitude, than unity.

Note that the near equilibrium assumption is not the only reason behind an upper bound of order one for $\overline{F}$ and $\overline{\nu}$, indeed as developed in Michely and

Krug (2012) and Krug (2005), a too high deposition rate (quantitatively $\overline{F}\Theta > 1$) would lead to island nucleation, i.e., the breaking of step flow growth.

These two considerations (satisfaction of the near equilibrium assumption and prevention of island nucleation) both lead to the requirement for a low deposition rate, which is exactly the condition (8.1) behind the quasistatic approximation detailed in Section 8.1.1. This implies that as far as step flow growth is concerned, this slow deposition condition is always satisfied or close to be satisfied, which justifies our discussion of the quasistatic approximation in that very regime.

Equilibrium adatom coverage Θ

The equilibrium adatom coverage for GaAs(001) and Si(111) has been measured by different groups, with the same technique consisting in rapid quenching of an equilibrium vicinal surface and observations of islands resulting from the crystallization of adatoms.

For GaAs(001), Johnson et al. (1996) (see also Johnson et al., 1997; Tersoff et al., 1997) measured the equilibrium adatom coverage under typical Molecular Beam Epitaxy (MBE) conditions. Noting that, as there is permanent exchange of As between the vapor and the surface, the limiting component of growth is Ga, the measurement of its typical equilibrium density coverage—which in addition to temperature, depends also on the As pressure—is between $\Theta = 0.05$ and $\Theta = 0.2$ for temperatures between 570°C and 600°C.

For Si(111), one should distinguish between the low temperature regime (650°C to 850°C) where silicon exhibits a 7×7 surface reconstruction—typical temperature of MBE crystal growth (see e.g. Ronda and Berbezier, 2004; Omi et al., 2005)—and the high temperature regime (850°C to 1200°C) where the Si(111) surface is in a disordered 1×1 phase—temperature at which evaporation is the major process. In the low temperature regime, without much information, we consider that the adatom coverage is low and we take the typical value of $\Theta = 0.01$. In the high temperature regime, the coverage has been measured by Yang and Williams (1994), who obtain $\Theta = 0.2$ at 900°C while more recently Rogilo et al. (2016) measured $\Theta = 0.14$ and $\Theta = 0.23$ at 1000°C and 1100°C, respectively. While those measurements are of the same order, the temperature dependence of the equilibrium coverage is not simple over the range 900°C to 1100°C, in particular Arrhenius type laws for $\Theta(T)$ experimentally reported by Tersoff et al. (1997) and Rogilo et al. (2016) in small temperature ranges are not valid when extended to larger ranges. Regarding the temperature dependence of the coverage on Si(111), Hibino et al. (1998) carried out medium-energy ion scattering measurements, which suggest a fairly constant adatom coverage ($\Theta \approx 0.2$ to 0.25) over the temperature range 830°C to 1200°C.

In sum, adatom equilibrium coverage typically ranges from $\Theta \sim 0.01$ for Si(111)-7×7 to $\Theta \sim 0.1$ to 0.2 for Si(111)-1×1 and GaAs.

Dimensionless deposition and evaporation rates $\overline{F}$ and $\overline{\nu}$

Estimation of $\overline{F}$ and $\overline{\nu}$ from microscopic parameters is difficult for most surfaces, mainly because of the lack of knowledge on the surface diffusion coefficient D. Hence, in most of our analysis $\overline{F}$ and $\overline{\nu}$ cover the range from 10^{-4} to 1, which corresponds to four decades below the upper bound discussed at the beginning of this appendix.

Nonetheless we can provide a quite reliable estimate of $\overline{F}$ for crystal growth experiments on GaAs(001) (Hata et al., 1993; Kasu and Fukui, 1992; Ishizaki et al., 1994, 1996; Shinohara and Inoue, 1995). Indeed, in these experiments, typical growth rates are 0.1 monolayer per second (or 10^{14} cm^{-2}.s^{-1}) on vicinal surfaces with initial terrace widths L_0 between 10 nm and 50 nm. The deposition is performed at temperatures between 600°C and 800°C where $\Theta \sim 0.2$ (i.e., $\rho^*_{eq} \sim 2 \times 10^{14}$ cm^{-2}). The surface diffusion coefficient D has been measured by reflection high-energy electron diffraction, yielding values between 3×10^{-13} cm^2.s^{-1} and 5×10^{-12} cm^2.s^{-1} for temperatures between 600°C and 650°C (Neave et al., 1985; Van Hove and Cohen, 1987). As a result, using (7.52) we obtain values of $\overline{F}$ between 0.1 and 1 for $L_0 = 10$ nm, which corresponds to the upper values of the range of $\overline{F}$ considered. For larger terraces, noting that $\overline{F} \propto L_0^2$, $\overline{F}$ should excess in order of magnitude the unity, which suggests that these growths are performed at the limit between step flow growth and island nucleation.

Kinetic a/d coefficient $\overline{\kappa}$, kinetic transparency coefficient $\overline{\kappa}_p$ and Schwoebel effect S

These three kinetic coefficients are all related to microscopic kinetics at steps for which measurements are particularly difficult.

Recall from (7.55) that $\overline{\kappa}$, expressing the ratio of attachment/detachment (a/d) kinetics to surface diffusion kinetics, reflects an a/d Limited (ADL) regime when $\overline{\kappa} \ll 1$ and a Diffusion Limited (DL) regime when $\overline{\kappa} \gg 1$. Given the absence of knowledge, *a priori*, on that quantity, we cover both ADL and DL regimes by considering values of $\overline{\kappa}$ ranging from 10^{-2} to 10^2. Similarly $\overline{\kappa}_p$ will be taken in the same range, *a priori*, having in mind—from the electric-circuit analogy of Pierre-Louis (2003b)—that when $\overline{\kappa}_p \ll \overline{\kappa}$, the transparency is ineffective.

The nature and scale of the Ehrlich-Schwoebel (ES) effect (embedded in S defined by (7.56)) is also rarely clearly determined experimentally. Hence, for general discussions in absence of accurate information on the Schwoebel barrier, we explore both direct and inverse ES effect with a maximum ratio of the upper and lower attachment coefficients of an order of magnitude, i. e., we take S between 0.1 and 10.

ES BARRIER IN SI(111)-7×7 Considering Si(111)-7×7, measurements of the Schwoebel effect have been performed by different techniques—comparison in the growth and decay rates of islands and holes (Ichimiya et al., 1996), denuded zones around steps (Voigtlander et al., 1995; Rogilo et al., 2013), island

nucleation distributions (Chung and Altman, 2002)—and lead to contradictory conclusions, i. e., a direct, negligible or inverse ES effect. As a result, we use the general range of S between 0.1 and 10 for the discussions relative to this surface.

ES BARRIER IN GAAS(001) For the surface of GaAs(001), different studies yield values for the Ehrlich-Schwoebel barrier in reasonable agreement. Indeed, by analyzing the characteristics of mounds in the epitaxial growth of GaAs Šmilauer and Vvedensky (1995) and Krug (1997) derived values of the direct Schwoebel energy barrier of $\Delta E_{-}^{Sm} = 0.175$ eV and $\Delta E_{-}^{Kr} = 0.06$ eV, respectively. Krug (1997) noted that their method underestimates—while the one of Šmilauer and Vvedensky (1995) overestimates—the value of the barrier so that these values should be considered as bounds. On the other hand, by performing atomistic computations that distinguish between two types of steps on the GaAs(001) surface (parallel and perpendicular to the arsenic dimers), Salmi et al. (1999) obtain a value of the barrier of $\Delta E_{-}^{Sa} = 0.25$ eV for one type of step and conclude that there is no barrier for the second type of step.

For discussions on the growth of GaAs(001), we use the intermediate value $\Delta E_{-} = 0.1$ eV, which can be translated in terms of the parameter S—using the relation between the a/d kinetic coefficients and the energetic barriers associated to the hopping of adatoms between different sites (Jeong and Williams, 1999)—with

$$S = \exp(\Delta E_{-}/k_B T). \tag{E.1}$$

The parameters S associated with the energetic barriers of Krug and Šmilauer and Vvedensky are $S^{Kr} = 2$ and $S^{Sm} = 10$, respectively.

Dipole-dipole $\overline{\alpha}$ and monopole-monopole $\overline{\beta}$ elastic interaction coefficients

Estimation of $\overline{\alpha}$ and $\overline{\beta}$ given by (7.58) rely mainly through (7.47) and (7.48) on the computation of the strength of the dipole (d_x^1, d_z^1) and monopole m representing the elastic field created by the steps in homoepitaxy and heteroepitaxy, respectively.

ESTIMATION OF $\overline{\alpha}$ IN SI(111)-7×7 For homoepitaxy, $\overline{\alpha}$ can be accurately estimated in Si(111)-7×7 from the work of Stewart et al. (1994). Combining experimental measurements of the displacement field of a step with atomistic simulations, they determined, for a Si(111)-7×7 step, the normal and tangential dipole moments: $d_z^1 = 0.6$ eV/Å and $d_x^1 = 1.5$ eV/Å. With the effective isotropic elastic properties of silicon $E = 166$ GPa and $\nu = 0.2$ (Stewart et al., 1994), we derive the elastic interaction coefficient $\alpha = 3$ eV.Å and its dimensionless counterpart at 1000 K for the reference terrace width $L_0^* = 20$ nm: $\overline{\alpha}^* = 5 \times 10^{-5}$. Note that since $\overline{\alpha} \propto L_0^{-3}$, if the initial terrace width is multiplied by two, $\overline{\alpha}$ is decreased by an order of magnitude. Hence, $\overline{\alpha}$ may vary over several decades and elasticity may have small or large effect on the stability depending on the initial miscut angle.

ESTIMATION OF $\overline{\alpha}$ IN GAAS(001) The interactions between steps of GaAs(001) has recently been studied with *ab initio* computations (specifically Density Functional Theory, DFT) by Magri et al. (2014, 2016). Through fitting of the atomic displacement field, they derived elastic dipole moments of the order of 0.1 eV/Å and a resulting elastic interaction coefficient of about $\alpha = 0.2$ eV.Å (the exact value depending on the structure of each step). For an initial terrace width $L_0 = 16$ nm (corresponding to a miscut angle of 1° with step height 0.28 nm), the dimensionless value of α is at 1000 K: $\overline{\alpha} = 5 \times 10^{-6}$.

It is interesting to note that in their work, Magri et al. find, by analyzing the surface energies of stepped surfaces, that the total interactions between steps—as it comes from the DFT computation which is not only elastic but accounts for other quantum effects—is attractive. After proposing that the total interaction is partly due to interaction between electrostatic dipoles located along the steps, they conclude that it is more likely a complex interaction, with origin in quantum mechanics. Whereas this energetic attractive interaction could be at the origin of step bunching in GaAs(001), its existence is not yet clear, all the more that the computations of Magri et al. are limited to terrace widths below 6 nm. In addition, the experimental observations of bunched surfaces of GaAs(001) by Pond (1994) show a minimum terrace width of about 4 nm within the bunches, which rather suggests the existence of an overall repulsive interaction.

E.2 MATERIAL PARAMETERS SI(111)-1×1 UNDER ELECTROMIGRATION

In this appendix, we estimate the dimensionless parameters $\overline{\nu}$, $\overline{e}$ and Θ and discuss, as well as for $\overline{\kappa}$ and $\overline{\kappa}_p$, their temperature dependence.

DIMENSIONLESS EVAPORATION RATE $\overline{\nu}$

Recalling that $\overline{\nu} := \nu L_0^2/D$, $\overline{\nu}$ can be directly estimated from the diffusion length $L_d := \sqrt{D/\nu}$, which has been recently measured by Rogilo et al. (2016) at 1000°C, $L_d = 30$ μm. For a initial terrace width of $L_0 = 100$ nm, we obtain $\overline{\nu} = 1 \times 10^{-5}$.

For the temperature dependence of L_d, both the diffusion and the evaporation probability follow Arrhenius laws,

$$D \propto \exp(-E_{dif}/k_B T) \qquad \text{and} \qquad \nu \propto \exp(-E_{des}/k_B T), \tag{E.2}$$

where E_{dif} and E_{des} are the diffusion and desorption activation energies, respectively. Hence, $\overline{\nu}$ follow an Arrhnenius law with activation energy $E_{dif} - E_{des} =$ 2.45 eV (value of Rogilo et al. 2016, consistent with Pang et al. 2008, who obtain $E_{dif} - E_{des} = 2.65$ eV). The resulting variation of $\overline{\nu}$ across the three temperature regimes is shown in Table E.1

T (°C) / regime	950 (I)	1150 (II)	1250 (III)
$\overline{\nu}$	4×10^{-6}	1×10^{-4}	4×10^{-4}

Table E.1: Estimation of the temperature dependence of $\overline{\nu}$.

DIMENSIONLESS ELECTROMIGRATION FORCE $\overline{e}$

The electric field circulating through silicon substrates is typically of the order of $e = 5$ V/cm (Yang et al., 1996; Stoyanov et al., 2000), estimates of the effective charge of adatoms are about one tenth of the elementary charge (cf. Chapter 6). As a result, $\overline{e} := q_e e L_0/(k_B T)$ is estimated for a terrace length $L_0 = 100$ nm at $\overline{e} = 5 \times 10^{-5}$. The variation of $\overline{e}$ across the three temperature regimes can be neglected (limited to 20% due to the temperature change and the change in electric field across the regimes).

ADATOM COVERAGE Θ

Rogilo et al. (2016) measures an equilibrium adatom coverage between $\Theta = 0.14$ and $\Theta = 0.22$ for the temperature range 1000°C-1100°C.

TEMPERATURE DEPENDENCE OF $\overline{\kappa}$ AND $\overline{\kappa}_p$

While measurements of $\overline{\kappa}$ and $\overline{\kappa}_p$ are not available, experiments indicate that in all three temperature regimes, the regime is diffusion limited, i. e., $\overline{\kappa} \gg 1$ (Gibbons et al., 2006; Man et al., 2007).

For the temperature dependence of $\overline{\kappa}$, we can appeal to the microscopic model of adatom hopping (Jeong and Williams, 1999). The diffusion constant D reads

$$D = a^2 \nu_0 \exp(-E_{dif}/k_B T), \tag{E.3}$$

with ν_0 the hopping attempt frequency. Similarly, neglecting any step asymmetry, the attachment/detachment rates $\kappa_\pm$ reads

$$\kappa\pm = a\nu_0 \exp\big(-(E_{dif} + E_{ad})/k_B T\big), \tag{E.4}$$

where E_{ad} is the supplementary energy barrier for attachment to steps and we have assumed the same attempt rate for adatom hopping on the terrace and with the steps. Current estimations of E_{ad} are between $E_{ad} = 0.23$ eV and $E_{ad} = 0.68$ eV (Rogilo et al., 2016).

Hence, we obtain

$$\overline{\kappa} = \frac{L_0}{a} \exp(-E_{ad}/k_B T). \tag{E.5}$$

This calls for a few remarks on the stability reversals discussed in Section 9.2.4. First as E_{ad} is usually considered positive, $\overline{\kappa}$ should be an increasing function of temperature, which would invalidate the proposed mechanism for the two stability inversions (cf. Section 9.2.4) where $\overline{\kappa}$ is a decreasing function of temperature. Second, if $E_{ad} \geq 0$, the highest reachable value of $\overline{\kappa}$ is in the limit

$E_{ad} = 0$, $\overline{\kappa} = L_0/a \approx 300$ for $L_0 = 100$ nm. This value is too low for reaching the region where step bunching occurs under step up current, which requires $\overline{\kappa} > 10^4$ (cf. Section 9.2.1). Hence, either the fast step kinetics mechanism is not a possible explanation for the stability observed in regime II or one should accept the possibility that $E_{ad} < 0$ (meaning that a/d to steps is easier than terrace diffusion).

Regarding the permeability coefficient $\overline{\kappa}_p$, as existence of permeability is even more speculative, estimations of its values have not been performed. By contrast to $\overline{\kappa}$, a simple reasoning based on the idea that the less kinks a step has, the more permeable the step is and assuming that with increasing temperature the step roughness increases (and simultaneously the kink density), $\overline{\kappa}_p$ is expected to decrease with temperature. However, the stability reversal still implies very large values of permeability $\overline{\kappa}_p > 10^4$ that would require that, at the atomic scale, the crossing of steps by adatoms involves a lower activation energy than the activation energy of terrace diffusion.

These remarks show that, although the mechanisms which have been proposed for explaining the stability reversals in the electromigration experiments are theoretically attractive, when one considers the conditions of their existence at the microscopic scale, many questions arise.

F

ATOMISTICALLY DERIVED COHESIVE ZONE MODEL OF INTERGRANULAR FRACTURE IN POLYCRYSTALLINE GRAPHENE

Reproduced from Guin, L., J. L. Raphanel, and J. W. Kysar (2016). "Atomistically derived cohesive zone model of intergranular fracture in polycrystalline graphene." In: *Journal of Applied Physics* 119.24, p. 245107. DOI: 10.1063/1.4954682

ABSTRACT Pristine single crystal graphene is the strongest known two-dimensional material and its nonlinear anisotropic mechanical properties are well understood from the atomic length scale up to a continuum description. However, experiments indicate that grain boundaries in the polycrystalline form reduce the mechanical behavior of polycrystalline graphene. Herein we perform atomistic-scale molecular dynamics simulations of the deformation and fracture of graphene grain boundaries and express the results as continuum cohesive zone models (CZMs) that embed notions of the grain boundary ultimate strength and fracture toughness. To facilitate energy balance, we employ a new methodology that simulates a quasi-static controlled crack propagation which renders the kinetic energy contribution to the total energy negligible. We verify good agreement between Griffith's critical energy release rate and the work of separation of the CZM and we note that the energy of crack edges and fracture toughness differ by about thirty-five percent which is attributed to the phenomenon of bond trapping. This justifies implementation of the CZM within the context of the finite element method (FEM). To enhance computational efficiency in the FEM implementation, we discuss the use of scaled traction-separation laws (TSLs) for larger element sizes. As a final result, we have established that the failure characteristics of pristine graphene and high tilt angle bicrystals differ by less than ten percent. This result suggests that one could use a unique or a few typical TSLs as a good approximation for the CZMs associated with the mechanical simulations of the polycrystalline graphene.

F.1 INTRODUCTION

Since its discovery by Novoselov and Geim, (Novoselov et al., 2004) graphene, a two-dimensional allotrope of carbon, has generated extensive interest owing to its extraordinary electric and mechanical properties, and the variety of potential applications which they may allow. Pristine graphene is the strongest 2D material ever measured with a Young's modulus of 348 N/m and intrinsic strength of 39.5 N/m (Wei et al., 2009). Upon normalizing by the distance between graphite basal planes (0.335 nm), the Young's modulus is equivalent

to $\approx$ 1 TPa and the intrinsic strength to about 100 GPa. These properties are however sensitive to the presence of defects, and in particular one-dimensional defects such as grain boundaries (GBs). The latter are inherent to scalable methods of graphene production such as chemical vapor deposition (CVD) (Huang et al., 2011). The specimens produced in this way are polycrystalline in nature but retain the two-dimensional character of graphene. Their size may be millimetric to metric (Bae et al., 2010) and the grain size may vary from very small (0.5 to 1 micrometer) to large (tens to hundreds of micrometers). They would be more suitable for a variety of applications than pristine graphene obtained by mechanical exfoliation, provided their mechanical properties remain attractive.

The mechanical properties of defect-free graphene have been investigated experimentally by Lee et al. (2008) who performed indentation experiments of free-standing circular monatomically thin membranes of graphene using the diamond tip of an atomic force microscope (AFM). Later, Wei et al. (2009) established from density functional theory (DFT) calculations a continuum constitutive law for pristine graphene which is modeled as an anisotropic nonlinear elastic material. This constitutive law has been validated referring to the aforementioned experiments by the development of a multiscale model combining the continuum description provided by the DFT calculations and a finite element method (FEM) simulation of the indentation of the circular graphene membrane (Wei and Kysar, 2012).

In 2013, Lee et al. (2013) performed a set of indentation experiments to investigate the mechanical properties of polycrystalline graphene produced by CVD with small and large grain sizes. The monatomically thin graphene samples were transferred onto a silicon substrate patterned with an array of circular wells (with diameters of 1 and 1.5 μm). The free-standing membranes were indented with a commercial nanoindenter up to rupture, see Figure F.1 adapted from Lee et al. (2013) and notice in Figure F.1(c) the false-colored graphene grains separated by GBs as revealed by dark field transmission electron microscopy (DF-TEM).

These experiments provide two important results for our own study. First, indentation experiments were performed on large grain CVD graphene for which the grain size is significantly larger than the well diameter that yield free-standing graphene specimens without GBs. Thus the specimens did not contain grain boundaries, but they contained uncharacterized zero-dimensional point (i.e. atomic) defects such as atomic vacancies or substitutional atoms. Statistical analysis of the results reveals no significant difference in both the elastic stiffness and the breaking strength between pristine exfoliated and CVD produced large grain graphene. This suggests that the point defect density may be neglected when modeling polycrystalline graphene with sufficiently low point defect density. Second, indentation experiments of small grain CVD graphene, for which the free-standing specimens contain GBs, show a statistically significant reduction in strength of the order of a few percent. Moreover, when GBs are directly indented, the weakening effect may reach fifteen percent and TEM images suggest that cracks are likely to initiate at the grain boundaries. Thus,

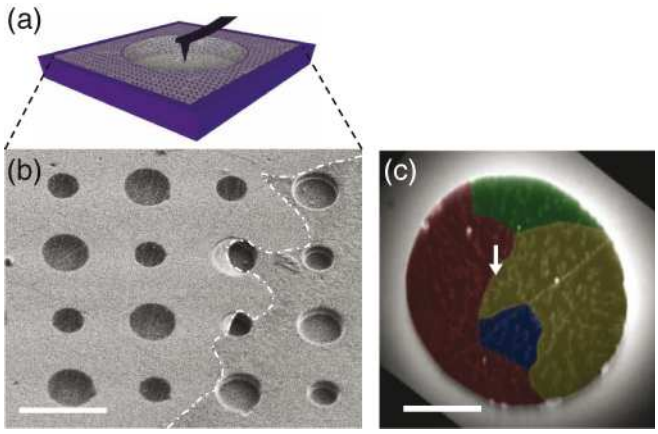

Figure F.1: From Lee et al. (2013) - Nano indentation experiments on polycrystalline graphene performed by Lee et al. (2013) (a) Schematic view of a graphene membrane suspended over a well under the AFM indenter tip. (b) Scanning electron microscopy image of the suspended graphene layer over holes. The dashed line indicates the border of the graphene-covered area. (c) False-color dark-field transmission electron microscopy image of the suspended graphene film over a hole before indentation. Different colors represent different grains. The white arrow indicates the indentation point. Scale bars, (b) 3 μm; (c) 1 μm.

the GBs are identified as constituting the main defects necessary to model mechanical failure in CVD graphene.

As a way to model crack initiation and propagation at the GB, a cohesive zone model (CZM) may be introduced in the FEM calculations of polycrystalline graphene deformation. The first step of this multiscale approach is to establish the characteristics of the CZM and this will be done at the atomistic scale, using molecular dynamics (MD) to simulate crack propagation along the GB of graphene bicrystals and thus derive a traction-separation law (TSL) characterizing the properties of the interface. The modeling of the mechanical properties of the GBs of graphene through the development of a characteristic TSL constitutes the main objective of this paper.

The CZM (Dugdale, 1960; Barenblatt, 1962) is a classical concept in fracture mechanics which has found its implementation in FEM simulations to account for crack initiation and propagation (Hillerborg et al., 1976). Intergranular fracture may be predicted by embedding cohesive surface elements along grain boundaries that incorporate a traction-separation law characterizing the interface properties.

Various functional forms of the TSL (bilinear, trapezoidal, exponential, polynomial) have been proposed for both ductile and brittle materials (Dugdale, 1960; Barenblatt, 1962; Needleman, 1987, 1990; Geubelle and Baylor, 1998). They account for the fracture process at a macroscopic scale and are often phenomenological laws derived from macroscopic experiments. In the case of polycrystalline graphene, the approach has to be somewhat different since direct experimentation is not available. However, owing to the 2D nature of the material, the grain boundaries are one dimensional. They can be imaged by

high resolution TEM and can be idealized in a fairly accurate way by periodic patterns of aligned defects in the honeycomb crystal lattice that characterizes graphene. The TSL can then be established by modeling, at the atomic scale, the crack propagation along grain boundaries. Molecular dynamics simulations that account for the aggregate behavior of hundreds of thousands of atoms are a powerful tool to establish a TSL for graphene.

Yamakov et al. (2006) have proposed a methodology to derive from MD simulations a CZM for intergranular fracture processes in aluminum and to incorporate it in continuum simulations. We shall use the main elements of that methodology with the objective of obtaining a quantitative TSL for intergranular fracture in graphene. Our need for a CZM that may be readily and consistently implemented in the FEM leads us to complement existing work (Yamakov et al., 2006; Zhou et al., 2008; Krull and Yuan, 2011) with first, an energetic validation of the thermomechanical process accounted for by the TSL and second an analysis of the scale effect on the parameters of the TSL with regards to the FEM mesh size. To achieve these goals, the fracture process that we simulate by MD is the displacement controlled fracture of a monatomically thin bicrystal of graphene in the form of a double cantilever beam (DCB).

The paper is organized as follows. We review, in Section F.2, fundamental concepts for describing pristine and polycrystalline graphene and some important results on their mechanical properties. In Section F.3 we present the methodology to derive a cohesive zone model from molecular dynamics and implement it via simulation of controlled crack propagation along a GB. The results of our simulations on a few representative GBs are presented and analyzed in terms of energy balance and mesh size effect in Section F.4. We conclude by discussing in Section F.5 the range of validity of this original approach and its potential extensions.

F.2 MECHANICAL PROPERTIES OF GRAPHENE AND ITS GRAIN BOUNDARIES

F.2.1 *Graphene single crystals and bicrystals*

Graphene is the newest experimentally accessible allotrope of carbon. A sheet of graphene is similar to a tiling of benzene where the hydrogen is replaced by carbon atoms to form neighboring hexagons. The atoms are arranged in a 2D regular honeycomb lattice due to their sp^2 hybridization. This lattice is not strictly a Bravais lattice since two neighboring sites are not equivalent. It may be viewed as a hexagonal Bravais lattice with a two-atom basis. Figure F.2(a) shows the two vectors ($\mathbf{a}_1$ and $\mathbf{a}_2$) that constitute along with an out of plane vector the commonly used basis of the 3D hexagonal Bravais lattice. The distance between nearest neighbor carbon atoms is $d = 0.142$ nm which is the average of single and double covalent bond distance for C. Hence, the lattice spacing that corresponds to the norm of basis vectors $\mathbf{a}_1$ and $\mathbf{a}_2$ is $a_0 = \sqrt{3}d = 0.246$ nm. A third vector $\mathbf{a}_3$, in the plane of ($\mathbf{a}_1$,$\mathbf{a}_2$), is usually introduced for the definition of

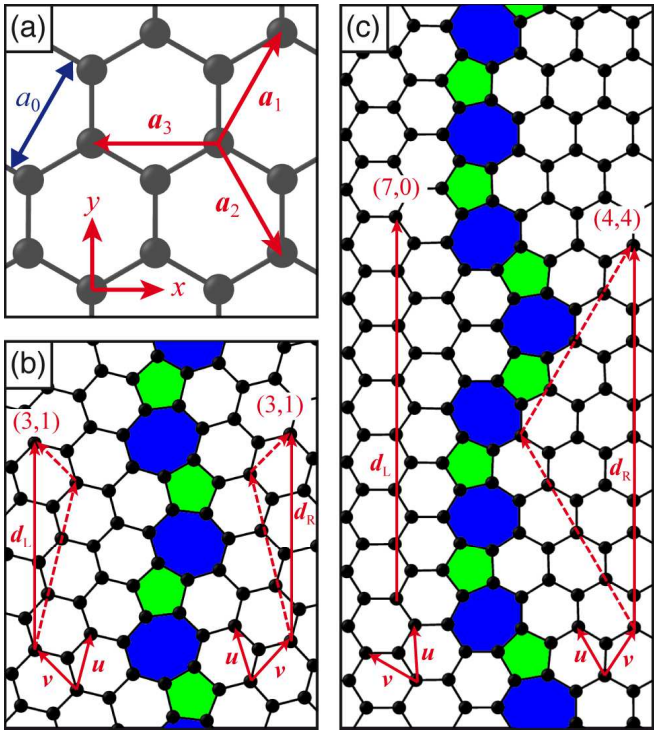

Figure F.2: (a) Graphene honeycomb lattice with the x and y directions for the definition of the constitutive law of graphene introduced Figure F.4 and the $(\mathbf{a}_1, \mathbf{a}_2, \mathbf{a}_3)$ basis for the definition of crystallographic directions. (b) and (c) Representation of the translation vectors on the GB $(3,1)|(3,1)$ and GB $(7,0)|(4,4)$ respectively.

the Miller-Bravais notation of crystallographic planes and directions (De Graef and McHenry, 2007).

Two orthogonal directions within the crystal lattice referred to as the zigzag and armchair directions can be expressed using the Miller-Bravais notation as $[11\bar{2}0]$ and $[1\bar{1}00]$ respectively, as well as the x-direction and y-direction, respectively in Figure F.2(a).

A graphene polycrystal is an assemblage of single crystals separated by grain boundaries that are 1D line defects. We are interested in the simplest of such structures: bicrystals, which are two crystalline domains linked by a GB. In order to characterize a bicrystal, two parameters are necessary. For instance one may use θ_L and θ_R ($0 \leq \theta_L, \theta_R \leq 30°$) defined as the angles between the unit normal vector to the GB and a particular crystallographic direction of the left and right crystals respectively (see Figure F.3). The misorientation angle θ between the two grains is expressed as: $\theta = \theta_L + \theta_R$ if $\theta_L + \theta_R \leq \pi/6$ and $\theta = \pi/3 - (\theta_L + \theta_R)$ if $\theta_L + \theta_R > \pi/6$. The equality $\theta_L = \theta_R$ defines the symmetric GBs.

In 2D materials, a GB is a 1D chain of edge dislocations. Yazyev and Louie (2010b) have shown that the atomic structure of a dislocation in graphene can be considered as a pair of positive and negative disclinations which consist of a five-ring and seven-ring atomic core, respectively. Hence graphene GBs contain pentagonal and heptagonal carbon rings.

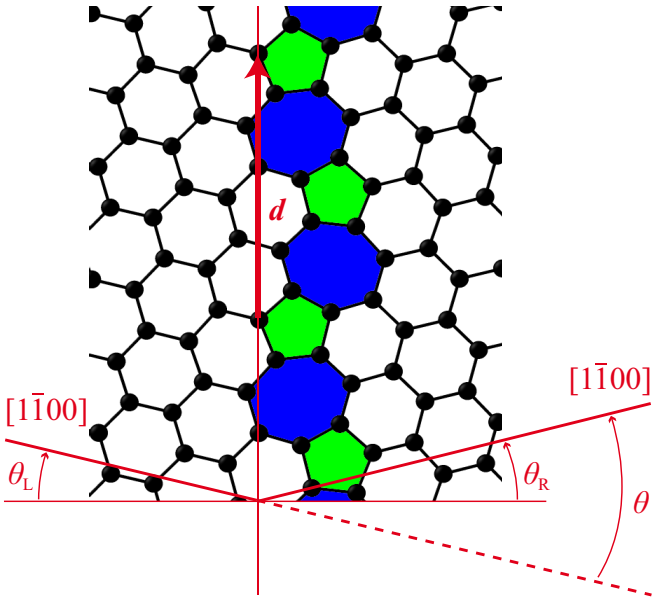

Figure F.3: Definition of the angles θ_L and θ_R that describe the orientations of the two crystals relatively to the GB for the example of the GB $(3,1)|(3,1)$. θ is the misorientation angle of the bicrystal and $\mathbf{d}$ the repeating vector of the GB.

GBs observed with high-resolution transmission electron microscopy (HR-TEM) (Huang et al., 2011; Kim et al., 2011; Rasool et al., 2014) appear to be composed of mixed regions of periodic and aperiodic sequences of dislocations resulting in sinuous GBs (Rasool et al., 2014). On the other hand, theoretical studies of graphene GBs (Yazyev and Louie, 2010b,a; Malola et al., 2010) deal with idealized periodic structures. It is important that the periodic structures consist of the periodic subsequences observed in TEM images of GBs. In particular, when the idealized periodic GB retains the sinuous character of a real GB, as is the case of our two model GBs, it has been shown that the idealized model accounts very well for the mechanical properties of the original GB (Rasool et al., 2014; Zhang et al., 2015b).

Alternately, a GB may be characterized by the components (n_L, m_L) and (n_R, m_R) of the two periodic translation vectors $\mathbf{d}_L$ and $\mathbf{d}_R$ of the two grains expressed in the respective $(\mathbf{u}, \mathbf{v})$ basis of the underlying hexagonal lattices (Figure F.2(b) and (c)). These vectors should match each other along the GB line to constitute the repeating vector of the GB. The GB is thus denoted $(n_L, m_L)|(n_R, m_R)$. This two-vector nomenclature, previously used by Yazyev and Louie (2010a), Zhang et al. (2012), Rasool et al. (2014), and Zhang et al. (2015b), encompasses the two angles that characterize a grain boundary and make apparent the symmetric or asymmetric character of the GB; in addition one may distinguish GBs for which the matching between the two crystal lattices is exact or not. In fact, the length L of each periodic translation vector is computed from its components (n, m) and the lattice spacing a_0: $L = a_0\sqrt{n^2 + nm + m^2}$. For all symmetric GBs ($(n_L, m_L) = (n_R, m_R)$) and some asymmetric GBs (e.g. $(5,3)|(7,0)$ in Yazyev and Louie (2010a)), these periodic vectors respect the commensurability condition in that they have the same norm.

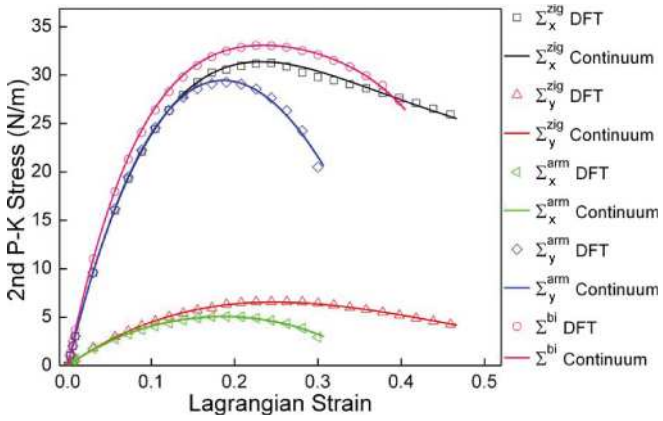

Figure F.4: From Wei et al. (2009) - Continuum stress-strain constitutive law developed by Wei et al. (2009) with a least square fit to *ab initio* calculations. Superscripts represent the direction in which uniaxial tension is applied and subscripts represent the component of the second Piola-Kirchhoff stress tensor in the $(\mathbf{x}, \mathbf{y})$ basis of Figure F.2.

For others asymmetric GBs there is a mismatch between the two vectors, as for instance $(7,0)|(4,4)$ in Figure F.2(c) for which $L_L = \sqrt{49}a_0$ and $L_R = \sqrt{48}a_0$. This small mismatch, responsible for a higher GB energy, is accommodated by local lattice distortions and the resulting repeating vector lies in between the two original vectors.

In our simulations we shall consider two GBs. The symmetric tilt GB $(3,1)|(3,1)$ and the asymmetric tilt GB $(7,0)|(4,4)$ as presented in Figure F.2(b) and (c).

F.2.2 *Mechanical properties*

Graphene exhibits nonlinear, anisotropic elastic behavior. From density functional theory (DFT) calculation, Wei et al. (2009) derived a continuum constitutive relationship suitable for incorporation into the finite element method. This relationship results from a Taylor expansion of the elastic strain energy in strain truncated after the fifth-order term (Figure F.4). It provides a continuum description of graphene, valid for finite and arbitrary in-plane deformation, that constitutes the basis of a multiscale model of graphene.

For modeling polycrystalline graphene, as grown by CVD for instance, in addition to the constitutive behavior of the bulk, the mechanical properties of the GBs need to be characterized and several studies have dealt with this issue, either by numerical simulations using molecular dynamics (MD) or by experiments using nanoindentation.

When one is interested in the failure mechanics of graphene GBs, two quantities are of interest. The cohesive strength, defined as the maximum stress that a GB can sustain and the fracture toughness, which is relevant to predict fracture propagation. Some authors have estimated the cohesive strength of GBs by MD simulations (Grantab et al., 2010; Wei et al., 2012; Wu and Wei, 2013) looking for dependence with respect to the misorientation angle of the grain boundary. However recent studies suggest that the detailed arrangement of defects at the

grain boundary and the orientation of the GB line are also determinant factors for the strength. Experimental nanoindentation studies (Lee et al., 2013; Rasool et al., 2013) are inconclusive regarding the misorientation angle dependence of the strength of GBs.

The fracture toughness of graphene (single crystalline and polycrystalline) has been the object of several studies both theoretical and experimental. Theoretical studies are based on MD and coupled quantum/molecular mechanics simulations. As summarized in the review paper of Zhang et al. (2015a), various studies have predicted fracture toughness values ranging from 2 to 4 eV/Å.

On the experimental side, Zhang et al. (2014) recently measured the mode I fracture toughness of polycrystalline graphene by performing pioneering tensile loading experiments in pre-cracked sheets of polycrystalline graphene. By using a microelectromechanical (MEMS) device, they were able to test several bilayer membranes of polycrystalline graphene in which cracks were initially introduced by focused ion beam (FIB) cutting with initial crack lengths ranging from tens of nanometers to one micron. Their results show that in the range of crack length studied, the Griffith criterion of fracture holds in the sense that the product of the critical stress with the square root of the crack length is constant. They measured a fracture toughness of 3.3 eV/Å. The typical size of the grains that constituted the polycrystalline graphene ranged from hundreds of nanometers to a few microns. Thus, the fracture toughness they measured corresponds to that within a graphene crystallite rather than the fracture toughness of the constituting GBs. By contrast, in our multiscale approach, we are interested in the specific properties of particular GBs.

The approach that we propose in this work, deriving a cohesive zone model of the GBs in graphene, encompasses these two notions of strength and fracture toughness. Moreover, it provides a description of the GB that may be incorporated in finite element models of polycrystalline graphene.

F.3 METHOD

In the present section, we introduce the concepts and the methods that we use to build a model that characterizes the mechanical properties of GBs in graphene. This model is a cohesive zone model of the GBs, for which our ultimate goal is the implementation in a FEM which simulates the indentation experiments of polycrystalline graphene. In the general case, a CZM should be mixed-mode in order to be able to take into account fracture processes that are a combination of different fracture modes (the opening, sliding and tearing modes), see for instance Park et al. (2009) In addition, the influence of stress triaxiality on the CZM may be important as it has been discussed by Siegmund and Brocks (1999). While the CZM cannot originally account for stress triaxiality, some authors (see for instance Remmers et al. (2013)) have proposed an extension of the CZM that incorporates that effect.

In the present study, our aim is to develop a single-mode CZM that is adapted to conditions typical of the indentation experiments of graphene films. In their FEM simulations of indentation, Wei and Kysar (2012) have shown that the

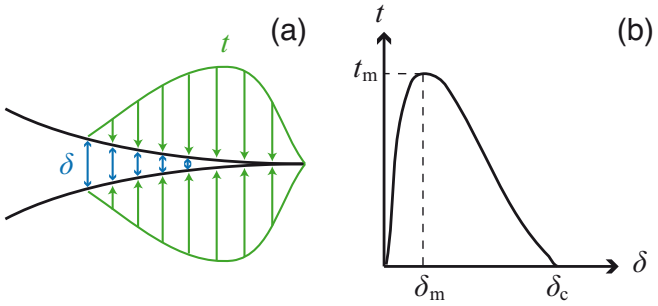

Figure F.5: (a) Schematic view of the cohesive zone at the tip of a crack where to a crack opening δ is associtated the traction t between the lips. (b) Typical profile of a traction-separation law embedded in the cohesive zone model.

highest stresses are concentrated under the indenter tip and that the corresponding stress state there is equibiaxial. Also, near the indenter tip, i.e. where a GB is likely to fail since stresses are high, the stress state is approximately equibiaxial tensile and the in-plane shear stress is very small as compared to the normal stresses. Therefore the operative mode of fracture is the opening separation (mode I fracture) and we can neglect the mode II contributions. Thus we aim herein at building a mode I CZM valid in a range of stress states close to equibiaxial. To quantify the notion of closeness to an equibiaxial stress state, we note that our simulations suggest that the cohesive zone parameters may change by 20% between a uniaxial tension and an equibiaxial tension. Therefore, when considering biaxial stress states for which the ratio of the principal stresses is less than two to one, we can expect that the CZM will be valid within a 10%.

In the first part of this section, we introduce the concepts that allow to build the CZM. We then develop the principles of the numerical tool that we use to derive our CZM, i.e. the molecular dynamics, and review the state of the art in the MD to CZM scale bridging. Finally, we describe first the simulation that we use for deriving our CZM, and second the averaging procedure to transition from the atomistic scale to the continuum.

F.3.1 *Cohesive zone model*

The concept of cohesive zone was first introduced by Barenblatt (1962) for brittle fracture and Dugdale (1960) for ductile fracture. We focus on the Barenblatt approach, well suited for the brittle fracture of graphene. It consists in considering a region near the tip of the crack where the two opposites sides are subjected to cohesive tractions as depicted on Figure F.5(a). The cohesive traction, for small crack openings, takes its origin from the interactions at the atomic scale, and allows to overcome the problem, present in the linear elastic fracture mechanics approach, of stress singularity at the tip of the crack. The region over which cohesive tractions are exerted is called the cohesive zone and its length, the cohesive zone length is often assumed to be small with respect to the crack length. Moreover, the distribution of tractions in the cohesive zone

is described by the so-called traction-separation law (TSL); see Figure F.5(b) for a typical TSL. The TSL relates the local opening displacement to the cohesive traction along the cohesive zone and characterizes the interface. The TSL is expressed as a function of the separation that increases up to a maximum traction t_m with corresponding separation δ_m beyond which failure occurs irreversibly and the force decreases to zero, which corresponds to the critical separation δ_c for which the crack is fully opened. The TSL is characterized by its shape and the values of t_m and δ_c. An important quantity is the area under the traction-separation curve which is called the work of separation, w_{sep} and corresponds to the energy absorbed by the fracture process per unit length of crack growth. Depending on the shape of the TSL, two or more parameters may be appropriate for its identification. If one chooses a bilinear law, as we shall explain later, the two main quantities to extract from these experimental curves are t_m and δ_c.

A common way to implement a CZM in a FEM model of fracture consists in deriving the parameters of the TSL from experiments. In the context of graphene GBs, the nanometric scale at which fracture is studied suggests to extract the TSL's parameters by performing MD simulations.

F.3.2 *Molecular dynamics*

MD simulations consist in solving Newton's equations of motion at the level of the atoms that compose the material. It is a phenomenological method of material modeling where the interactions between the atoms are seen from a classical mechanics perspective. In MD, time is typically discretized at the scale of the femtosecond (fs) or 10^{-15} s, which corresponds to the smallest time scale that we need to resolve, i.e. atomic vibrations.

Concepts of statistical physics allow then to relate the trajectories of the atoms and the interatomic forces to macroscopic quantities such as the strain, the stress, the potential and kinetic energies. The primary outputs of MD are, at each time step, the position and the velocity of each atom in the system. From these quantities one may derive, given the potential of interaction between the atoms: the force exerted on each atom; the potential energy of the system U_{pot} that results from the sum of the potential energy of all the atomic interactions; the kinetic energy of the system U_{kin} which is the sum of the kinetic energy over all the atoms and which is directly related to the temperature. For less straightforward macroscopic quantities such as the stress, there exist different methods to derive them from the primary MD outputs. In Section F.3.5, we discuss the Virial definition of stress. For an exhaustive discussion on the different atomic-based definitions of stress, see for instance Zimmerman et al. (2004), Admal and Tadmor (2010), and Tadmor and Miller (2011).

The atomic interactions are accounted for by a phenomenological interatomic potential that embeds all the physics of the material. Therefore, the accuracy of the results derived from MD simulations is completely dependent on the validity of the chosen interatomic potential.

The most widely used interatomic potentials for MD simulations of graphene are the second generation reactive empirical bond order (REBO) potential (Brenner et al., 2002) and its variant, the adaptive intermolecular REBO (AIREBO) (Stuart et al., 2000). These potentials are designed for carbon and hydrocarbon molecules, and are based on the Abell-Tersoff bond order formalism. REBO and AIREBO are pair potentials where only nearest neighbors interactions are taken into account while many-body effects are introduced through a bond order function that parametrizes the properties of each bond with regards to its environment. The bond order term accounts for the modification in atomic hybridization when bonds are breaking and forming. However, it has been noted that the process of fracture in graphene, as modeled by REBO or AIREBO is significantly different from the predictions of the density functional theory (Khare et al., 2007; Pastewka et al., 2008). This problem has been addressed by changing the cut-off functions that turn off the atomic interactions beyond the nearest neighbors (Grantab et al., 2010; Wei et al., 2012; Wu and Wei, 2013; Zhang et al., 2014).

Alternately, other groups have developed improved versions of the REBO potential, especially designed for the study of bond-breaking processes in carbon-based materials (Pastewka et al., 2008; Perriot et al., 2013). As noted by Perriot et al. (2013) the use of REBO or AIREBO potential, as well as the modified cut-off function versions, has not been properly validated and fails to describe the bond breaking phenomena. The problem, encountered in large deformations, in the REBO potential comes from the contradiction between the need to increase the cut-off distance to fully describe the nearest-neighbor interactions and to exclude the second-nearest-neighbor interactions originally not accounted for in the REBO potential.

The improvement proposed by Pastewka et al. (2008) and Perriot et al. (2013) to the REBO potential consists in incorporating an environment-dependent screening function that allows to increase the cut-off distance while only keeping the nearest-neighbor interactions. When the local environment is such that second- and further-nearest-neighbor interactions are detected, a function screens these interactions. These screened environment-dependent potentials have been compared to the predictions of DFT computations, that are the benchmark results, in the range of large deformations and for the processes of fracture, and have proven to yield very good predictions with regards to energy and force profiles as a function of the interatomic distance. The development and validation of these potentials is of fundamental interest for the MD simulations of fracture processes in graphene.

In the present work, we have used the screened environment-dependent potential of Pastewka et al. (2008) called REBO2+S, as implemented in the atomistica package of the MD software LAMMPS.

F.3.3 *Derivation of CZM from MD*

Gall et al. (2000) and Spearot et al. (2004) were pioneering in using MD to investigate the cohesive interface constitutive relations for a bi-material interface

and a GB interface respectively. They simulated tensile tests perpendicular to the interface on small samples of typical size 4 to 8 nm. By defining a measure of the opening and the tension in the sample, they derived interface separation relations. However, as noticed by Yamakov et al. (2006) the small size of the sample and the boundary conditions are such that these authors tend to model interface adhesion rather than crack propagation.

Instead of interface adhesion, the CZM has originally been developed to describe the system of cohesive forces in the terminal region of a crack. Yamakov et al. (2006) extended the previous work by switching from MD simulations of homogeneous interface decohesion to simulations of crack propagation. The simulated cell, of typical size 100 nm, represents a bicrystal with a central crack along the GB. This bicrystal is loaded in order to trigger crack propagation along the GB. Yamakov et al. (2006) proposed a methodology that takes local measures of the stress and the opening displacement along the propagating crack to compute the TSL. The main elements of this methodology have been used again by Zhou et al. (2008) and Krull and Yuan (2011) who have investigated the TSL of interfaces in other contexts.

Herein, we adapt the methodology mentioned above to the case of mode I intergranular fracture in graphene and complement it by a quantitative analysis of the TSL for the purpose of incorporation in a FEM. For our simulations, we devise boundary conditions that allow an energetic verification of the derived TSL and we discuss the mesh size effect for the implementation of the TSL in FEM simulations.

F.3.4 *Description of the simulations*

Following Yamakov et al. (2006) we derive the TSL characterizing GBs in graphene by defining local measures of stress and strain in a MD simulation of crack propagation. We use the MD software LAMMPS (Large-scale Atomic/-Molecular Massively Parallel Simulator) (Plimpton, 1995) with the REBO2+S potential (Pastewka et al., 2008). Unlike previous studies (Yamakov et al., 2006; Zhou et al., 2008; Krull and Yuan, 2011) we choose the sample, the boundary conditions and the loading conditions in order to control the rate of crack propagation. The above cited studies are based on simulations where, because of an elastodynamic instability, the crack propagates dynamically. By contrast the controlled propagation allows us to perform an energetic verification of the TSL.

We simulate a finite size specimen that has the shape of a double cantilever beam (30 nm in width, 120 nm in length, one atomic layer of thickness) made of a bicrystal of graphene as seen in Figure F.6. The specimen contains, depending on the GB that it models, around 140 000 atoms of carbon. The motion of atoms is constrained in the (x, y) plane through reflective walls located on each side of the sheet so that, while the local motion of the atoms remains 3D, the graphene sheet cannot ripple or fold out of plane. This constraint does not significantly affect either the qualitative behavior of the fracture or the quantitative values of the observables. The edges at $y = \pm h$ are free. On the

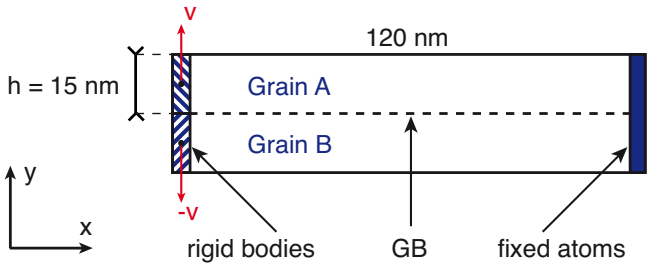

Figure F.6: Schematic view of the double cantilever beam with the boundary and loading conditions used in MD to derived the TSL.

right end of the beam, atoms within a 0.5 nm wide strip are fixed. On the left end of the beam, and independently for the two grains, the atoms belonging to a 0.5 nm wide strip are bound together in order to form two rigid bodies. These rigid bodies constitute useful subsets of the structure where one can apply kinematic boundary conditions. Indeed, the displacement along the x direction and the rotation around the z axis of these two rigid bodies are free while the displacement of their center of mass along the y direction is prescribed by applying uniform equal and opposite velocities of magnitude $v = 4$ nm/ns. Thus vertical prescribed displacements are $q(t) = \pm vt$. With such boundary conditions, a controlled fracture process is simulated. The resulting local stress state at the tip of the crack is quasi-equibiaxial, thus reproducing the stress state under and near the indenter in the indentation experiment that we aim at modeling.

The time step is set to 1 fs and the total simulated duration is 2.5 ns. To focus on the mechanics of the decohesion and avoid thermal activation effects, the simulation is performed in the NVT ensemble at the prescribed temperature of 0.1 K through a Nose-Hoover thermostat. Before the loading, the atoms in the bicrystal beam are properly relaxed to cancel out any initial internal stress which may have been introduced by the design of the bicrystal and its GB, that fixes exactly the position of all the atoms. When the prescribed velocity is applied, the mode I crack propagates in a controlled way along the GB.

The crack tip velocity is of the order of 25 m/s, which may be compared to the velocity under uncontrolled steady-state dynamic propagation observed in MD simulations, at 1500 m/s, which is about one seventh of the Rayleigh wave speed (Kim and Park, 2011). The difference between these values is about two orders of magnitude which justifies the assumption that the controlled crack propagation is quasi-static.

F.3.5 *Definition of the traction and opening displacement*

We define N cohesive zone volume elements (CZVE) of dimensions L_x by L_y along the GB. These CZVE are 2D-volumes that are called volumes to highlight the fact that they are used to consider atoms that are within it. More precisely, atoms inside these areas in the reference configuration are definitively assigned to the CZVE (Figure F.7(b)). The stresses in these regions are computed from

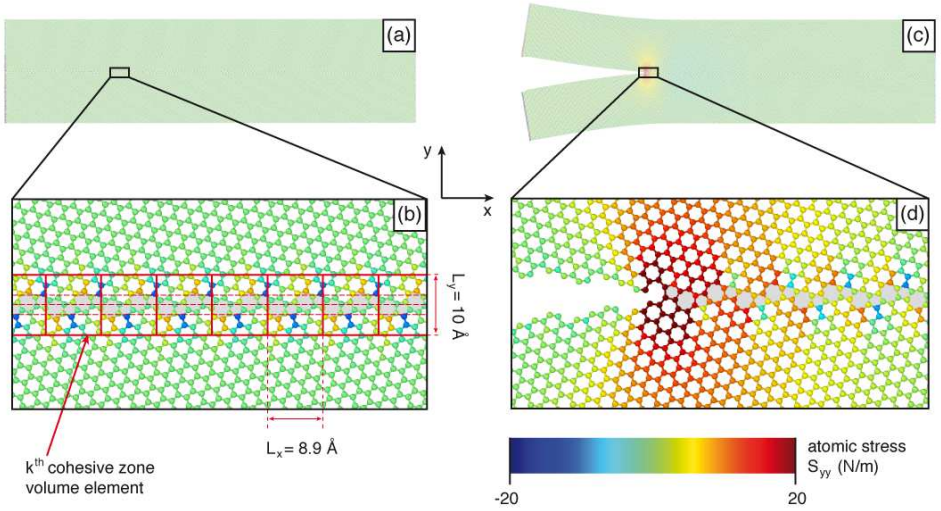

Figure F.7: Double cantilever beam sample for the calculation of the CZM with the GB $(3,1)|(3,1)$. (a) and (b) correspond to the relaxed reference configuration. Red solid lines delimit the CZVE on which stress is averaged. Red dashed lines delimit the atoms considered for defining the opening displacement. (c) and (d) correspond to snapshots of the propagating crack at the time 1.25 ns. Colors represent the yy-component of the atomic stress. For viewing we used the software OVITO (Stukowski, 2010).

the 2D-adapted definition of the atomic stress, based on the Virial theorem (Tadmor and Miller, 2011) and defined by:

$$S_{ij}^{\alpha} = -\frac{1}{\Omega^{\alpha}}(m^{\alpha}v_i^{\alpha}v_j^{\alpha} + \frac{1}{2}\sum_{\beta\in N(\alpha)} r_i^{\alpha\beta}f_j^{\alpha\beta}), \tag{F.1}$$

where i and j are the Cartesian coordinates, m^{α} denotes the mass of atom α and $\mathbf{v}^{\alpha}$ its velocity relatively to the macroscopic motion. Ω^{α} is the surface area of atom α in the present configuration, that may be approximated, when possible, to the one of an atom in the honeycomb lattice in the reference configuration: $\Omega_0^{hon} = \frac{3\sqrt{3}}{4}d^2$ with d the interatomic distance. $\mathbf{r}^{\alpha\beta} = \mathbf{r}^{\alpha} - \mathbf{r}^{\beta}$ is the displacement vector between atoms α and β and $\mathbf{f}^{\alpha\beta}$ is the interatomic force exerted on atom α by atom β. The sum is performed over the set of atoms $N(\alpha)$, neighbors of atom α that are in its interaction range. The 2D character of the above defined atomic stress lies in the division, in Eq. (F.1), by the atomic surface area instead of the atomic volume as it is done in the usual 3D definition of the atomic stress.

The 2D-stress in the k^{th} CZVE is then deduced through a time and volume average of the atomic stress over the CZVE:

$$\sigma_{ij}^{k} = \frac{1}{N_{\tau}\Omega^{k}}\sum_{t=1}^{N_{\tau}}\sum_{\alpha\in A^{k}}\Omega^{\alpha}S_{ij}^{\alpha(t)}, \tag{F.2}$$

where $N_{\tau} = 2500$ is the number of time steps t in the interval $\tau = 2.5$ ps over which the average is performed and A^{k} is the set of atoms belonging to the k^{th}

CZVE. Ω^k denotes the surface area of the k^{th} CZVE and is computed as the surface area Ω_0^{hon} times the number of atoms in the CZVE. This measure of Ω^k neglects the inhomogeneities in atomic surfaces introduced by the pentagonal and heptagonal defects (mesoscopically compensated) as well as the small local strain around the crack tip.

Note that the atomic stress as defined in Eq. (F.1) is of practical interest and provides qualitative information regarding the stress field at the atomic level but shall not be considered to be a macroscopic stress measure (Tadmor and Miller, 2011). By contrast, space and time average of the atomic stress is related to the continuum notion of Cauchy stress to which it converges in the thermodynamic limit (Zimmerman et al., 2004; Tadmor and Miller, 2011; Admal and Tadmor, 2010). The tension perpendicular to the GB, which is of interest for the mode I TSL, is defined as the yy component of the 2D-stress measure: σ_{yy}^k.

Since the crack is atomically sharp, the opening displacement in the k^{th} CZVE is defined as the average distance between the atom lines forming the crack edges in this particular CZVE (the opening is defined as zero in the relaxed configuration). Like for the stress, the opening displacement in each CZVE is averaged over 2500 time steps.

The selection of the size of the CZVE over which the stress is averaged and our choice of measure of the opening displacement at the crack edges is developed and justified in Section F.4.3.

F.4 RESULTS AND DISCUSSION

We focus our study on two high angle grain boundaries. The first one denoted (3,1)|(3,1) is a symmetric GB of tilt angle 27.8°, the second one denoted (7,0)|(4,4) is an asymmetric GB of tilt angle 30.0° (Figure F.2(b) and (c)). Fracture simulations of low angle GBs show a competition between crack propagation along the GB and deviation of the crack inside one of the grains. This may be due to the structure of low angle GBs where the atomic defects (pentagons and heptagons) do not form an almost continuous line but are separated by domains of undisturbed lattice (hexagons).

As a reference, we also determine the TSL for a crack that propagates in the bulk of pristine graphene along the $[1\bar{1}00]$ direction (or armchair), i.e. the direction y shown on Figure F.2(a).

F.4.1 *Traction separation laws*

For each one of the 55 CZVEs dispersed along the GB, we superpose in Figure F.8 all the traction-separation points measured from the beginning of the simulation to the time 1.25 ns. In fact, each CZVE goes through the steps where the local stress increases until the point where the crack goes through the CZVE and the stress drops. These different steps appear in Figure F.8 for all the 55 CZVE and it can be seen that the traction-separation relation propagates in a self-similar way as the crack propagates through the sample.

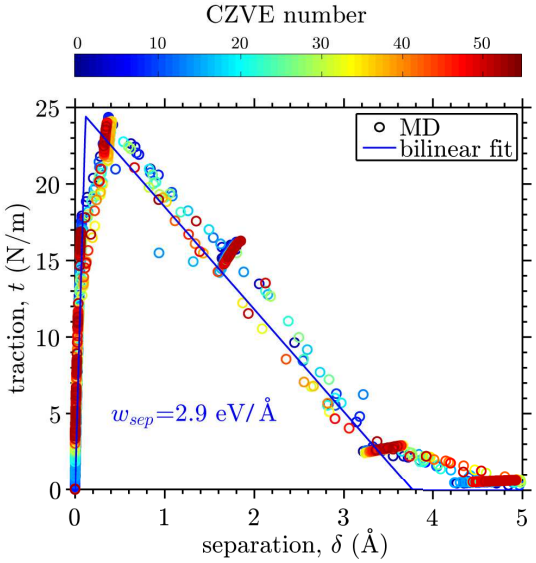

Figure F.8: Superposition of the MD computations of the traction and opening displacement measured in 55 CZVE along the GB $(3,1)|(3,1)$ during crack propagation from $\tau = 0$ to $\tau = 1.25$ ns. Different colors represent the values computed in different CZVEs. A bilinear traction-separation law is fitted to the MD measures. The work of separation w_{sep} corresponds to the area under the bilinear fit.

For the purpose of implementation in FEM, we need to derive from the set of tractions and separations obtained in MD an analytical expression of the TSL that includes physically significant parameters, namely the peak traction t_m and the work of separation w_{sep}. Figure F.8 suggests the use of a bilinear TSL such as the one proposed by Geubelle and Baylor (1998) that is entirely defined by three parameters: the peak traction t_m and the corresponding separation δ_m for the ascending part and the critical separation δ_c at which the traction vanishes for the decreasing part. The work of separation is then expressed by

$$w_{sep} = \frac{1}{2} t_m \delta_c. \tag{F.3}$$

One notices that the value of δ_m does not appear in the expression of w_{sep} given the approximate triangular shape chosen for representing the TSL. Figure F.8 shows the bilinear TSL fitted to the simulation points for the GB (3,1)|(3,1) and Table F.1 reports the parameters that characterize the bilinear TSL for armchair bulk graphene, the GB (3,1)|(3,1) and the GB (7,0)|(4,4). The comparison of the parameters of the three derived TSL shows that, the main characteristics of the TSL differ by less than 10%. In particular, the work of separation that corresponds to the fracture toughness of the GB shows little difference with pristine graphene. Quantitatively, the fracture toughness of the two studied GBs are less than 7% lower than the one of pristine graphene with a $[1\bar{1}00]$ crack.

Specimen	t_m (N/m)	δ_m (Å)	δ_c (Å)	w_{sep} (eV/Å)
Pristine (AC crack)	24	0.2	4.1	3.1
GB (3,1)|(3,1)	24	0.1	3.8	2.9
GB (7,0)|(4,4)	24	0.2	4.0	3.0

Table F.1: Parameters of the bilinear TSLs obtained by a fit to the MD computations for the three studied configurations: Pristine graphene with a crack along the $[1\bar{1}00]$ armchair (AC) direction, the GB (3,1)|(3,1) and the GB (7,0)|(4,4). For instance, the parameters of the GB (3,1)|(3,1) corresponds to the TSL drawn Figure F.8.

F.4.2 *Energetic analysis*

The CZM approach has to be consistent with the energetic approach of crack propagation developed by Griffith (1921) for virgin homogeneous solids and generalized by Orowan (1949) to fracture occurring between unlike bodies or at singular interfaces.

This consistency lies in the equality between the work of separation w_{sep} of the CZM and the fracture toughness G_c of the material or the GB (Hillerborg et al., 1976; Shet and Chandra, 2002). For a demonstration of the equivalence between w_{sep} and G_c based on the J-integral, see Lawn (Lawn, 1993). On the one hand, the work of separation corresponds to the mechanical energy absorbed by the cohesive forces per unit length of fully opened crack ($\delta \geq \delta_c$). It is a characteristic of the TSL that describes the cohesive traction. On the other hand, the fracture toughness, also called crack-resistance energy, expresses the ability of a material or an interface to resist to crack propagation. It gives a criterion for an equilibrium crack propagation called the Griffith energy balance concept (Lawn, 1993):

$$G = G_c, \tag{F.4}$$

where G is the mechanical energy release rate defined by:

$$G = -\frac{\partial \Pi}{\partial a}, \tag{F.5}$$

with Π the mechanical potential energy and a the crack length.

We are thus able to investigate the internal consistency of the TSL in terms of energy by comparing the values of w_{sep} and G_c.

First, the calculation of w_{sep} from TSL parameters is straightforward by applying Eq. (F.3). We can estimate that there is an uncertainty of about 10% on the value of w_{sep} that comes from an uncertainty of $\approx 5\%$ on both t_m and δ_c.

Second, to derive G_c, we use the equilibrium crack propagation condition Eq. (F.4). Indeed, in our simulations, the crack propagation is controlled in the sense that to a continuously varying prescribed displacement corresponds a quasi-continuous variation of the crack length. As may be seen on Figure F.9, the crack moves by successive jumps that correspond to the periodic pattern of

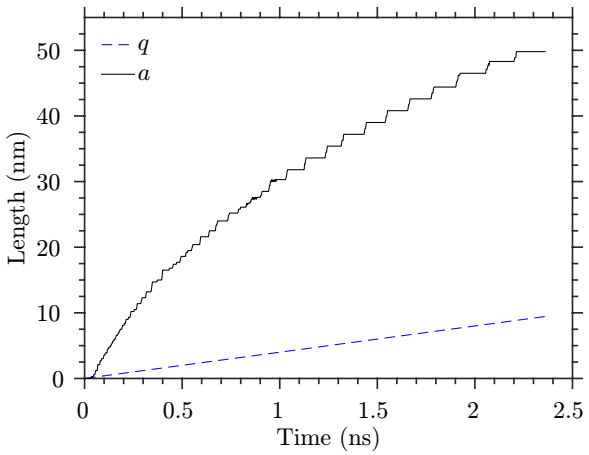

Figure F.9: Evolution of the crack length $a(t)$ under the constant velocity prescribed displacement $q(t)$ in the double cantilever beam simulation described Section F.3.4 for the GB $(3,1)|(3,1)$.

the GB and this characterizes bond trapping, a phenomenon that we discuss later. Notwithstanding this atomic scale specificity, from the continuum point of view we observe on average controlled crack propagation unlike the typical catastrophic failure observed in uniform tensile loading experiments.

With the displacement boundary conditions applied in our simulation, the mechanical potential energy Π involved in the definition of G Eq. (F.5) is equal to the elastic energy U_{el}.

U_{el} appears as a component of the internal energy U_{int} that is a primary output of FMD defined as the sum of the potential U_{pot} and kinetic U_{kin} energies introduced in Section F.3.2. Note that in our simulations, because of the thermostat at 0.1 K and the low velocity of the prescribed displacement, the kinetic energy which is three orders of magnitude less than the potential energy is negligible, hence $U_{int} = U_{pot}$.

To compute U_{el}, we note that:

$$U_{int} = U_{el} + U_{edge} = U_{el} + 2\gamma_e^g a, \tag{F.6}$$

where γ_e^g is a generalized measure of the edge energy per unit of length, that is:

- For a crack in the bulk, $2\gamma_e^g = 2\gamma_e$ with γ_e the edge energy per unit of length of the new created edge.
- For a crack along a GB, $2\gamma_e^g = 2\gamma_e - \gamma_{GB}$ with γ_e the edge energy per unit of length of the new created edge and γ_{GB} the energy recovered from the destruction of the GB. Note however that this decomposition is in the case of graphene rather artificial. Indeed, some pentagon and heptagon defects may remain, after fracture, on either side of the crack, making thus the decomposition of $2\gamma_e^g$ in surface energy created and grain boundary energy recovered meaningless.

In both cases, $2\gamma_e^g$ is defined and obtained from the difference in potential energy U_{pot} between the broken and non-broken relaxed configurations with

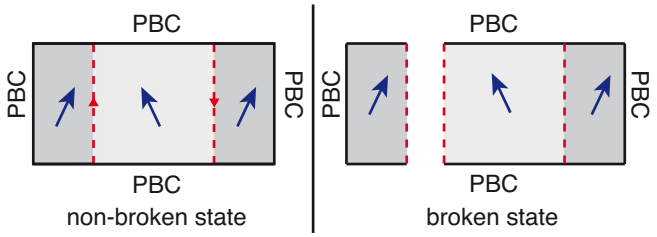

Figure F.10: Schema of the two configurations used to compute the generalized edge energy γ_e^g as defined in Section F.4.2. γ_e^g is computed from the difference in potential energy between the broken and non-broken states divided by twice the length of the crack.

periodic boundary conditions (PBCs) shown in Figure F.10 divided by the crack length. Indeed, from Eq. (F.6), the difference in internal energy (that is potential energy in the absence of kinetic energy) between the two configurations of Figure F.10 corresponds to $2\gamma_e^g a$.

We then compute the evolution of U_{el} - and thus Π - by inverting Eq. (F.6).

We describe the state of the system at time t with two variables: $q(t)$ the prescribed displacement (see Section F.3.4) and $a(t)$ the crack length, hence $\Pi(q,a) = U_{el}(q,a)$ is a function of these two variables that are linked, at equilibrium crack propagation, by Eq. (F.4).

We use a simple Bernoulli-Euler beam model of the DCB simulation with an isotropic linear elastic constitutive law to relate G to the total derivative of $\Pi(q,a)$ with respect to a taking into account the relation $q(a)$ satisfied during crack propagation. The linear isotropic model is reasonable given that strains in the DCB are, except near the crack tip, less than 0.5% (see Figure F.4). Denoting E the 2D-Young's modulus with dimension force per length and h the width of DCB's arms (Figure F.6), the mechanical potential energy can be written (Freund, 1998):

$$\Pi(q,a) = Eh^3 \frac{q^2}{4a^3}. \tag{F.7}$$

Writing the equilibrium crack propagation condition Eq. (F.4) with G computed with Eqs. (F.5) and (F.7), we obtain the relation between a and q:

$$q(a) = \sqrt{\frac{4G_c}{3Eh^3}} a^2. \tag{F.8}$$

That allows us to write Π as a function of a only:

$$\widetilde{\Pi}(a) = \Pi(q(a),a) = \frac{G_c a}{3}. \tag{F.9}$$

Hence, G_c may be deduced from the total derivative of $\widetilde{\Pi}(a)$ that is computed from molecular dynamics outputs,

$$G_c = 3\frac{\mathrm{d}\widetilde{\Pi}}{\mathrm{d}a}. \tag{F.10}$$

On Figure F.11 we plot the function $\widetilde{\Pi}(a)$ as computed from MD. We can

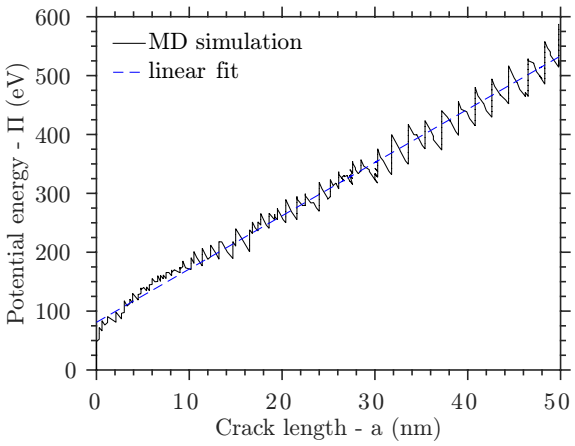

Figure F.11: Mechanical potential energy of the double cantilever beam as computed in the MD simulation with a linear fit of the average evolution in accordance with Eq. (F.10) of the continuum model.

Specimen	w_{sep}	G_c	$2\gamma_e^g$
Pristine	3.1	2.7	2.2
GB (3,1)|(3,1)	2.9	2.7	1.9
GB (7,0)|(4,4)	3.0	2.8	1.9

Table F.2: Work of separation w_{sep} of the TSL, fracture toughness G_c and generalized edge energy $2\gamma_e^g$ for the three studied configurations: Pristine graphene with a crack along the $[1\bar{1}00]$ (or armchair) direction, the GB (3,1)|(3,1) and the GB (7,0)|(4,4). All linear energies are expressed in eV/Å.

see that, notwithstanding the saw-tooth pattern in $\widetilde{\Pi}(a)$ related to atomic scale phenomena, the overall evolution of the function that is to be considered in the continuum approach is linear in accordance with Eq. (F.9), except in the crack initiation region where the beam model is not appropriate. The slope of the linear fit to the function $\widetilde{\Pi}(a)$ and Eq. (F.10) yield G_c. For the GB $(3,1)|(3,1)$ we obtain $G_c = 2.7$ eV/Å.

Table F.2 presents the values of the work of separation for the modeled TSLs, the fracture toughness and the edge energy for the three studied configurations. Their comparison shows that the work of separation of the derived TSLs falls within 10% of the fracture toughness for the configurations studied. Therefore, the TSLs proposed for FEM implementation are energetically consistent with the energy based approach of Griffith for crack propagation. The values of fracture toughness obtained for the grain boundaries and the bulk graphene are consistent with the empirical measures of the fracture toughness of polycrystalline graphene performed by Zhang et al. (2014) They have measured the critical fracture stress of nanocracked polycrystalline graphene sheets and obtained an empirical value of the fracture toughness of 15.9 J/m^2 or 3.3 eV/Å. This measure which represents a microscopic homogenized measure of the fracture toughness is expected to lie in the range of the nanoscopic fracture

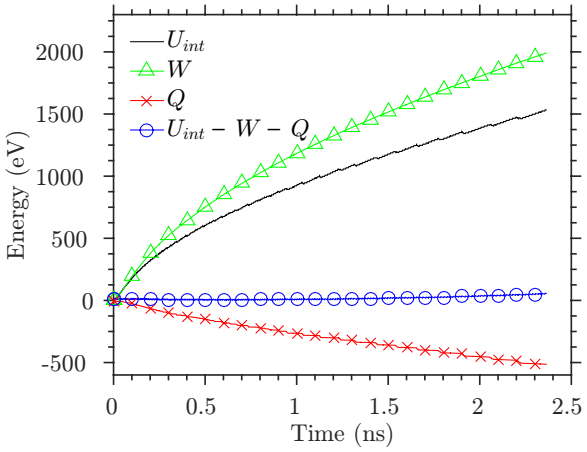

Figure F.12: Energy balance of the delamination simulation of the GB $(3,1)|(3,1)$. U_{int}, W, and Q are respectively the internal energy of the DCB system, the work received from the two external reaction forces causing the delamination and the heat received from the thermostat. Kinetic energy is negligible. That $U_{int} - W - Q$ is constant and zero to within the accuracy of the MD simulation demonstrates conservation of energy.

toughnesses of bulk graphene and its grain boundaries. Indeed, our computation of nanoscopic fracture toughnesses reported in Table F.2 are of the same order as the microscopic fracture toughness measured by Zhang et al. (2014).

Table F.2 also reports the values of $2\gamma_e^g$ that correspond to $2\gamma_e$ for the bulk and $2\gamma_e - \gamma_{GB}$ for the GBs. In all the cases, the fracture toughness is about 35% higher than $2\gamma_e^g$ which is consistent with the fact that $2\gamma_e^g$ is a lower bound of the energy per unit length required to propagate a crack. The difference between $2\gamma_e^g$ and fracture toughness is likely to be attributed to the phenomenon of bond trapping (Thomson et al., 1971; Möller and Bitzek, 2014). Whereas it is often assumed that the fracture toughness corresponds to the edge energy created decreased by the grain boundary energy, bond trapping at the atomic scale may require greater amount of energy to propagate the crack. The concept of bond trapping comes from the fact that fracture propagation is ultimately determined by the strength of interatomic bonds. The crack may be caught in a metastable state where an energy barrier needs to be crossed to allow the propagation (Holland and Marder, 1999; Bitzek et al., 2015). The extra energy is supposed to be transported in the lattice vibrations or, for the thermostated case, in the heat bath itself.

This thermal dissipation appears clearly when we check the energy balance of the global system. Thermodynamic quantities that characterize energy transfers are the internal energy U_{int}, the work W received by the system from external forces and the heat Q received by the system from the thermostat. Figure F.12 shows that during the delamination process, the work provided by the external reaction forces is larger than the change in internal energy and concurrently heat is released by the system to the thermostat ($Q < 0$). Since we check that $U_{int} - W - Q$ is constant with time (see Figure F.12, numerically the

deviation in $U_{int} - W - Q$ from zero remains less than 3% of W), the first law of thermodynamics $\Delta U_{int} = W + Q$ is satisfied, which is to say in MD terms, that the energy is conserved. The difference between U_{int} and W indicates that not all the work provided by the external forces to the system is transmitted to the internal energy. This thermal dissipation is consistent with the bond trapping that we have previously identified.

F.4.3 *Mesh size choice and effect*

Because of the high gradients of stress at the tip of the crack, we expect the traction-separation response to depend on the size of the CZVE. An interesting discussion on the dependence of the traction-separation relation on the exact definition of the opening displacement and the traction at the atomic scale can be found in Gall et al. (2000). We explain here that the choice of the CZVE size in which stress and displacement are computed is justified by quantitative analysis of the TSL. Generally speaking, the CZVE should be small enough to resolve the stress gradient near the crack tip but large enough to ensure that the atomic scale variations of the atomic stress (i.e. the value of the Virial stress for individual atoms) are smoothened. The last condition ensures that the Virial stress averaged over the CZVE converges sufficiently close to the Cauchy stress. Nevertheless, since the TSL is itself an interpolation of the stress-separation measures, a perfect convergence of the CZVE average to the continuum definition of the Cauchy stress is not necessary.

First, the width L_y in Figure F.7 of the CZVE should be large enough to encompass the pre-stress field, due to the pentagon-heptagon defects, whose size characterizes the 'width of the GB'. The lower bound for L_y thus lies about 8 Å. The choice of L_y should also resolve the stress gradient in y-direction that spans over about 30 Å (30 Å is the length over which the atomic stress is reduced by four). Within this range, we choose $L_y = 10$ Å noting that any value between 8 Å and 20 Å provides TSL's parameters that differ by less than 5%.

The second parameter is the length L_x of the CZVE. Yamakov et al. (2006) noticed that the length of the CZVE gives a length scale inherent to the computed TSL. This length scale will be used in the FEM as the interface element length. Thus, considering the mesh size of the FEM in which the TSL will be implemented provides an enlightening insight for the choice of L_x.

There exists an intrinsic length scale along the crack path when implementing the CZM which is the cohesive zone length. The cohesive zone length is a characteristic length of the process zone over which traction are exerted. It is defined by Hillerborg et al. (1976) as:

$$l_{cz} = \frac{EG_c}{{t_m}^2}, \tag{F.11}$$

where E is the Young's modulus of the material.

For the FEM implementation of the CZM to converge, the FE mesh along the cohesive surface elements must resolve the stress gradient in the cohesive zone, practically the cohesive zone length should contain at least two to three

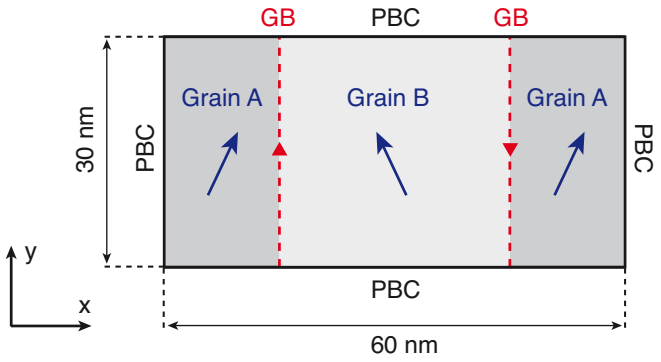

Figure F.13: Schema of the simulation cell used to compute the intrinsic strength of the grain boundaries. Periodic boundary conditions are enforced along the x and y directions.

elements (Turon et al., 2007). In the case of graphene, taking $E = 340$ N/m (Lee et al., 2008) and $G_c = 3.0$ eV/Å, $t_m = 25$ N/m as average values for the studied GBs, the cohesive zone length is: $l_{cz} = 2.6$ nm. Therefore, in order to have three elements or more within the cohesive zone, the length of the cohesive zone elements should be less than or equal to $l_e = 0.9$ nm. This first analysis provides an upper bound for the length L_x of the CZVE. On the other hand, L_x should be large enough to give a good estimate of the Cauchy stress and, if possible, should be a multiple of the repeating length of the pattern of defects in order to smooth out the atomic scale stress variations.

Giving these constraints, the length of the CZVE is taken close to 9 Å, the exact values being adjusted with the repeating length of the GB that are 8.9 Å for the GB $(3,1)|(3,1)$ and 17.0 Å for GB $(7,0)|(4,4)$. We therefore choose for the CZVE length: $L_x = 8.9$; 8.5 ; 9 Å, for the GB $(3,1)|(3,1)$, the GB $(7,0)|(4,4)$ and bulk graphene respectively.

The modification of L_x on the TSL is such that an increase in L_x reduces t_m while keeping the work of separation w_{sep} constant. Therefore the comparison of the maximum traction t_m of the TSL with the expected value provides another way to set the value of L_x. Indeed, t_m corresponds physically to the maximum stress sustainable by the grain boundary and gives the criterion for crack initiation. By performing equibiaxial tensile simulations on flawless bicrystals (that correspond to the crack tip stress state for which the TSL is derived) we have determined the expected value of t_m. We have performed simulations on bicrystal samples of dimensions 60 nm by 30 nm containing two GBs to enforce periodic boundary conditions in the two in-plane directions. See Figure F.13 for a schematic view of the performed tensile simulations. We have obtained, under equibiaxial stress state, the strength of the grain boundary and the bulk by computing the maximum normal component of the stress in the x-direction, reached before failure. For the three configurations, GB $(3,1)|(3,1)$, GB $(7,0)|(4,4)$ and bulk graphene we compute a strength under equibiaxial stress state of (24 ± 0.5) N/m. The maximum stresses t_m of the TSLs given in Table F.1 correspond to this reference value of strength, further confirming the consistency of the choice of 9 Å for L_x.

Last we discuss the definition of the opening displacement. Yamakov et al. (2006) defines the separation as the distance between the CZVE averaged over all the atoms in the CZVE while Krull and Yuan (2011) only takes the pair of closer atoms on both sides of the crack to define the separation. It can be understood that the location where the opening displacement is measured only affects the value of the separation δ_m at which the maximum stress is reached. This is because the opening displacement is, regardless of where it is measured, defined relative to the uncracked state for which δ=0; whether it is defined between the crack edges or between areas encompassing the edges does not change the value of δ when the crystals are relaxed. Thus, the critical displacement δ_c at which the traction falls to zero is independent of the exact definition of the separation and it is only δ_m and consequently the initial slope of the TSL that is affected by that choice. The dependence of the TSL on the definition of the separation, as described above, has been numerically observed by Zhou et al. (2008). Given that the modification of the definition of the separation amounts to changing the initial slope of the cohesive zone while keeping the other parameters t_m and δ_c unchanged, we examine the meaning of the initial slope with respect to the FEM implementation of the TSL. The slope of the increasing part of the TSL is referred as the interface stiffness, however it does not really correspond to a physical concept since it depends on the size of the volume that is considered to be the interface. Instead, the value of the interface stiffness is rather based on numerical considerations in the FEM implementation. The interface stiffness should be large enough to make sure that the contribution of the cohesive elements to the global compliance remains small but not too high to avoid numerical problems such as stress oscillations (Turon et al., 2007; De Borst, 2003). Given the fact that it is mainly numerical aspects related to FEM that govern the choice of the interface stiffness used in the implementation of the CZM, we provide herein a TSL based on the physical definition of the separation for an atomically sharp crack. This definition corresponds to a measure of the separation exactly at the atoms forming the crack edges. A measure further away from the crack would include a contribution of the bulk to the interface description. For the FEM implementation, the interface stiffness would have to be properly adapted to the numerical context.

F.4.4 *Discussion on the FEM implementation*

As discussed in Section F.4.3, for a successful implementation of the CZM in the FEM, the cohesive zone length should contain at least three elements, bringing the element size down to $l_e = 0.9$ nm. To reduce the computational cost of such a FEM simulation it is of practical interest to be able to implement the CZM with coarser mesh sizes that exceed the cohesive zone length. Such a method has been proposed by Turon et al. (2007) who showed that delaminations were well predicted by FEM simulations with a mesh size up to three times the cohesive zone length provided that the TSL was properly scaled. In short, the scaling of the TSL consists, when the length l_e of a cohesive interface

element does not resolve the cohesive zone length any longer, in reducing the peak traction as $1/\sqrt{l_e}$ while keeping the fracture toughness constant.

More precisely, the scaling procedure proposed by Turon et al. (2007) to accurately model a delamination process with CZM implemented in a FEM with elements larger than the cohesive zone length l_{cz} is based on the following idea: Although it is the peak traction of the TSL t_m that governs the crack initiation, the crack propagation is essentially controlled by the work of separation w_{sep}. Further it was observed numerically that changing the peak traction does not significantly alter the FEM predictions of a delamination process but that lowering that peak traction improves the convergence of the results with respect to the element size l_e. To be understood, these observations may be put in perspective with the need to resolve the cohesive zone length with the element size. The cohesive zone length is related to the size of the elements that discretize it through the formula:

$$l_{cz} = N_e l_e. \tag{F.12}$$

Then, by combining equations (F.11) and (F.12) one gets the relation between the peak traction and the size of one element:

$$t_m = \sqrt{\frac{EG_c}{N_e l_e}}. \tag{F.13}$$

Eq. (F.13) is a way to express the finite element size l_e given the peak traction t_m of the TSL and by fixing the number of elements N_e in the cohesive zone length to a value large enough in order to discretize the stress profile accurately enough.

The strategy proposed consists in scaling the TSL in such a way that first N_e is kept to the chosen value - $N_e = 3$ is a minimum for a resolution of the cohesive zone - and second Eq. (F.13) is satisfied. Practically one may fix l_e to an arbitrary value $\overline{l_e}$ larger than l_{cz}/N_e and scale the peak traction of the TSL to the artificial value $\overline{t_m}$ that result from Eq. (F.13) in which $\overline{l_e}$ has been substituted to l_e. This amounts to defining an artificial larger cohesive zone length $\overline{l_{cz}} = N_e\overline{l_e}$ that is properly discretized. Moreover, the scaling of the TSL should be done at a constant work of separation in order to conserve a good mechanical energy balance. The critical opening displacement δ_c will be increased accordingly.

Turon et al. (2007) have shown numerically that this procedure allows to accurately predict the delamination process for an element size $\overline{l_e}$ set to up to three times the cohesive zone length l_{cz}. The accuracy of the results can be seen in the estimate of the macroscopic load versus displacement. However, with such a scaled TSL, the stress concentration at the crack tip will not be well predicted.

We have observed a quite similar rescaling behavior when changing the CZVE length L_x in the MD extraction of the TSL. Indeed, Figure F.14 and the TSL parameters reported in Table F.3 show that when the length of the CZVE exceeds 0.9 nm (i.e. one third of the cohesive zone length), that is to say does not resolve the cohesive zone length, the peak traction of the TSL is reduced as $1/\sqrt{L_x}$ while conserving w_{sep}. Saether (2008) has suggested that the length

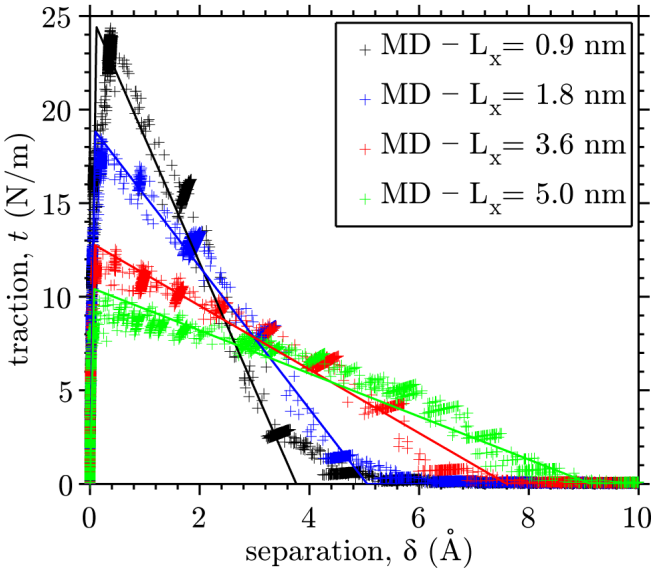

Figure F.14: Dependence of the TSL on the length L_x of the CZVE for the GB $(3,1)|(3,1)$. Individual crosses show the traction-separation MD measures and solid lines represent the bilinear fitted TSLs. Note that when L_x increases, t_m decreases while keeping the work of separation conserved.

L_x (nm)	t_m (N/m)	δ_m (Å)	δ_c (Å)	w_{sep} (eV/Å)	$t_m\sqrt{L_x}$ (10^{-4} N.m$^{-1/2}$)
0.9	24	0.1	3.8	2.9	7.2
1.8	19	0.1	5.1	3.0	8.1
3.6	13	0.1	7.6	3.0	7.8
5.0	10	0.1	9.1	3.0	7.1

Table F.3: Parameters of the bilinear TSLs obtained by a fit to the MD computations for the GB (3,1)|(3,1) when changing the length L_x of the CZVE. The parameters correspond to the TSLs shown Figure F.14.

of the CZVE L_x should be the same as the cohesive surface element size l_e in the FEM mesh and our numerical results put in perspective with the work of Turon et al. (2007) tend to confirm this idea.

On the basis of the work of Turon et al. (2007) we expect that a FEM simulation with a cohesive surface element size of 5 nm embedding the corresponding scaled-TSL will properly model the crack propagation for a lower computational cost although the stress concentration at the crack tip will not be resolved. Table F.4 gives the scaled-TSL parameters for the two GBs and the bulk corresponding to an element size l_e=5 nm. However, this scaling procedure has been validated for the delamination process only and it may be, since the crack initiation is governed by the value of t_m, that the prediction of the crack initiation will not be accurate when using the elements that are larger than 0.9 nm. The proposed scaled-TSL may be a way to model a phenomenon at a

Specimen	t_m (N/m)	δ_m (Å)	δ_c (Å)	w_{sep} (eV/Å)
Pristine	10	0.2	9.9	3.1
GB (3,1)|(3,1)	10	0.1	9.1	3.0
GB (7,0)|(4,4)	10	0.2	9.6	3.1

Table F.4: Parameters of the scaled bilinear TSLs that goes with a FEM mesh size $l_e = 5.0$ nm.

reasonable computational cost, but will miss other features for which a finer mesh will remain necessary.

F.5 CONCLUSION

For the purpose of developing a multiscale model of nanoindentation experiments performed on polycrystalline graphene, we have developed cohesive zone models of intergranular fracture that may be implemented in FEM. We have derived, from molecular dynamics, traction-separation laws that characterize high tilt angle grain boundaries. Grain boundaries of tilt angle 27.8°, 30.0° and pristine graphene have been investigated. We have performed MD simulations that reproduce the biaxial stress state to which the graphene is subjected during the indentation experiments in order to derive TSLs that correspond to the framework in which they will be implemented.

The MD simulations are designed to ensure a controlled crack propagation that allow an energetic validation of the TSL based on a comparison of the work of separation of the TSL and the fracture toughness of the sample. The energy absorbed by the cohesive tractions corresponds to the fracture toughness measured through the energy release rate during the equilibrium crack propagation. Our computation agrees with the experimental measures of the fracture toughness of polycrystalline graphene performed by Zhang et al. (2014) at the microscale. However, the fracture toughness turns out to be greater by about 35% than the energy thermodynamically necessary to create the two new edges: $2\gamma_e - \gamma_{GB}$. We attribute this difference to the phenomenon of bond trapping that specifically appears in atomic scale fracture.

The consistency of the TSL is discussed in relation to the mesh size effects introduced by the averaging procedure over the cohesive zone volume elements. When the scale over which atomic quantities are averaged is too large to resolve the traction distribution in the cohesive zone, in our case larger than 0.9 nm, the parameters of the TSL depend on the length of the volume elements. This dependence is such that the maximum traction t_m of the TSL is lower for coarser meshes while conserving the work of separation. When considering the FEM implementation of the CZM, the optimization of the computational cost encourages us to provide a TSL that could be implemented with coarser meshes. Therefore, we propose particular scaled-TSLs adapted to finite element surface elements ranging from 0.9 to 5 nm.

We have focused our study on two high angle grain boundaries and one type of intragranular crack under conditions of biaxial traction at the crack tip. The TSLs derived show that the TSL parameters, and in particular the fracture toughness of the high angle grain boundaries, remain comparable to the fracture toughness of the bulk. This provides a new point of view on the impact of the grain boundaries on the mechanical properties of graphene. Further work will be needed to extend the cohesive zone model to low angle grain boundaries. Moreover we have noticed a dependence of the TSL on the stress state applied at the tip of the crack, the TSLs are currently derived for quasi-equibiaxial stress states that correspond to what a graphene sheet experiences under the indentation tip. Supplementary investigations would be necessary to extend the TSL to other stress states.

BIBLIOGRAPHY

Adams, A. R. (2011). "Strained-Layer Quantum-Well Lasers." In: *IEEE Journal of Selected Topics in Quantum Electronics* 17.5, pp. 1364–1373. DOI: 10.1109/jstqe.2011.2108995 (cit. on p. 3).

Bardeen, J. and W. Shockley (1950). "Deformation Potentials and Mobilities in Non-Polar Crystals." In: *Physical Review* 80.1, pp. 72–80. DOI: 10.1103/physrev.80.72 (cit. on pp. 3, 4, 138, 145, 146).

Barlian, A., W.-T. Park, J. Mallon, A. Rastegar, and B. Pruitt (2009). "Review: Semiconductor Piezoresistance for Microsystems." In: *Proceedings of the IEEE* 97.3, pp. 513–552. DOI: 10.1109/jproc.2009.2013612 (cit. on p. 3).

Bir, G. L., G. E. Pikus, P. Shelnitz, and D. Louvish (1974). *Symmetry and strain-induced effects in semiconductors*. Vol. 624. Wiley New York (cit. on pp. 3, 138, 145, 146, 148).

Chadwick, P. (1976). *Continuum mechanics*. Wiley New York (cit. on p. 10).

Chu, M., Y. Sun, U. Aghoram, and S. E. Thompson (2009). "Strain: A Solution for Higher Carrier Mobility in Nanoscale MOSFETs." In: *Annual Review of Materials Research* 39.1, pp. 203–229. DOI: 10.1146/annurev-matsci-082908-145312 (cit. on p. 3).

Coleman, B. D. and W. Noll (1963). "The thermodynamics of elastic materials with heat conduction and viscosity." In: *Archive for Rational Mechanics and Analysis* 13.1, pp. 167–178. DOI: 10.1007/BF01262690 (cit. on pp. 8, 13, 69).

Coleman, J. (2000). "Strained-layer InGaAs quantum-well heterostructure lasers." In: *IEEE Journal of Selected Topics in Quantum Electronics* 6.6, pp. 1008–1013. DOI: 10.1109/2944.902149 (cit. on p. 3).

Creemer, J. F., F. Fruett, G. C. M. Meijer, and P. J. French (2001). "The piezojunction effect in silicon sensors and circuits and its relation to piezoresistance." In: *IEEE Sensors Journal* 1.2, pp. 98–. DOI: 10.1109/JSEN.2001.936927 (cit. on pp. 4, 145).

Creemer, J. and P. French (2000). "The piezojunction effect in bipolar transistors at moderate stress levels: a theoretical and experimental study." In: *Sensors and Actuators A: Physical* 82.1 - 3, pp. 181 –185. DOI: 10.1016/S0924-4247(99)00362-3 (cit. on pp. 4, 139).

Creemer, J. F. (2002). "The effect of mechanical stress on bipolar transistor characteristics." PhD thesis. Delft University of Technology. URL: http://resolver.tudelft.nl/uuid:ff17cb76-7599-486b-b287-3123c806ac0f (cit. on pp. 4, 138, 139, 145, 146, 148–150).

Datta, A., J. Damon-Lacoste, P. Roca i Cabarrocas, and P. Chatterjee (2008). "Defect states on the surfaces of a P-type c-Si wafer and how they control the performance of a double heterojunction solar cell." In: *Solar Energy Materials and Solar Cells* 92.11, pp. 1500–1507. DOI: 10.1016/j.solmat.2008.06.015 (cit. on p. 50).

Ding, X., W. H. Ko, and J. M. Mansour (1990). "Residual stress and mechanical properties of boron-doped p+-silicon films." In: *Sensors and Actuators A: Physical* 23.1, pp. 866 –871. DOI: 10.1016/0924-4247(90)87048-N (cit. on p. 22).

Ericson, F. and J.-A. Schweitz (1990). "Micromechanical fracture strength of silicon." In: *Journal of Applied Physics* 68.11, pp. 5840–5844. DOI: 10.1063/1.346957 (cit. on p. 22).

Fischetti, M. V. and S. E. Laux (1996). "Band structure, deformation potentials, and carrier mobility in strained Si, Ge, and SiGe alloys." In: *Journal of Applied Physics* 80.4, p. 2234. DOI: 10.1063/1.363052 (cit. on pp. 3, 138, 139, 148).

Fonash, S. (2012). *Solar cell device physics*. Elsevier. DOI: 10.1016/C2009-0-19749-0 (cit. on pp. 18, 49).

Freund, L. and H. Johnson (2001). "Influence of strain on functional characteristics of nanoelectronic devices." In: *Journal of the Mechanics and Physics of Solids* 49.9. The J.W. Hutchinson and J.R. Rice 60th Anniversary Issue, pp. 1925 –1935. DOI: 10.1016/S0022-5096(01)00039-4 (cit. on p. 4).

Fried, E. and M. E. Gurtin (1999). "Coherent Solid-State Phase Transitions with Atomic Diffusion: A Thermomechanical Treatment." In: *Journal of Statistical Physics* 95.5, pp. 1361–1427. DOI: 10.1023/A:1004535408168 (cit. on p. 8).

Fried, E. and M. E. Gurtin (2004). "A Unified Treatment of Evolving Interfaces Accounting for Small Deformations and Atomic Transport with Emphasis on Grain-Boundaries and Epitaxy." In: *Advances in Applied Mechanics* 40, pp. 1 –177. DOI: 10.1016/S0065-2156(04)40001-5 (cit. on p. 8).

Friedel, P., M. S. Hybertsen, and M. Schlüter (1989). "Local empirical pseudopotential approach to the optical properties of Si/Ge superlattices." In: *Phys. Rev. B* 39 (11), pp. 7974–7977. DOI: 10.1103/PhysRevB.39.7974 (cit. on p. 138).

Goddard, J. D. (2011). "On the Thermoelectricity of W. Thomson: Towards a Theory of Thermoelastic Conductors." In: *Journal of Elasticity* 104.1, pp. 267–280. DOI: 10.1007/s10659-011-9309-6 (cit. on p. 11).

Gurtin, M. E. and A. S. Vargas (1971). "On the classical theory of reacting fluid mixtures." In: *Archive for Rational Mechanics and Analysis* 43.3, pp. 179–197. DOI: 10.1007/BF00251451 (cit. on pp. 8, 11, 13).

Herring, C. and E. Vogt (1956). "Transport and Deformation-Potential Theory for Many-Valley Semiconductors with Anisotropic Scattering." In: *Physical Review* 101.3, pp. 944–961. DOI: 10.1103/physrev.101.944 (cit. on pp. 3, 138, 145, 146).

Johnson, H. T., L. B. Freund, C. D. Aky'uz, and A. Zaslavsky (1998). "Finite element analysis of strain effects on electronic and transport properties in quantum dots and wires." In: *Journal of Applied Physics* 84.7, pp. 3714–3725. DOI: 10.1063/1.368549 (cit. on p. 4).

Johnson, H. and L. Freund (2001). "The influence of strain on confined electronic states in semiconductor quantum structures." In: *International Journal of Solids and Structures* 38.6-7, pp. 1045 –1062. DOI: 10.1016/S0020-7683(00)00072-X (cit. on p. 4).

Kanda, Y. (1967). "Effect of Stress on Germanium and Silicon p - n Junctions." In: *Japanese Journal of Applied Physics* 6.4, p. 475. DOI: 10.1143/JJAP.6.475 (cit. on pp. 4, 138, 139, 148).

Kanda, Y. (1991). "Piezoresistance effect of silicon." In: *Sensors and Actuators A: Physical* 28.2, pp. 83–91. DOI: 10.1016/0924-4247(91)85017-i (cit. on pp. 3, 145).

Kittel, C. (2004). *Introduction to Solid State Physics*. 8th. New York: Wiley New York (cit. on p. 3).

Kittel, C. and H. Kroemer (1980). *Thermal physics*. Macmillan (cit. on pp. 14, 17).

Kleimann, P., B. Semmache, M. Le Berre, and D. Barbier (1998). "Stress-dependent hole effective masses and piezoresistive properties of *p*-type monocrystalline and polycrystalline silicon." In: *Phys. Rev. B* 57 (15), pp. 8966–8971. DOI: 10.1103/PhysRevB.57.8966 (cit. on pp. 3, 145, 148).

Kovetz, A. (2000). *Electromagnetic theory*. Oxford University Press Oxford (cit. on pp. 8, 10, 11, 13, 14).

Kroemer, H. (1957). "Quasi-electric and quasi-magnetic fields in nonuniform semiconductors." In: *Rca Rev* 18.3, pp. 332–342 (cit. on p. 4).

Lange, D., P. Roca i Cabarrocas, N. Triantafyllidis, and D. Daineka (2016). "Piezoresistivity of thin film semiconductors with application to thin film silicon solar cells." In: *Solar Energy Materials and Solar Cells* 145, Part 2. Selected papers of the {EMRS} 2015 Spring meeting Ű Symposium C on Advanced Inorganic Materials and Structures for Photovoltaics, pp. 93 –103. DOI: 10.1016/j.solmat.2015.09.014 (cit. on p. 6).

Lorenzi, H. G. de and H. F. Tiersten (1975). "On the interaction of the electromagnetic field with heat conducting deformable semiconductors." In: *Journal of Mathematical Physics* 16.4, pp. 938–957. DOI: 10.1063/1.522600 (cit. on p. 4).

Manku, T. and A. Nathan (1993). "Electrical properties of silicon under nonuniform stress." In: *Journal of Applied Physics* 74.3, pp. 1832–1837. DOI: 10.1063/1.354790 (cit. on pp. 4, 18).

Markowich, P., C. Ringhofer, and C Schmeiser (1990). *Semiconductor Equations*. Springer-Verlag Wien, New York. DOI: 10.1007/978-3-7091-6961-2 (cit. on p. 33).

Markowich, P. A. (1986). *The stationary semiconductor device equations*. Springer-Verlag Wien, New York. DOI: 10.1007/978-3-7091-3678-2 (cit. on pp. 5, 28, 31, 142).

Markowich, P. A. and C. A. Ringhofer (1984). "A Singularly Perturbed Boundary Value Problem Modelling a Semiconductor Device." In: *SIAM Journal on Applied Mathematics* 44.2, pp. 231–256. DOI: 10.1137/0144018 (cit. on p. 5).

Marshak, A. H. and C. M. V. Vliet (1984). "Electrical current and carrier density in degenerate materials with nonuniform band structure." In: *Proceedings of the IEEE* 72.2, pp. 148–164. DOI: 10.1109/PROC.1984.12836 (cit. on pp. 4, 18).

Marshak, A. H. and K. M. van Vliet (1978). "Electrical current in solids with position-dependent band structure." In: *Solid-State Electronics* 21.2, pp. 417 –427. DOI: 10.1016/0038-1101(78)90272-1 (cit. on pp. 4, 18).

Müller, I. (1968). "A thermodynamic theory of mixtures of fluids." In: *Archive for Rational Mechanics and Analysis* 28.1, pp. 1–39. DOI: 10.1007/BF00281561 (cit. on p. 11).

Najafi, K and K Suzuki (1989). "Measurement of fracture stress, young's modulus, and intrinsic stress of heavily boron-doped silicon microstructures." In: *Thin Solid Films* 181.1, pp. 251 –258. DOI: 10.1016/0040-6090(89)90492-6 (cit. on p. 22).

Nelson, J. (2003). *The physics of solar cells*. Vol. 1. Imperial College Press, UK. DOI: 10.1142/p276 (cit. on pp. 18, 36, 49).

Pierret, R. F. (1987). *Advanced semiconductor fundamentals*. Vol. 6. Addison-Wesley Reading, MA (cit. on pp. 9, 19).

Please, C. P. (1982). "An Analysis of Semiconductor P-N Junctions." In: *IMA Journal of Applied Mathematics* 28.3, pp. 301–318. DOI: 10.1093/imamat/28.3.301 (cit. on p. 5).

Ritter, D., K. Weiser, and E. Zeldov (1987). "Steady-state photocarrier grating technique for diffusion-length measurement in semiconductors: Theory and experimental results for amorphous silicon and semi-insulating GaAs." In: *Journal of Applied Physics* 62.11, pp. 4563–4570. DOI: 10.1063/1.339051 (cit. on p. 50).

Sah, C. tang, R. Noyce, and W. Shockley (1957). "Carrier Generation and Recombination in P-N Junctions and P-N Junction Characteristics." In: *Proceedings of the IRE* 45.9, pp. 1228–1243. DOI: 10.1109/jrproc.1957.278528 (cit. on p. 44).

Selberherr, S. (1984). *Analysis and Simulation of Semiconductor Devices*. Springer Vienna. DOI: 10.1007/978-3-7091-8752-4 (cit. on p. 21).

Shockley, W. (1949). "The Theory of p-n Junctions in Semiconductors and p-n Junction Transistors." In: *Bell System Technical Journal* 28.3, pp. 435–489. DOI: 10.1002/j.1538-7305.1949.tb03645.x (cit. on p. 24).

Smith, C. S. (1954). "Piezoresistance Effect in Germanium and Silicon." In: *Physical Review* 94.1, pp. 42–49. DOI: 10.1103/physrev.94.42 (cit. on pp. 3, 139, 149, 150).

Sobkowicz, I. P. (Dec. 2014). "Study and optimization of the growth of a-Si:H on wet-chemically textured c-Si substrates for the enhancement of a-Si:H/c-Si heterojunction solar cells." Theses. Ecole Doctorale Polytechnique. URL: https://pastel.archives-ouvertes.fr/tel-01120054 (cit. on p. 50).

Steigmann, D. J. (2009). "On the Formulation of Balance Laws for Electromagnetic Continua." In: *Mathematics and Mechanics of Solids* 14.4, pp. 390–402. DOI: 10.1177/1081286507080808 (cit. on p. 8).

Suckow, S. (2014). *2/3-Diode Fit*. URL: https://nanohub.org/resources/14300 (cit. on p. 46).

Suckow, S., T. M. Pletzer, and H. Kurz (2012). "Fast and reliable calculation of the two-diode model without simplifications." In: *Progress in Photovoltaics: Research and Applications* 22.4, pp. 494–501. DOI: 10.1002/pip.2301 (cit. on pp. 44, 46).

Sun, Y., S. E. Thompson, and T. Nishida (2010). *Strain Effect in Semiconductors*. Springer Nature. DOI: 10.1007/978-1-4419-0552-9 (cit. on p. 149).

Sze, S. M. and K. K. Ng (2006). *Physics of semiconductor devices*. John wiley & sons. DOI: 10.1002/0470068329 (cit. on pp. 7, 19, 21, 44, 148).

Tadmor, E. B., R. E. Miller, and R. S. Elliott (2012). *Continuum mechanics and thermodynamics: from fundamental concepts to governing equations*. Cambridge University Press. DOI: 10.1017/CBO9781139017657 (cit. on p. 14).

Taguchi, M., E. Maruyama, and M. Tanaka (2008). "Temperature Dependence of Amorphous/Crystalline Silicon Heterojunction Solar Cells." In: *Japanese Journal of Applied Physics* 47.2, pp. 814–818. DOI: 10.1143/jjap.47.814 (cit. on p. 49).

Thompson, S. et al. (2004). "A 90-nm Logic Technology Featuring Strained-Silicon." In: *IEEE Transactions on Electron Devices* 51.11, pp. 1790–1797. DOI: 10.1109/ted.2004.836648 (cit. on p. 3).

Thompson, S., G. Sun, Y. S. Choi, and T. Nishida (2006). "Uniaxial-process-induced strained-Si: extending the CMOS roadmap." In: *IEEE Transactions on Electron Devices* 53.5, pp. 1010–1020. DOI: 10.1109/ted.2006.872088 (cit. on p. 3).

Walle, C. G. Van de (1989). "Band lineups and deformation potentials in the model-solid theory." In: *Phys. Rev. B* 39 (3), pp. 1871–1883. DOI: 10.1103/PhysRevB.39.1871 (cit. on p. 138).

Wolf, M., G. Noel, and R. Stirn (1977). "Investigation of the double exponential in the current—Voltage characteristics of silicon solar cells." In: *IEEE Transactions on Electron Devices* 24.4, pp. 419–428. DOI: 10.1109/t-ed.1977.18750 (cit. on p. 44).

Wortman, J. J. and R. A. Evans (1965). "Young's Modulus, Shear Modulus, and Poisson's Ratio in Silicon and Germanium." In: *Journal of Applied Physics* 36.1, p. 153. DOI: 10.1063/1.1713863 (cit. on pp. 37, 150).

Wortman, J. J. and J. R. Hauser (1966). "Effect of Mechanical Stress on p-n Junction Device Characteristics. II. Generation-Recombination Current." In: *Journal of Applied Physics* 37.9, pp. 3527–3530. DOI: 10.1063/1.1708894 (cit. on p. 4).

Wortman, J. J., J. R. Hauser, and R. M. Burger (1964). "Effect of Mechanical Stress on p-n Junction Device Characteristics." In: *Journal of Applied Physics* 35.7, pp. 2122–2131. DOI: 10.1063/1.1702802 (cit. on pp. 4, 146).

Xiao, Y. and K. Bhattacharya (2008). "A Continuum Theory of Deformable, Semiconducting Ferroelectrics." In: *Archive for Rational Mechanics and Analysis* 189.1, pp. 59–95. DOI: 10.1007/s00205-007-0096-y (cit. on pp. 5, 16).

Bales, G. S. and A. Zangwill (1990). "Morphological instability of a terrace edge during step-flow growth." In: *Physical Review B* 41.9, pp. 5500–5508. DOI: 10.1103/physrevb.41.5500 (cit. on p. 81).

Burton, W. K., N. Cabrera, and F. C. Frank (1951). "The Growth of Crystals and the Equilibrium Structure of their Surfaces." In: *Philosophical Transactions of the Royal Society A: Mathematical, Physical and Engineering Sciences* 243.866, pp. 299–358. DOI: 10.1098/rsta.1951.0006 (cit. on p. 62).

Cermelli, P. and M. E. Jabbour (2007). "Possible mechanism for the onset of step-bunching instabilities during the epitaxy of single-species crystalline films." In: *Phys. Rev. B* 75 (16), p. 165409. DOI: 10.1103/PhysRevB.75.165409 (cit. on pp. 63, 69).

Cermelli, P. and M. Jabbour (2005). "Multispecies epitaxial growth on vicinal surfaces with chemical reactions and diffusion." In: *Proceedings of the Royal Society of London A: Mathematical, Physical and Engineering Sciences* 461.2063, pp. 3483–3504. DOI: 10.1098/rspa.2005.1495 (cit. on pp. 62, 65, 68, 69).

Chandrasekhar, S. (1981). *Hydrodynamic and hydromagnetic stability*. Dover, New York (cit. on p. 103).

Chernov, A. A. (1961). "The spyral growth of crystals." In: *Soviet Physics Uspekhi* 4.1, pp. 116–148. DOI: 10.1070/pu1961v004n01abeh003328 (cit. on p. 62).

Chung, W. F. and M. S. Altman (2002). "Kinetic length, step permeability, and kinetic coefficient asymmetry on the Si(111) (7X7) surface." In: *Physical Review B* 66.7. DOI: 10.1103/physrevb.66.075338 (cit. on pp. 87, 118, 119, 158).

Coleman, B. D. and W. Noll (1963). "The thermodynamics of elastic materials with heat conduction and viscosity." In: *Archive for Rational Mechanics and Analysis* 13.1, pp. 167–178. DOI: 10.1007/BF01262690 (cit. on pp. 8, 13, 69).

Degawa, M., H. Minoda, Y. Tanishiro, and K. Yagi (2000). "Direct-current-induced drift direction of silicon adatoms on Si(111)-(1×1) surfaces." In: *Surface Science* 461.1-3, pp. L528–L536. DOI: 10.1016/s0039-6028(00)00593-8 (cit. on p. 125).

Degawa, M., H. Minoda, Y. Tanishiro, and K. Yagi (2001). "New Phase Diagram of Step Instabilities on Si(111) Vicinal Surfaces Induced by DC Annealing." In: *Journal of the Physical Society of Japan* 70.4, pp. 1026–1034. DOI: 10.1143/jpsj.70.1026 (cit. on p. 123).

Dufay, M., T. Frisch, and J.-M. Debierre (2007). "Role of step-flow advection during electromigration-induced step bunching." In: *Physical Review B* 75.24. DOI: 10.1103/physrevb.75.241304 (cit. on pp. 81, 84–86).

Eshelby, J. D. (1951). "The Force on an Elastic Singularity." In: *Philosophical Transactions of the Royal Society A: Mathematical, Physical and Engineering Sciences* 244.877, pp. 87–112. DOI: 10.1098/rsta.1951.0016 (cit. on pp. 72, 75).

Fu, E. S., D.-J. Liu, M. Johnson, J. Weeks, and E. D. Williams (1997). "The effective charge in surface electromigration." In: *Surface Science* 385.2-3, pp. 259–269. DOI: 10.1016/s0039-6028(97)00188-x (cit. on p. 59).

Ghez, R. and S. S. Iyer (1988). "The kinetics of fast steps on crystal surfaces and its application to the molecular beam epitaxy of silicon." In: *IBM Journal of Research and Development* 32.6, pp. 804–818. DOI: 10.1147/rd.326.0804 (cit. on p. 86).

Ghez, R., H. G. Cohen, and J. B. Keller (1990). "Stability of crystals that grow or evaporate by step propagation." In: *Applied Physics Letters* 56.20, pp. 1977–1979. DOI: 10.1063/1.103016 (cit. on p. 86).

Ghez, R., H. G. Cohen, and J. B. Keller (1993). "The stability of growing or evaporating crystals." In: *Journal of Applied Physics* 73.8, pp. 3685–3693. DOI: 10.1063/1.352928 (cit. on pp. 81, 84, 86, 133).

Gibbons, B. (2006). "Electromigration induced step instabilities on silicon surfaces." PhD thesis. Ohio State University. URL: http://rave.ohiolink.edu/etdc/view?acc_num=osu1143235175 (cit. on p. 123).

Gibbons, B., J. Noffsinger, and J. Pelz (2005). "Influence of Si deposition on the electromigration induced step bunching instability on Si(111)." In: *Surface Science* 575.1-2, pp. L51–L56. DOI: 10.1016/j.susc.2004.11.020 (cit. on pp. 123–125, 131).

Gibbons, B., S. Schaepe, and J. Pelz (2006). "Evidence for diffusion-limited kinetics during electromigration-induced step bunching on Si(111)." In: *Surface Science* 600.12, pp. 2417–2424. DOI: 10.1016/j.susc.2006.03.046 (cit. on pp. 123, 124, 128, 130, 160).

Gillet, F (2000). "Dynamique non linéaire de surfaces vicinales hors de équilibre." PhD thesis. Université Joseph Fourier, Grenoble, France. URL: http://fred.gillet.free.fr/These/these_F_Gillet.pdf (cit. on pp. 81, 84–87, 133).

Gurtin, M. E. (1993). *Thermomechanics of Evolving Phase Boundaries in the Plane*. Ed. by O. U. Press (cit. on p. 66).

Hata, K., A. Kawazu, T. Okano, T. Ueda, and M. Akiyama (1993). "Observation of step bunching on vicinal GaAs(100) studied by scanning tunneling microscopy." In: *Applied Physics Letters* 63.12, pp. 1625–1627. DOI: 10.1063/1.110716 (cit. on pp. 118, 157).

Hibino, H., K. Sumitomo, T. Fukuda, Y. Homma, and T. Ogino (1998). "Disordering of Si(111) at high temperatures." In: *Phys. Rev. B* 58 (19), pp. 12587–12589. DOI: 10.1103/PhysRevB.58.12587 (cit. on p. 156).

Homma, Y. and N. Aizawa (2000). "Electric-current-induced step bunching on Si(111)." In: *Physical Review B* 62.12, pp. 8323–8329. DOI: 10.1103/physrevb.62.8323 (cit. on pp. 59, 123).

Ichimiya, A., Y. Tanaka, and K. Ishiyama (1996). "Quantitative Measurements of Thermal Relaxation of Isolated Silicon Hillocks and Craters on the Si(111)-(7X7) Surface by Scanning Tunneling Microscopy." In: *Physical Review Letters* 76.25, pp. 4721–4724. DOI: 10.1103/physrevlett.76.4721 (cit. on pp. 118, 157).

Ishizaki, J. ya, S. Goto, M. Kishida, T. Fukui, and H. Hasegawa (1994). "Mechanism of Multiatomic Step Formation during Metalorganic Chemical Vapor deposition Growth of GaAs on (001) Vicinal Surface Studied by Atomic Force Microscopy." In: *Japanese Journal of Applied Physics* 33.1S, p. 721. DOI: 10.1143/JJAP.33.721 (cit. on pp. 118, 157).

Ishizaki, J. ya, K. Ohkuri, and T. Fukui (1996). "Simulation and Observation of the Step Bunching Process Grown on GaAs (001) Vicinal Surface by Metalorganic Vapor Phase Epitaxy." In: *Japanese Journal of Applied Physics* 35.2S, p. 1280. DOI: 10.1143/JJAP.35.1280 (cit. on pp. 118, 157).

Jabbour, M. E. (2005). "Epitaxy of Binary Compounds and Alloys." In: *Journal of Elasticity* 80.1-3, pp. 153–182. DOI: 10.1007/s10659-005-9030-4 (cit. on pp. 62, 65, 69).

Jeong, H.-C. and E. D. Williams (1999). "Steps on surfaces: experiment and theory." In: *Surface Science Reports* 34.6, pp. 171 –294. DOI: 10.1016/S0167-5729(98)00010-7 (cit. on pp. 61, 69, 70, 158, 160).

Johnson, M., K. Leung, A. Birch, B. Orr, and J. Tersoff (1996). "Adatom concentration on GaAs(001) during MBE annealing." In: *Surface Science* 350.1, pp. 254 –258. DOI: 10.1016/0039-6028(95)01110-2 (cit. on p. 156).

Johnson, M., K. Leung, A. Birch, and B. Orr (1997). "Adatom concentration on GaAs(0 0 1) during annealing." In: *Journal of Crystal Growth* 174.1. American Crystal Growth 1996 and Vapor Growth and Epitaxy 1996, pp. 572 –578. DOI: 10.1016/S0022-0248(97)00039-0 (cit. on p. 156).

Kandel, D. and E. Kaxiras (1996). "Microscopic Theory of Electromigration on Semiconductor Surfaces." In: *Physical Review Letters* 76.7, pp. 1114–1117. DOI: 10.1103/physrevlett.76.1114 (cit. on pp. 59, 125).

Kasu, M. and T. Fukui (1992). "Multi-Atomic Steps on Metalorganic Chemical Vapor Deposition-Grown GaAs Vicinal Surfaces Studied by Atomic Force Microscopy." In: *Japanese Journal of Applied Physics* 31.7A, p. L864. DOI: 10.1143/JJAP.31.L864 (cit. on pp. 118, 157).

Keller, J. B., H. G. Cohen, and G. J. Merchant (1993). "The stability of rapidly growing or evaporating crystals." In: *Journal of Applied Physics* 73.8, pp. 3694–3697. DOI: 10.1063/1.352929 (cit. on pp. 81, 84, 86).

Kosolobov, S. and A. Latyshev (2010). "Step Bunching on Silicon Surface Under Electromigration." In: *Nanophenomena at Surfaces*. Springer Berlin Heidelberg, pp. 239–258. DOI: 10.1007/978-3-642-16510-8_11 (cit. on p. 60).

Krug, J. (1997). "Origins of scale invariance in growth processes." In: *Advances in Physics* 46.2, pp. 139–282. DOI: 10.1080/00018739700101498 (cit. on pp. 118, 158).

Krug, J. (2005). "Introduction to Step Dynamics and Step Instabilities." In: *Multiscale Modeling in Epitaxial Growth*. Ed. by A. Voigt. Basel: Birkhäuser Basel, pp. 69–95. DOI: 10.1007/3-7643-7343-1_6 (cit. on pp. 60, 61, 64, 70, 78, 81, 83, 134, 156).

Kukta, R. V., A. Peralta, and D. Kouris (2002). "Elastic Interaction of Surface Steps: Effect of Atomic-Scale Roughness." In: *Physical Review Letters* 88.18. DOI: 10.1103/physrevlett.88.186102 (cit. on p. 75).

Kukta, R. and K. Bhattacharya (2002). "A micromechanical model of surface steps." In: *Journal of the Mechanics and Physics of Solids* 50.3, pp. 615–649. DOI: 10.1016/s0022-5096(01)00079-5 (cit. on p. 75).

Latyshev,
on clean Si(111) stepped surface during sublimation." In: *Surface Science* 213.1, pp. 157–169. DOI: 10.1016/0039-6028(89)90256-2 (cit. on pp. 59, 123).

Latyshev, A., L. Fedina, S. Kosolobov, S. Sitnikov, D. Rogilo, E. Rodyakina, D. Nasimov, D. Sheglov, and A. Aseev (2017). "Atomic Processes on the Silicon Surface." In: *Advances in Semiconductor Nanostructures*. Elsevier, pp. 189–221. DOI: 10.1016/b978-0-12-810512-2.00008-1 (cit. on p. 58).

Liu, D.-J. (1996). "Relaxation of the step profile for different microscopic mechanisms." In: *Journal of Vacuum Science & Technology B: Microelectronics and Nanometer Structures* 14.4, p. 2799. DOI: 10.1116/1.588836 (cit. on p. 59).

Liu, D.-J. and J. D. Weeks (1998). "Quantitative theory of current-induced step bunching on Si(111)." In: *Physical Review B* 57.23, pp. 14891–14900. DOI: 10.1103/physrevb.57.14891 (cit. on p. 59).

Love, A. E. H. (2013). *A treatise on the mathematical theory of elasticity*. Cambridge university press. URL: https://hal.archives-ouvertes.fr/hal-01307751/ (cit. on p. 75).

Magri, R., S. K. Gupta, and M. Rosini (2014). "Step energy and step interactions on the reconstructed GaAs(001) surface." In: *Physical Review B* 90.11. DOI: 10.1103/physrevb.90.115314 (cit. on p. 159).

Magri, R., S. K. Gupta, and M. Rosini (2016). "Erratum: Step energy and step interactions on the reconstructed GaAs(001) surface [Phys. Rev. B 90 , 115314 (2014)]." In: *Physical Review B* 94.23. DOI: 10.1103/physrevb.94.239909 (cit. on p. 159).

Man, K., A. Pang, and M. Altman (2007). "Kinetic length and step permeability on the Si(111) (1×1) surface." In: *Surface Science* 601.20, pp. 4669–4674. DOI: 10.1016/j.susc.2007.05.039 (cit. on p. 160).

Marchenko, V. and A. Y. Parshin (1980). "Elastic properties of crystal surfaces." In: *Sov. Phys. JETP* 52.1, pp. 129–131. URL: http://jetp.ac.ru/cgi-bin/dn/e_052_01_0129.pdf (cit. on pp. 73, 75).

Métois, J. and S. Stoyanov (1999). "Impact of the growth on the stability–instability transition at Si (111) during step bunching induced by electromigration." In: *Surface Science* 440.3, pp. 407–419. DOI: 10.1016/s0039-6028(99)00817-1 (cit. on pp. 64, 123–125, 130, 131).

Michely, T. and J. Krug (2012). *Islands, mounds and atoms*. Vol. 42. Springer Science & Business Media. DOI: 10.1007/978-3-642-18672-1 (cit. on pp. 57, 61, 81, 83, 84, 155).

Misbah, C., O. Pierre-Louis, and Y. Saito (2010). "Crystal surfaces in and out of equilibrium: A modern view." In: *Reviews of Modern Physics* 82.1, pp. 981–1040. DOI: 10.1103/revmodphys.82.981 (cit. on pp. 61, 64).

Muller, P (2004). "Elastic effects on surface physics." In: *Surface Science Reports* 54.5-8, pp. 157–258. DOI: 10.1016/j.surfrep.2004.05.001 (cit. on pp. 74, 75).

Mysliveček, J, C Schelling, F Schäffler, G Springholz, P Šmilauer, J Krug, and B Voigtländer (2002). "On the microscopic origin of the kinetic step bunching instability on vicinal Si(001)." In: *Surface Science* 520.3, pp. 193–206. DOI: 10.1016/s0039-6028(02)02273-2 (cit. on p. 61).

Natori, A. (1994). "Step Structure Transformation Induced by DC on Vicinal Si(111)." In: *Japanese Journal of Applied Physics* 33.Part 1, No. 6A, pp. 3538–3544. DOI: 10.1143/jjap.33.3538 (cit. on pp. 72, 125).

Neave, J. H., P. J. Dobson, B. A. Joyce, and J. Zhang (1985). "Reflection high-energy electron diffraction oscillations from vicinal surfaces—a new approach to surface diffusion measurements." In: *Applied Physics Letters* 47.2, pp. 100–102. DOI: 10.1063/1.96281 (cit. on p. 157).

Omi, H., Y. Homma, V. Tonchev, and A. Pimpinelli (2005). "New Types of Unstable Step-Flow Growth onSi(111)-(7X7)during Molecular Beam Epitaxy: Scaling and Universality." In: *Physical Review Letters* 95.21. DOI: 10.1103/physrevlett.95.216101 (cit. on pp. 60, 118–120, 156).

Pang, A. B., K. L. Man, M. S. Altman, T. J. Stasevich, F. Szalma, and T. L. Einstein (2008). "Step line tension and step morphological evolution on the Si(111)(1×1)surface." In: *Physical Review B* 77.11. DOI: 10.1103/physrevb.77.115424 (cit. on p. 159).

Peyret, R. (2002). *Spectral methods for incompressible viscous flow*. Vol. 148. Springer-Verlag. DOI: 10.1007/978-1-4757-6557-1 (cit. on pp. 104–107).

Pierre-Louis, O. (2003a). "Phase field models for step flow." In: *Physical Review E* 68.2. DOI: 10.1103/physreve.68.021604 (cit. on p. 126).

Pierre-Louis, O. (2003b). "Step bunching with general step kinetics: stability analysis and macroscopic models." In: *Surface Science* 529.1, pp. 114 –134. DOI: 10.1016/S0039-6028(03)00075-X (cit. on pp. 69, 72, 81, 84–86, 94, 98, 118, 125, 128, 157).

Pierre-Louis, O. (2006). "Local Electromigration Model for Crystal Surfaces." In: *Physical Review Letters* 96.13. DOI: 10.1103/physrevlett.96.135901 (cit. on p. 126).

Pierre-Louis, O. and J.-J. Métois (2004). "Kinetic Step Pairing." In: *Physical Review Letters* 93.16. DOI: 10.1103/physrevlett.93.165901 (cit. on pp. 59, 126).

Pierre-Louis, O. and C. Misbah (1998). "Dynamics and fluctuations during MBE on vicinal surfaces. I. Formalism and results of linear theory." In: *Physical Review B* 58.4, pp. 2259–2275. DOI: 10.1103/physrevb.58.2259 (cit. on pp. 81, 84).

Pimpinelli, A. and A. Videcoq (2000). "Novel mechanism for the onset of morphological instabilities during chemical vapour epitaxial growth." In: *Surface Science* 445.1, pp. L23–L28. DOI: 10.1016/s0039-6028(99)01100-0 (cit. on p. 118).

Pimpinelli, A, I Elkinani, A Karma, C Misbah, and J Villain (1994). "Step motions on high-temperature vicinal surfaces." In: *Journal of Physics: Condensed Matter* 6.14, pp. 2661–2680. DOI: 10.1088/0953-8984/6/14/005 (cit. on p. 81).

Pimpinelli, A., V. Tonchev, A. Videcoq, and M. Vladimirova (2002). "Scaling and Universality of Self-Organized Patterns on Unstable Vicinal Surfaces." In:

Physical Review Letters 88.20. DOI: 10.1103/physrevlett.88.206103 (cit. on p. 134).

Politi, P. and J. Krug (2000). "Crystal symmetry, step-edge diffusion, and unstable growth." In: *Surface Science* 446.1-2, pp. 89–97. DOI: 10.1016/s0039-6028(99)01104-8 (cit. on p. 118).

Pond, K. (1994). "Step bunching and step equalization on vicinal GaAs(001) surfaces." In: *Journal of Vacuum Science & Technology B: Microelectronics and Nanometer Structures* 12.4, p. 2689. DOI: 10.1116/1.587232 (cit. on pp. 60, 118, 159).

Ranguelov, B. and S. Stoyanov (2007). "Evaporation and growth of crystals: Propagation of step-density compression waves at vicinal surfaces." In: *Physical Review B* 76.3. DOI: 10.1103/physrevb.76.035443 (cit. on pp. 81, 84–86).

Ranguelov, B. and S. Stoyanov (2008). "Instabilities at vicinal crystal surfaces: Competition between electromigration of adatoms and kinetic memory effect." In: *Physical Review B* 77.20. DOI: 10.1103/physrevb.77.205406 (cit. on p. 85).

Ranguelov, B., P. MÃijller, J.-J. Metois, and S. Stoyanov (2017). "Step density waves on growing vicinal crystal surfaces – Theory and experiment." In: *Journal of Crystal Growth* 457, pp. 184–187. DOI: 10.1016/j.jcrysgro.2016.06.041 (cit. on p. 85).

Rogilo, D. I., L. I. Fedina, S. S. Kosolobov, B. S. Ranguelov, and A. V. Latyshev (2013). "Critical Terrace Width for Two-Dimensional Nucleation during Si Growth on Si(111)-(7X7) Surface." In: *Physical Review Letters* 111.3. DOI: 10.1103/physrevlett.111.036105 (cit. on pp. 118, 157).

Rogilo, D. I., N. E. Rybin, L. I. Fedina, and A. V. Latyshev (2016). "Adatom concentration distribution on an extrawide Si(111) terrace during sublimation." In: *Optoelectronics, Instrumentation and Data Processing* 52.5, pp. 501–507. DOI: 10.3103/S8756699016050125 (cit. on pp. 156, 159, 160).

Ronda, A and I Berbezier (2004). "Self-patterned Si surfaces as templates for Ge islands ordering." In: *Physica E: Low-dimensional Systems and Nanostructures* 23.3-4, pp. 370–376. DOI: 10.1016/j.physe.2003.12.136 (cit. on pp. 61, 156).

Salmi, M., M Alatalo, T Ala-Nissila, and R. Nieminen (1999). "Energetics and diffusion paths of gallium and arsenic adatoms on flat and stepped GaAs(001) surfaces." In: *Surface Science* 425.1, pp. 31–47. DOI: 10.1016/s0039-6028(99)00180-6 (cit. on pp. 118, 158).

Sato, M., M. Uwaha, and Y. Saito (2000). "Instabilities of steps induced by the drift of adatoms and effect of the step permeability." In: *Physical Review B* 62.12, pp. 8452–8472. DOI: 10.1103/physrevb.62.8452 (cit. on p. 98).

Schwoebel, R. L. (1969). "Step Motion on Crystal Surfaces. II." In: *Journal of Applied Physics* 40.2, pp. 614–618. DOI: 10.1063/1.1657442 (cit. on p. 62).

Shilkrot, L. E. and D. J. Srolovitz (1996). "Elastic field of a surface step: Atomistic simulations and anisotropic elastic theory." In: *Physical Review B* 53.16, pp. 11120–11127. DOI: 10.1103/physrevb.53.11120 (cit. on p. 72).

Shinohara, M. and N. Inoue (1995). "Behavior and mechanism of step bunching during metalorganic vapor phase epitaxy of GaAs." In: *Applied Physics Letters* 66.15, pp. 1936–1938. DOI: 10.1063/1.113282 (cit. on pp. 118, 157).

Slanina, F., J. Krug, and M. Kotrla (2005). "Kinetics of step bunching during growth: A minimal model." In: *Physical Review E* 71.4. DOI: 10.1103/physreve.71.041605 (cit. on p. 118).

Šmilauer, P. and D. D. Vvedensky (1995). "Coarsening and slope evolution during unstable spitaxial growth." In: *Physical Review B* 52.19, pp. 14263–14272. DOI: 10.1103/physrevb.52.14263 (cit. on pp. 61, 118, 158).

Stewart, J., O. Pohland, and J. M. Gibson (1994). "Elastic-displacement field of an isolated surface step." In: *Phys. Rev. B* 49 (19), pp. 13848–13858. DOI: 10.1103/PhysRevB.49.13848 (cit. on pp. 73–75, 119, 158).

Stoyanov, S. (1990). "Heating Current Induced Conversion between 2X1 and 1X2 Domains at Vicinal (001) Si Surfaces–Can it be Explained by Electromigration of Si Adatoms?" In: *Japanese Journal of Applied Physics* 29.4A, p. L659. DOI: 10.1143/JJAP.29.L659 (cit. on p. 59).

Stoyanov, S. (1998). "New type of step bunching instability at vicinal surfaces in crystal evaporation affected by electromigration." In: *Surface Science* 416.1-2, pp. 200–213. DOI: 10.1016/s0039-6028(98)00582-2 (cit. on pp. 59, 125).

Stoyanov, S., J. Métois, and V. Tonchev (2000). "Current induced bunches of steps on the Si(111) surface – a key to measuring the temperature dependence of the step interaction coefficient." In: *Surface Science* 465.3, pp. 227–242. DOI: 10.1016/s0039-6028(00)00652-x (cit. on pp. 123, 125, 160).

Stoyanov, S. (1991). "Electromigration Induced Step Bunching on Si Surfaces – How Does it Depend on the Temperature and Heating Current Direction?" In: *Japanese Journal of Applied Physics* 30.Part 1, No. 1, pp. 1–6. DOI: 10.1143/jjap.30.1 (cit. on pp. 125, 128).

Suga, N., J. Kimpara, N.-J. Wu, H. Yasunaga, and A. Natori (2000). "Novel Transition Mechanism of Surface Electromigration Induced Step Structure on Vicinal Si(111) Surfaces." In: *Japanese Journal of Applied Physics* 39.Part 1, No. 7B, pp. 4412–4416. DOI: 10.1143/jjap.39.4412 (cit. on p. 125).

Teichert, C., J. Bean, and M. Lagally (1998). "Self-organized nanostructures in Si 1-x Ge x films on Si(001)." In: *Applied Physics A: Materials Science & Processing* 67.6, pp. 675–685. DOI: 10.1007/s003390050839 (cit. on p. 61).

Tejedor, P., F. Allegretti, P. Šmilauer, and B. Joyce (1998). "Temperature-dependent unstable homoepitaxy on vicinal GaAs(110) surfaces." In: *Surface Science* 407.1-3, pp. 82–89. DOI: 10.1016/s0039-6028(98)00149-6 (cit. on p. 118).

Tersoff, J., Y. H. Phang, Z. Zhang, and M. G. Lagally (1995). "Step-Bunching Instability of Vicinal Surfaces under Stress." In: *Phys. Rev. Lett.* 75 (14), pp. 2730–2733. DOI: 10.1103/PhysRevLett.75.2730 (cit. on pp. 72, 73, 98).

Tersoff, J., M. D. Johnson, and B. G. Orr (1997). "Adatom Densities on GaAs: Evidence for Near-Equilibrium Growth." In: *Phys. Rev. Lett.* 78 (2), pp. 282–285. DOI: 10.1103/PhysRevLett.78.282 (cit. on p. 156).

Thürmer, K., D.-J. Liu, E. D. Williams, and J. D. Weeks (1999). "Onset of Step Antibanding Instability due to Surface Electromigration." In: *Physical Review*

Letters 83.26, pp. 5531–5534. DOI: 10.1103/physrevlett.83.5531 (cit. on p. 59).

Van Hove, J. and P. Cohen (1987). "Reflection high energy electron diffraction measurement of surface diffusion during the growth of gallium arsenide by MBE." In: *Journal of Crystal Growth* 81.1-4, pp. 13–18. DOI: 10.1016/0022-0248(87)90357-5 (cit. on p. 157).

Vladimirova, M., A. D. Vita, and A. Pimpinelli (2001). "Dimer diffusion as a driving mechanism of the step bunching instability during homoepitaxial growth." In: *Physical Review B* 64.24. DOI: 10.1103/physrevb.64.245420 (cit. on p. 118).

Voigtlander, B., A. Zinner, T. Weber, and H. P. Bonzel (1995). "Modification of growth kinetics in surfactant-mediated epitaxy." In: *Physical Review B* 51.12, pp. 7583–7591. DOI: 10.1103/physrevb.51.7583 (cit. on pp. 118, 157).

Yang, Y.-N. and E. D. Williams (1994). "High atom density in the 1X1 phase and origin of the metastable reconstructions on Si(111)." In: *Phys. Rev. Lett.* 72 (12), pp. 1862–1865. DOI: 10.1103/PhysRevLett.72.1862 (cit. on p. 156).

Yang, Y.-N., E. S. Fu, and E. D. Williams (1996). "An STM study of current-induced step bunching on Si(111)." In: *Surface Science* 356.1, pp. 101 –111. DOI: 10.1016/0039-6028(96)00033-7 (cit. on pp. 123, 125, 160).

Zhao, T. and J. D. Weeks (2005). "A two-region diffusion model for current-induced instabilities of step patterns on vicinal Si(111) surfaces." In: *Surface Science* 580.1-3, pp. 107–121. DOI: 10.1016/j.susc.2005.02.015 (cit. on p. 126).

Zhao, T., J. D. Weeks, and D. Kandel (2004). "Unified treatment of current-induced instabilities onSisurfaces." In: *Physical Review B* 70.16. DOI: 10.1103/physrevb.70.161303 (cit. on p. 126).

Admal, N. C. and E. B. Tadmor (2010). "A unified interpretation of stress in molecular systems." In: *Journal of Elasticity* 100.1-2, pp. 63–143. DOI: 10.1007/s10659-010-9249-6 (cit. on pp. 172, 177).

Bae, S., H. Kim, Y. Lee, X. Xu, J.-S. Park, Y. Zheng, J. Balakrishnan, T. Lei, H. R. Kim, Y. I. Song, et al. (2010). "Roll-to-roll production of 30-inch graphene films for transparent electrodes." In: *Nature nanotechnology* 5.8, pp. 574–578. DOI: 10.1038/nnano.2010.132 (cit. on p. 164).

Barenblatt, G. I. (1962). "The mathematical theory of equilibrium cracks in brittle fracture." In: *Advances in applied mechanics* 7.1, pp. 55–129. DOI: 10.1016/S0065-2156(08)70121-2 (cit. on pp. 165, 171).

Bitzek, E., J. R. Kermode, and P. Gumbsch (2015). "Atomistic aspects of fracture." In: *International Journal of Fracture* 191.1-2, pp. 13–30. DOI: 10.1007/s10704-015-9988-2 (cit. on p. 183).

Brenner, D. W., O. A. Shenderova, J. A. Harrison, S. J. Stuart, B. Ni, and S. B. Sinnott (2002). "A second-generation reactive empirical bond order (REBO) potential energy expression for hydrocarbons." In: *Journal of Physics: Condensed Matter* 14.4, p. 783. DOI: 10.1088/0953-8984/14/4/312 (cit. on p. 173).

De Borst, R. (2003). "Numerical aspects of cohesive-zone models." In: *Engineering fracture mechanics* 70.14, pp. 1743–1757. DOI: 10.1016/S0013-7944(03)00122-X (cit. on p. 186).

De Graef, M. and M. E. McHenry (2007). *Structure of materials: an introduction to crystallography, diffraction and symmetry*. Cambridge University Press. DOI: 10.1107/S0108767312016534 (cit. on p. 167).

Dugdale, D. (1960). "Yielding of steel sheets containing slits." In: *Journal of the Mechanics and Physics of Solids* 8.2, pp. 100–104. DOI: 10.1016/0022-5096(60)90013-2 (cit. on pp. 165, 171).

Freund, L. B. (1998). *Dynamic fracture mechanics*. Cambridge university press. DOI: 10.1017/CBO9780511546761 (cit. on p. 181).

Gall, K., M. Horstemeyer, M. Van Schilfgaarde, and M. Baskes (2000). "Atomistic simulations on the tensile debonding of an aluminum–silicon interface." In: *Journal of the Mechanics and Physics of Solids* 48.10, pp. 2183–2212. DOI: 10.1016/S0022-5096(99)00086-1 (cit. on pp. 173, 184).

Geubelle, P. H. and J. S. Baylor (1998). "Impact-induced delamination of composites: a 2D simulation." In: *Composites Part B: Engineering* 29.5, pp. 589–602. DOI: 10.1016/S1359-8368(98)00013-4 (cit. on pp. 165, 178).

Grantab, R., V. B. Shenoy, and R. S. Ruoff (2010). "Anomalous strength characteristics of tilt grain boundaries in graphene." In: *Science* 330.6006, pp. 946–948. DOI: 10.1126/science.1196893 (cit. on pp. 169, 173).

Griffith, A. A. (1921). "The phenomena of rupture and flow in solids." In: *Philosophical transactions of the royal society of london. Series A, containing papers of*

a mathematical or physical character, pp. 163–198. DOI: 10.1098/rsta.1921.0006 (cit. on p. 179).

Hillerborg, A., M. Modéer, and P.-E. Petersson (1976). "Analysis of crack formation and crack growth in concrete by means of fracture mechanics and finite elements." In: *Cement and Concrete Research* 6.6, pp. 773–781. DOI: 10.1016/0008-8846(76)90007-7 (cit. on pp. 165, 179, 184).

Holland, D. J. M. and M. Marder (1999). *Cracks and atoms*. University of Texas at Austin. DOI: 10.1002/(SICI)1521-4095(199907)11:10<793::AID-ADMA793>3.0.CO;2-B (cit. on p. 183).

Huang, P. Y., C. S. Ruiz-Vargas, A. M. van der Zande, W. S. Whitney, M. P. Levendorf, J. W. Kevek, S. Garg, J. S. Alden, C. J. Hustedt, Y. Zhu, et al. (2011). "Grains and grain boundaries in single-layer graphene atomic patchwork quilts." In: *Nature* 469.7330, pp. 389–392. DOI: 10.1038/nature09718 (cit. on pp. 164, 168).

Khare, R., S. L. Mielke, J. T. Paci, S. Zhang, R. Ballarini, G. C. Schatz, and T. Belytschko (2007). "Coupled quantum mechanical/molecular mechanical modeling of the fracture of defective carbon nanotubes and graphene sheets." In: *Physical Review B* 75.7, p. 075412. DOI: 10.1103/PhysRevB.75.075412 (cit. on p. 173).

Kim, K., Z. Lee, W. Regan, C Kisielowski, M. Crommie, and A Zettl (2011). "Grain boundary mapping in polycrystalline graphene." In: *ACS nano* 5.3, pp. 2142–2146. DOI: 10.1021/nn1033423 (cit. on p. 168).

Kim, S. Y. and H. S. Park (2011). "On the effective plate thickness of monolayer graphene from flexural wave propagation." In: *Journal of Applied Physics* 110.5, p. 054324. DOI: 10.1063/1.3633230 (cit. on p. 175).

Krull, H. and H. Yuan (2011). "Suggestions to the cohesive traction–separation law from atomistic simulations." In: *Engineering Fracture Mechanics* 78.3, pp. 525–533. DOI: 10.1016/j.engfracmech.2009.12.014 (cit. on pp. 166, 174, 186).

Lawn, B. R. (1993). *Fracture of brittle solids*. Cambridge university press. DOI: 10.1017/CBO9780511623127 (cit. on p. 179).

Lee, C., X. Wei, J. W. Kysar, and J. Hone (2008). "Measurement of the elastic properties and intrinsic strength of monolayer graphene." In: *science* 321.5887, pp. 385–388. DOI: 10.1126/science.1157996 (cit. on pp. 164, 185).

Lee, G.-H., R. C. Cooper, S. J. An, S. Lee, A. van der Zande, N. Petrone, A. G. Hammerberg, C. Lee, B. Crawford, W. Oliver, et al. (2013). "High-strength chemical-vapor–deposited graphene and grain boundaries." In: *Science* 340.6136, pp. 1073–1076. DOI: 10.1126/science.1235126 (cit. on pp. 164, 165, 170).

Malola, S., H. Häkkinen, and P. Koskinen (2010). "Structural, chemical, and dynamical trends in graphene grain boundaries." In: *Physical Review B* 81.16, p. 165447. DOI: 10.1103/PhysRevB.81.165447 (cit. on p. 168).

Möller, J. J. and E. Bitzek (2014). "Fracture toughness and bond trapping of grain boundary cracks." In: *Acta Materialia* 73, pp. 1–11. DOI: 10.1016/j.actamat.2014.03.035 (cit. on p. 183).

Needleman, A (1987). "A continuum model for void nucleation by inclusion debonding." In: *Journal of applied mechanics* 54.3, pp. 525–531. DOI: 10.1115/1.3173064 (cit. on p. 165).

Needleman, A (1990). "An analysis of tensile decohesion along an interface." In: *Journal of the Mechanics and Physics of Solids* 38.3, pp. 289–324. DOI: 10.1016/0022-5096(90)90001-K (cit. on p. 165).

Novoselov, K. S., A. K. Geim, S. Morozov, D Jiang, Y. Zhang, S. Dubonos, I. Grigorieva, and A. Firsov (2004). "Electric field effect in atomically thin carbon films." In: *science* 306.5696, pp. 666–669. DOI: 10.1126/science.1102896 (cit. on p. 163).

Orowan, E (1949). "Fracture and strength of solids." In: *Rep. Prog. Phys* 12, p. 185. DOI: 10.1088/0034-4885/12/1/309 (cit. on p. 179).

Park, K., G. H. Paulino, and J. R. Roesler (2009). "A unified potential-based cohesive model of mixed-mode fracture." In: *Journal of the Mechanics and Physics of Solids* 57.6, pp. 891–908. DOI: 10.1016/j.jmps.2008.10.003 (cit. on p. 170).

Pastewka, L., P. Pou, R. Pérez, P. Gumbsch, and M. Moseler (2008). "Describing bond-breaking processes by reactive potentials: Importance of an environment-dependent interaction range." In: *Physical Review B* 78.16, p. 161402. DOI: 10.1103/PhysRevB.78.161402 (cit. on pp. 173, 174).

Perriot, R., X. Gu, Y. Lin, V. V. Zhakhovsky, and I. I. Oleynik (2013). "Screened environment-dependent reactive empirical bond-order potential for atomistic simulations of carbon materials." In: *Physical Review B* 88.6, p. 064101. DOI: 10.1103/PhysRevB.88.064101 (cit. on p. 173).

Plimpton, S. (1995). "Fast parallel algorithms for short-range molecular dynamics." In: *Journal of computational physics* 117.1, pp. 1–19. DOI: 10.1006/jcph.1995.1039 (cit. on p. 174).

Rasool, H. I., C. Ophus, W. S. Klug, A Zettl, and J. K. Gimzewski (2013). "Measurement of the intrinsic strength of crystalline and polycrystalline graphene." In: *Nature communications* 4. DOI: 10.1038/ncomms3811 (cit. on p. 170).

Rasool, H. I., C. Ophus, Z. Zhang, M. F. Crommie, B. I. Yakobson, and A. Zettl (2014). "Conserved Atomic Bonding Sequences and Strain Organization of Graphene Grain Boundaries." In: *Nano letters* 14.12, pp. 7057–7063. DOI: 10.1021/nl503450r (cit. on p. 168).

Remmers, J. J. C., R. De Borst, C. V. Verhoosel, and A. Needleman (2013). "The cohesive band model: a cohesive surface formulation with stress triaxiality." In: *Int J Fract* 181.2, pp. 177–188. DOI: 10.1007/s10704-013-9834-3 (cit. on p. 170).

Saether, E. (2008). "A Multiscale Method for Simulating Fracture in Polycrystalline Metals." PhD thesis. Virginia Polytechnic Institute and State University. URL: https://vtechworks.lib.vt.edu/handle/10919/27816 (cit. on p. 187).

Shet, C and N Chandra (2002). "Analysis of energy balance when using cohesive zone models to simulate fracture processes." In: *Journal of engineering materials and technology* 124.4, pp. 440–450. DOI: 10.1115/1.1494093 (cit. on p. 179).

Siegmund, T. and W. Brocks (1999). "Prediction of the work of separation and implications to modeling." In: *International Journal of Fracture* 99.1-2, pp. 97–116. DOI: 10.1023/A:1018300226682 (cit. on p. 170).

Spearot, D. E., K. I. Jacob, and D. L. McDowell (2004). "Non-local separation constitutive laws for interfaces and their relation to nanoscale simulations." In: *Mechanics of Materials* 36.9, pp. 825–847. DOI: 10.1016/j.mechmat.2003.08.002 (cit. on p. 173).

Stuart, S. J., A. B. Tutein, and J. A. Harrison (2000). "A reactive potential for hydrocarbons with intermolecular interactions." In: *The Journal of chemical physics* 112.14, pp. 6472–6486. DOI: 10.1063/1.481208 (cit. on p. 173).

Stukowski, A. (2010). "Visualization and analysis of atomistic simulation data with OVITO–the Open Visualization Tool." In: *Modelling and Simulation in Materials Science and Engineering* 18.1, p. 015012. DOI: 10.1088/0965-0393/18/1/015012 (cit. on p. 176).

Tadmor, E. B. and R. E. Miller (2011). *Modeling materials: continuum, atomistic and multiscale techniques*. Cambridge University Press. DOI: 10.1017/CBO9781139003582 (cit. on pp. 172, 176, 177).

Thomson, R., C Hsieh, and V Rana (1971). "Lattice trapping of fracture cracks." In: *Journal of Applied Physics* 42.8, pp. 3154–3160. DOI: 10.1063/1.1660699 (cit. on p. 183).

Turon, A., C. G. Davila, P. P. Camanho, and J Costa (2007). "An engineering solution for mesh size effects in the simulation of delamination using cohesive zone models." In: *Engineering fracture mechanics* 74.10, pp. 1665–1682. DOI: 10.1016/j.engfracmech.2006.08.025 (cit. on pp. 185–188).

Wei, X. and J. W. Kysar (2012). "Experimental validation of multiscale modeling of indentation of suspended circular graphene membranes." In: *International Journal of Solids and Structures* 49.22, pp. 3201–3209. DOI: 10.1016/j.ijsolstr.2012.06.019 (cit. on pp. 164, 170).

Wei, X., B. Fragneaud, C. A. Marianetti, and J. W. Kysar (2009). "Nonlinear elastic behavior of graphene: Ab initio calculations to continuum description." In: *Physical Review B* 80.20, p. 205407. DOI: 10.1103/PhysRevB.80.205407 (cit. on pp. 163, 164, 169).

Wei, Y., J. Wu, H. Yin, X. Shi, R. Yang, and M. Dresselhaus (2012). "The nature of strength enhancement and weakening by pentagon–heptagon defects in graphene." In: *Nature materials* 11.9, pp. 759–763. DOI: 10.1038/nmat3370 (cit. on pp. 169, 173).

Wu, J. and Y. Wei (2013). "Grain misorientation and grain-boundary rotation dependent mechanical properties in polycrystalline graphene." In: *Journal of the Mechanics and Physics of Solids* 61.6, pp. 1421–1432. DOI: 10.1016/j.jmps.2013.01.008 (cit. on pp. 169, 173).

Yamakov, V, E Saether, D. Phillips, and E. Glaessgen (2006). "Molecular-dynamics simulation-based cohesive zone representation of intergranular fracture processes in aluminum." In: *Journal of the Mechanics and Physics of Solids* 54.9, pp. 1899–1928. DOI: 10.1016/j.jmps.2006.03.004 (cit. on pp. 166, 174, 184, 186).

Yazyev, O. V. and S. G. Louie (2010a). "Electronic transport in polycrystalline graphene." In: *Nature materials* 9.10, pp. 806–809. DOI: 10.1038/nmat2830 (cit. on p. 168).

Yazyev, O. V. and S. G. Louie (2010b). "Topological defects in graphene: Dislocations and grain boundaries." In: *Physical Review B* 81.19, p. 195420. DOI: 10.1103/PhysRevB.81.195420 (cit. on pp. 167, 168).

Zhang, J., J. Zhao, and J. Lu (2012). "Intrinsic strength and failure behaviors of graphene grain boundaries." In: *Acs Nano* 6.3, pp. 2704–2711. DOI: 10.1021/nn3001356 (cit. on p. 168).

Zhang, P., L. Ma, F. Fan, Z. Zeng, C. Peng, P. E. Loya, Z. Liu, Y. Gong, J. Zhang, X. Zhang, et al. (2014). "Fracture toughness of graphene." In: *Nature communications* 5. DOI: 10.1038/ncomms4782 (cit. on pp. 170, 173, 182, 183, 189).

Zhang, T., X. Li, and H. Gao (2015a). "Fracture of graphene: a review." In: *International Journal of Fracture*, pp. 1–31. DOI: 10.1007/s10704-015-0039-9 (cit. on p. 170).

Zhang, Z., Y. Yang, F. Xu, L. Wang, and B. I. Yakobson (2015b). "Unraveling the Sinuous Grain Boundaries in Graphene." In: *Advanced Functional Materials* 25.3, pp. 367–373. DOI: 10.1002/adfm.201403024 (cit. on p. 168).

Zhou, X., J. Zimmerman, E. Reedy, and N. Moody (2008). "Molecular dynamics simulation based cohesive surface representation of mixed mode fracture." In: *Mechanics of Materials* 40.10, pp. 832–845. DOI: 10.1016/j.mechmat.2008.05.001 (cit. on pp. 166, 174, 186).

Zimmerman, J. A., E. B. WebbIII, J. Hoyt, R. E. Jones, P. Klein, and D. J. Bammann (2004). "Calculation of stress in atomistic simulation." In: *Modelling and Simulation in Materials Science and Engineering* 12.4, S319. DOI: 10.1088/0965-0393/12/4/S03 (cit. on pp. 172, 177).

université PARIS-SACLAY
ÉCOLE DOCTORALE
Sciences mécaniques et énergétiques, matériaux et géosciences (SMEMAG)

Titre : Couplages électromécaniques et instabilités de croissance dans les semi-conducteurs

Mots clés : Multiphysique, semi-conducteur, couplage, épitaxie, instabilité, croissance.

Résumé : Ces dernières décennies, la mécanique des solides est allée au-delà de ses problématiques originelles ayant trait aux propriétés mécaniques des matériaux et des structures pour embrasser des questions issues d'autres champs scientifiques et en particulier de la physique. Les semi-conducteurs, matériaux de base de tous les dispositifs électroniques, sont un bon exemple où des solides cristallins présentent des couplages mutiphysiques. En effet, la mécanique y joue un rôle important, à la fois dans le processus de fabrication et dans l'utilisation des dispositifs électroniques. Dans ce travail, nous examinons ces deux aspects en étudiant dans une première partie les couplages entre les phénomènes de transport électronique et les déformations mécaniques et dans une seconde partie les instabilités morphologiques qui apparaissent lors de la croissance épitaxiale des semi-conducteurs.
Premièrement, en développant une théorie entièrement couplée des semi-conducteurs déformables qui inclut les champs mécaniques, électrique et électroniques, nous montrons, pour la première fois, l'existence d'une contribution électronique à la contrainte mécanique. Alors que pour les semi-conducteurs cristallins cette contribution est faible, l'effet des déformations sur le transport électronique demeure important par les modifications qu'elles induisent sur les niveaux d'énergie de bandes, les densités d'états et les mobilités des électrons et des trous. Compte tenu de l'avènement de nouvelles technologies d'électronique flexible, nous mettons en application la théorie générale pour calculer, au moyen de développements asymptotiques, l'effet de la flexion – qui entraîne des déformations non uniformes – sur la caractéristique courant-tension d'une jonction p-n, la brique élémentaire des cellules solaires. Pour compléter ce tableau, nous mesurons les changements induits par des contraintes uniaxiales sur la caractéristique électronique de cellules solaires silicium à hétérojonction.
Dans la deuxième partie de ce travail, en descendant à l'échelle atomique, nous étudions le phénomène de la croissance épitaxiale sur des surfaces vicinales. Sur ces surfaces, le cristal croît par propagation de marches atomiques, qui peuvent développer de la mise en paquets, une instabilité par laquelle l'espacement régulier entre marches est brisé, donnant lieu à un motif alternant entre de larges terrasses atomiques et des paquets de marches. Au travers d'une analyse de stabilité linéaire exhaustive des équations de la dynamique des marches, nous discutons de l'influence de chaque mécanisme physique sur l'instabilité de la mise en paquets. En particulier, nous clarifions l'incidence sur la stabilité de la dynamique, de l'effet de saut d'adatomes ainsi que de l'élasticité, au-delà de l'hypothèse d'interactions de plus proches voisins. De plus, nous montrons que nos résultats généraux de stabilité, c'est-à-dire obtenus sans négliger les termes dynamiques, sont significativement différents de ceux obtenus avec l'approximation quasi-statique, et ce, même dans les régimes de déposition ou d'évaporation lentes où cette dernière était considérée comme suffisante. Non seulement intéressants d'un point de vue théorique, ces nouveaux résultats fournissent des explications possibles pour certains cas de mise en paquets observés sur le silicium et l'arséniure de gallium. Compte tenu de ces nouveaux aspects, nous réexaminons le phénomène de la mise en paquets sous électromigration et montrons que les effets de saut d'adatomes et de la dynamique n'affectent pas la dépendance de la stabilité à la direction du courant d'électromigration.
Enfin, nous étudions les propriétés mécaniques, à l'échelle atomique, d'un autre matériau cristallin aux propriétés semiconductrices, le graphène polycristallin. En utilisant des simulations de dynamique moléculaire, nous développons un modèle de zone cohésive pour la rupture le long des joints de grains.

Title : Electromechanical couplings and growth instabilities in semiconductors

Keywords : Multiphysics, semiconductor, coupling, epitaxy, instability, growth.

Abstract : In the last decades, solid mechanics has gone beyond its original issues of mechanical properties of materials and structures to embrace problems coming from other scientific fields and in particular physics. Semiconductors, the base materials of all electronic devices, are a prime example where crystalline solids show multiphysics couplings. Indeed, mechanics plays there an important role both in the fabrication process and in the operation of electronic devices. In this work, we examine these two aspects by studying first the couplings between electronic transport phenomena and mechanical deformations and second the morphological instabilities that develop in semiconductor epitaxial growth.
First, developing a fully-coupled theory of deformable semiconductors that includes mechanical, electrical and electronic fields, we show for the first time the existence of an electronic contribution to mechanical stress. While for crystalline semiconductors this contribution is weak, the effect of strains on electronic transport remains significant through their modification on band energy levels, density of states and mobility of electrons and holes. Considering the advent of new technologies of flexible electronics, we apply the general theory to compute through asymptotic expansions, the effect of bending—causing non-uniform strains—on the current-voltage characteristic of a p-n junction, the basic device of solar cells. To complete this picture, we measure the changes induced by uniaxial stresses on the electronic characteristic of a silicon heterojunction solar cell.
In the second part of this work, going down to the atomic scale, we consider the problem of epitaxial growth on vicinal surfaces. On these surfaces, the crystal grows through the propagation of the atomic steps, which may develop step bunching, an instability whereby the regular step spacing breaks down, resulting in an alternating pattern of wide atomic terraces and step bunches. Through a comprehensive linear stability analysis of the step dynamics governing equations, we discuss the influence of each physical mechanism on the step bunching instability. In particular, we clarify the impact on stability of the dynamics, of the recently pointed out adatom jump effect, and of elasticity, beyond the assumption of nearest-neighbor interactions. In addition, we show that our general stability results, i.e., obtained without neglecting the dynamics terms, are significantly different from those derived with the quasistatic approximation, even in regimes of slow deposition or evaporation where the latter was considered sufficient. Not only valuable from a theoretical prospective, these new results provide possible explanations for some cases of step bunching observed in silicon and gallium arsenide. In view of these new aspects, we reexamine the problem of step bunching under electromigration and show that the adatom jump and dynamics effects do not affect the stability dependence on the direction of the electromigration current.
Finally, we investigate the mechanical properties at the atomic scale of another crystalline material with semiconducting properties, polycrystalline graphene. Using molecular dynamics simulations, we develop a cohesive zone model for fracture along grain boundaries.

Université Paris-Saclay
Espace Technologique / Immeuble Discovery
Route de l'Orme aux Merisiers RD 128 / 91190 Saint-Aubin, France